Behaviour of Beam-Column Joints Retrofitted with High Strength Fiber Reinforced Concrete at Varying Levels of Corrosion Damage

A
Thesis
Submitted in fulfilment of the requirement
for the award of the degree of

DOCTOR OF PHILOSOPHY

by

Shubham Dangwal

(Reg No: 901802008)

Under the supervision of

Dr. Heaven Singh

Assistant Professor

Department of Civil Engineering

THAPAR INSTITUTE
OF ENGINEERING & TECHNOLOGY
(Deemed to be University)

Department of Civil Engineering
Thapar Institute of Engineering and Technology
Patiala-147004 (Punjab), India

February 2024

CERTIFICATE

I hereby certify that the work being presented in the Thesis entitled "**Behaviour of Beam-Column Joints Retrofitted with High Strength Fiber Reinforced Concrete at Varying Levels of Corrosion Damage**" in fulfillment of the requirement for the award of the degree of ***Doctor of Philosophy*** submitted in the **Civil Engineering Department** of the **Thapar Institute of Engineering and Technology** is an authentic record of my work carried out under the supervision of Dr. Heaven Singh and refer other researcher's work, which are duly listed in the reference section.

The matter presented in this Thesis has not been submitted for the award of any other degree of this or any other University.

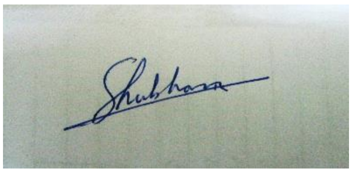

Shubham Dangwal **Date: 28-02-2024**

Reg. No. 901802008

This is to certify that the above-mentioned statement made by the candidate is correct to the best of my knowledge.

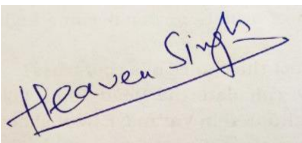

Dr. Heaven Singh
Assistant Professor
Department of Civil Engineering
Thapar Institute of Engineering &
Technology, Patiala

ACKNOWLEDGEMENT

In pursuit of my academic endeavour, I have been fortunate to have had a supportive and encouraging journey throughout these years. It feels difficult to put into words the sense of gratitude I feel for the people who helped me directly and indirectly during this phase.

With due regards, I would like to acknowledge my sincere gratitude and appreciation to my guide Dr. Heaven Singh, Assistant Professor, Department of Civil Engineering, Thapar Institute of Engineering and Technology, Patiala for his guidance and time throughout my research work. He was always available to support, guide, and advise whether my problem was professional or personal.

I would like to take this opportunity to express my sincere gratitude towards the doctoral committee members Dr. Prem Pal Bansal, Professor, Dr. Naveen Kwatra, Professor, Dr. A.B. Danie Roy, Assistant Professor, Civil Engineering Department and Dr. Tarun Nanda, Associate Professor, Mechanical Engineering Department, for providing with their valuable time and inputs in reviewing and critically examining the work during the regular monitoring in the progress monitoring meetings.

I would like to sincerely thank all the laboratory technical staff of the Department of Civil Engineering, TIET, Patiala. Special thanks to Mr. Atul Pandey, and Mr. Ram Sumiran for their advice in tackling the laboratory challenges faced during my experimental research work.

I would like to express my dearest gratitude to my fellow research scholars. I take this chance to give special thanks to Ms. Zinnia Kaur, Dr. Purnima, Dr. Ashish Tiwari, and Dr. Sanjoli Jain for always providing love and support to me in my high and low moments.

No words of mine can be sufficient to express my thanks and respect to my parents. I would especially like to thank my father for always believing in me and always encouraging me irrespective of any situation. My brother Rajat Dangwal, sister-in-law Sakshi Dangwal, and my nephew Reyansh Dangwal have been of great support throughout this phase of my life. I hope they shall always continue to be my torchbearers and inspire me towards new goals.

At the end, I thank the almighty, for giving me his blessing throughout my research work and providing me strength enough to finish this task.

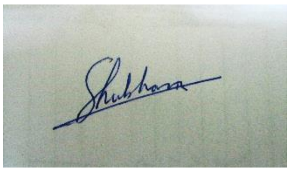

Place: Patiala **Shubham Dangwal**

Date: 28-02-2024

ABSTRACT

The exterior beam-column joints (BCJs) within a moment-resisting frame must possess high resistance against shear forces which goes hand in hand with the ability to withstand large deformations when subjected to seismic loading. The failure of RC framed structure can occur not only due to mechanical reasons but from environmental factors also. Corrosion is a prime example of the premature deterioration of RC structures by degrading strength and ductility of reinforcement.

Corrosion leads to the deposition of rust on the surface of reinforcing steel which causes a volumetric expansion in the reinforcing bars. A volume increment of approximately six to ten times that of the original steel bar can be experienced due to the formation of hydrated ferric oxide (rust) ($Fe_2O_3.xH_2O$). Due to this volume expansion at the concrete/steel interface, cracks can be experienced on the concrete surface once the concrete tensile strength surpasses. Over a significant time, corrosion can lead to a drastic reduction in rebar cross-sectional area. A deterioration of concrete and steel bond is also experienced due to the de-scaling of reinforcing bars. These phenomena can severely degrade the energy dissipation and load-carrying capacity of a corrosion-affected structure upon exposure to extreme loading conditions like an earthquake, resulting in catastrophic failure.

The present experimental study is categorized into two parts where total 16 Exterior Beam-Column joint specimens were cast and tested. In the first part, the seismic performance of Exterior BCJ specimens subjected to corrosion damage at different levels was investigated. Two different reinforcement detailing were adopted for BCJ (i.e. non-seismic and seismic). The specimens were subjected to accelerated corrosion at three levels, finalized with the help of pilot specimens. The corrosion was targeted at the junction of beam-column. Thereafter, performance of control and corroded non-seismically and seismically detailed specimens were reported and compared through various seismic parameters. The post-peak behaviour, damage progression at higher displacements, and the ultimate failure modes of corrosion-damaged specimens were covered extensively.

After assessing the performance degradation in corrosion-damaged specimens, the rehabilitation of the specimens was a requirement to ensure safety within their service period. Therefore, the second part of the experimental study focused on retrofitting of the corrosion-

damaged specimens was performed using High Strength Fiber Reinforced Concrete (HSFRC). A new retrofitting scheme was proposed to address the treatment of the corrosion-damaged reinforcing bars prior to the application of retrofitting material. The area to be retrofitted was finalized by visually monitoring the corroded reinforcement cage of the pilot specimen. The retrofitting material i.e. HSFRC was developed in the laboratory after performing several trials focusing on workability and strength. The retrofitted specimens were tested under reverse cyclic loading and the seismic performance was evaluated using similar seismic parameters to first part of the study, so as to generate a comparison between corrosion-damaged non-retrofitted and retrofitted specimens.

From the first part of the experimental study, it was concluded that seismically detailed specimens having different levels of corrosion show superior performance when compared to non-seismically detailed specimens. In general, the pitting effect on reinforcing bars leads toward bar fracture under repetitive loading ultimately resulting in reduced ductility. The ultimate failure mode shifted from shear failure at the junction of uncorroded BCJ to flexural failure at beam surface (having fractured reinforcing bars) under corrosion damage. The second part of the experimental study showed the significantly improved performance of corrosion-damaged retrofitted specimens in terms of maximum load-carrying capacity, stiffness, energy dissipation, and ductility. Due to the superior mechanical properties of HSFRC, the delay in the fracture of severely pitted reinforcing bars was experienced. Moreover, the damage progression during the cyclic loading was due to the presence of hybrid steel fibers providing the crack bridging mechanism.

The results obtained from the first part of the experimental study were numerically validated for all the tested specimens. Three-dimensional non-linear finite element (FE) models were prepared for all the specimens in the software. The numerical models were validated with the results obtained from the experimental study. It was noticed that the peak load-carrying capacity values from numerical simulations agreed acceptably with the experimental values. After the validation, the load-carrying capacity and damage progression of uncorroded and corroded specimens were captured and evaluated with the help of parameters such as Von Mises stress levels and Plastic Strain magnitude (PEMAG).

LIST OF PUBLICATIONS

The following publications in peer reviewed journals are the outcome of the present research work:

1. **S. Dangwal**, H. Singh, Behavior of corrosion damaged non-seismically and seismically detailed reinforced concrete beam-column sub-assemblages under cyclic loading, Eng. Fail. Anal. 146 (2023) 107135. https://doi.org/10.1016/j.engfailanal.2023.107135. **Impact Factor: 4**

2. **S. Dangwal,** H. Singh, Seismic performance of corroded non-seismically and seismically detailed RC beam-column joints rehabilitated with High Strength Fiber Reinforced Concrete, Eng. Struct. 291 (2023) 116481. https://doi.org/10.1016/j.engstruct.2023.116481. **Impact Factor: 5.5**

3. S. Dangwal and H. Singh, Numerical investigation of corroded reinforced concrete exterior beam-column joints under quasi-static reverse cyclic loading. https://doi.org/10.1002/suco.202400132 **Impact Factor: 3.2**

TABLE OF CONTENTS

LIST OF FIGURES

LIST OF TABLES

CHAPTER 1

INTRODUCTION

1.1 GENERAL

Reinforced concrete is a globally adopted building material used to construct durable structures due to its low construction and maintenance cost, superior mechanical properties, and excellent service life (Jung et al. 2022). However, certain factors including environmental conditions, design errors, and changes in material properties may gradually degrade the serviceability and life of the RC structure. Amongst various degrading factors, corrosion of reinforcement bars is amongst the most frequent and leading causes of the premature failure or collapse of RC structures (Goyal et al. 2018; Sharma 2018; Jung et al. 2022) . The concrete having a protective passive layer of alkaline nature (pH range of 12 to 13) is penetrated with the continuous ingress of chloride ions under extreme environmental conditions. Thereafter, the presence of oxygen and moisture encourages new chemical reactions in rebar and the surrounding concrete, which initiates corrosion (Sharma 2018). Figure 1.1 shows that the corrosion can cause severe damage to the reinforcement and may also shatter the concrete cover. This will ultimately degrade the serviceability and the structural behaviour of reinforced concrete (RC) structure (Duvnjak et al. 2021). Corrosion affects the durability of structures in two major ways. Firstly, the deposition of rust product at the rebar surface significantly increases the volume of bars, thereby, generating additional tensile stress at the interface of rebar-concrete, which eventually leads to the cracking and spalling of concrete cover. Secondly, at the severe corrosion stage, a localized cross-sectional area reduction of rebar accompanied by development of pits owing to localized dissolution of steel leads to the decline of their ultimate tensile strength and ductility, which reduces the structure’s load-bearing capacity (Almusallam et al. 1996; Cabrera 1996; Ahmad 2003; Zhang et al. 2009; Goyal et al. 2019; Kanavaris et al. 2023).

Corrosion is amongst the most unavoidable problems being faced worldwide causing immense loss of lives, infrastructure, and economic section at an immense rate (Javaherdashti 2011; Sharma 2018). In 2013, a global study on the cost of corrosion and preventive strategies was conducted by the National Association of Corrosion Engineers (NACE). An estimated cost of US$2.5 Trillion was reported for the global cost of corrosion (Koch 2017). This study was utilized in Gross Domestic Product (GDP) and World Bank Economic sector data to estimate the cost of corrosion. The global cost of corrosion was reported to be approximately 3.4% of the GDP (Javaherdashti 2000, 2011; El-Meligi 2010; Jafar Mazumder 2020). Table 1.1 below displays the Global cost (Billion US$) of corrosion in different sectors.

Figure 1. 1 Severely corroded reinforcement bars degrading the performance of RC structure (Duvnjak et al. 2021)

Table 1. 1 Global cost of corrosion by region by sectors (Billion US$ 2013) (Jafar Mazumder 2020)

Economic Regions	Sector					
	Agriculture US$ Billion	Industry US$ Billion	Services US$ Billion	Total US$ Billion	Total GDP US$ Billion	% GDP
United States	2	303.2	146	451.3	16,270	2.7
India	17.7	20.3	32.3	70.3	1,670	4.2
European Region	3.5	401	297	701.5	18,331	3.8
Arab World	13.3	34.2	92.6	140.1	2,789	5
China	56.2	192.5	146.2	394.9	9,330	4.2
Russia	5.4	37.2	41.9	84.5	2,113	4
Japan	0.6	45.9	5.1	51.6	5,002	1
Four Asian Tigers Plus Macau	1.5	29.9	27.3	58.6	2,302	2.5
Rest of the World	52.4	382.5	117.6	552.5	16,057	3.4
Global	152.7	1446.7	906	2505.4	74,314	3.4

1.2 CORROSION RELATED DAMAGE/ACCIDENTS

In general, the ingress and propagation of corrosion may accelerate the degradation of structural properties and severely reduce its service life (Otieno et al. 2016; Bahekar and Gadve 2017). In many cases, this can lead to catastrophic failure of structures resulting in the destruction of property and livelihood. Numerous corrosion-related incidents have gone unreported throughout history for reasons of liability, or in some cases, mass level of demolition of structure destroys the evidence of failure (Jafar Mazumder 2020). Some recent disasters noticed globally due to corrosion damage were the Morandi bridge in Genoa, Italy on August 14, 2018 (Rania et al. 2019) and the collapse of the Champlain Tower South Condo, Florida on June 25, 2021 (Logan and Singh 2023). Additionally, frequent earthquakes were experienced all around the globe with severe damage to infrastructure (Dogan 2015). The severe corrosion of RC structures in earthquake-prone areas will surely impact their seismic performance. Figure 1.2 shows the fractured corrosion-damaged structural members under the Niigata-Ken Chuetsu earthquake (2004) in Japan, and the Pohang earthquake (2017) in Korea (Jung et al. 2019). The propagation of corrosion degraded the tensile performance of reinforcement bars over time. In addition, it also reduced the adhesion between the surrounding concrete and steel reinforcing bars (Otieno et al. 2010; Andrade 2023). This degraded the seismic performance of structural members under severe earthquakes resulting in complete failure (Dogan 2015). Table 1.2 lists some of the major corrosion-related accidents and structural collapses that have occurred all over the world in the last 50-60 years. From the table, it is evident that this problem has claimed many human lives, and caused substantial monetary and environmental losses.

(a) (b)

Figure 1. 2 Corroded RC beams and columns damaged during earthquakes (a) Niigata-Ken Chuetsu earthquake (2004) in Japan, (b) Pohang earthquake (2017) in Korea (Jung et al. 2019)

Table 1. 2 List of some renowned corrosion accidents (Jafar Mazumder 2020)

Accidents	Place	Year	Damage and Reason
Collapse of Silver Bridge	Ohio, USA	1967	The U.S. Highway 35 bridge connecting West Virginia, Kanauga, Ohio, and Point Pleasant collapsed into the Ohio River. Corrosion fatigue and stress corrosion cracking were the prime reasons for the collapse, claiming 46 lives.
Bhopal Accident	Bhopal, India	1984	The leakage of methylisocyanate (MIC) gas from the storage tanks due to corroded valves, pipelines, and other safety equipment. The death rate was claimed to be more than 3000 and 500,000 people were reported to be injured.
Collapse of the roof of Swimming Pool	Uster, Switzerland	1985	The collapse of the concrete roof due to the stress corrosion cracking of stainless steel which was supporting the roof. The loss of lives was reported to be 12.
The Aloha Incident	Island of Maui, Hawaii	1988	A significant portion of the upper fuselage of a Boeing 737 was lost in an operating flight due to multiple corrosion fatigue damage. One flight attendant lost her life.
EL AL Boeing 747 Crash	Amsterdam, The Nether-lands	1992	Two right engines separated from the wing because the corrosion-damaged fuse pins were unable to hold the strut to the wings, resulting in the crash. 4-people were killed on board and more than 50 people on the ground.
Sewer Ex-plosion in Guadalajara	Guadalaja-ra, Mexico	1992	The galvanic corrosion of a galvanized steel pipeline blocked with a steel gasoline pipeline resulted in the sewer explosion. The death and injury rates were reported to be 215 and 1500 people.
Sinking of the Erika	Brittany, France	1999	Approximately 19800 tons of heavy fuel oil spilled and caused severe economic consequences for the region The reason was the corrosion in the main deck coaming, the portside, and starboard inert gas system risers.
Pipeline Explosion at Carlsbad	New Mexi-co, USA	2000	A severe internal corrosion in a 30-inch natural gas pipeline led to a Natural Gas explosion in El Paso. 12 people were killed.
Prudhoe Bay Oil Spill	Prudhoe Bay, Alaska	2006	A leakage of approximately 267,000 gallons of crude oil was reported due to a corroded transit pipeline.
Rupture of a High-Pres-sure Vessel	Illinois, USA	2009	The Nihon Dempa Kogyo (NDK) Company experienced an explosion due to the stress corrosion cracking of the walls of a pressure vessel. This explosion killed 1-person and wounded several others.
Rupture of a Natural Gas Transmission Pipeline	Pennsylva-nia, USA	2016	Rupturing of a 30-inch diameter natural gas transmission pipeline due to corrosion along with two of the circumferential welds. One home was destroyed, three were partially damaged, and several homes were evacuated.
Ohio State Fair accident	Ohio, USA	2017	Rust caused the failure of a pendulum-type thrill ride during operation (due to rust the thickness of the ride beam's wall was reduced). The malfunction left 1-person dead and several others injured.

1.3 CORROSION IN REINFORCED CONCRETE STRUCTURES

Corrosion degrades structural performance primarily in two ways i.e., by causing the spalling and cracking of surrounding concrete and through a gradual reduction in the cross-sectional area of rebar. Therefore, comprehending the corrosion mechanism in relation to its beginning, advancement, and severe damage is crucial.

Once the passive layer of concrete around the steel bar is breached, electrons and ions exchange commence and reactions taking place result in the appearance of rust on the steel surface. The oxidation of iron takes place in the anodic reaction when steel in concrete corrodes thereby, releasing electrons and ferrous ions (Andrade 2007).

$$Fe \rightarrow Fe^{+2} + 2e^{-} \quad \textit{(anodic reaction)} \tag{1.1}$$

The reaction will take place in the availability of water and oxygen forming hydroxyl ions (OH^-) (JP. 1390).

$$2e^{-} + H_2O + 1/2\ O_2 \rightarrow 2OH^{-} \ \textit{(cathodic reaction)} \tag{1.2}$$

Hydroxyl ions generated from cathodic reaction combine with the ferrous ions to form ferrous hydroxide ($Fe(OH)_2$). It can undergo additional oxidation to produce other oxides, including ferric hydroxide. After undergoing several stages of oxidation and hydration reactions, hydrated ferric oxide (rust) Fe_2O_3, is formed (JP. 1390).

$$Fe^{2+} + 2OH^{-} \rightarrow Fe(OH)_2 \tag{1.3}$$

$$4Fe(OH)_2 + O_2 + 2H_2O \rightarrow 4Fe(OH)_3 \tag{1.4}$$

$$2Fe(OH)_3 \rightarrow Fe_2O_3.H_2O + 2H_2O \tag{1.5}$$

Due to the accumulation of rust products over reinforcement, volume of the bar is significantly increased. The presence of unhydrated ferric oxide can cause the volume of a steel bar to swell to almost twice its original volume. In a hydrated state, a massive volume increment of six to ten times of original steel volume at the steel-concrete interface is experienced (JP. 1390; Andrade 2007; Dabas 2022). Owing to their volumetric dilation, the rust-deposited bars exert additional tensile stress on concrete leading to the spalling and cracking of the concrete, as shown in Figure 1.3. Ultimately, this leads to the exposure of reinforcement bars within RC structures to the outer environment for further severe damage (El Maaddawy et al. 2006; Sharma 2018).

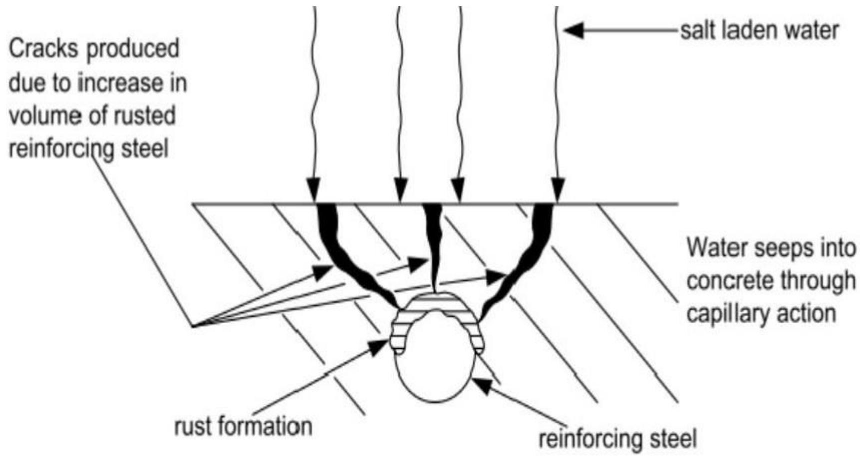

Figure 1. 3 Chloride-induced reinforcement corrosion in concrete (Ontario. Transportation Engineering Branch. Bridge Office. 2008)

The two primary causes of corrosion of steel in any RC structures are ***Carbonation*** and ***Chloride attack*** where through the pores in the concrete, foreign species enter and target the steel reinforcement directly.

1.3.1 Carbonation

Carbonation leads to corrosion when the carbon dioxide penetrates the concrete through pores and interacts with the hydroxides present in the concrete (Sharma 2018). Carbon dioxide reacts to form carbonic acid (H_2CO_3) which neutralizes the alkalies in the pore water without attacking the cement paste. After that, the carbonic acid combines with the calcium hydroxides found in the pores of the concrete to create calcium carbonate ($CaCO_3$) (JP. 1390). This process significantly reduces the pH level resulting in the passive layer depletion of concrete and the commencement of uniform steel corrosion. Uniform corrosion is experienced in carbonation with a severe reduction of pH level from pH > 13 to pH < 8 (Andrade 2007).

1.3.2 Chloride-Induced Corrosion

The two dominant sources of chloride intrusion in reinforced concrete structures are structure exposure to marine surroundings along with splashing of de-icing agents against the concrete structure surface during cold climates (Andrade 2007; Dabas 2022). The chloride penetration severely attacks the passive layer while the pH of concrete does not drop overall (unlike carbonation). The chlorides act as a catalyst for corrosion and react with the iron compound to disintegrate the passive layer of oxides on the steel thereby, accelerating the process of corrosion (JP. 1390; Andrade 2007; Dabas 2022). Mostly, localized pitting is associated with the chloride attack on steel surface whereas, carbonation of concrete typically causes uniform corrosion (CONTECVET IN309021 2001; Andrade 2007). The damage caused by localized reinforcement corrosion is approximately 5 to 8 times higher than the damage caused by uniform reinforcement corrosion along the rebar length (Dabas 2022). The reaction of chloride ions with the iron compounds causes the production of FeCl in the passive layer.

$$Fe^{+2} + 2Cl^{-} \rightarrow FeCl_2 \text{ (cathodic reaction)} \quad (1.6)$$

$$Fe^{+2} + 2Cl^{-} + 2H_2O \rightarrow Fe(OH)_2 + HCl \quad (1.7)$$

Ferrous hydroxide ($Fe(OH)_2$) forms rust when water and oxygen are present. The corrosion product formation along with spalling, cracking, and delamination of steel bars is similar to that of carbonation corrosion. However, a faster rate of corrosion is experienced for chloride corrosion than compared to carbonation corrosion (Sharma 2018).

The phenomena and mechanism of steel corrosion in extreme marine environmental conditions are generally referred to as the phenomenological model of steel corrosion, which was proposed by Melchers 2003a. The entire corrosion procedure is divided into four parts under this concept, as shown in Figure 1.4. The phases are briefly explained in the flowchart given below, as shown in Figure 1.5. A comprehensive description of all phases is provided later in section 2.2.1.

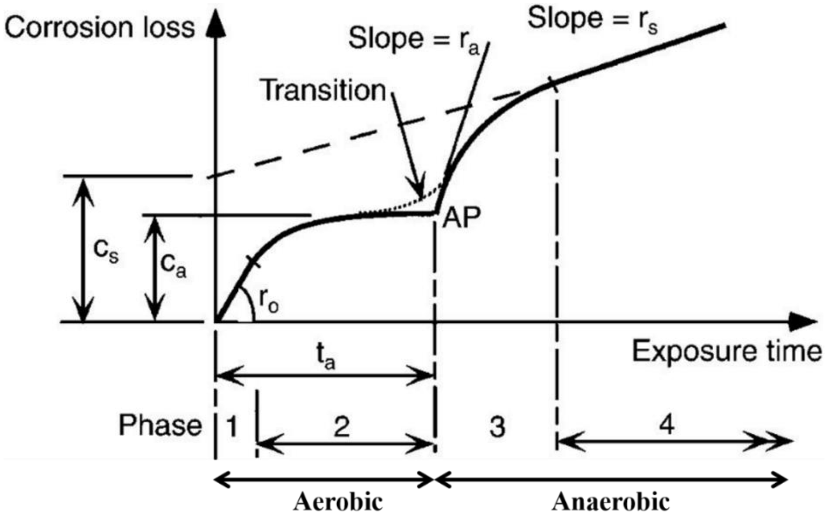

Figure 1. 4 Proposed model of mean-value corrosion loss with respect to time of exposure (Melchers 2003a)

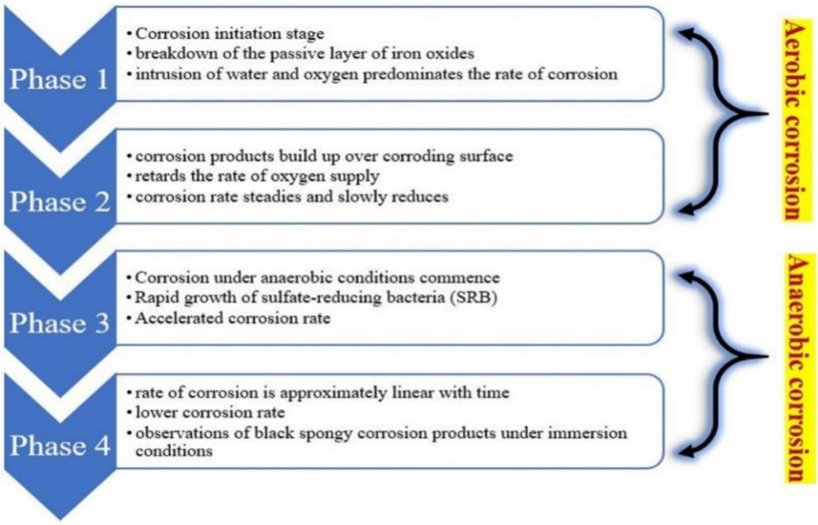

Figure 1. 5 Description of corrosion phases in the proposed model (Melchers 2003a)

1.4 CORROSION EFFECTS ON THE STRUCTURAL PERFORMANCE OF RC MEMBERS

1.4.1 General

The initiation and propagation periods can be used to broadly classify the service life of RC structures exposed to corrosion (Cement 1982). In the period of initiation, the threshold value of chloride concentration on the steel reinforcement surface is reached at which the passive layer is destroyed causing the initiation of corrosion. Post the initiation period, the deposition of rust on the reinforcement continues through the propagation period (Cement 1982; Bertolini 2008). Further, corrosion degrades the strength and ductility of corrosion-damaged reinforcements significantly at the material level. Both the longitudinal and transverse reinforcements within the structural member experience reduced cross-section area, mechanical properties, and deteriorated bond strength due to corrosion (Gadve et al. 2010; Kanchanadevi and Ramanjaneyulu 2018; Zhang and Li 2018a). The corrosive environment also degrades the confining effect provided by the transverse reinforcements which results in lower joint shear resistance (Vu et al. 2017). At the steel/concrete interface, the volume may increase by a factor of six to ten (JP. 1390) due to reinforcement corrosion, which leads to concrete cracking and spalling. Corrosion will not only shorten the life of existing structures but also affect the seismic performance drastically, as can be seen in various research performed on corroded structural members (Meda et al. 2014; Zhu and François 2014; Yu et al. 2015; Ou and Nguyen 2016; Yang et al. 2016; Liu et al. 2017; Li et al. 2018).

1.4.2 Corrosion-damaged Beam-Column Joints

In an RC moment-resisting frame under seismic loading, the beam-column joints (BCJ) are exposed to severe structural damage as they endure a combination of concentrated forces i.e. (compressive, tensile, and shear). The external BCJ must possess high resistance against shear forces which goes hand in hand with the ability to withstand large deformations when subjected to seismic loading. It has been documented that shifting from traditional detailing to seismic detailing practices can significantly arrest the loss of load-carrying capacity and enhance post-peak ductility under cyclic loading. As the BCJs serve as the most critical section in the RC structural frame when seismic and corrosion aspects are considered, the assessment of this zone requires more attention for better understanding. In the existing literature, very little research on the seismic behaviour of sub-assemblages affected by corrosion has been published. Further, these studies mostly focus on the evaluation of a decline in seismic performance either due to corroded stirrups or corroded longitudinal reinforcement within BCJ. Targeting corrosion damage of both the transverse and longitudinal reinforcements at the junction is necessary in order to fully examine the seismic performance of a corroded exterior BCJ, which has not been reported in the literature in depth. Moreover, the investigation and comparison of two types of reinforcement detailing regimes for the BCJ (i.e., non-seismically and seismically detailed) having different rates of corrosion damage have also not been covered extensively. The comparison would have presented the importance of close stirrup arrangement, which is nowadays practiced all over the world for reinforcement detailing regimes.

1.4.3 Retrofitting of Corroded Beam-Column Joints

Prevention of a catastrophic failure of the corrosion-damaged structures under extreme loading conditions such as earthquakes, cyclones, etc. monitoring, assessing the damage level, and repairing and strengthening is necessary. The serviceability and strength of RC structural buildings deteriorate significantly due to the progression of corrosion, resulting in degraded structural integrity and performance (Ahmad 2003). Thus, in order to improve the service levels and timely restoration of corroded reinforced concrete structures, new materials and techniques are desperately needed (Hou et al. 2019; Kamde and Pillai 2020; Yang et al. 2023).

Different repairing and strengthening techniques are applied using several advanced materials to restore the degraded seismic properties of corrosion-damage structural members (Harilal et al. 2021). Fiber-reinforced polymer (FRP) composites have a high strength-to-weight ratio and exceptional corrosion resistance, making them a very appealing alternative to existing confinement techniques (external steel hoop confinement or concrete jacketing) (Hosseini et al. 2020; Yang et al. 2023). However, due to some disadvantages shown by FRP composites at elevated temperatures (Journal 2005), cementitious matrices such as Fibre-reinforced cementitious matrix (FRCM), textile-reinforced mortar (TRM) (de Felice et al. 2018), and mineral-based composites (MBCs) (Blanksvärd et al. 2009), have been recently practiced for strengthening. The cementitious matrix plays a major role in determining how well the FRCM strengthens the constrained concrete (Triantafillou et al. 2006; García et al. 2010; Liu et al. 2020b; Dai et al. 2021).

Majorly, all the retrofitting schemes, and materials adopted are applied externally at the surface of corrosion-active concrete (Li et al. 2009, 2022a; Shen et al. 2021a). In some other cases, the corroded concrete is chipped up to the cover depth, thereafter retrofitting material is applied (Kobayashi and Rokugo 2013; Jayasree et al. 2016; Meda et al. 2016; Rajput et al. 2019). However, in the case of corrosion-affected surfaces, the entire removal of damaged concrete, cleaning, and treating of damaged reinforcement bars for restraining the further progression of corrosion is of prime concern. Otherwise, the formation of incipient anodes continues adjacent to the repaired section, leading to further progression of corrosion (Mackechnie and Alexander 2001). As the corrosion is still active within the RC member, the bars will continue to undergo pitting despite the application of retrofitting material. To date, apart from limited corrosion patch-repairing studies of small sections, no major research studies have proposed retrofitting techniques concerning this problem.

1.4.4 Numerical Investigation

The reinforcement corrosion within the concerned RC structural member is a complex process including several factors. A significantly higher cost is associated with the process of experimentally investigating and determining the consequence of corrosion. Therefore, numerical analysis for the assessment of the behaviour of corroded RC structural members will render a potentially significant cost-beneficial analysis procedure with a short computational time and will allow the inclusion of various parameters. The numerical simulation using non-linear Finite Element Analysis (FEA) has recently been widely adopted for analyzing the complex physical phenomenon of corrosion damage. However, limited numerical investigations have been performed on the seismic behaviour of different levels of corroded Exterior BCJ subjected to reverse-cyclic loading. As of yet, no numerical work comparing and analyzing the seismic performance of two types of reinforcement detailing regimes with varying degrees of corrosion on exterior BCJs has been published.

1.5 RESEARCH OBJECTIVES

The current research primarily intends to comprehensively study the seismic performance of Exterior BCJ exposed to different levels of corrosion damage. Moreover, the aim is to propose and experimentally investigate a retrofitting technique that includes the treatment of corrosion-active reinforcement bars to arrest the existing corrosion, before the application of new material for retrofitting corrosion-damaged BCJ specimens. This research also intends to numerically investigate and compare the seismic performance of non-seismically detailed and seismically detailed specimens using FE Analysis. The objectives of this research are mentioned below:

1. To compare the behaviour of both seismically vs non-seismically detailed exterior Beam-Column Joint (BCJ) subjected to various levels of corrosion induced damage under quasi-static cyclic loading with uncorroded control exterior BCJs.

2. To compare the effect of retrofitting using High Strength Fiber Reinforced Concrete (HSFRC) on the behaviour of seismically vs non-seismically detailed exterior Beam Column Joint (BCJ) subjected to various levels of corrosion induced damage under quasi-static cyclic loading.

3. To develop the Finite element models for the tested BCJ specimens and validate the developed models using corresponding experimental results.

1.6 THESIS ORGANIZATION

Chapter 1 provides an idea related to the corrosion problems, calamities faced due to corrosion worldwide, cost of corrosion, etc. The corrosion mechanism has been discussed and its effect on reinforced concrete structures has been highlighted in brief. The research objectives have also been outlined in this chapter.

Chapter 2 presents a comprehensive literature review which is categorized into four parts. The first segment covers the field evidence supporting the phenomenological model of reinforcement corrosion. In the second and third parts, the literature concerning the study of corrosion-damaged RC structural members’s seismic behaviour and its behaviour after retrofitting application has been presented. The fourth part covers the literature regarding the numerical investigation of the corrosion-damaged RC members.

Chapter 3 discusses the experimental methodology, including properties of materials used, accelerated corrosion test set-up, testing procedure, retrofitting strategy, and material used.

Chapter 4 reports experimental results and comparison of the seismic performance of varying levels of corrosion-damaged Exterior BCJ specimens having two reinforcement detailing types (i.e., non-seismic and seismic detailing).

Chapter 5 presents the result of corroded Exterior BCJs retrofitted with High Strength Fiber Reinforced Concrete (HSFRC). Retrofitted specimens' seismic performance was examined and contrasted with their respective control specimens.

Chapter 6 cover the findings of numerical studies on the seismic behaviour of Exterior BCJs damaged by corrosion. The experimental tests results were validated by means of numerical study.

Chapter 7 lists the key conclusions drawn from the experimental and numerical investigation and future research recommendations.

1.7 CLOSING REMARKS

The corrosion damage to RC structures has been discussed in this chapter. The corrosion mechanism and progression in RC structures are briefly discussed, along with the severe damage imparted to the RC structures. Finally, the corrosion effect on the structural performance was highlighted along with the need to strengthen corrosion-damaged structures for improving the performance and the service lifetime. The objectives of this research study are briefly outlined.

CHAPTER 2

LITERATURE REVIEW

2.1 GENERAL

To assess the severity of corrosion issues and the likelihood of their occurrence, models for reinforcement corrosion are desirable (Melchers and Li 2006). Considering the fundamental mechanics of corrosion and various influences of the concrete cover, a phenomenological model was anticipated by Melchers in 1997 for the prediction of corrosion as a function of time (MELCHERS 1997). The model, revised in 2003 (Melchers 2003a), as shown in Figure 1.4 categorized the entire corrosion process into four phases. Phases 1 and 2 in the corrosion process are undertaken in aerobic conditions with a metal oxidation process while phases 3 and 4 are achieved under anaerobic conditions due to bacterial activity (Melchers 2003a, 2007; Melchers and Li 2006).

The safety, as well as performance of the corroded steel reinforcements within concrete structures certainly will deteriorate with time. Therefore, it is a subject that continues to be of interest to affected and existing structures worldwide. For this experimental research work, the pilot specimen introduced to accelerated corrosion showed corrosion phases similar to the phases experienced in the corrosion loss-time duration model proposed by Melchers 2003a; Melchers and Li 2006. Therefore, the Melchers model has been followed to determine and categorize the various phases of corrosion corresponding to time exposure duration.

2.2 PHENOMENOLOGICAL MODEL OF REINFORCEMENT CORROSION IN THE MARINE ENVIRONMENT

2.2.1 Corrosion of Steel in Marine Environment

In 1997, Melchers postulated that the process of corrosion undergoes changes along with time and could be categorized under a certain number of sequential phases (MELCHERS 1997). The classification and detailed explanation of the four phases in the corrosion loss-exposure time model is presented below:

Phase 1

Phase 1 is also known as the initiation phase of corrosion where the oxygen rate entering through the water at the rusting rebar governs the rate of corrosion. The entire phase is under oxygen concentration control (Jones 1992). During this phase, the corrosion layer starts building and depositing on the target corrosion surface. Due to its thin and permeable state, the corrosion layer does not influence diffusion of oxygen. Phase 1, is, therefore, roughly represented as a linear function, given by the initial corrosion rate 'r_o' (Melchers 2007), shown in Figure 1.4.

Phase 2

The accumulation of the corrosion product layer over the corroded surface takes place in this phase which eventually controls oxygen diffusion rate. The deposited corrosion film is increased up to a limit that results in a decline in the oxygen supply rate which ultimately results in lowering the rate of corrosion (Melchers 2003b, 2004). Due to building up of corrosion layer with time, oxygen's accessibility to the damaged surface gets delayed and the corrosion phase starts shifting towards an anaerobic environmental condition which is assumed to occur at the time 't_a' as shown in Figure 1.4. The transition point 'AP' shows the theoretical point of initiation of anaerobic conditions. It can also be concluded that the transition from one phase of corrosion to another need not be smooth (Melchers 2003a).

Phase 3

By the end of phase 2 at the time 't_a' and from the transition point 'AP' as shown in Figure 1.4, the corrosion process steadily shifted from aerobic conditions to an anaerobic environment. In this phase, the corrosion process commences under anaerobic conditions, leading to the accelerated rate of corrosion because of growth of sulfate-reducing bacteria (SRB). Rate of corrosion is high in this particular phase due to the rapid growth of SRB which corresponds to the higher production rate of hydrogen sulfide at the metal interface. Phase 3 is a brief, high-bacterial activity phase that causes a transient increase in corrosion rate.

Phase 4

This phase also has an anaerobic environment for corrosion and is also governed by the rate of metabolism of SRB. This phase is almost at a steady state, with a corrosion rate that is nearly linear with time. Unlike Phase 3, this phase of the corrosion process is categorized under long-term, and several laboratory and experimental data support this behaviour. The long-term corrosion rate 'r_s' is shown in Figure 1.4.

2.2.2 Corrosion of Steel in Concrete

The chemical protection of steel due to cement alkalinity and the physical barrier provided against the external atmosphere due to the concrete cover persuaded everyone that the reinforced concrete structures were going to have everlasting durability. However, the RC structures exhibited corrosion after 20 to 50 years of exposure to different environmental conditions and emerged as the most serious problem from the durability and economic perspective. During the past two decades, service life prediction or corrosion occurrence time has been a topic of keen interest among researchers (Andrade 2007).

As per the phenomenological model for reinforcement corrosion in concrete proposed by Melchers and Li 2006, the corrosion process should resemble the model suggested for bare steel bars in a saltwater environment once the surrounding concrete's alkaline influence is eliminated. The phases experienced in the corrosion loss-time duration model (Melchers 2003a) as shown in Figure 1.4 were similar to the reinforcement corrosion model, as can be seen in Figure 2.1.

This model works on the assumption that the chloride ions are present on the surface of RC at the time zero which also represents the beginning of the diffusion phase D1. In phase D1, the diffusion of chlorides into the concrete is the principal activity leading to the commencement of local cracks at the time "t_{ic}" on the surface of the concrete cover. The timing of "t_{ic}" depends on the application of the loading system type and intensity on the reinforced concrete. In case of no load applied, no early microcracking was observed and t_{ic} will either shift to t_i or become t_{ac}, where t_i represents the time at which chlorides reach reinforcement and t_{ac} represents the threshold chloride/hydroxide ratio reached.

In phase D2, there is a continuous or discontinuous supply of chlorides penetrating the concrete, and simultaneously leaching of hydroxyl ions out of the concrete is experienced. During this phase, the corrosion influence is almost negligible on the concrete but the localized permeability increases due to the presence of cracks. At $t_{i,}$ the chloride concentration has reached the reinforcement surface, and at time t_{ac} the threshold limit reaches where the chloride and hydroxyl ions and pH behave in a manner that directs towards the commencement of corrosion.

During phase C0, corrosion rate increament can be observed as there is a continuous process of diffusion, leading to a reduction in pH (Bentur 1997), as can be experienced in practical situations and lab studies. Rebars are completely in the active corrosion phase and do not affect the surrounding concrete cover.

Phase C1 represents the continuous rise in the corrosion rate which is governed by the rate of supply of oxygen and water onto the surface of steel reinforcement. Due to the presence of microcracks on the concrete surface, ingress of chloride ions, and greater permeability control the corrosion rate "r_o". Under the same environment, the corrosion rate of the reinforcement bar in Phase C1 corresponds to the corrosion rate of a bare bar in Phase 1, as shown in Figure 1.4.

During phase C1, the ongoing build-up of corrosion product over the reinforcement increases the radial stress at the interface of concrete-reinforcement, leading towards longitudinal cracking and eventually concrete spalling. The piling up of corrosion products will increase the resistance to oxygen diffusion, thereby retarding the rate of corrosion. This stage indicates that the corrosion process has entered Phase C2 and is also represented by the reduction in the slope of the curve. The longitudinal cracks will widen during this phase which eventually will lead to severe spalling of concrete (Andrade et al. 1993). This phase corresponds to Phase 2 of the corrosion in the bare bar as per the corrosion loss-time duration model.

Due to the rust deposition on the reinforcement, oxygen diffusion rate is extremely less and aerobic condition will shift towards anaerobic conditions and the corrosion process will undergo in the presence of SRB. This condition is represented as Phase C3 and corresponds to Phase 3 in Figure 1.4. The degradation of reinforcement and the widening of concrete cracks occurs at an increasing pace. At this point, immersion-condition structures or externally waterproofed RC structures show signs of corrosion products (black spongy). (JP. 1390).

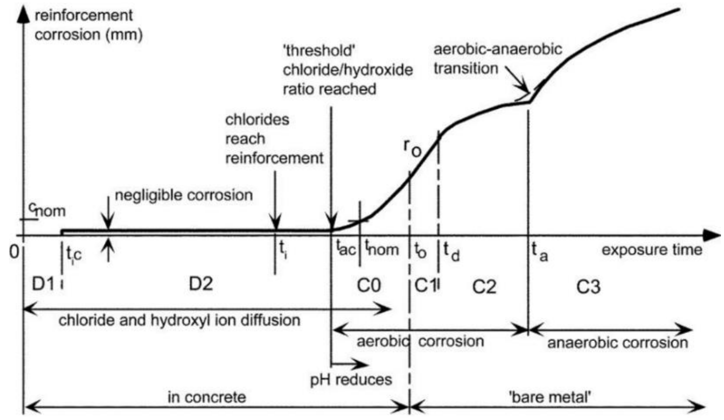

Figure 2. 1 Proposed phenomenological model for reinforcement corrosion in concrete (Melchers and Li 2006)

2.2.3 Supporting Field Evidence

The corrosion of steel reinforcement in fresh and brackish settings has been studied based on various field observations and analyzed using the corrosion loss-time duration model as a framework, as shown in Figure 1.4.

Kure Beach and Point Reyes

The data set for carbon and copper bearing steel at the 25m site in Kure Beach and 400m site in Point Reyes (California Pacific coast) exposed for 12 years has been briefed by Albrecht and Hall 2003 and shown in Figure 2.2 (a). The circled region in Figure 2.2 (a) indicates a shift from phase 2 to phase 3 and the corresponding value of t_a which is approximately 5 years. The nearly identical corrosion trend is experienced as was proposed by the Melchers model of corrosion losses with time as shown in Figure 1.4.

Murmansk, Russia

Based on the data report of Knotkova and Vlckova 1995, the corrosion loss under extremely cold climatic conditions at Murmansk is presented in Figure 2.2 (b). As reported by (Hughes et al. 1996), the corrosion loss drops down to negligible at a temperature of around -5°C, therefore a slow rate of corrosion would be expected, as the average temperature experienced in Murmansk, is around 1°C. From Figure 2.2 (b), despite the harsh environmental circumstances, it is evident that the data and best-fit curves show a higher level of consistency with Melchers' theoretical model of corrosion loss.

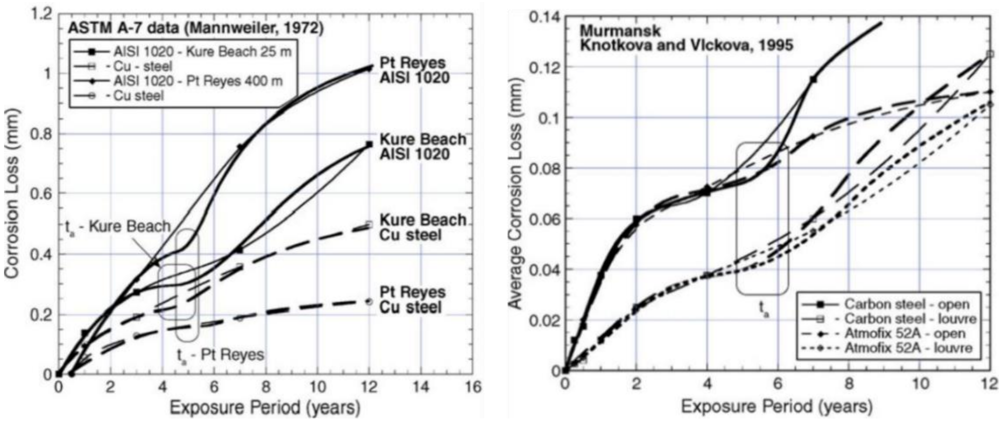

(a) (b)

Figure 2. 2 Corrosion loss data for (a) Kur Beach and the Point Reyes sites for both carbon steel and copper steel, (b) for coupons exposed at Murmansk with interpreted trend lines (bold) and best-fit lines (light) (Melchers 2007).

Hikari, Japan

The copper-bearing and carbon steel vertical coupons were exposed for 8 years and were oriented in a southerly direction. After almost three years of exposure, the data published by Komp et al. 1993 and the best-fit trend lines clearly demonstrated a shift in the phase 2 to phase 3 transition. The stages aligned with the model as shown in Figure 1.4. A similar change in the corrosion phase was experienced in three types of steel exposed for 16 years at Hainan Island, China. From the data reported by C. Liang 2004, the line of best fit for all three types of steel showed a distinct tendency of phase 2 to phase 3 transition after three years of exposure.

UK waters

Booth et al. 1967, 2007 reported the corrosion data for mild steel in the downstream and upstream of the River Thames for up to 5 years. Due to the heavy pollutant inflow, a high rate of corrosion is experienced due to high levels of nitrogen and ammonium level in the water. The trend of corrosion and phases follows the phases proposed in the Melchers theoretical corrosion loss-time duration model.

European Waters

Blekkenhorst et al. 1986, 1988 have reported the data for high strength low alloy (HSLA) steel immersed in the Harbour at Den Helder, the Netherlands at a depth of 45mm and 90mm for the duration of 1.6 to 7.2 years. The corrosion data sets for copper-bearing steel reported by Phull et al. 1997 at Isefjord, Studsvik, and Bohus-Malmon were used by Melchers 2003c to construct the trend curves for t_a, r_o, and c_a for the steel samples from different places. Despite different transition time "t_a" observed for every data set, the trend curves of these parameters stand very close to the trend proposed by Melchers, as shown in Figure 1.4.

The Corrosion-Time Curve for Steel Bars Embedded in Concrete

The experimental data presented by Shalon and Rapheal 1959 displays the trend for corrosion progress in mild steel reinforced bars immersed in seawater for the exposure period of 4 years. The corrosion percentage was measured by adopting a weight-loss analysis by extracting the corroded rebar out of the specimen and weighing it. The corrosion loss-exposure time data points are shown in Figure 2.3 and are consistent with the trend observed in practice by Roberts et al. 2000. As per the reported corrosion data and Figure 2.3, it can be found that the rate of corrosion increases rapidly from the time of corrosion initiation up to 3 months of corrosion duration. The gradual decrease in the rate of corrosion was experienced from 0.5 years up to 2 years of corrosion duration, following the corrosion trend similar to the bare steel bar in seawater (Melchers 2003a). After the exposure duration of 2 years, a noteworthy increase in corrosion rate can be seen in Figure 2.3 representing the shift from aerobic corrosion to anaerobic corrosion. The corrosion trend stands consistent with the trend observed in the case of bare steel bars as shown in Figure 1.4.

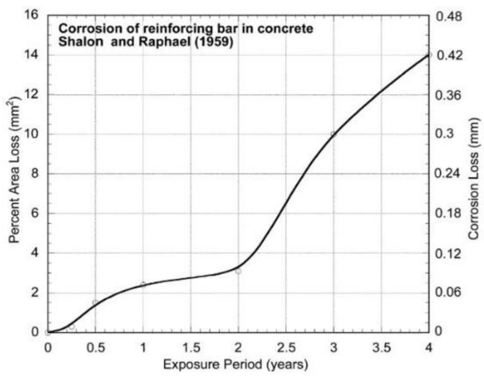

Figure 2. 3 Corrosion-time curve for steel bars inserted into concrete (Shalon 1959; Shalon and Rapheal 1959)

2.3 ACCELERATED REINFORCEMENT CORROSION: CONSTANT VOLTAGE METHOD

In an RC structure, corrosion is a time-consuming process in its natural environment and will take years or even decades, depending on the circumstances of exposure, before a discernible deterioration occurs or cracks propagate (Tuutti 1977; Angst 2018). Getting enough information about corrosion damage from field instances is a highly difficult and time-consuming process for researchers. In order to reproduce reinforcement corrosion in a laboratory setting more quickly, a number of accelerated corrosion procedures have been used.

Utilizing the impressed current approach (electrolytic cell), advanced stages of degradation can be reached in a comparatively short amount of time. Between the stainless steel mesh and reinforcing bar, a direct electric current is impressed at a steady voltage. The corresponding corrosion current is noted and via Faraday's law target mass loss is obtained. The embedded reinforcement serves as an anode in this manner by being connected to the DC power supply's positive terminal. The stainless-steel wire mesh serves as the cathode and is connected to the negative terminal of the DC power supply. The current is impressed from the cathode, via the concrete electrolyte solution to the embedded reinforcement, with or without chloride ions.

Numerous studies have been reported on experimental testing using accelerated corrosion (Andrade et al. 1993; El Maaddawy and Soudki 2003; Fang et al. 2004; Caré and Raharinaivo 2007), indicating that it is a controlled and convenient method to assess how corrosion affects RC structural members' performance. Some literature regarding corrosion studies on the reinforcement bars and RC structural members by adopting the constant voltage method has been discussed below.

Sharma et al. 2018a, b investigated the deterioration in corroding RC beams using active and passive techniques. Accelerated corrosion was introduced by maintaining a constant voltage of 20V for the applied impressed current between rebars and stainless steel mesh. An experimental study on the RC beams having different levels of corrosion was performed by Acoustic Emission monitoring by Garhwal et al. 2020. To introduce accelerated corrosion in the RC beams, a 10 V constant voltage was maintained throughout the experimental duration.

Similarly, 10 V and 20 V was maintained for the accelerated corrosion in the testing done by Garhwal et al. 2021 and Yadav et al. 2019. Sharma et al. 2020 studied corrosion inhibition and adopted the accelerated corrosion technique by maintaining the constant voltage source.

2.4 REINFORCEMENT CORROSION ON BEAM-COLUMN JOINT

As prior earthquakes have demonstrated, under severe ground motion, the breakdown of a Beam-Column joint (BCJ) in the framed constructions results in the worldwide failure of a structure (Gujrat 2001, Indonesia 2004, Japan 2011, and Nepal 2015) (Chidambaram and Agarwal 2016; Sharma and Bansal 2022). As a result, the frame structures, BCJ is designed to improve inelastic response without compromising critical strength (Joint ACI-ASCE Committee 352 2002; Committee and Institute 2008). However, joint behaviour deteriorates under seismic events due to reinforcement corrosion, particularly for coastal structures (Zhang and Li 2018a). A decreased energy dissipation capacity and bond failure are experienced among RC members, resulting in degraded structural performance. The literature on the structural and seismic performance of RC beam-column junctions exposed to varying degrees of corrosion is covered in this section. The load-carrying capacity, stiffness, energy dissipation and ductility of corrosion damaged BCJ were primarily focused and analysed.

2.4.1 Experimental Studies

Kanchanadevi and Ramanjaneyulu 2018 investigated the seismic behaviour of corroded exterior beam-column sub-assemblage (without and with seismic detailing). In this study, only the longitudinal rebar present in the beam of the selected length was corroded. The column rebars and stirrups of the beam and column were insulated from corrosion contact using polyvinyl chloride self-adhesive tapes (shown in Figure 2.4). It was observed through the damage progression of corroded specimens that the flexural crack initiates at the localized pitting location. The longitudinal and splitting cracks along the rebars caused the corrosion specimens to ultimately fail. Moreover, at higher drift fracturing of corroded rebars occurred. When compared to corresponding control specimens, the experimental results showed an alarming drop in the corroded specimens' maximum load-carrying capacity, cumulative energy dissipation, and ductility. The extreme load-carrying capacity in the non-seismic and seismic corroded specimens was 0.67 and 0.64 times while cumulative energy dissipation was 0.4 times and one-seventh of the value of the equivalent control specimens. Both the corroded specimens (i.e., non-seismic and seismic) could withstand only a 2.94% drift ratio against 5.88% drift and a 7.05% drift ratio sustained by control non-seismic and seismic specimens.

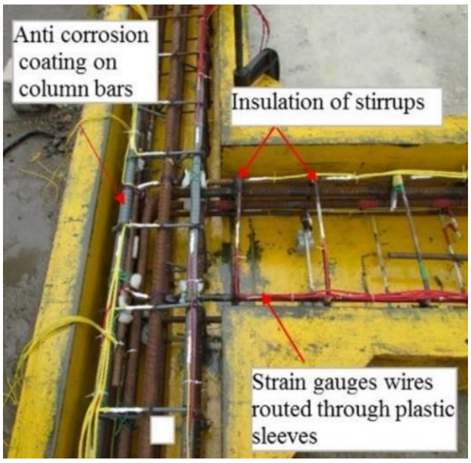

Figure 2. 4 PVC insulation on stirrups of beam and column and at longitudinal rebars of column (Kanchanadevi and Ramanjaneyulu 2018)

Zhang and Li 2021 conducted a study to evaluate the seismic response of corroded RC exterior joints at two different column axial force ratio values (0.15 and 0.3). The specimens were immersed in a 5% NaCl solution, and 500 µA/cm^2 of current density was maintained by the use of an accelerated corrosion scheme. It was noted that the longitudinal reinforcements of the beam and column were the main locations where the cracks originated and spread. From the experimental results, it was noted that the highest average lateral resistance capacity of highly corroded specimens having column axial ratios 0.15 and 0.3 reduced up to 20.6% and 18.4%, respectively. Both axial force and corrosion had an impact on stiffness and showed a reduction of up to 16.7% and 14% when compared to respective control specimens. The joint shear force and joint shear strength transmitted from the beam have been deteriorated by the corrosion of reinforcements. It was observed that the deteriorated bond conditions at moderate and high corrosion levels were improved by a higher axial force ratio thereby, resulting in better energy dissipation capacity.

Yang et al. 2019 reported a drop in each corroded specimens' energy dissipation when compared with uncorroded specimens. The longitudinal and U-shaped steel rebars were where the corrosion cracks initially started to show and more intense and longer cracks were experienced at the higher level of corrosion. The specimens having short key slot lengths show higher load-bearing capacity and energy dissipation than the longer key slot length specimens, under the same corrosion level. From this study, it was reported that for the Structure Comprised of Precast Prestressed Concrete Components (SCOPE) system in the coastal region, the increased length of lapped splice between the steel strands and U-shape bars cannot enhance the seismic performance of the structure.

Zhang and Li 2020 investigated the impact of corrosion using acoustic emission monitoring on the RC-BCJ under cyclic loading. To introduce accelerated corrosion within the specimens, a constant current density of 500 $\mu A/cm^2$ was maintained, and the entire specimens were dipped in a 5% NaCl solution within the water tank. Due to corrosion, after beam-yield failure, joint shear failure was the next failure mode for both corroded specimens. A decrement of approximately 5.9% and 15.8% in the peak strength of corroded joints was experienced for the specimens having corrosion levels of 2.86% and 6.15%, respectively. As the corrosion level increased, cracks became wider in the beam region rather than in the joint region, as can be seen through AE hits analysis. The AE hits collected in corroded specimens were 1.6 and 4.2 times that of the uncorroded specimen, indicating that corrosion level increment would result in the emission of more AE signals.

Zhang and Li 2022 conducted an experimental and analytical study on the seismic performance of Interior BCJ with various levels of corrosion. A linear decrease in the joint shear strength of the interior BCJ is observed as the corrosion level increases. A notable reduction of 31.5% in lateral load resistance of corroded specimens was observed when compared to the uncorroded specimen. A reduction of approximately 25.5% in the energy dissipation was observed for the specimen having a 10% corrosion rate. Moreover, the energy dissipated was augmented by the axial force. In this study, the specimens with a higher axial force ratio had an average improvement in energy dissipation capacity of 21.5% (shown in Figure 2.5). The model that was suggested using Open Sees was validated by a finite element analysis, which demonstrated a respectable correlation with the outcomes of the experimental tests.

Yang et al. 2020 performed an experimental and computational study of the precast prestressed concrete frame's internal BCJ’s seismic response at various corrosion levels. According to the authors, at the first stage of corrosion, cracks are generated in the direction of longitudinal and U-shaped reinforcement bars. As the corrosion ratio increases, transversal cracks appear and propagate wider resulting in bulging and cover falling off. The yield and ultimate load of the corroded specimens undergo a significant drop along with the degraded ductility as the corrosion level rises. A numerical simulation representing the degradation of corroded joints under seismic loading was conducted by developing a 3D FE model. A better agreement between experimental results and analytical simulations was experienced when the corrosion level was not very serious. When corrosion is more advanced, the structure deteriorates unstably under cyclic loading.

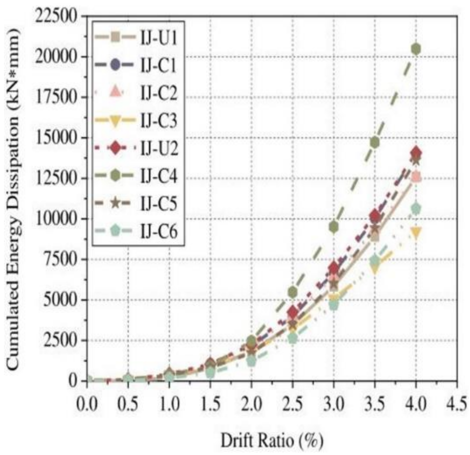

Figure 2. 5 Energy dissipation of specimens

Guan and Zheng 2018 performed an experimental pilot study on RC frame BCJ under an acid rain cycle. Different concentrations of SO_4^{2-} were adopted for simulating acid rain for this experimental study. Different levels of corrosion were decided based on the number of spray cycles on the specimens (i.e., 60, 120, 240, 360, and 480 circles). At an 11.6% corrosion level which was achieved after spraying 480 cycles, a significant reduction of 90% in the corroded specimens' energy dissipation coefficient was experienced with respect to control specimen. In comparison to the corroded specimen with a lower axial compression ratio, the corroded specimen with a higher axial compression ratio demonstrated a greater ultimate bearing capacity and initial stiffness. The energy dissipation coefficient, total energy consumption, and equivalent viscous coefficient all gradually dropped with rise in corrosion level.

Cheng et al. 2020 investigated the effect of stirrup corrosion on RC beam specimens at joints. There were six full-scale RC beams casted. One specimen was kept uncorroded which acted as a control specimen while in the other five specimens, accelerated corrosion was introduced in the stirrups at five different levels (i.e., 6%, 12%, 18%, 24%, and 30%). The current density was 0.4 mA/cm^2 and was kept constant throughout the entire corrosion duration and the corrosion current was 2.0 A. The shear-bearing capacity decreases significantly as corrosion in stirrups increases. Seismic performance is enhanced by the stirrups' mild degree of corrosion due to bond enhancement between corroded stirrups and surrounding concrete. At higher corrosion levels, a significant reduction in the energy dissipation and ductility coefficient was experienced and shear brittle failure replaced seismic failure as the mode of failure. The corroded stirrups were even fractured during loading and had a minor confinement effect on the core concrete. A bond slip between steel bars and concrete was seen at a greater corrosion level (15.4%), which eventually lowers energy dissipation and plastic deformation capability. The displacement ductility showed a reduction of up to 25.2% and the stiffness degradation was increased by up to 29.5% respectively when compared to the control specimen.

Ye et al. 2018 investigated the degradation of RC beams' shear behaviour by corroded stirrups and longitudinal reinforcements. Thirteen RC beams in all, split into three groups, were cast. Specimens with varying rates of stirrup corrosion make up the first category. It was stated that as the rate of corrosion increases, shear cracks in the concrete cover occur and the cross-sectional area of stirrups diminishes. Both shear and flexural cracks were seen on the beam surface as the stirrups' corrosion rate rose. Furthermore, the critical shear cracks entered the beam surface and resulted in the brittle shear failure. The shear cracks spread and widened at a faster rate of corrosion. The stirrups and longitudinal reinforcement of the specimens in group two have corroded at varying rates. The longitudinal steel bar corrosion for beams with similar levels of stirrup corrosion had little impact on the shear behaviour. The growth of stresses in the stirrups developed similarly to the increase in longitudinal reinforcement bars' corrosion level, however the longitudinal reinforcement bars' strains rose more quickly. The group two specimens showed a progressive decline in their bending capacity, and the failure mode changed from shear failure to bending failure. The purpose of the third group was to examine how the shear behaviour of corroded RC beams was affected when either loss of bond behaviour or stirrup end anchorages was there. The specimens from the third group indicate that, provided there is a strong link between the concrete and the stirrups, corroded stirrups can still add to shear strength. The shear strength of the beam is not affected by the corroded stirrups without end anchorage, and beam can be considered as a beam without stirrups.

Zhang et al. 2018 investigated the combined impact of prolonged loads and reinforcement corrosion on RC beam structural performance. The authors reported that the deflection of the specimen corroded at 50 μA/cm^2 current density under a 50% load level was about 1.2 times higher than under 33% load level and 3.7% higher than under 17% load level, provided with the same corrosion density. From the experimental results, it was experienced that at lower current density and higher load levels oxidation of corrosion progresses at an increasing rate. This causes a high reinforcement volume expansion rate, which causes corrosion cracks to initiate prematurely and spread quickly. This study indicates that when taking into account the deflection of beams under simultaneous loadings, the corrosion effect cannot be disregarded.

Zhu et al. 2013 performed an experimental investigation on the mechanical performance of corroded reinforced concrete beams kept for 26 years in a chloride environment. Continuous service loading was applied to the beams in order to simulate actual structural and climatic conditions. A thorough investigation was conducted on the width of the beam cracks, the reduction of the cross-sectional area, and the bond strength of the reinforcement. A three-point loading technique was used to examine the load-deflection behaviour in order to gain a better understanding of the mechanical performance of reinforced concrete beams as well as the slip of corroded tensile bars. Approximately 67% of the diametric reduction of the corroded reinforcement bars and a reduction of more than 50% in the ductility of corroded bars were experienced when compared to the respective uncorroded bars. Because the flexural capacity is more affected by the reduced cross-sectional area of corroded reinforcements than the shear capacity, the failure mode shifted from brittle shear failure to flexural failure mode.

Luo et al. 2020 reported a study on the seismic behaviour of concrete column joints having individually corroded longitudinal or transverse reinforcements within the specimens. As the rate of stirrup corrosion increased, there was a noticeable decrease in the specimens' shear-bearing capacity and a weakening of the confining impact on core concrete. At the initial level of stirrups corrosion, a small increment in the seismic performance was seen due to the expansion of the steel surface thereby, imparting a strong bond between stirrups and surrounding concrete. Specimen's ductility and energy dissipation, having a 14.7% corrosion ratio in the longitudinal, was reduced by 13% and 22% when compared with the uncorroded specimen. However, for a specimen having a 15.2% corrosion ratio in the stirrup, a significant reduction of 20% and 36% was noted. It was determined that stirrup corrosion had a more pronounced impact on stiffness and energy dissipation than longitudinal reinforcement corrosion.

Rajput and Sharma 2018 reported reduced ductility ratio as the end result of a reduced sustained load at the post-peak period caused by the severe corrosion of both longitudinal and transverse reinforcement bars. Comparing the 10% and 15% corroded specimens to the uncorroded specimen, the displacement ductility factor decreased to roughly 34% and 53%, respectively. At greater corrosion levels, buckling of the corroded rebars with spalling and crushing of the concrete cover as well as stirrup fracture were observed. Reduced strain capacities and subsequently lower curvature values were the outcome of the deteriorating state of the transverse reinforcement, which also caused an inferior mobilization of the tri-axial state of stress.

Ma et al. 2012 conducted an experimental investigation to look at how circular RC columns affected by corrosion would respond to cyclic loading. Tests were conducted on a total of 13 RC columns with corrosion ratios ranging from 0% to 15.1% and axial load ratios from 0.15 to 0.9. Due to their smaller diameter and thin clear concrete cover, the stirrups showed more severe pitting and degradation when compared to the longitudinal reinforcement in the column specimens. When lateral load increases on corroded specimens with an axial load ratio of less than 0.5, transverse flexure cracks follow corrosion cracks in size, which ultimately results in brittle failure. First, transverse flexure cracks were seen in the corroded specimens with an axial load ratio greater than 0.5. As the lateral load rose, new diagonal flexural cracks also appeared. As the load was increased further, longitudinal cracks got wider, longitudinal rebars buckled, and the concrete at the column end spalled and got crushed.

Yang et al. 2016 investigated the hysteretic behaviour of RC columns having corrosion-damaged longitudinal rebars and stirrups at four different percentages. A total of five cantilever RC columns were cast and corroded at four different corrosion rates i.e., 5%, 10%, 15%, and 20%. The corrosion crack width increases as the corrosion level increases and the maximum crack width obtained was 1.5mm for a 16.8% corrosion rate. No obvious variation in the energy dissipation was noted for the column specimen having a 5.1% corrosion damage ratio. As the corrosion rate increases, a significant decrease in energy dissipation was experienced and for the specimen having a 16.8% corrosion rate, it drops by 50.8%. The strength, stiffness, and mechanical characteristics of columns made of steel and concrete are negatively impacted by an increase in corrosion, according to the authors' research.

2.5 RETROFITTING OF CORROSION-DAMAGED BEAM-COLUMN JOINT

The deteriorated strength, energy dissipation, and stiffness due to corrosion damage especially for RC structures situated near coastal zones or in earthquake-prone areas will lead to catastrophic failure (Biondini et al. 2014; Meda et al. 2014). Total replacement of such deficient structural members will be time-consuming as well as costly, therefore suitable rehabilitation and strengthening strategies can be introduced to regain their original strength and accordingly extend their service life (Ramachandra Murthy et al. 2018). The selection of the appropriate retrofitting material is one of the biggest challenges for employing retrofitting operations. The popular retrofitting techniques using Fibre-reinforced polymer (FRP) composites such as Glass FRP (Olumns et al. 2001), aramid FRP (Zhang and Wu 2019), carbon FRP (Masoud et al. 2001; Jiang et al. 2014; Hsu et al. 2019), basalt FRP (Wei et al. 2010; Shen et al. 2016), externally pre-stressed tendons (Nordin 2005), etc have been extensively investigated. Apart from the extreme popularity and various dimensional benefits (Buyukozturk 1998; Bakis et al. 2003; Attari et al. 2012), several drawbacks have been identified including brittle failure, bond failure, and pre-mature failure under repetitive loads (Ramachandra Murthy et al. 2018).

Because these materials are compatible with the current concrete, they have been developed as cement-based retrofitting materials in response to these restrictions (Ramachandra Murthy et al. 2018). Numerous Engineered cementitious composites (ECC) (Victor C. Li and Cynthia Wu; Yu et al. 2018), including ultra-high strength concrete (UHSC) (Alaee and Karihaloo 2003; Shin et al. 2015), high-performance fiber reinforced cementitious composite (HPFRCC) (Bandelt and Billington 2016), Textile-reinforced concrete (TRC) (Yin et al. 2017)(Hegger et al. 2006), basalt reinforced mortar (BRM) (Di Ludovico et al. 2010) have been developed for the strengthening of RC structures. These materials have great bonding capacity with regular structural concrete, high toughness (ductility), high tensile and compressive strength, and low permeability (Alaee and Karihaloo 2003; Benson and Karihaloo 2005; Ramachandra Murthy et al. 2013; Shin et al. 2015). For this study, High strength fiber reinforced concrete (HSFRC) was used for the retrofitting of corrosion-damaged seismically and non-seismically detailed beam-column joints.

2.5.1 Experimental Studies

Li et al. 2022b studied the performance of BCJ having corrosion damage and retrofitted with basalt fiber-reinforced polymer (BFRP) sheets. For the rehabilitation scheme, one layer of the BFRP sheet (thickness of 0.121 mm) was wrapped up to a certain length on all sides of the beam and column surface (shown in Figure 2.6). The load-bearing capacity and ductility of corrosion-damaged specimens improved significantly even though serious bulging and delamination of BFRP sheets and spalling of concrete in the core area were found. A similar degradation rate in the stiffness of test specimens was experienced and a decreasing pattern was noted as the displacement increased. The advantage of BFRP sheet rehabilitation over the seismic performance of corroded specimens was up to a certain extent, indicating that the rehabilitating effectiveness was influenced by the reinforcement corrosion rate. From the experimental observations, it was noted that the spalling and crushing of core concrete along with the buckling of stirrups got retarded due to the BFRP sheets utilization, resulting in a seismic behaviour. The increase of up to 23.3% in the cumulative energy dissipation of corroded retrofitted specimens shows the effectiveness of the application of BFRP sheets.

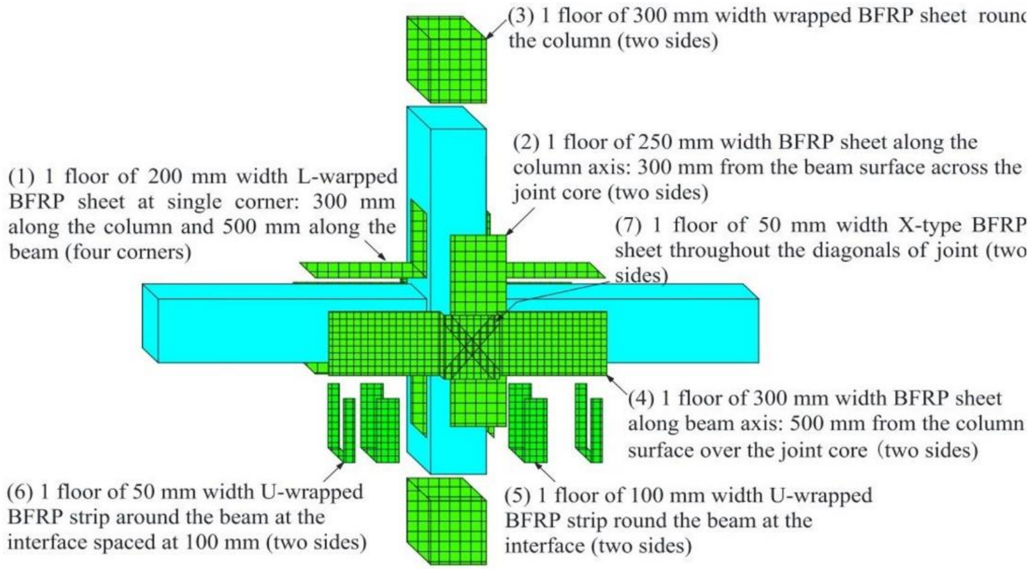

Figure 2. 6 Rehabilitating schemes for specimens

Shen et al. 2021b repaired corrosion-damaged interior RC beam-column joints with basalt fiber-reinforced polymer (BFRP) sheets. It was observed that at higher displacements all the repaired specimens showed the development of failure from the delaminating of BFRP sheets to the crushing of the core concrete and local bucking of stirrups. With the exception of the specimen with a 15% corrosion rate, all of the repaired specimens' displacement and load-bearing capacity were restored to those of the reference specimen due to high corrosion damage. Before the peak load, the viscous damping ratio of every repaired specimen was higher than that of the reference specimen. It then decreased throughout the intermediate stage and increased dramatically again at the higher drift ratio. The reason supporting this behaviour is (a) an increase in brittleness due to hardened epoxy resins with BFRP sheets ; (b) high bond strength between corroded reinforcement and surrounding concrete due to corroded product filling (c) due to BFRP sheets, the buckling of corroded reinforcements and concrete spalling in the joint area was delayed, resulting in higher viscous damping ratios at the later loading stage. The BFRP sheet repair exhibited an improved strain reduction and bond behaviour of the corroded stirrups, resulting in a seismic failure mode instead of brittle failure at higher corrosion damage.

Shen et al. 2022 retrofitted earthquake-damaged corroded interior BCJ with basalt fiber-reinforced polymer (BFRP) sheets. The corroded joints exhibited a notable rise in load-bearing capacity and displacement up until the point at which the BFRP sheets separated from the joint surface. After installing BFRP sheets, the buckling of damaged stirrups and the spalling of concrete were successfully postponed, and the ductility of corroded specimens injured by earthquakes suggests that they may recover. A similar failure mode i.e., bulging of BFRP sheets at higher displacement resulting in delamination, stirrups buckling, and core concrete crushing was experienced for all retrofitted specimens. When compared to the corresponding control specimen, the corroded retrofitting specimens that had suffered extensive and destructive pre-damage had a far reduced initial stiffness and energy dissipation capability. The reason supporting this behaviour might be residual cracks on the specimen surface and the yielding of corroded bars during earthquake damage, resulting in the brittle failure mode.

Pan et al. 2022 examined RC beams for their flexural behaviour when subjected to the coupled effect of corrosion damage and sustained loading strengthened with a Carbon Fibre Reinforced Polymer (CFRP) anchorage system. Only the tensile reinforcements of the specimens were corroded at a mild, moderate, and severe level of corrosion damage (5%, 10%, and 20%) excluding the stirrups. The tensile bars' yielding and the concrete's crushing at the top beam surface caused the failure mode for the control specimens. A completely different failure mode for the strengthened specimens was observed which occurred due to debonding between CFRP sheets and concrete interface followed by anchor pullout. When compared to specimens that failed because of anchor pull-out and concrete cover separation, the installation of CFRP anchors delayed the debonding of CFRP sheets, displaying higher ductility to the damaged specimens. Along with the quick increase in displacement, the reinforced specimens' load-carrying ability in the elastic region increased noticeably. The utilization of the CFRP anchorage system resulted in a notably increased stiffness prior to yielding, since CFRP sheets and anchors postponed the premature debonding of CFRP from the concrete substrate, hence greatly enhancing the flexural performance of beams. The yield and ultimate load of the reinforced specimens were negatively impacted by the prolonged loading as they showed inferior performance when compared to strengthened specimens which were not subjected to sustained loading.

Hou et al. 2019 repaired corroded RC beams repaired with ultra-high toughness cementitious composite (UHTCC) and checked its flexural behaviour. Eight of the nine RC beams that were cast were exposed to rapid corrosion. In this study, the maximum target corrosion ratio was designated as 15%. The replacement of damaged concrete in the tension side of the corroded specimens with the UHTCC layer varied from 30mm depth to 80mm layer depth. Due to the UHTCC repairing, the macro cracks experienced in the specimens at the post-yield stage were dispersed into many fine cracks. The initial load-carrying capability and initial flexural capability in corrosion-damaged RC beams can be fully recovered within an 11.2% corrosion ratio by replacing the damaged concrete with UHTCC.

Jayasree et al. 2016 examined flexural performance experimentally in RC beams with corroded reinforcements that were patched using the ferrocement jacketing method. Twenty-one RC beams in all were cast; three of them were left uncorroded, and the other eleven were corroded at three different percentages (5, 10%, and 15%). Three examples from each stage of corrosion were tested without being repaired, and the remaining three were preloaded to 70% of their maximum loading capacity before the retrofit procedure (U-wrap ferrocement jacketing) was carried out. In comparison to the control specimens, the modified specimens exhibited reduced deflection. Comparing the corrosion-damaged beams to the control specimens, ferrocement retrofitting with a 1.2% volume fraction of mesh reinforcement can increase the final load-carrying capability of the beams.. Nevertheless, it was found that ferrocement retrofitting with a 1.2% volume fraction of mesh reinforcement was insufficient for a higher corrosion ratio (i.e., 15%). Therefore, an extra mesh reinforcing layer is required in order to restore the load-carrying capability.

El Maaddawy et al. 2007 examined the effectiveness of different degrees of corrosion-damaged RC beams restored using carbon fiber-reinforced polymer (CFRP) sheets. When compared to the ultimate strength of the corroded unrepaired and control specimens, there was an increase of 51% and 41%, respectively, following the CFRP repair of the specimen that corroded at a 9% corrosion rate. The rate of yield and ultimate load reductions for the specimens restored with scheme 1 (continuous wrapping) were about 25% and 10% lower, respectively, than that of the specimens fixed with scheme 2 (intermittent wrapping), as corrosion advanced following repair. Nonetheless, after reinforcement mass loss of 28% and 34% in scheme 1 and scheme 2, the specimens' respective end strengths were roughly 22% and 12% greater than those of the control specimen. When comparing the peak and ultimate strength of the sustained load CFRP-repaired specimens to the non-sustaining load CFRP-repaired specimens, no further discernible impacts were observed, with the exception of a slightly elevated corrosion rate. The reason for the failure of the CFRP-repaired specimens was the rupture or debonding of the CFRP sheets from the concrete interface, while the failure of the control specimens was the yielding of reinforcement and the crushing of concrete.

Yin et al. 2017 examined the seismic behaviour of RC columns that have been corroded and reinforced with textile-reinforced concrete (TRC). Seven RC column specimens in all were produced; two of these served as control specimens, and the other five underwent three separate corrosion ratios of 5%, 10%, and 15%. Out of five corroded specimens, two of them were strengthened with TRC first and then corroded and the remaining three specimens were first corroded at three different corrosion ratios and then strengthened with TRC layers. According to the findings, there is less of a chloride ion influence on the corrosion of steel reinforcements when TRC reinforcement is applied. Furthermore, in comparison to the corresponding control specimens, has also postponed and restricted the appearance of cracks in the strengthened specimens. When compared to specimens strengthened with TRC reinforcement after corrosion damage, those whose application occurred prior to corrosion damage exhibited superior seismic performance. When compared to the uncorroded specimens, the TRC-strengthened corroded specimens showed a notable improvement in both initial stiffness and load-bearing capacity.

Meda et al. 2016 studied the performance of RC columns that had corroded and were strengthened with jackets made of high-performance fiber reinforced concrete (HPFRC). Three specimens are available: the first was a reference specimen which was not corroded, the second was corroded, and the third has been corroded initially and subsequently repaired with a 40 mm thick HPFRC jacket. Only the column's longitudinal reinforcement was targeted for corrosion damage, and it corroded to the 20% target corrosion level. The maximum strength and maximum deformation of the corroded specimen were found to be 26% and 50% lower, respectively, in comparison to the uncorroded specimen. When compared to the uncorroded specimen, the HPFRC jacket repaired corroded specimen not only recovered but also shown a notable improvement in ductility and load-carrying ability. When comparing the maximum load-carrying capacity of HPFRC repaired specimens to uncorroded and corroded specimens, respectively, an increase of 65% and 118% was observed. A macro-crack that appeared between the foundation and column base caused the restored specimen's strength to abruptly drop when it reached its max load. Because layer HPFRC acted as a confinement, there was no concrete cover scattering or longitudinal reinforcement deformation in the HPFRC-repaired specimen.

Rajput et al. 2019 investigated the seismic performance of corroded RC columns retrofitted with advanced materials. The corroded specimen retrofitted with an HPFRC jacket, as compared to control ones, holds good command over crack propagation at higher drifts. The retrofitted specimens show appreciable recovery in the ultimate curvature as well as in the flexural strength when compared to control under-confined and well-confined column specimens. The retrofitted specimens show superior energy dissipation (i.e., up to 25% higher) when compared to control specimens (shown in Figure 2.7). However, after a 3% drift ratio, the energy dissipation reduces, and a steep post-peak response was experienced in the retrofitted specimens. Due to the application of HPFRC jackets and GFRP sheets on the retrofitted specimens, the spalling of concrete was resisted. Therefore, at higher drifts, no sectional loss and no premature buckling of corrosion-damaged rebars were experienced which resulted in better axial load-carrying capacity. It was noted that the specimen retrofitted with HPFRC and GFRP sheet showed improved strength and ductility when compared to control well-confined specimen. According to the experimental findings, the retrofitted specimens' seismic response was strengthened, and their deformability was noticeably less than that of the control specimen. This behaviour was observed due to the inferior post-peak response of HPFRC and GFRP material in tension.

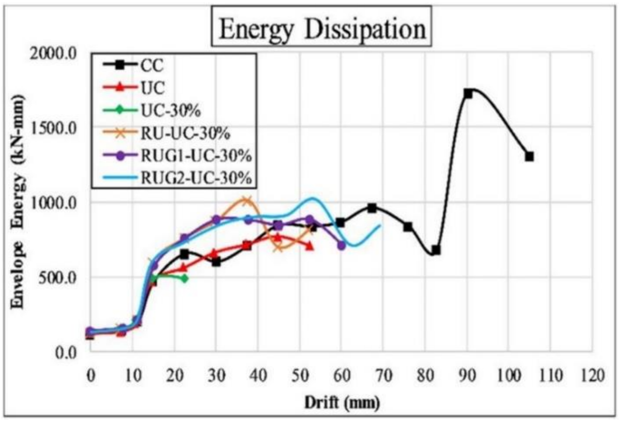

Figure 2. 7 Energy dissipation behaviour of column specimens

Yang et al. 2023 examine how corrosion-damaged RC columns that have been modified with a BFRP-ultrahigh performance concrete (BFRP-UHPC) jacket behave in terms of axial compressive behaviour. The concrete cover that was chipped and shredded due to corrosion was replaced with BFRP sheets that were implanted internally in the UHPC matrix. The replacement of corrosion-damaged stirrups with FRP composites at different spacing was also considered under the retrofitting approach. When UHPC jackets were used to strengthen corrosion-damaged specimens, there was a modest decrease in their ductility because UHPC is a brittle material with a finite strain capacity, which means that once it cracks, it stops giving strength. On the other hand, the specimens that were damaged by corrosion and reinforced with a BFRP sheet and UHPC jacket wrapping exhibited higher ductility values. When compared to specimens with wider stirrup spacing, the BFRP-wrapped UHPC jacket-strengthened specimens with lower stirrups spacing exhibit a considerable rise in the peak load as well as greater post-strengthening gains in axial load capacity. When reinforced with a BFRP-UHPC jacket, the corrosion-damaged specimens fitted with UHPC shown an additional increase in peak load of up to 18.92%. The specimens showed an increment of roughly 74.6%-96.5%. However, due to consistent confining stresses and the larger confining effect of circular cross-section RC columns, the post-strengthening rise in the axial load was much higher in circular specimens than in square specimens in all examined specimens. The efficacy of this retrofitting method for RC columns with a circular cross-section was indicated by an overall increase in the axial load capacity of 105.6% and 76.8%, respectively, for the square and circular cross-section RC columns.

Yin et al. 2017 conducted an investigation to determine the extent to which reinforced concrete (RC) columns could be enhanced with textile-reinforced concrete (TRC) at various corrosion levels. Seven RC column specimens in all were cast an fabricated. In two uncorroded control specimens, two specimens were strengthened with TRC first and then corroded, and the remaining three were corroded first and then strengthened with TRC. Three different corrosion rates i.e. 5%, 10%, and 15% were used for corrosion damage and two layers of TRC were applied for strengthening purposes. When compared to control specimens, the strengthened specimens showed slow crack development and fewer surface cracks and exhibited better seismic performance. For specimens having a high corrosion rate, a certain degree of damage is observed even though sufficiently high bearing capacity was seen with the ultimate failure mode as bending failure. From the results of test specimens, it was observed that the TRC strengthening method before corrosion was superior to that of strengthening after corrosion. The TRC reinforcement reduced the corrosion degree by inhibiting the erosion caused by chloride ions. For the high-level corrosion damage specimen (i.e., 15%), the bearing capacity and deformation at the early phase of loading were better than the control one but degraded rapidly at later stages due to severely damaged reinforcements.

Karimipour and Edalati 2021 performed experimental investigation to look at the performance of RC columns affected by corrosion that had been retrofitted with GFRP and CFRP fabrics. It should be highlighted that CFRP had a greater impact than GFRP fabric in preventing cracks from forming, spreading, and widening. Up to 10% corrosion level, the specimens retrofitted with CFRP and GFRP layers showed significant improvements in flexural strength and lateral deformation when compared to corroded specimens not retrofitted with fiber fabrics. Furthermore, because CFRP fabric has a higher elasticity modulus than GFRP, it has a greater impact on enhancing bearing capacity and flexural strength than specimens that have been retrofitted with GFRP layers. A significant improvement of approximately 58% in the ductility of severely damaged specimens having a corrosion rate of 20% was seen by retrofitting with CFRP and GFRP retrofitting. It was found that specimens without any retrofitting for corrosion levels below 15% exhibited a lower maximum deformation due to the action of CFRP and GFRP fabric. Retrofitting's impact on lateral displacement was reduced by increasing the reinforcements' degree of corrosion.

Yao et al. 2019 strengthened corroded RC columns with Textile reinforced concrete (TRC) under a chloride environment. The specimens were corroded and then strengthened with two layers of TRC and afterward subjected to dry-wet cycles of chloride. The higher level corroded strengthened specimen showed an increment in cumulative energy dissipation up to 75.73% when compared to the corroded unstrengthened specimen (shown in Figure 2.8). This shows that TRC strengthening of corrosion damage specimens can recover and improve the seismic performance at higher corrosion damage. It was found that the uncorroded strengthened specimen, which was subjected to more dry-wet chloride cycles, performed better seismically than the corroded strengthened specimen experiencing fewer dry-wet chloride cycles. Indicating that the invasion rate of chloride ions can be delayed by adopting the permanent templates produced by TRC.

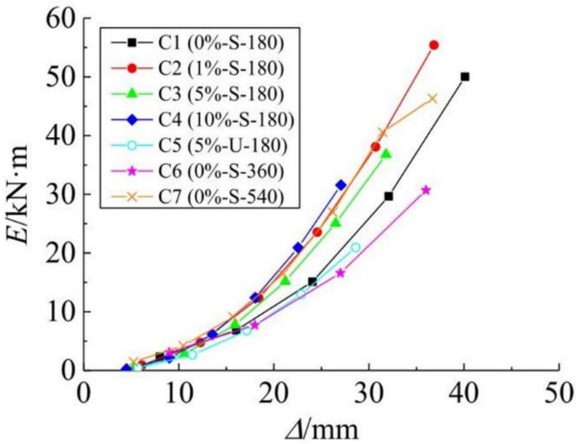

Figure 2. 8 Cumulative energy curves of specimen C1–C7

Note: ‘‘S” represents TRC strengthened specimens; ‘‘U” represents that the specimen was not strengthened

2.6 FINITE ELEMENT MODELING

The numerical simulation using non-linear Finite Element Analysis (FEA) has recently been widely adopted for analyzing the complex physical phenomenon of corrosion damage. The low associated cost, short computational time, and the inclusion of various parameters influencing corrosion damage are among the listed benefits numerical simulation holds over the experimental work (Zhao et al. 2018; Van Nguyen et al. 2022). The FEA is being used in solving diverse engineering problems ranging from the analysis of simple parameters such as material properties (Partheepan et al. 2007) to complicated and tedious problems such as crack behaviour (Choubey et al. 2006) and joint failure of the RC structural member (Kaviani et al. 2021; Yang et al. 2021).

Zhang and Li 2018b developed a two-dimensional non-linear FE model for simulating the seismic load of corroded RC exterior and interior BCJs using OpenSees software. The corrosion damage to the concrete and steel reinforcement has been incorporated within the model by adopting certain models. The primary parameters for simulating the corrosion damage in the FE model are the decrease in the strength of the concrete cover, the reduction in the cross-sectional area of steel bars, the degradation of yield strength and elastic modulus, and the modified bond-slip behaviour. Following the experimental data' validation of the suggested model, a parametric investigation was carried out on a total of 360 FE models (i.e., 180 interior BCJ and 180 exterior BCJ specimens). The key parameters such as concrete compressive strength, axial force ratio, corrosion levels, and stirrups spacing that influence the joint behaviour under cyclic loadings were covered and analyzed. Regression equations that predict the shear strength of corroded exterior and interior BCJs are developed using the findings of the numerical analysis.

Yang et al. 2020 conducted a computational and experimental study on the seismic behaviour of inner BCJ at different corrosion levels. The experimental data from this investigation alone were used to validate the conclusions of the numerical simulation. By using a certain model, parameters of corroded steel reinforcements, such as yield strength, ultimate strength, and elastic modulus, were changed. Precast and cast-in-situ concrete were used to create a surface-to-surface interface for the development of a three-dimensional (3D) FE model. There is a considerable agreement between the experimental data and the envelope curve behaviour of the corroded specimens derived from numerical simulations. A better agreement amongst the numerical analysis results and experimental results was seen when the corrosion rate was below 18%. Major cracks at middle of key slots occur as corrosion levels rise, increasing the equivalent plastic strain (Figure 2.9). The findings indicate that the numerical model could be applied to other research projects, like seismic fragility analysis, etc.

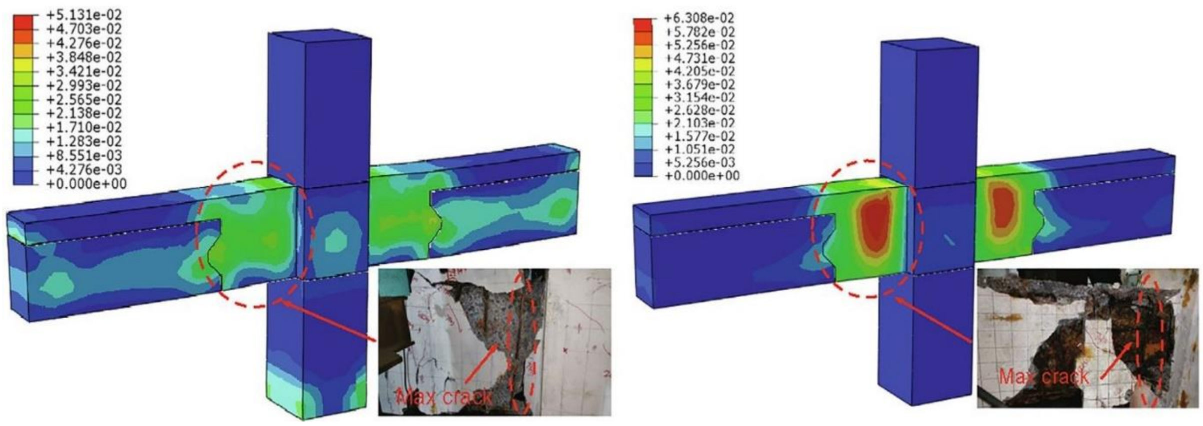

(a) (b)

Figure 2. 9 Equivalent plastic strain of concrete: (a) uncorroded and (b) corroded specimen

Di Carlo et al. 2017 proposed a three-dimensional FE model for examining the cyclic behaviour of RC columns damaged by corrosion. Using TNO Diana (2005) software, the nonlinear response of corrosion-damaged RC columns was investigated numerically. The structure was modeled using eight-node isoparametric solid brick elements (HX24L), while the reinforcement was described as a two-node, one-dimensional element. By changing a few characteristics, such as the concrete cover's compressive strength, the tensile behaviour of the concrete, the reinforcing bars' stress-strain relationship by using certain models, and the local bond-slip behaviour in accordance with the model code, corrosion has been included to the model. The author's experimental results validated the proposed model. A parametric study was then conducted by modeling two more corrosion ratios (i.e., 10 and 30%) besides the already discussed corrosion level of 20% to analyze the seismic performance.

Biswas et al. 2020 numerically examine numerically how RC beams with uneven reinforcement corrosion behave structurally. This study proposes a three-dimensional (3D) non-linear FE model as a simplified modeling approach to anticipate the reaction of reinforced concrete (RC) structures under non-uniform corrosion. By incorporating specific critical elements, such as corrosion-induced cracking, altering the mechanical characteristics of the concrete and the steel reinforcing bars, and strengthening the link between the steel and the concrete, the corrosion damage has been included to the model. The experimental results acquired from this investigation alone were used to validate the suggested numerical model with corrosion damage. A thorough parametric study was conducted following the numerical model's validation to ascertain the effects of the volumetric transverse reinforcement ratio and the compressive strength of the concrete on the structural performance of RC beams with uneven rebar corrosion.

Liu et al. 2021a conducted a numerical analysis to look at how the reinforcement corrosion ratio affected the deformed behaviour of RC beams using the program ABAQUS. Certain parameters, like the cross-section, yield, and ultimate strength of the corroded steel reinforcements, were adjusted in accordance with specific models in order to account for the corrosion damage. To replicate the impact of reinforcement corrosion on the numerical model, the residual strength of the concrete damaged by corrosion and the bond deterioration model were also used. The simulation revealed that the lateral load versus displacement behaviour of the specimens with a corrosion rate of less than 7.5% is comparable to that of the uncorroded specimen. A notable decrease in post-peak load and stiffness was observed as displacement increased, for the specimens with a corrosion rate over 7.5%. As the corrosion ratio rose, there was a noticeable decline in the bond stress between the surrounding concrete and the corroded reinforcement as well as a decrease in ultimate plastic rotation. Longitudinal reinforcement ratio and shear span ratio show a substantial effect on the deformation capacity for specimens with corrosion ratios up to 7.5%; for specimens with higher corrosion ratios, the effect is negligible. The equations for calculating the deformations of corroded reinforcing steel beams at respective yield and ultimate limit states were derived based on numerical simulation results. The research findings can be applied to the design and assessment of RC structures' seismic performance from a life-cycle perspective.

Yang et al. 2015 used the ABAQUS to do numerical simulation analysis of the load bearing capacity of corroded RC beams. To mimic the effects of corrosion damage and cyclic stress, parameters including the steel cross-section area, yield, and ultimate strength of corroded reinforcements are changed. In order to validate the ABAQUS software, the load-carrying capability of the non-corroded RC beam was examined first. Next, the impact of fatigue and corrosion on the model was examined. Seventy load cases in all were examined in the numerical simulation including several corrosion ratios (i.e., 0%, 3%, 5%, 8%, 10%, 13%, and 15%) and fatigue loading having cycle numbers ranging from 10 to 100 million. The corroded specimens exhibited a considerable reduction in structural performance, precisely the yield load and ultimate deflection, under the combined impacts of cyclic loading and corrosion damage. The yield load shows an abrupt downfall when the cyclic number becomes large and the corrosion ratio is beyond 10%. Under the influence of increasing fatigue loading cycle number and corrosion rate, RC beams' ultimate deflection was found to grow both nonlinearly and linearly. It is evident from the numerical analysis that the influence of the rate of corrosion outweighs that of the number of cyclic loadings, and that the effect becomes more pronounced with higher loading counts.

Biondini and Vergani 2015 have proposed the three-dimensional non-linear FE analysis of corroded RC beams. Both uniform and localized (pitting) corrosion are taken into account in the numerical damage model. The key parameter modified to replicate the corrosion damage after following certain models includes cross-section area reduction of the corroded bars, diminished concrete strength and the corroded bars' decreased ductility due to splitting cracks and spalling of concrete. The FE model of the corrosion-damaged beam has been validated against the experimental results obtained from accelerated and natural corrosion-damaged RC beams. In the second phase of the study, the three-dimensional non-linear RC arch bridge having different damage scenarios and corrosion penetration levels was analyzed. The simulation results have effectively displayed the performance of structural components and members under corrosion attack. Based on the simulation response, a hierarchy of protection techniques along with the maintenance and repair techniques against corrosion damage can be proposed and adopted.

2.7 RESEARCH GAPS

Based on the literature review presented above, the following research gaps are listed below:

- There are very few experimental studies related to the comparison of seismic behavior of Non-Seismically and Seismically detailed Exterior BCJs having corrosion damage at the junction of beam-column at different rates.

- No experimental study has been reported on entirely replacing the corrosion-affected concrete from the BCJ specimens and treating the damaged reinforcement bars prior to the application of retrofitting material. The research studies present in the existing literature are mostly focused on improving the mechanical performance of corrosion-damaged structural members without concerning the possibility of reoccurrence of corrosion in the pre-affected area.

- FE modeling displaying and comparing the seismic performance of corroded Non-Seismically and Seismically detailed Exterior BCJs at varying rates has not been reported in the existing literature. The damage progression and ultimate failure pattern of control and corroded BCJ specimens have not been covered in any of the existing research studies.

2.8 RESEARCH SIGNIFICANCE

As the beam-column joint serves as the most critical section in the RC structural frame when seismic and corrosion aspects are considered, the assessment of this zone requires more attention for better understanding. A new retrofitting scheme has been proposed in this study concerning the enhanced mechanical performance of corrosion-damaged structural members and the assurance of a low probability of reoccurrence of corrosion in the pre-affected area. The proposed retrofitting scheme can be a better alternative (when corrosion is considered) to the jacketing technique that is commonly practiced at the actual site. This retrofitting scheme will help restore the mechanical performance of corrosion-damaged structural members near the coastal region and the structures lying under the high seismic zone.

Alongside, a numerical simulation was also performed via Finite Element (FE) models for the corrosion-damaged exterior BCJs. The efficiency of the developed FE model was validated based on a comparison with the results obtained from the experimental study performed by the author. The developed FE models accurately predict the peak load-carrying capacity of the corroded Exterior BCJs at any corrosion rate and also generate possible damage patterns and ultimate failure modes. This may significantly reduce the cost of experimental study by eliminating the need for testing a large number of specimens, and further also promote a quicker understanding of the effect of damage caused by different corrosion rates on BCJs among future researchers.

2.9 CLOSING REMARKS

This chapter covers the field evidence portraying the corrosion trend as per the Melchers model. A comprehensive literature on the structural and seismic performance of corroded RC structural members (precisely Exterior beam-column joint) with or without retrofitting application was presented. The literature review of the numerical investigation performed on the failure mode and performance of corroded members using FE modeling has also been covered in detail.

CHAPTER 3

EXPERIMENTAL PROGRAM

3.1 GENERAL

This part of the dissertation aims to determine the material physical properties used to prepare M25-grade concrete and steel bars to cast the exterior BCJ specimens. Also, the various levels of corrosion damage introduced in the BCJ specimens by adopting the accelerated corrosion method have been discussed in detail in this chapter. In this study, a High Strength Fiber Reinforced Concrete (HSFRC) was developed to retrofit the corrosion-damaged BCJ specimens and is discussed in detail in this chapter. The entire methodology for the experimental study has been presented in Figure 3.1.

Stage 1 (Exposure to accelerated corrosion)

- Design RC Exterior BCJs with non-seismically and seismically reinforcement detailing,
- Prepare respective steel reinforcement cages with the parallel copper wire connection on them for introducing accelerated corrosion,
- After casting, expose the BCJs to the accelerated corrosion regime.

Stage 2 (Structural testing) is divided into two parts:

Part 1

- Preparing loading setup,
- Apply quasi-static reverse cyclic loading.

Part 2

- The damage severity and extent were visually inspected after extracting the corrosion-damaged reinforcement cage,
- Retrofitting scheme was decided,
- Retrofitting material (HSFRC) was developed,

➢ After 28 days of curing, testing was performed under quasi-static reverse cyclic loading.

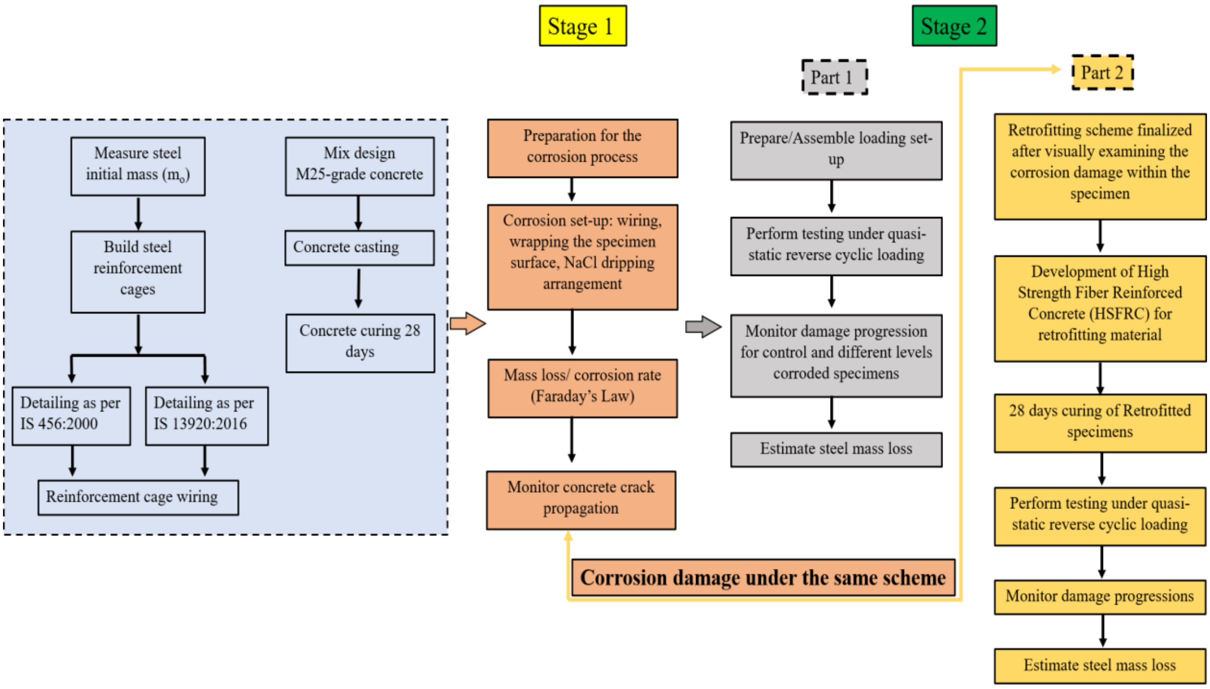

Figure 3. 1 Methodology for the experimental program

A total of 16 BCJ specimens have been cast and the entire experimental study has been categorized into two parts. In the 1st part of the experimental study, two different reinforcement detailing regimes (i.e., non-seismically detailed and seismically detailed) exterior BCJ specimens were cast. The specimens were subjected to corrosion damage at different levels. The seismic behaviour of all the corroded BCJ specimens was determined and compared, under the effect of reverse cyclic loading. In the 2nd part of the experimental study, a retrofitting scheme was proposed by entirely removing corrosion-damaged concrete. Thereafter, corroded reinforcing bars were treated with an anti-corrosive agent to arrest further progression of corrosion. The corrosion-damaged BCJ specimens were then retrofitted with the HSFRC to regain the load-bearing capacity and the seismic performance, which was degraded due to the corrosion attack.

Out of the two reference specimens from each reinforcement detailing regime type, one reference specimen was tested under reverse cyclic loading until the lateral load of specimens dropped by 20% of the peak load, as reported in Chidambaram and Agarwal 2015; Sharma and Bansal 2022. Thereafter, the damage index (DI) was determined using the Park and Ang model (Park and Ang 1985). The ultimate displacement (i.e., displacement at which DI > 1) was evaluated from this model at which the specimen achieves complete failure. The second reference specimen was selected for the pilot study to determine the pattern of corrosion progression corresponding to corrosion exposure duration. The pilot specimen shows variation in the corrosion pattern at certain durations (days) similar to the corrosion phases proposed in the Phenomenological model of corrosion by Melchers and Li 2006. Based on the different phases of corrosion experienced at a certain duration (days), three different levels of corrosion were set for this experimental study.

3.2 MATERIALS

3.2.1 Binder

Ultratech 43-grade Ordinary Portland cement (OPC) was taken as a binder for developing the M25-grade concrete. The cement was tested in the laboratory as per IS 8112: 2013. Table 3.1 lists the physical properties of the cement used.

Table 3. 1 Physical properties of cement

Sr No	Characteristics	Test values	Values specified by IS 8112: 2013
1	Standard consistency (%)	31	---
2	Specific Gravity	3.12	3.15
3	Setting time (minutes)		
	Setting time (Initial)	80	30 (minimum)
	Setting time (Final)	280	600 (maximum)
4	Compressive strength (MPa)		
	a) 3 days	25	23 (minimum)
	b) 7 days	34	33 (minimum)
	c) 28 days	46	43 (minimum)
5	Fineness (m^2/kg)	310	225 (minimum)
6	Soundness (mm)	1.6	10 (maximum)

3.2.2 Aggregates

Two types of aggregates (i.e., fine aggregates and coarse aggregates) were used. The natural river sand was taken as fine aggregates. The sieve analysis of sand was performed as per

(IS:383 1970) (Reaffirmed 2002). The sand was classified as Zone III FA. Coarse aggregates of 20 mm (Maximum size of Aggregate, MSA) were used for making the concrete. The experimental tests were conducted on the fine and coarse aggregates to evaluate certain physical properties as per the guidelines provided in (IS:2386 (Part I) 1963) (Reaffirmed 2002) and (IS 2386- Part III 1963) (Reaffirmed 2002), which are presented in Table 3.2.

Table 3. 2 Physical properties of Fine and Coarse aggregates

Sr. No.	Characteristics	Test values	
		Fine Aggregates	Coarse Aggregates
	Type	Natural sand	Crushed
1	Specific Gravity	2.65	2.6
2	Water Absorption	1.03%	1.8%
3	Particle size range	150 microns - 4.75 mm	4.75 mm – 20 mm

3.2.3 Reinforcement

8mm, 10mm, and 12mm diameter HYSD-TMT bars confirming (IS:1786 2008) were used as reinforcements in the exterior BCJ specimens. The reinforcement bars were tested in a Universal Testing machine having a capacity of 1000kN. The yield and ultimate tensile strength of 12mm, 10mm, and 8mm diameter bars were found to be 528.59 MPa and 621.11 MPa; 640.96 MPa, and 715.91 MPa; and, 691.97 MPa and 784.85 MPa; respectively. The load-displacement representation of the uncorroded reinforcing bars of different diameters is shown in Figure 3.2.

3.2.4 Copper Wires

Fire-resistant copper wires were used to make the parallel connection on the reinforcement cage to introduce corrosion into the steel bars. To complete the connection established over the reinforcement bars by connecting them to the DC power supply, copper wires of two different diameters (i.e., 1 and 1.5 sq mm) were used. The thicker wire was used at the corrosion-exposed reinforcement cage. It acts as a safeguard against the breaking of connections during severe corrosion levels at longer corrosion exposure duration.

3.2.5 Stainless Steel Mesh

A stainless-steel wire mesh confirming ASTM E2016 and ISO 9044 standards having hole sizes ranging from 0.2-0.5 mm was used. The stainless-steel wire mesh acts as a cathode in the accelerated corrosion process.

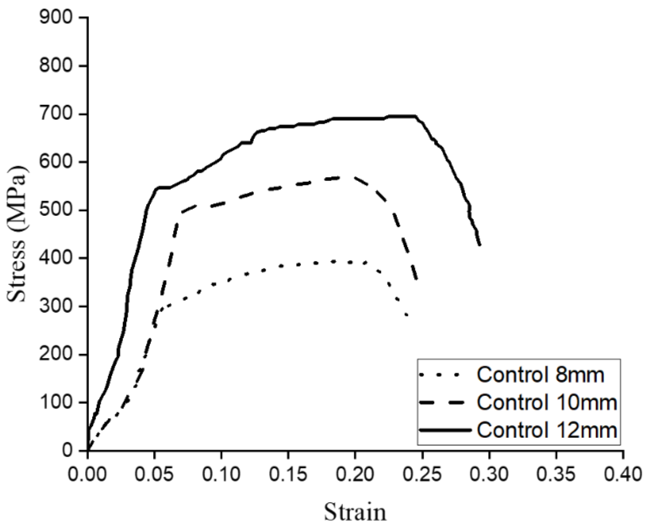

Figure 3. 2 Stress-strain curve for control/uncorroded steel bars

3.3 DESIGN MIX DETAILS

3.3.1 Design Mix

The exterior BCJ specimens (i.e., non-seismically detailed and seismically detailed) were cast using normal-strength concrete with a characteristic concrete compressive strength of 25MPa. The M25 grade concrete mix was designed as per (IS 10262 : 2019 2019) and is presented in Table 3.3. The average compressive strength of the mix was determined by casting and testing six cubes (i.e., three each for 7, and 28 days strength) of standard size of 150 mm, as per (IS 516 1959), respectively.

Table 3. 3 M25 grade concrete mix design as per IS 10262 : 2019

Particulars	Cement (kg/m^3)	Sand (kg/m^3)	Coarse Aggregate (kg/m^3)	Water (kg/m^3)	7 days strength (MPa)	28 days strength (MPa)
Quantity	388	670	1113	187	23	29

3.4 CASTING OF EXTERIOR BEAM-COLUMN JOINT (BCJ) SPECIMENS

3.4.1 Description of Test Units

A total of 16 RC exterior BCJ specimens were cast. Two types of reinforcement detailing regimes i.e., non-seismically detailed and seismically detailed specimens were adopted.

The non-seismically detailed Exterior BCJ specimens were designed as per the specification of IS 456 2000, followed by the conventional detailing as per (SP34 1987). The reinforcement configuration of the seismically detailed exterior BCJs was done as per the specifications of IS 13920: 2016 (Indian Standard 2016). All the specimens had the same dimensions.

For all the beam-column joint specimens, the beams were reinforced with the 2 nos. of 8 mm and 3 nos. of 10 mm diameter deformed steel bars as top and bottom longitudinal reinforcements. 8 mm diameter 2L stirrups were provided as the shear reinforcement. For the column, 4 nos. of 12mm diameter were used as longitudinal reinforcing bars however for transverse reinforcement 8 mm diameter bars were used. Figure 3.3 (a) shows the reinforcement detailing for non-seismically detailed specimens. A spacing of 140 mm was provided for the stirrups for the entire length of the beam. Whereas, for seismically detailed specimens, a closer arrangement of stirrups with a spacing of 100 mm was provided, shown in Figure 3.3 (b). Moreover, additional stirrups were also provided in the seismically detailed specimens inside the joint core region at a spacing of 50 mm.

All the Exterior BCJ specimens were designed by following the strong column weak beam concept. As per IS 13920:2016 (Indian Standard 2016), the sum of flexural capacities of columns ($\sum M_c$) meeting at any joint must be at least 1.4 times the sum of flexural capacities of beams ($\sum M_b$) for a strong column-weak beam joint. For this experimental study, all the specimens designed have a column-to-beam flexural capacity ratio ($\sum M_c / \sum M_b$) of 2.6.

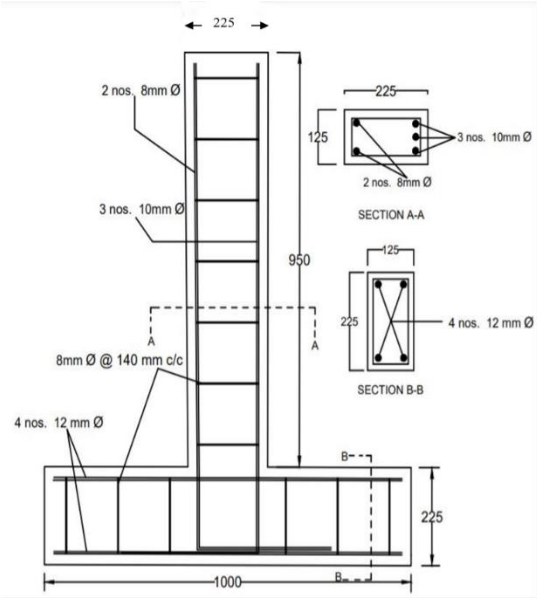

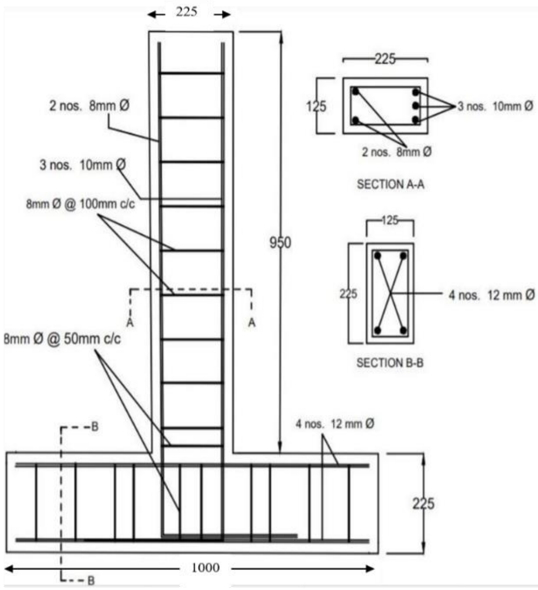

(a) (b)

Figure 3. 3 Reinforcement detailings of RC Exterior (a) non-seismically detailed, and (b) seismically detailed BCJ

3.4.2 Casting of the BCJ Specimens

The BCJ specimens were cast in mild steel moulds of the designated dimensions. The reinforcement cages prepared for the non-seismically detailed and seismically detailed specimens are shown in Figure 3.4 (a). The parallel connections of the copper wires were installed on the reinforcement cages for the accelerated corrosion process (see Figure 3.4 (b). Before casting, oiling of the mould is done to facilitate easy de-moulding. The cover blocks of 25 mm were provided between the shuttering and the reinforcement cage to provide the nominal cover all around the BCJ specimen (see Figure 3.4 (b)). The pouring of concrete into the mould was done in two layers; each layer was vibrated uniformly using a 60 mm diameter needle vibrator for voids removal from the fresh concrete (see Figure 3.4 (c)). Post-casting, wet gunny bags were used to cover the specimens to provide curing for 28 days, as shown in Figure 3.4 (d).

(a) Reinforcement cage

(b) Reinforcement cage inside the mould

(c) Needle vibrator used for uniform vibration

(d) Curing of the specimens

Figure 3. 4 Construction details of beam-column joint specimens

3.5 CORROSION OF BEAM-COLUMN JOINT SPECIMENS

3.5.1 Accelerated Corrosion Scheme

Under natural environmental conditions, it takes numerous years for the corrosion to occur, effectively making it a very time-consuming process. Therefore, to conduct an experimental study on the RC structural members having corrosion damage at different levels, an electro-chemically accelerated corrosion method is adopted. The viability of this method can be authenticated by the literature of numerous researchers (Meda et al. 2016; Liu and Li 2018; Rajput et al. 2019; Shen et al. 2021a; Li et al. 2022a) and has manifested similar results as those obtained from corrosion in the natural environment (Yuan et al. 2007; Mak et al. 2019). For this study, accelerated corrosion was introduced and was targeted primarily at the junction of BCJ, therefore all the wire connections were made within this region only, as can be seen in Figure 3.5 (a). For introducing accelerated corrosion, the test setup includes a DC power supply (scientiFic PSD3210), stainless steel wire mesh, 3.5% NaCl solution, 1 and 1.5 sq. mm copper wires, alligator clips, and gunny bags.

The specimen was wrapped with gunny bags all around the target corrosion area. Above the gunny bag wrapping, a stainless-steel wire mesh covering is provided. The stainless-steel mesh is connected via an alligator clip to the DC power supply (at the negative terminal) acting as a cathode. The reinforcement bars (with the help of a parallel wire connection provided on the reinforcement cage, as shown in Figure 3.5 (a)), are connected to the DC power supply (at the positive terminal) acting as an anode, as shown in Figure 3.5 (c). A continuous dripping of 3.5% NaCl solution is maintained over the mesh-covered region of the BCJ specimens (Figure 3.5 (d)).

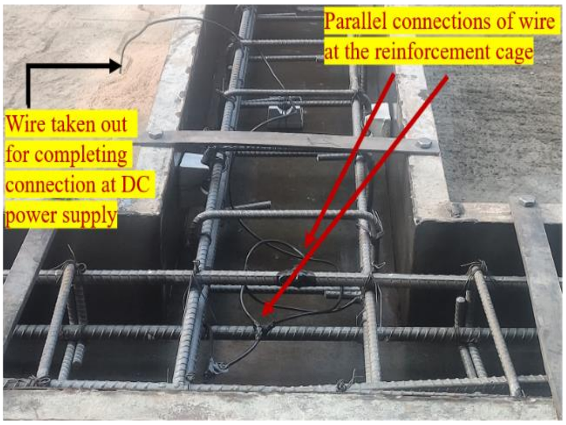

(a) Parallel connections of wire

(b) Casting of BCJs

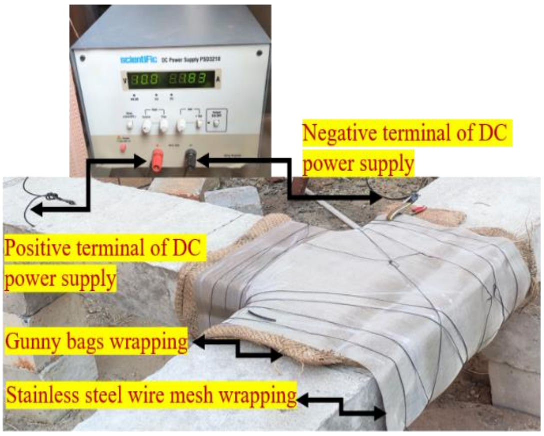

(c) Wrapping of specimens along with connections

(d) Setup for accelerated corrosion

Figure 3. 5 Accelerated corrosion test set-up

3.5.2 Pilot Study for the Corrosion

One reference test specimen each from both the reinforcement detailing regimes was taken to perform the pilot study. The behaviour and pattern of corrosion progression within the specimens corresponding to corrosion exposure duration were observed. The accelerated corrosion process starts by introducing the impressed current to the specimens via a DC power supply. A steady voltage (10 V) was maintained throughout the experimental corrosion exposure duration along with the continuous dripping of 3.5% NaCl solution. As the corrosion exposure duration increases, variation in the impressed current intensity is observed. The pilot specimens were visually monitored on a daily basis and the current intensity was recorded with respect to the exposure duration of the corrosion. The specimens were corroded up to the stage at which a constant rate of impressed current was noticed after going through certain variations in the impressed current readings. Based on literature regarding various corrosion models, it was observed that the corrosion pattern observed in the pilot specimens shows a close resemblance to the pattern shown in the Phenomenological model for reinforcing bar corrosion in concrete (Melchers and Li 2006).

Based on the current intensity-time duration plot of the pilot specimen with reference to the Melchers model of corrosion (Melchers and Li 2006), four major phases of corrosion in the pilot test specimens were categorized, as shown in Figure 3.6. The current intensity-time duration plot for the non-seismically detailed pilot specimen is shown in Figure 3.6 (a) while Figure 3.6 (b) shows that for the seismically detailed pilot specimen. Due to the difference in the reinforcement detailing for both pilot specimens, the number of days required to achieve the four phases of corrosion was different.

At every phase change of corrosion, the specimens were visually monitored and were also unwrapped to check for the cracks generated due to the induced corrosion. The visual description of each phase of corrosion is explained below and also illustrated in Figure 3.7.

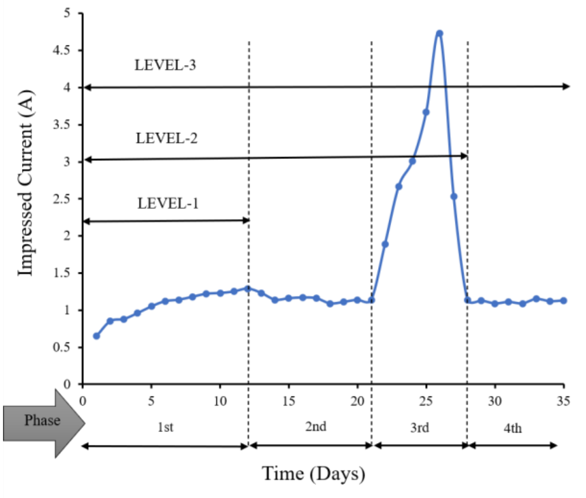

(a)

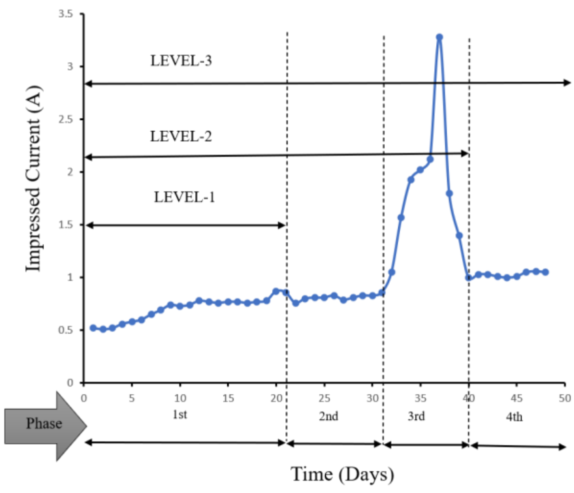

(b)

Figure 3. 6 Impressed current-time duration representation of pilot specimens (a) non-seismically detailed and (b) seismically detailed for determining different phases and categorizing different levels of corrosion

Phase 1: A linear increasing trend of the impressed current was experienced as the corrosion duration proceeded. After a few days of initiation of the corrosion process, some brown patches representing the rust products were visible on the gunny bags as well as on the steel mesh surface, as shown in Figure 3.7 (a). When the specimens were unwrapped for checking, fine hairline cracks were visible on the longitudinal surface of the column and beam (see Figure 3.7 (b).

Phase 2: In this phase, a drop in the current intensity was experienced which lasted for some instance of time. More rust deposition was seen on the mesh surface along with several new red and brown patches (see Figure 3.7 (c). The reddish-brown liquid oozes out from the specimen, as shown in Figure 3.7 (d).

Phase 3: This phase shows a sudden upward trend in the current intensity after a particular duration. The rust deposits are denser at this phase and have taken the shape of long suspended peaks at the surface of the mesh, as can be seen in Figure 3.7 (e). A dark brown liquid carrying washed-off rust products was observed coming out of the specimens. When the specimen was unwrapped, it was experienced that some new hairline cracks had appeared and the existing cracks from 1st phase had widened (see Figure 3.7 (f).

Phase 4: A drop in current intensity was observed in this phase and after that, a constant rate was experienced throughout the entire corrosion duration. The black liquid oozes out of cracks along with some black rust particles, as shown in Figure 3.7 (g). During the unwrapping of the specimen, deposited rust on the surface of the mesh surface is shown in Figure 3.7 (h). The wider cracks along the longitudinal surface of beam and column were experienced, as shown in Figure 3.7 (i). A noticeable reduction in the concrete cover around the mesh and gunny bags-wrapped surface of BCJs was also experienced.

(a) Initial stage of corrosion

(b) Hairline cracks due to corrosion

(c) More rust deposition

(d) Reddish-brown liquid oozing out

(e) Long suspended peaks of deposited rust

(f) Wide cracks at higher levels of corrosion

(g) Black liquid oozes out of cracks

(h) Deposited rust on the mesh surface

(i) Wider cracks along the longitudinal surface of the column

Figure 3. 7 A visual description of specimens under different levels of corrosion

3.5.3 Corrosion Levels and Crack Width Measurements

From Figure 3.6, it was observed that the reference test specimen undergoes certain phases of corrosion corresponding to corrosion-exposure durations. The impressed current–time duration graph of the pilot specimens was used to decide the three levels of corrosion for this study. The corrosion levels are explained below in detail and are also highlighted in Figure 3.6 (a) and (b) for the non-seismically detailed and seismically detailed pilot specimens.

Level-1: Level-1 of corrosion was set at the end of phase 1, where the impressed current stops increasing linearly and begins to follow a constant flow pattern.

Level-2: Level-2 of corrosion was set at the end of phase 3, where a sudden upward shoot in impressed current drops down.

Level-3: The last phase i.e., Phase 4 was set as Level-3 of corrosion, where the current follows a constant pattern against corrosion duration and shows no sign of variation. This level represents the most severe level of corrosion investigated in this study

After every level of corrosion, the pilot specimens were unwrapped and checked for the cracks generated due to the induced corrosion. The width of these cracks on the beam and column surface was measured with the help of a Dino-Lite edge digital microscope (series AM7915). This instrument has a resolution of 5 M pixels (2592x1944) and a magnification range of 10x ~ 220x which allows for capturing a crystal-clear image of the crack. Thereafter, the captured images were processed in the associated software (DinoCapture 2.0 version 1.5.44) for the exact dimensioning of the crack width, as shown in Figure 3.8.

Figure 3. 8 Crack monitoring and measuring via Dino-Lite edge digital microscope

All the non-seismic and seismic specimens were corroded by adopting the same accelerated corrosion scheme as was followed for the pilot test specimens. The nomenclature adopted for the corrosion-damaged specimens is shown in Table 3.4. The impressed current-time duration plots for each specimen are provided in their respective results section of Chapter 4. These respective plots are used to decide the corrosion duration for each specimen as per the description of levels provided above.

Table 3. 4 Nomenclature used for control and corroded specimens

Detailing Regime	Specimen ID	Corrosion level	Accelerated corrosion duration (days)
Non-Seismic	NDU	Control/Uncorroded	-
	NDC-1	1	9
	NDC-2	2	22
	NDC-3	3	30
Seismic	DU	Control/Uncorroded	-
	DC-1	1	25
	DC-2	2	39
	DC-3	3	45

3.5.4 Estimation of Corrosion Mass Loss

To determine the corrosion ratio for different corrosion levels, the estimation of mass loss is performed. In this study, the mass loss of the respective corroded specimens was calculated by adopting two different approaches i.e., Theoretical and Actual mass loss. To calculate the theoretical mass loss of the corrosion-damaged reinforcing bars, the data from the impressed current-time duration plot is required. The impressed current and time duration (in seconds) were incorporated into the Faradays formula, shown in Equation 3.1 for calculating theoretical mass loss for respective corrosion levels.

$$\Delta m = \frac{MIt}{ZF} \tag{3.1}$$

Where,

- Δm is the corrosion mass loss (grams);
- I is impressed current (ampere);
- t represents duration of corrosion (seconds);
- M is the molar mass of a steel bar (grams per mole);
- Z is the valency of iron;
- F represents Faraday's constant (96,485 C/mol).

To validate the theoretical mass loss from the corroded bars, the actual mass loss of reinforcement was determined using gravimetric analysis. For the actual mass loss calculation, the specimens were distorted after the reverse cyclic loading test, and the corrosion-damaged reinforcement cage was extracted, as shown in Figure 3.9. The corroded bars of the desired length (550 mm, based on the visual inspection, also shown in Figure 3.9) were cut from the corroded reinforcement cage, as shown in Figure 3.10 (a). The rust deposits along with loose concrete were knocked by a wire brush and were further cleaned with the help of a 10% HCL solution, as shown in Figure 3.10 (b). Due to severe corrosion damage, the localized pitting on the stirrups and longitudinal reinforcement bars can be visible, resulting in the fracture of stirrups, cross-sectional area reduction, and de-scaling of longitudinal reinforcing bars, as shown in Figure 3.11. The weight of bars of decided length before corrosion and after the cleaning process of corroded reinforcement was noted, as shown in Figure 3.12. The actual mass loss is determined by using the following formula shown in Equation 3.2. After cutting and cleaning of corrosion-damaged reinforcing bars of 8mm, 10mm and 12mm diameters, tensile testing was done and the corresponding load-displacement graphs are shown in Figure 3.13.

$$\text{Mass loss } (\%) = \frac{w_i - w_c}{w_i} \times 100 \qquad (3.2)$$

Where,

- w_i represents the initial mass of the decided length of rebars before corrosion;
- w_c represents the mass of reinforcing bars after the corrosion damage and cleaning with acid.

Figure 3. 9 Specimens were distorted after the cyclic loading test for calculating mass loss

(a) Corroded bars of desired length were cut (b) Cleaning and removal of deposited rust

Figure 3. 10 Cutting and cleaning of corrosion-damaged reinforcement bars for the mass loss

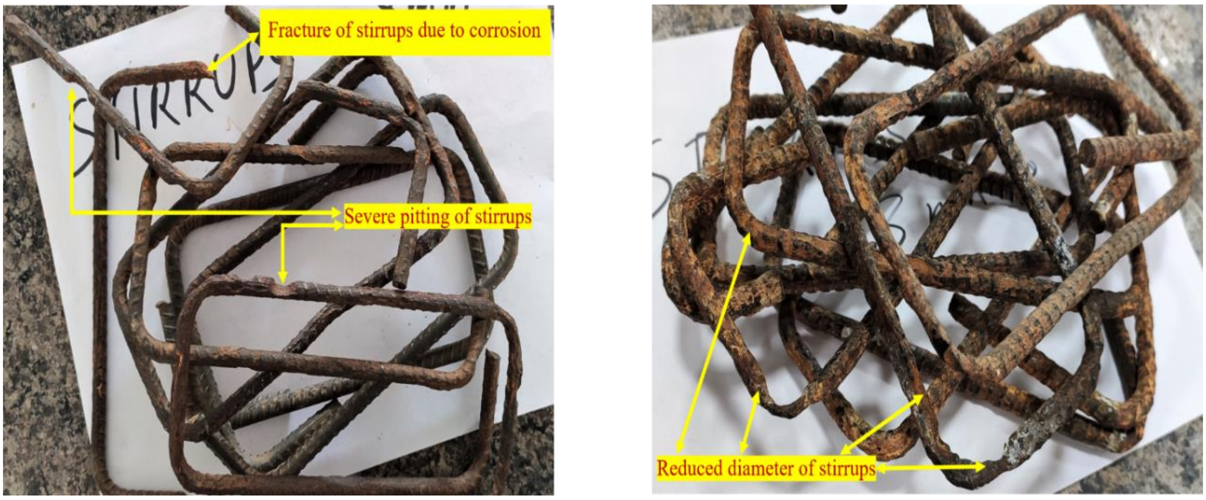

(a) (b)

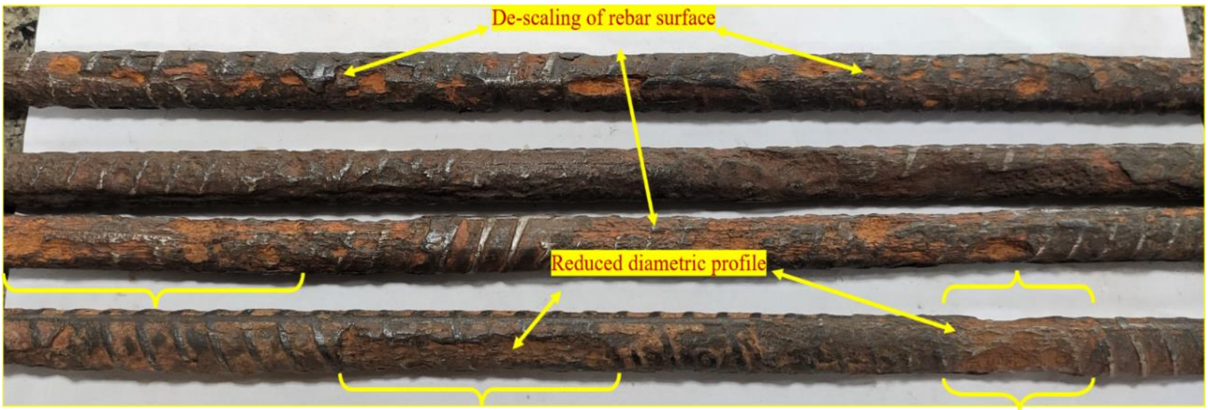

(c)

(d)

Figure 3. 11 (a) & (b) Fractured stirrups, (c) & (d) cross-sectional area reduction and de-scaling of longitudinal reinforcement bars

Figure 3. 12 Determining the mass loss for different levels of corroded specimens

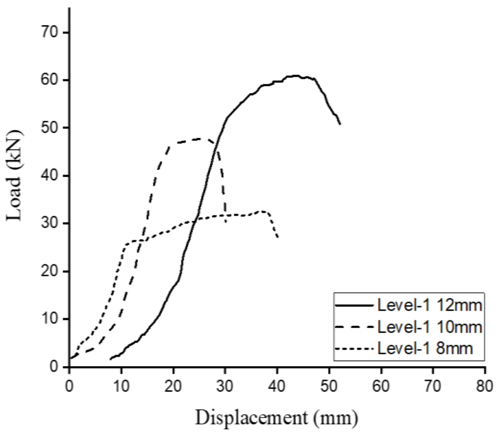

(a)

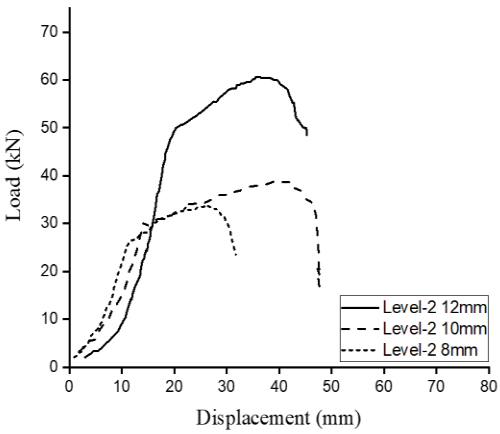

(b)

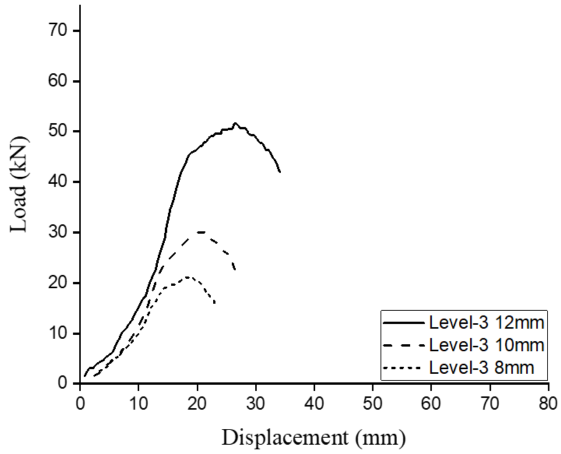

(c)

Figure 3. 13 Load-displacement curve for tensile test for steel bars of different diameter

3.6 TEST SETUP AND LOADING PROTOCOL

The BCJ test specimens were placed on the fixed loading frame and were provided with boundary conditions to keep them in a fixed position for testing purposes. For this test setup, the column was positioned horizontally on the strong steel base of the frame, and the beam was positioned at an angle of 90° to the base. The nut-J bolt (16 mm diameter) assembly along with four roller plates was used to fix the column against cyclic loading. The column was rested horizontally on the two roller plates, one at each side 100 mm from each end. Similarly, two more roller plates were placed on the column surface aligned with the plates placed at the bottom surface of the column. The two sets of plates are provided at each side of the column containing four 16mm diameter nut-J bolt assemblies (two J-bolts on each side) to hold the column surface at a fixed position against the strong loading frame. At one end of the column, an axial force (approximately equal to $0.1f_cA_g$) was applied with the help of a double-acting hydraulic jack having a capacity of 300 kN, where f_c represents the compressive strength of concrete and A_g represents the area of cross-section of the column. The axial load applied at the column was in the range of 70–75 kN. After the desired load was applied at the column end, the loading knobs were firmly closed to keep the pressure intact and arrest any drop in axial load throughout the experimental testing. The column from the other end was supported against a fixed steel angle in order to produce an equal reaction. The quasi-static reverse cyclic loading jack and related assembly are fixed through nut and bolt arrangements on the reaction wall to apply lateral loading on the beam surface. The experimental test setup (schematic and actual) including the loading system and instrumentation is shown in Figure 3.14 (a) and (b), respectively.

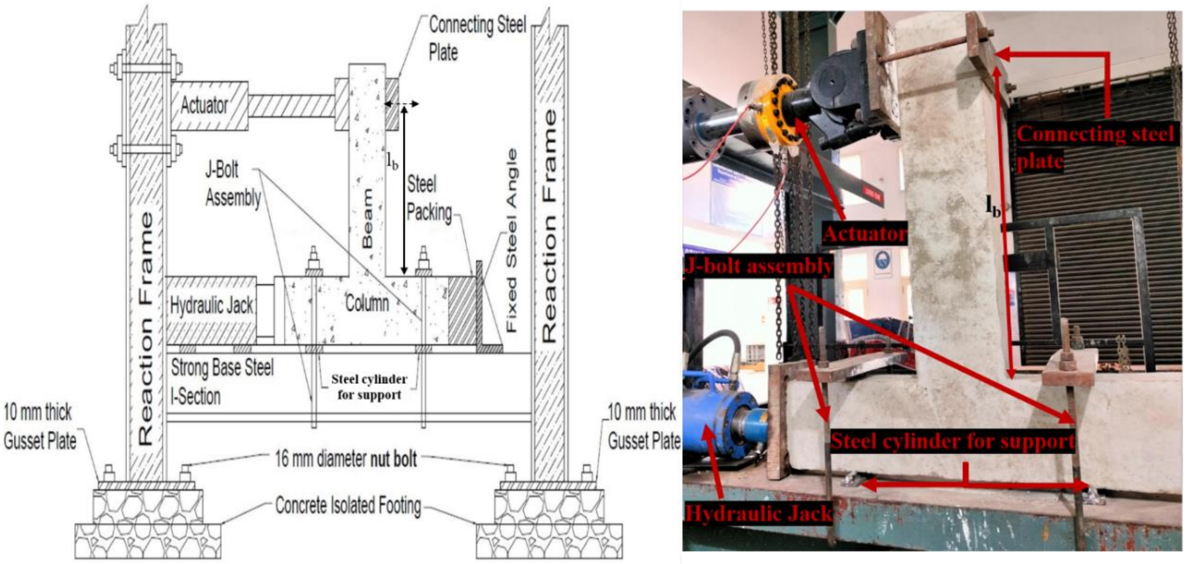

(a) (b)

Figure 3. 14 (a) Schematic diagram of the test setup, (b) Actual test setup for specimen under reverse cyclic loading

The displacement-controlled cycles for this study were adopted as per the guidelines of the American Concrete Institute (ACI) for acceptance criteria for moment frames (ACI 374.1-05 2005), as shown in Figure 3.15. With steps that are neither too small nor too large, the sequence is meant to guarantee that displacements are increased gradually. Step sizes that are too large could make it difficult to accurately estimate the system's drift capacity. Should the steps be excessively small, loading repetitions could unreasonably soften the system, leading to fictitious high maximum drifts and fictitious low maximum lateral resistances. Step sizes that are too small can also cause the system's energy storage to shift more slowly than it would during a significant event. In this regime, each drift increment consists of three large reverse cycles followed by one small cycle (approximately 1/3 in the magnitude of the big cycle) in negative and positive drift directions.

The reverse cyclic loading is applied via a hydraulic actuator having a capacity of 250 kN, at the beam surface (see Figure 3.14). The loading is purely displacement-controlled with a frequency of 0.2 Hz and the displacement is fed to the actuator through a program generated in the computer and auxiliary controller. This sequence of controlled displacement cycles represents the similarity in drifts that are expected under earthquake motions and is adopted by several researchers for the study of the behaviour of BCJs under seismic loading.

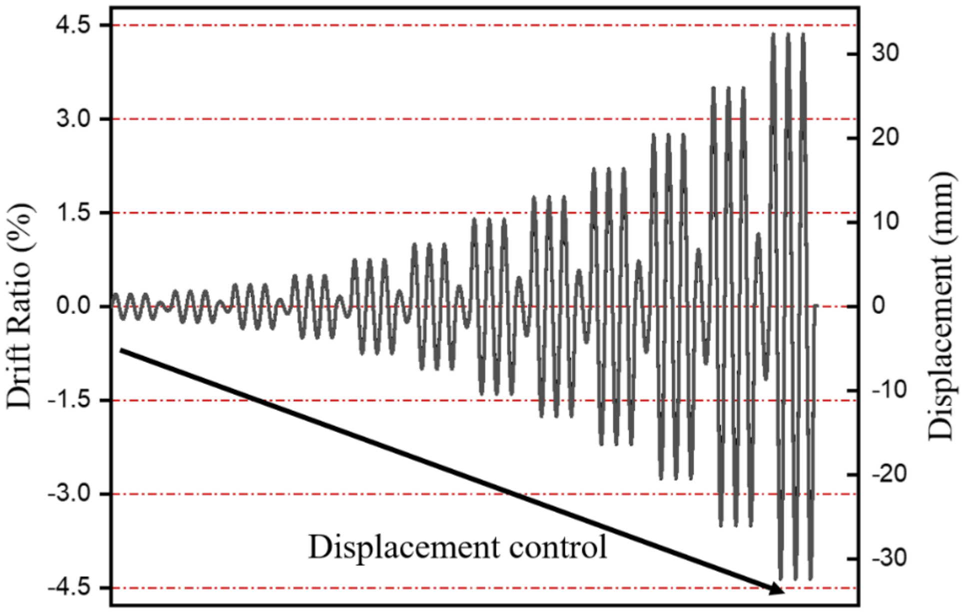

Figure 3. 15 Applied displacement-controlled cycle history

3.6.1 Damage Level of BCJ Specimens

To set the loading protocol, two pilot specimens (one uncorroded specimen from each reinforcement detailing regime) were tested under the reverse cyclic loading condition. As the displacement progressed, flexural cracks developed along the beam and column surface of these reference specimens, and the specimens failed ultimately due to the dislocation of the beam from the beam-column junction. The damage caused by the reverse cyclic loading was quantified using a damage index (DI). The damage index for the reference specimens was calculated using the Park and Ang model which states that if (DI ≥ 1.0), it indicates complete collapse or failure of the member. From the experimental data of the pilot specimens, it was experienced that the DI ≥ 1.0 limit was achieved between the 11th and 12th displacement cycle. Therefore, ultimate displacement was set at the 12th cycle (34 mm). Hence, all the test specimens whether non-seismic or seismic were tested up to the displacement of 34 mm. The damage index is calculated as per the Equation 3.3.

$$\mathrm{DI} = \frac{\delta_M}{\delta_U} + \frac{\beta}{F_y \delta_U} \int \mathrm{dE} \qquad (3.3)$$

Where,

- δ_M represents the maximum displacement obtained under cyclic loading;
- δ_U represents ultimate displacement capacity;
- dE shows incremental dissipated hysteretic energy;
- F_y is the corresponding yield strength;
- β symbolizes the strength degradation parameter with a value of 0.1 (I.Villemure and E.Ventura 1995), for well-reinforced concrete structures

3.7 DEVELOPMENT OF HIGH STRENGTH FIBER REINFORCED CONCRETE (HSFRC)

An ideal shift has been experienced in the field of concrete with the evolution of high-strength concrete (HSC). The superior mechanical properties along with the much-improved durability parameters over conventional concrete have been reported from the various experimental studies. Also, the presence of hybrid steel fibers in HSC forming High Strength Fiber Reinforced concrete (HSFRC) renders higher ductility. These advantages have encouraged the use of HSFRC as a retrofitting/repairing material in both field and research applications. Therefore, the present experimental study applies HSFRC as a retrofitting material for corrosion-damaged specimens along with the novel retrofitting technique.

3.7.1 Material

3.7.1.1 Cement

Ultratech 43-grade OPC was used to develop the High Strength Fiber Reinforced Concrete (HSFRC). The physical properties are listed in Table 3.1.

3.7.1.2 Pozzolanic Materials

Along with the cement, certain pozzolanic materials were used as binders. The densified Silica fume, and Metakaolin procured from Jaipur, Rajasthan (India) were used to develop HSFRC. The physical properties of Silica fume and Metakaolin are shown in Table 3.5.

3.7.1.3 Aggregates

The fine and coarse aggregates were used to develop the HSFRC. Natural river sand was used as fine aggregates. For the coarse aggregates, a maximum size of up to 12.5 mm as per IS 10262 : 2019 was adopted.

Table 3. 5 Physical properties of Silica Fume and Metakaolin

Sr No	Characteristics	Test Values	
		Silica Fume	Metakaolin
1	Color	off-white	off-pink
2	Specific Gravity	2.2	2.5
3	Mean Particle Size	0.15 microns	3 microns

3.7.1.4 Steel Fibers

Steel fibers of two types i.e., hooked-end steel fibers and crimped steel fibers were used in the present study, as shown in Figure 3.16. The hooked-end steel fibers had mechanically deformed hooks at both ends of the fibers while the crimped steel fibers had an undulated surface along the length of the fibers. The aspect ratio and tensile strength of both steel fiber types are presented in Table 3.6.

Figure 3. 16 Crimped and hooked-end steel fibers

Table 3. 6 Properties of Steel Fibers

Fiber Types	Length (mm)	Diameter (mm)	Aspect ratio	Ultimate tensile strength (MPa)
Crimped Steel fibers	30	0.55	54.54	1200
Hooked steel fibers	60	0.75	80	1200

3.7.1.5 Superplasticizers

To reduce the water/binder ratio without compromising the flowability of concrete, superplasticizers are used. For this study, a polycarboxylic ether-based superplasticizer i.e., Auramix 400 variant 456 manufactured by Fosroc, was used.

3.7.2 Mix Procedure and Sample Preparation

The variation in the water/binder ratio and superplasticizer dosage was done through several trials to achieve good flowability along with higher compressive strength. The mix proportion for HSFRC is presented in Table 3.7. The procedure for preparing the HSFRC is explained below:

- Initially, the fine aggregates and coarse aggregates are mixed in the dry state in a concrete mixer for 2 minutes.
- Thereafter, all the powder content including cement, silica fume, and metakaolin is added to the mixer and dry mixed for approximately 2 minutes.
- The addition of hybrid steel fibers into the mix.
- The polycarboxylate ether-based superplasticizer is added to the calculated amount of water content and the complete solution is added to the mix in three parts.
- 25% of the water solution (water + superplasticizer) was incorporated into the dry mixture and for approximately 5 minutes the mixing was done. Again, 50% of the water solution was added to the mix and the mixer was rotated for another 10 to 15 minutes. The method of addition of the water solution in parts was adopted to minimize the water loss to the internal surface of the drum mixer. The concrete mixer was timely stopped to break the ball-shaped formation of concrete which forms due to the presence of steel fibers.

- The remaining 25% of the water solution was added to the mix after breaking the concrete balls within the mixer which entraps water inside them. Finally, the mixer is rotated for approximately 10 minutes. The mixer was stopped at regular intervals to break the concrete balls and to loosen up the concrete which gets struck at the surface of the rotating drum during the continuous rotation.
- The prepared mix was filled in 150×150×150 mm cube moulds. The demoulding of the cube specimens was done after 24 ± 1 hours and cured in the temperature-controlled water bath throughout the curing period of 28 days.

Table 3. 7 HSFRC mix proportions

Materials	Cement	Fine Aggregate	Coarse aggregate	Silica fume	Metakaolin	Super-plasticizer	Water binder ratio	Comp. Strength (MPa)	Flex. Strength (MPa)
HSFRC	1	0.98	1.23	0.14	0.14	0.02	0.23	85	9.5

3.7.3 Material Testing Methodology

3.7.3.1 Compressive strength test

The compressive strength of the mix was determined with the help of a Compression Testing Machine (500-ton loading carrying capacity). The loading rate was 140 Kg/square cm/minute. The average of three 150×150×150 mm size cubes was used to evaluate and report the compressive strength, as shown in Figure 3.17. The average 28-day compressive strength was experienced to be 85 MPa.

The cylinders of size 150 mm × 300 mm were cast to determine the axial stress-strain behaviour of the developed HSFRC. At the surface of the test cylindrical specimen, two strain gauges (60 mm gauge length) were installed in the axial direction, one each on the opposing vertical faces, as shown in Figure 3.18. Figure 3.19 shows the experimental stress-stain curve of the tested HSFRC cylindrical specimen.

Figure 3. 17 Test setup for determining compressive strength of HSFRC

Figure 3. 18 Test setup to evaluate the stress-strain behaviour of HSFRC

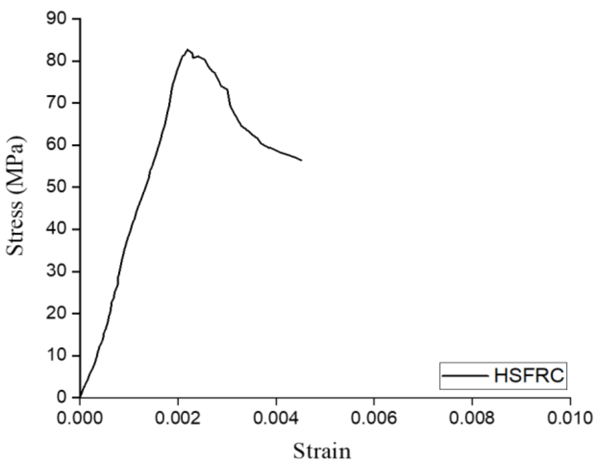

Figure 3. 19 Stress-strain curve of HSFRC cylindrical specimen

3.7.3.2 Flexural strength test

The flexural strength of the developed mix was calculated as per the guidelines of IS 516 1959. The specimens of size 100×100×500 mm were cast and were tested after 28 days under a two-point loading system, as shown in Figure 3.20. The rate of loading provided to the specimen during the test was 180 kg/min, as per IS 516: 1959. The dominant flexural crack can be seen progressing under bending, as shown in Figure 3.21. The flexural strength (f_b) has been calculated using equation 3.4 and is reported to be 9.5 MPa.

$$f_b = 3pa/bd^2 \tag{3.4}$$

where,

- p = maximum load (N)
- a = distance between the nearer support and the line of fracture
- L = supported length (mm)
- b = width of the specimen (mm)
- d = depth of the specimen at the fracture (mm)

Figure 3. 20 Two-point bending test Set-up arrangement

Figure 3. 21 Flexural failure of beam specimens

3.8 RETROFITTING OF CORROSION-DAMAGED SPECIMENS USING HSFRC

The damaged concrete of the specimens due to severe corrosion is entirely removed up to a particular length and is replaced by HSFRC. To identify the target region for repair, the reference test specimen used for the pilot study of corrosion (refer to section 3.5.2) was cut open by removal of the entire concrete to expose the corrosion-damaged reinforcement cage (see Figure 3.22). From Figure 3.22, it can be observed that severe damage to the reinforcement bars was experienced in the corrosion target area (i.e., around the junction of the beam-column). It was visually observed that the corrosion-affected length for the beam main reinforcement was up to 350 mm, initiating from the junction of BCJ. Similarly, the column reinforcing bars were damaged up to a length of 150 mm from either side of the junction. Therefore, a length of 400 mm for the beam and 200 mm length for either side of the column from the interface of BCJ was finalized for the repairing scheme for this study. Figure 3.23 (a) shows the removal of damaged concrete from the corroded BCJ specimens up to the decided length. The removed concrete dimensions up to the selected length in the beam and column side are illustrated in Figure 3.23 (b). After removing the damaged concrete from test specimens, the fracture, localized pitting of stirrups, descaling, and cross-sectional reduction of longitudinal bars due to severe corrosion were observed, as shown in Figure 3.24. To restore the ductility and strength of corrosion-damaged specimens, the HSFRC rehabilitation scheme was performed in certain steps:

1) Removing the existing damaged concrete entirely from the target repair region. The end portion of the removed concrete surface is chipped at the slope of 1:8 in order to avoid the abrupt plane change between the surface of the old concrete and HSFRC.

2) The rust products bonded on the reinforcing bar surface were extracted using a steel wire brush. Thereafter, an anti-corrosive coating (Sika Rustop) was applied to the damaged reinforcing bar to prevent further corrosion after the repair, as shown in Figure 3.25 (a). This epoxy is applied in two coats with a time difference of 2-3 hours. Subsequent concreting is done after 24 hours of coating.

3) A bonding agent (Sika Hibond) is applied at the surface of clean existing concrete to provide a better bonding layer between old and new concrete and the specimen is placed in a formwork, as shown in Figure 3.25 (b). The new concrete was added within 4-5 hours of the bonding agent application.

4) The HSFRC is prepared and poured at the removed concrete area within the formwork. Table vibration is provided to the entire specimen for uniform distribution of fibers and concrete. Figure 3.26 shows the specimen retrofitted with HSFRC.

After 24 hours, the entire formwork is removed as HSFRC is set properly and is covered with wet gunny bags for 28 days of curing. All the corrosion-damaged non-seismically and seismically detailed BCJ specimens were similarly retrofitted with HSFRC and were tested under the influence of quasi-static reverse cyclic loading. The nomenclature representing the HSFRC retrofitted specimens is shown in Table 3.8. The words R, ND, D, and U indicate Retrofitted, Non-seismic, Seismic, and Uncorroded, respectively. The impressed current-time duration plots for each specimen are provided in their respective results section of Chapter 5.

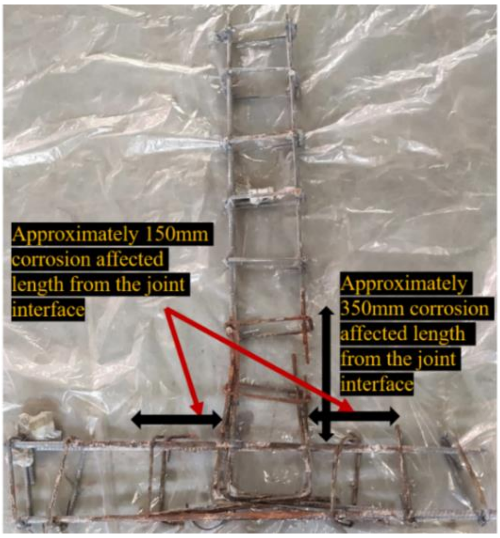

Figure 3. 22 Corrosion-damaged reinforcement cage of reference specimen

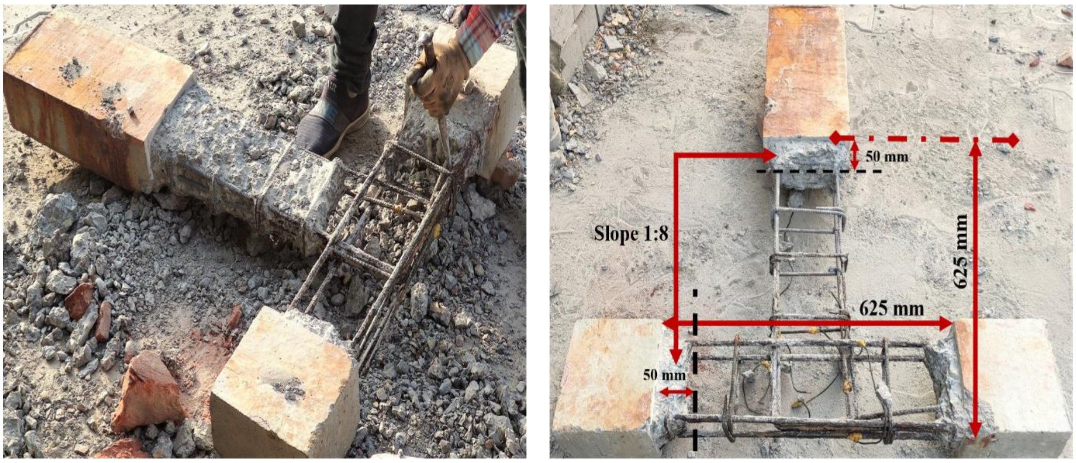

(a) Removal of corrosion damage concrete (b) Dimensioning of dismantled concrete area

Figure 3. 23 Geometrical dimensioning of dismantled concrete for HSFRC retrofitting in corrosion-damaged specimens

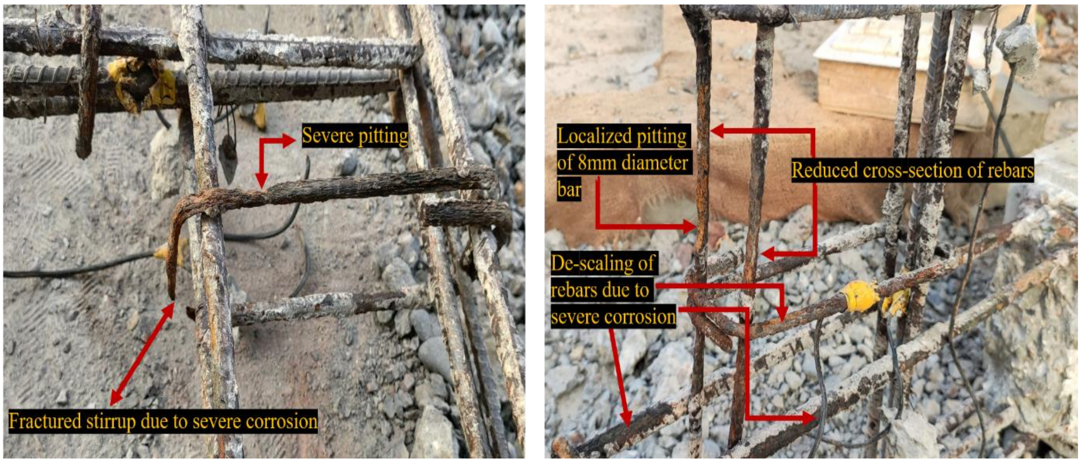

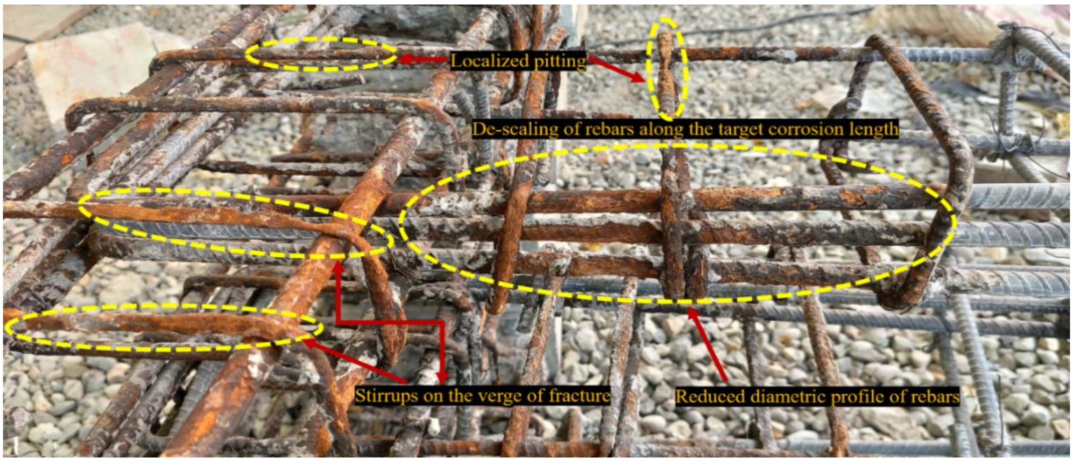

Figure 3. 24 The fracture, localized pitting of stirrups, descaling, and cross-sectional reduction of longitudinal bars due to severe corrosion

(a) (b)

Figure 3. 25 (a) Application of anti-corrosive coating on the surface of corroded reinforcing bar, (b) Specimen placed in formwork for retrofitting

Figure 3. 26 Table vibration provided to the retrofitted specimen

Table 3. 8 Nomenclature used for control and retrofitted specimens

Specimen ID	Corrosion level	Accelerated corrosion duration (days)
NDU	Control/Uncorroded	-
RND-1	1	13
RND-2	2	23
RND-3	3	32
DU	Control/Uncorroded	-
RD-1	1	22
RD-2	2	34
RD-3	3	45

3.9 CLOSING REMARKS

This chapter lists the experimental tasks undertaken to complete the entire testing and retrofitting program. A pilot study was conducted on uncorroded specimens of each detailing regime to determine and establish the ultimate displacement via damage index and different corrosion levels for both the non-seismically and seismically detailed beam-column joint specimens. High Strength Fiber Reinforced Concrete (HSFRC) was developed to be used as a retrofitting material for corrosion-damaged specimens. The experimental study results are presented in Chapters 4 and 5.

CHAPTER 4

SEISMIC BEHAVIOUR OF CORRODED BEAM-COLUMN JOINTS

4.1 GENERAL

In this part of the dissertation, the results of stage 1 (accelerated corrosion exposure) and stage 2 (part 1-structural testing of corroded BCJ specimens under reverse cyclic loading), are presented. The detailed methodologies of both stages have already been explained previously in Section 3.1. The BCJ specimens were subjected to corrosion (three different levels) and then were tested under reverse cyclic loading conditions. To achieve this objective, firstly, two reference specimens (one each from different reinforcement detailing regimes) were selected for the pilot study of corrosion. Based on the pilot study, the test specimens (i.e., non-seismically and seismically detailed) were corroded to three different levels (explained in detail in Section 3.5.2), also shown in Table 3.4.

The reference specimens were tested under cyclic loading in order to set the loading protocol, explained in detail in section 3.6.1. The control (uncorroded) and corroded specimens were then tested to the pre-decided drift ratio. After the cyclic loading test was performed, the corroded specimens were dismantled via a jackhammer, and the corrosion-damaged reinforcement cage was extracted to calculate the mass loss. The theoretical and the actual mass loss of reinforcement bars of each corrosion level specimen (calculated as per Section 3.5.4) along with the corresponding crack width is listed in Table 4.1.

The seismic performance of corrosion-damaged BCJ specimens has been determined in terms of the load-displacement hysteresis curve and envelope curve, displacement ductility, energy dissipation, stiffness degradation, and principal tensile stress. The obtained results of respective control and corrosion-damaged specimens are analyzed and discussed in the subsequent section. The seismic behaviour of different levels of corroded non-seismically detailed and seismically detailed BCJ specimens has been reported and compared below.

4.2 MONITORING DAMAGE IN CORRODED BCJ SPECIMENS

Figure 4.1 displays the experimental test setup for the continuous monitoring of impressed current and behavioural changes occurring at the surface of specimens corresponding to the time duration. A visual inspection of all the corroded BCJ specimens was done to determine the damage level due to corrosion. For level 1 corroded specimens, minor spots of rust were visible after 5 to 7 days of the active accelerated corrosion process. As the time duration progresses, the deposition of rust increases, as seen in Figure 4.2 (a), and reddish-brown colour water was observed dripping down the specimen. When the specimens were unwrapped and cleaned, hairline cracks were visible on the longitudinal reinforcement direction of the column and beam surface, shown in Figure 4.2.

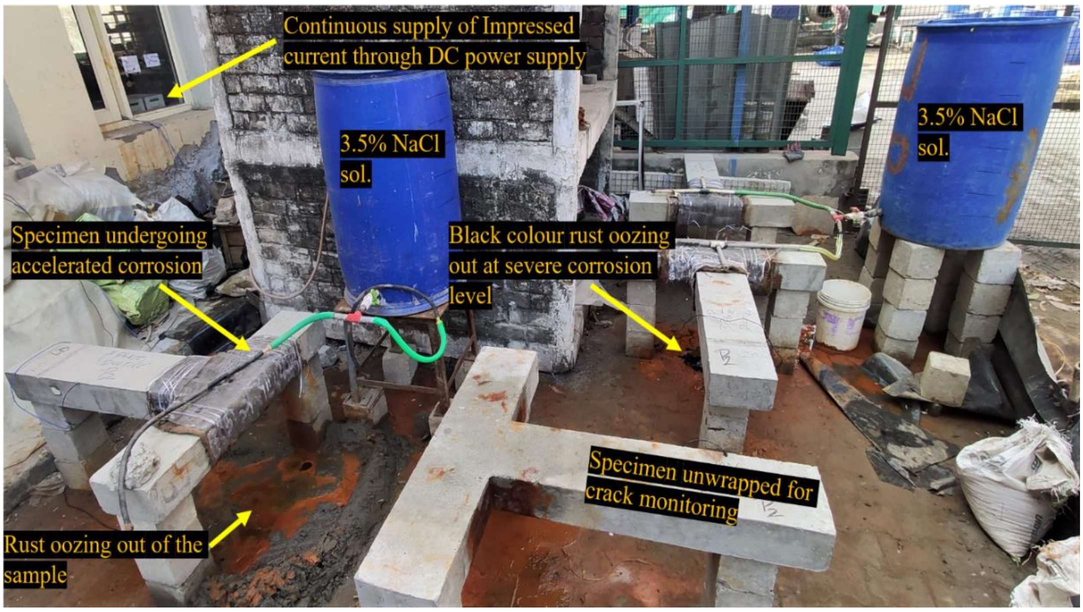

Figure 4. 1 Set-up created for accelerated corrosion and continuous monitoring

(a)

(b)

Figure 4. 2 (a) Rust deposition on the surface of stainless-steel mesh and (b) maximum crack width for Level-1 corroded specimen

As the corrosion-exposure duration increases, severe rust deposition on the surface of steel mesh can be experienced in the shape of long suspended peaks, as shown in Figure 4.3 (a). The water dripping down the specimen now appeared to be dark brown, carrying the washed-out rust products from inside the specimens. The specimens when unwrapped and cleaned showed wider cracks on the longitudinal reinforcement direction of the column and beam surface when compared to Level-1 specimens. The cracks were measured with the help of a Dino-Lite edge digital microscope (series AM7915) having a magnification range of 10x ~ 220x. These images were then processed in the associated software for accurate dimensioning of crack width, as shown in Figure 4.3 (b).

(a)

(b)

Figure 4. 3 (a) Dense rust deposition and (b) crack width measurement of Level-2 corroded specimen

At Level-3 corrosion, the specimen showed immense deposition of rust on the mesh surface. The black colour water along with rust products oozes out of the specimens, as shown in Figure 4.4 (a). The cracks extended on the longitudinal surface of the beam and column and were visible without even unwrapping the specimen. The crack width (up to 1.5 mm) as shown in Figure 4.4 (b) was experienced on the surface of the specimen, which is alarmingly dangerous for any structure.

(a)

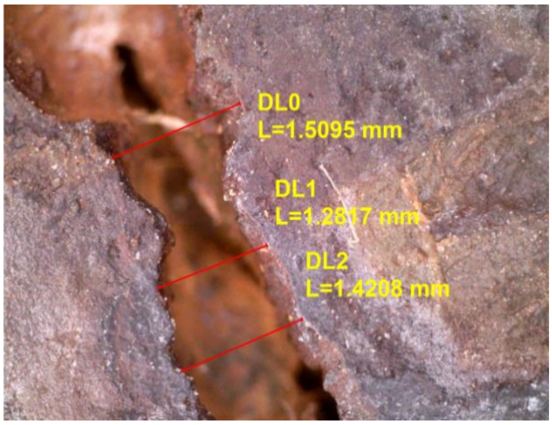

(b)

Figure 4. 4 (a) black colour water oozing out of the specimen along with rust at severe corrosion level (b) measured crack width of Level-3 corroded specimen

Table 4. 1 Summary of corrosion measurement in rebars

Specimens	Corrosion level	Rebars diameter (mm)	Mass after corrosion damage (g)	Average actual mass loss (%)	Theoretical mass loss (%)	Average crack width (mm)
NDC-1	1	8 10 12 Stirrups	405 959 1809 1253.5	5.193	5.869	0.629
NDC-2	2	8 10 12 Stirrups	378.5 902.5 1727 1186	10.173	11.43	0.989
NDC-3	3	8 10 12 Stirrups	361.5 867.5 1707.5 1074	14.103	14.425	1.509
DC-1	1	8 10 12 Stirrups	398.5 951 1785.5 1679	7.85	7.77	0.286
DC-2	2	8 10 12 Stirrups	382.5 912 1698 1490	14.2	14.93	0.482
DC-3	3	8 10 12 Stirrups	396 943 1726 1318.5	16.09	16.77	0.852

4.3 IMPRESSED CURRENT-TIME DURATION PLOT

The impressed current corresponding to the time duration of the accelerated corrosion process was recorded on an hourly basis every day. The variation in the current intensity is an indicator of the change in the corrosion phases and was experienced in the test specimens also. The impressed current-time duration plot for the corroded non-seismically and seismically detailed BCJ specimens is displayed in Figure 4.5 and Figure 4.6, respectively. A continuous linear rise in the impressed current was observed for the NDC-1 and DC-1 specimens at different durations, representing Level-1. After that, a constant rate of impressed current can be observed representing the calm phase of corrosion, also reported in the Melchers model, (refer to Figure 1.4). Thereafter, a sudden jump in the impressed current can be noticed indicating the passive layer breakdown by the continuous ingress of chloride ions resulting in the rapid corrosion process (i.e., Level-2). This can be visually experienced by the amount of rust deposition on the mesh surface and reddish-brown liquid oozing out of the wide cracks. With the increase of corrosion level (i.e., Level-3), the dark colour liquid was seen oozing out of the specimens along with the washed-away rust products. The time duration for the non-seismically and seismically detailed BCJ specimens are seen to be different due to the reinforcement detailing, however, the levels of corrosion achieved were similar.

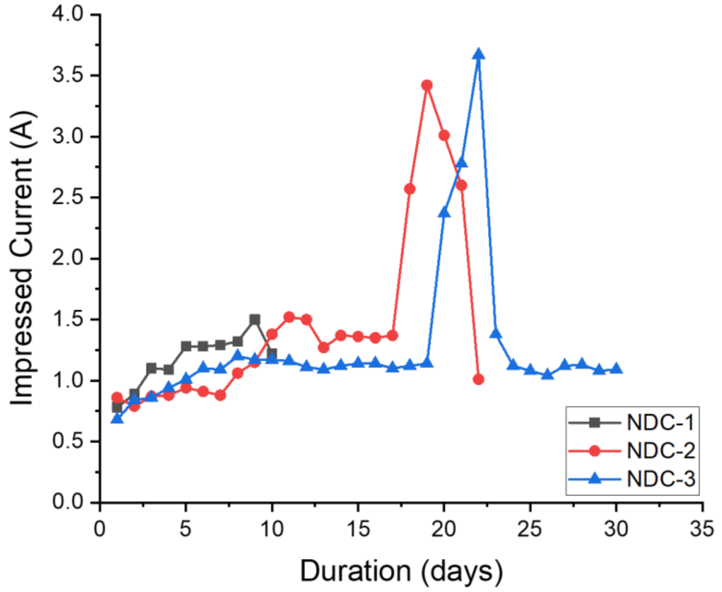

Figure 4. 5 Impressed current variation with respect to the time duration for all the non-seismic BCJ specimens

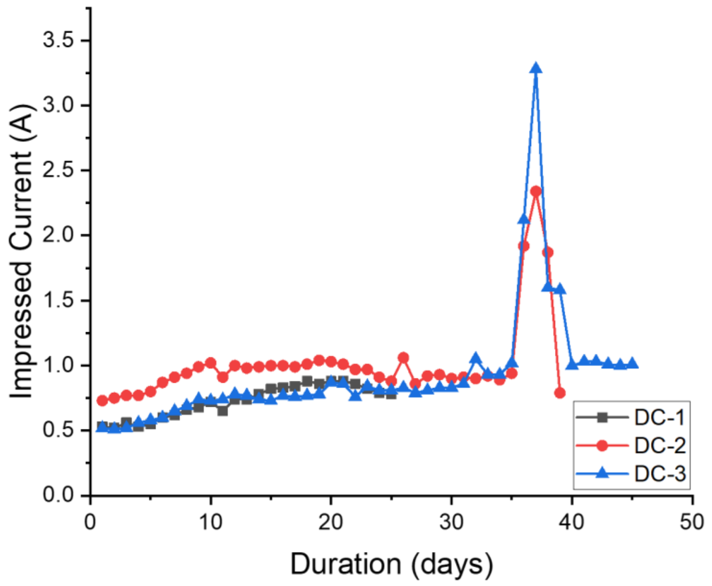

Figure 4. 6 Impressed current variation with respect to the time duration for all the seismic BCJ specimens

4.4 DAMAGE PROGRESSION OF BEAM-COLUMN JOINT SPECIMENS

The damage progression and the cracking pattern of the control and corrosion-damaged non-seismically detailed and seismically detailed BCJ specimens were observed throughout the displacement-controlled loading. During the test, the specimens were visually analyzed for damage progression, crack propagation, and failure mode. The ultimate failure of the control uncorroded specimen was due to a wide shear crack at the beam-column junction and the propagation of the major cracks was up to 100 mm from the joint region towards the beam and the column direction. Therefore, this area was selected for the target corrosion region and all the parallel wire connections were made within this region only. The occurrence and progression of cracks along the surface of the beam and column during loading are reported in this section. The mode of failure for control and different levels of corroded specimens are also discussed.

4.4.1 Damage Progression of Control Non-Seismic Specimen (NDU)

The control non-seismic BCJ specimens were positioned as shown in the experimental test setup (described in section 3.6), shown in Figure 3.14. The specimen is subjected to displacement-controlled loading and the corresponding damage is noted. At the drift ratio of ± 0.35%, the hairline shear cracks at the beam-column junction start to appear from one side of the diagonal. From ± 0.5% drift ratio onwards, the shear cracks were propagated from both the diagonal sides of the beam-column junction. Along with the diagonal shear cracks at the junction, hairline flexural cracks at the beam surface were observed as the drift ratio progressed. At the beam surface more flexural cracks were observed accompanied by the initiation of similar cracks at the surface of the column from ± 1% drift ratio onwards. At a drift of ± 1.75% and onwards, a clear sight of the widening of the shear cracks at the junction of the beam-column was observed and the widening of flexural cracks was also seen. The specimen ultimately failed due to the shear crack failure at the junction of BCJ, as shown in Figure 4.7. This failure was noted at a drift ratio of ±3.5% and higher. Simultaneously, the spalling and scattering of the concrete cover were also experienced along with the buckling of the longitudinal reinforcements.

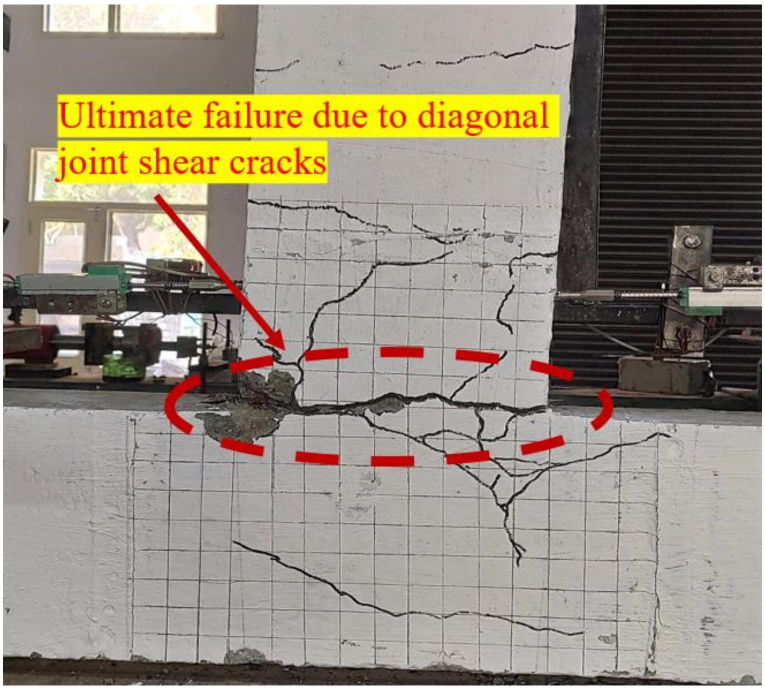

Figure 4. 7 Ultimate failure of NDU

4.4.2 Damage Progression of Corroded Non-Seismic (NDC) Specimens

From the corroded test specimens, it was observed that the first flexural crack was generated at a distance of 100 to 150 mm away from the joint region on the beam surface. Figures 4.8-4.10 show the failure mode of different levels of corrosion damage specimens and the dominant flexure crack at the beam surface. The appearance of flexural cracks during the early loading stage at this location was due to the localized pitting of the longitudinal reinforcement bars.

In the level 1 corroded specimen (i.e., NDC-1), it was seen that ± 0.25% drift ratio onwards, the hairline flexural crack originated from one side of the beam surface, i.e., at the localized pitting location. After the drift ratio of ± 0.5%, the flexural crack propagated from both sides of the beam surface at the location of 100 to 150 mm away from the joint region. As the drift ratio progressed, the widening of the dominant flexural crack was experienced along with the occurrence of some more flexural cracks on the surface of the beam and column.

The corrosion cracks which were already present at the longitudinal reinforcements directions of the specimen widened at the higher drift ratio and the dismantling of loose concrete was experienced from the cracks. From ± 2.75% drift ratio onwards, the crumbling and scattering of the concrete cover from the dominant wide flexural cracks were seen. The ultimate failure of the NDC-1 specimen was due to the dismantling of the beam from the wide flexural crack location, as shown in Figure 4.8.

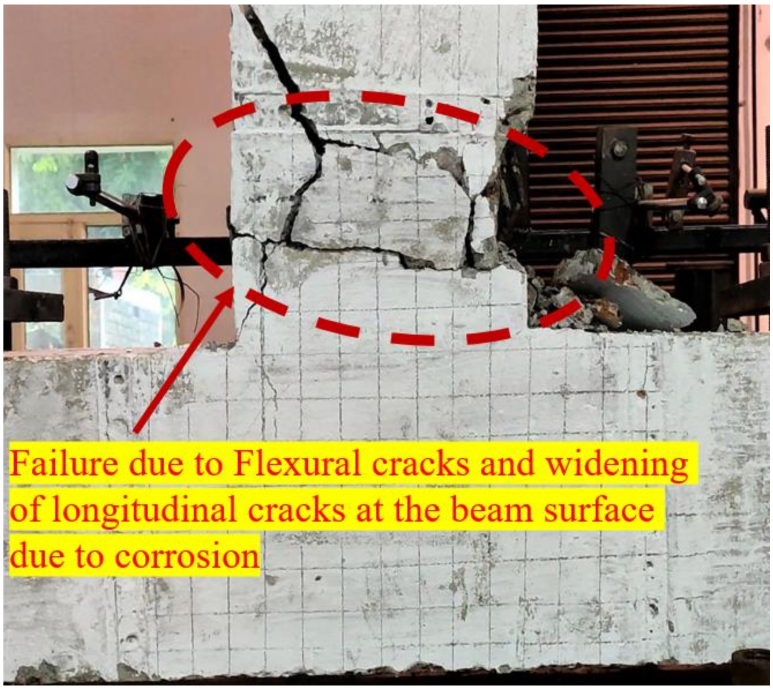

Figure 4. 8 Ultimate failure of NDC-1

The Level 2 and Level 3 corroded specimens (i.e., NDC-2 and NDC-3) show the failure pattern in the same manner as was experienced for the Level 1 corroded specimen. At the drift of ± 2.2%, a breaking sound of the fracture of the reinforcement bar in the NDC-2 specimen was heard during the reverse cyclic loading. Correspondingly, a sudden drop in the specimen load-carrying capacity was experienced during the load-displacement cycles. The same was experienced for the Level 3 corroded specimen at the drift ratio of ± 1.75%.

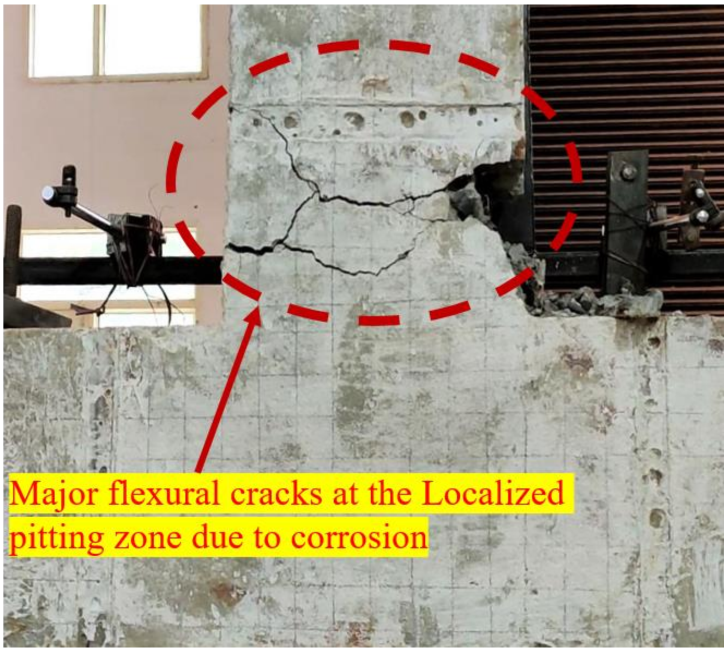

Figure 4. 9 Ultimate failure of NDC-2

Figure 4. 10 Ultimate failure of NDC-3

The fracture of the 8mm diameter bar was visually confirmed when the loading test was completed, as shown in Figure 4.11. The bar fracture was also noted when the corroded specimens were cut open after the cyclic loading test for determining mass loss. The spalling and shredding of a large amount of damaged concrete from the core region can be experienced at higher displacement. The damage progression corresponding to the drift ratios of control and corroded non-seismic specimens is shown in Table 4.2.

Figure 4. 11 Fracture of corroded reinforcement bar

Table 4. 2 Damage progression of all the non-seismic test specimens

<table>
<tr><th>Drift Ratio</th><th>NDU</th><th>NDC-1</th><th>NDC-2</th><th>NDC-3</th></tr>
<tr><td>0.2</td><td rowspan="3">Hairline shear cracks originate at the beam-column junction</td><td rowspan="4">Hairline flexural cracks originate on one side of the beam surface</td><td rowspan="4">Hairline flexural cracks originate on one side of the beam surface from a severe pitting location</td><td rowspan="2">Hairline flexural cracks initiate from severe pitting location on the beam surface</td></tr>
<tr><td>0.25</td></tr>
<tr><td>0.35</td><td>Flexural cracks generated from both sides of the beam surface</td></tr>
<tr><td>0.5</td><td>Propagation of Shear cracks, Hairline flexural cracks observed at beam surface</td><td rowspan="4">Widening of dominant flexural crack, Widening of the longitudinal corrosion cracks present at the beam surface, Flexural failure mode</td></tr>
<tr><td>0.75</td><td rowspan="3">New flexural cracks form on the beam surface, Propagation of Shear cracks</td><td rowspan="3">Wide flexural cracks propagating on both sides of the beam surface</td><td rowspan="2">Flexural cracks propagating on both sides of the beam surface</td></tr>
<tr><td>1</td></tr>
<tr><td>1.4</td><td rowspan="2">Widening of dominant flexural crack, New flexural cracks, Widening of the longitudinal corrosion cracks</td></tr>
<tr><td>1.75</td><td rowspan="4">Widening of shear cracks</td><td rowspan="3">Widening of dominant flexural cracks, Hairline cracks at column surface</td><td>Fracture of severely pitted 8 mm reinforcing bar</td></tr>
<tr><td>2.2</td><td>Fracture of severely pitted 8 mm reinforcing bar</td><td>Dislocation of the beam at the location of dominant flexural crack</td></tr>
<tr><td>2.75</td><td>Crumbling and scattering of concrete cover</td><td rowspan="3">Shattering of concrete cover</td></tr>
<tr><td>3.5</td><td>Crumbling of concrete cover</td><td rowspan="2">Dislocation of the beam at the location of dominant flexural crack</td></tr>
<tr><td>4.36</td><td>Ultimate failure due to diagonal shear cracks, Crumbling, and spalling of concrete</td><td>Dislocation of the beam at the location of the dominant flexural crack</td></tr>
</table>

4.4.3 Damage Progression of Control Seismic Specimen (DU)

In the control seismic specimen, the damage was initiated with the occurrence of a hairline shear crack at ± 0.35% drift ratio, originating at the beam-column junction from one side. From ± 0.5% drift onward, the diagonal shear cracks start to propagate from both sides of the specimen at the junction of the beam-column. From ± 1% drift ratio onwards, hairline flexural cracks were experienced on the beam surface which also appeared on the surface of the column as the drift ratio progressed. Post a drift of ± 2.2%, severe damage in the form of diagonal shear cracks widening at the beam-column junction was experienced along with the formation of a few more flexural cracks on the surface of the beam and column. When compared to the control non-seismic specimen, few hairline cracks were experienced in the control seismic specimen during initial drifts. This can be attributed to the closer stirrups detailing in the seismic specimens within the corrosion target area, thereby arresting the widening and progression of the cracks. The ultimate failure of the control seismic specimens was due to the dismantling of the beam from the beam-column junction due to the widening of diagonal shear cracks, as shown in Figure 4.12. It was noticed that at the higher drifts, the spalling and scattering of the concrete cover in the control seismic specimens was comparatively less when compared to the uncorroded non-seismic specimen. The close stirrups arrangement within the joint region holds the damaged concrete in place up to some extent.

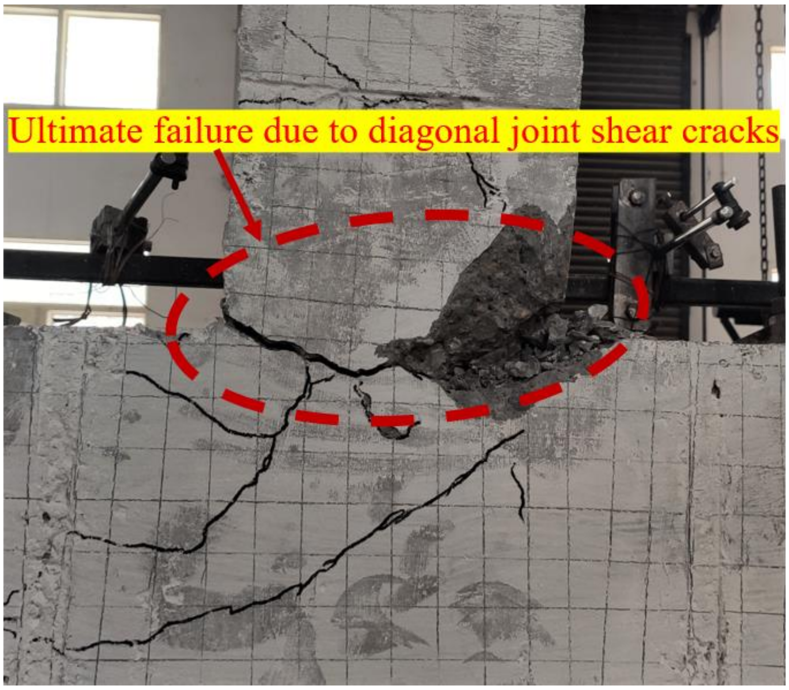

Figure 4. 12 Ultimate failure of DU

4.4.4 Damage Progression of Corroded Seismic Specimens (DC)

The corroded seismic specimens showed a similar ultimate flexural failure as was experienced for the non-seismic corroded specimens. For the 1st level corroded seismic specimen (DC-1), the damage initiates in the form of diagonal shear cracks at the junction of BCJ, at the drift of ± 0.5%. At the drift ratio of ± 1%, the hairline flexural cracks start to appear at a distance of approximately 150 mm from the joint intersection from one side of the beam surface (i.e., the side having localized reinforcing bar pitting). From a drift ratio ± 1% onwards up to ± 2.2%, the occurrence of new hairline flexural cracks was noticed along with the widening of the dominant flexural crack on the beam surface. Also, the hairline cracks on the surface of the column were propagated during this drift range. The hairline corrosion cracks present on the longitudinal surface of the column and the beam also widen and the damaged concrete starts to shred at a higher drift ratio. At ± 3.5% drift ratio, the spalling and scattering of the concrete cover were noticed and the specimen ultimately failed due to the widening of the dominant flexural crack, as shown in Figure 4.13.

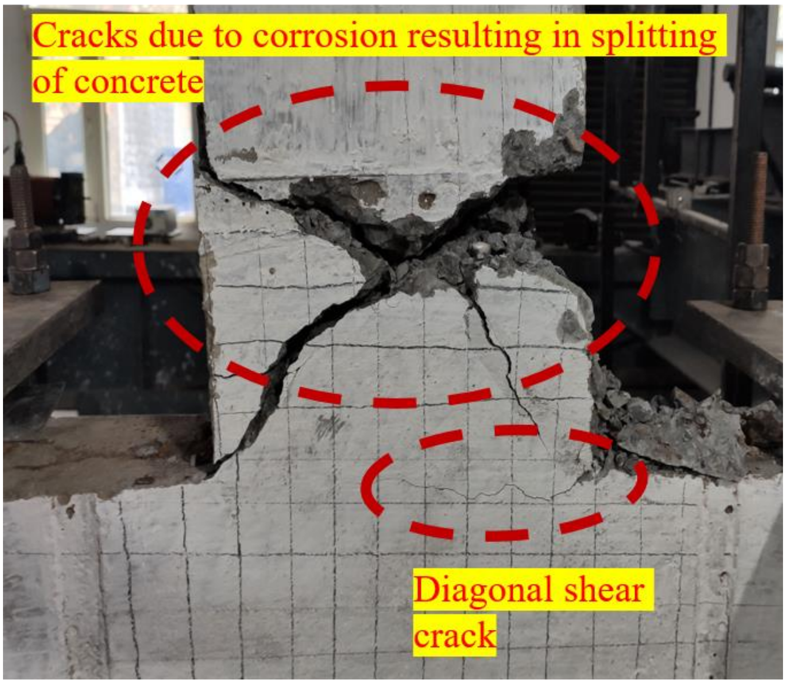

Figure 4. 13 Ultimate failure of DC-1

A similar failure pattern was shown by level 2 and level 3 corroded seismic specimens i.e., DC-2 and DC-3), as was experienced in the DC-1 specimen. For DC-2 and DC-3 specimens, the flexural cracks on the beam surface were visible at ± 0.5% drift ratio. For both specimens, the hairline diagonal shear crack occurred at the junction of the beam-column at ±1% drift ratio. As the drift progresses, new hairline flexural cracks on the column and beam surface originate and the widening of the existing flexural crack takes place. At the higher drift ratio, a loud sound of rebar fracture was heard, as was experienced in the NDC-2 and NDC-3 specimens. Due to the close arrangement of stirrups in the target corrosion area of the seismic specimens, the initiation of flexural cracks was slightly delayed. The failure mechanism was transferred at the junction of the beam-column during initial displacement, resulting in the occurrence of a hairline diagonal shear crack. However, the ultimate failure for both the specimens was due to the widening of the dominant flexural crack and the beam dismantling from that region only, as shown in Figure 4.14 and Figure 4.15. The corrosion cracks present in the longitudinal reinforcing bars direction of the beam and column expand at a higher drift ratio, as shown in Figure 4.16. The shredding of the concrete cover was experienced around the region of wide flexural cracks. The damage progression corresponding to the drift ratios of control and corroded seismic specimens is shown in Table 4.3.

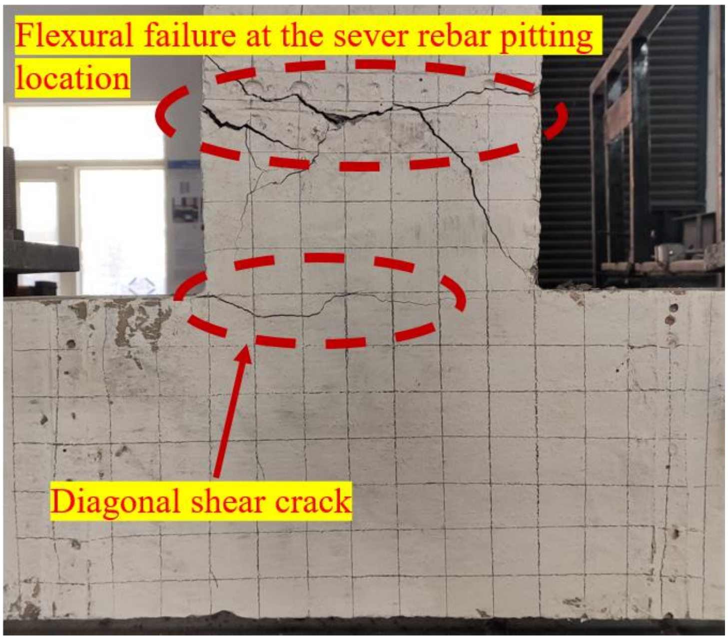

Figure 4. 14 Ultimate failure of DC-2

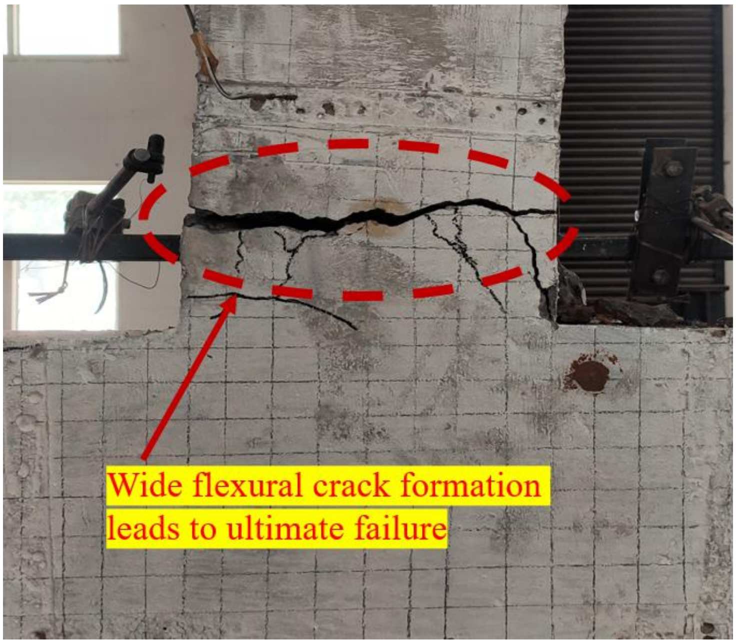

Figure 4. 15 Ultimate failure of DC-3

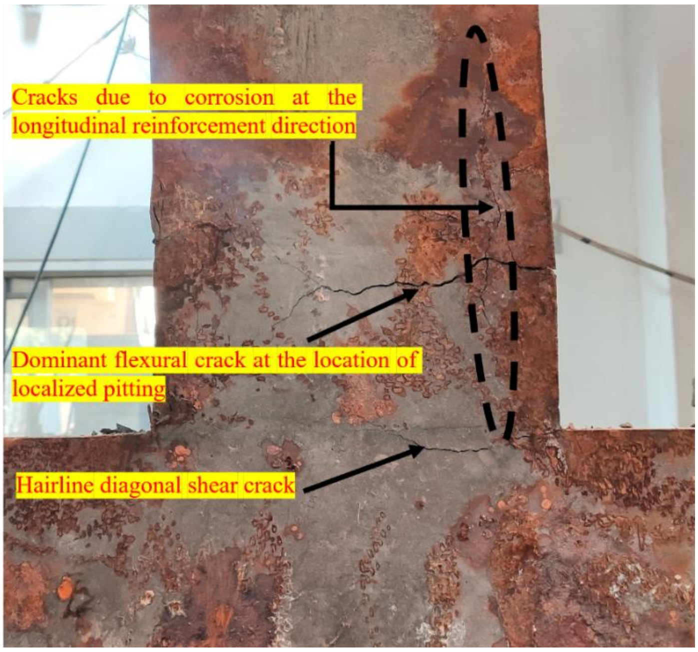

Figure 4. 16 Widening of corrosion cracks at a higher drift ratio

Table 4. 3 Damage progression of all the seismic test specimens

Drift Ratio	DU	DC-1	DC-2	DC-3
0.2	Hairline shear cracks initiate at the junction of BCJ from one side	Hairline diagonal shear crack initiates from one side of the joint surface	Hairline flexural crack originates on one side of the beam surface	Hairline flexural cracks originate on one side of the beam surface at severe pitting location
0.25				
0.35				
0.5			Hairline flexural crack on one side of the beam surface, initiation of hairline diagonal shear cracks	Hairline flexural crack form on both sides of the beam surface
0.75	Shear cracks observed at the junction of BCJ from both sides	Hairline flexure cracks originate at the severely pitted location on one side of the beam surface, Hairline diagonal shear crack		
1			Propagation of flexural cracks on one side of beam, Diagonal shear cracks observed	Widening of dominant flexural crack, new flexure cracks at beam surface
1.4		Long flexural cracks form on both sides of the beam surface	Long and wide flexural cracks form on both sides of the beam surface	
1.75	Widening of diagonal shear cracks, hairline flexural cracks observed at the column surface			Fracture of 8 mm reinforcing bar
2.2		Widening of dominant flexural crack, new flexural cracks at beam surface	Widening of dominant flexural crack, Fracture of severely pitted reinforcing bar, Crumbling of concrete cover	Widening of dominant flexural crack
2.75	New flexural cracks observed at the column and beam surface	Widening of dominant flexural crack, Shattering of concrete cover		
3.5			Dislocation of the beam at the location of the dominant flexural crack	Dislocation of the beam from the location of dominant flexural crack
4.36	Ultimate failure due to diagonal shear cracks, Crumbling of concrete cover	Dislocation of the beam at the location of the dominant flexural crack		Spalling and shattering of concrete cover

4.5 HYSTERETIC BEHAVIOUR OF SPECIMENS

4.5.1 Hysteretic Load-Displacement Behaviour of Non-seismic Control and Corroded Specimens

The load-displacement hysteretic plot represents the cyclic behaviour of specimens subjected to reverse cyclic loading. The hysteresis load-displacement curve determines the structural deformation, pinching effect, and load-slip behaviour of specimens under repeated cycles via sensors provided within the actuator which is connected at the surface of the beam. In general, during initial drifts, it was observed that the load-displacement hysteresis curves were narrow representing a small area of the hysteresis loop, smaller residual distortion, and low energy dissipation within the specimens. As the drift progresses, the wide hysteresis loops were experienced soon after the yielding of longitudinal reinforcement indicating increased dissipation of seismic energy due to the seismic nature of reinforcing bars. After reaching the peak load, the hysteresis loop gradually starts to decline representing the fall in stiffness and energy dissipation. During the ultimate stage of specimens, the hysteresis loop shows a continuous declining trend thereby, representing the continuous reduction of the load-carrying capacity and energy dissipation of the specimen. Due to the incrementation of repeated cyclic loading, the plastic deformation accumulates at the plastic hinge region of the specimens and degrades the overall mechanical performance.

A smooth and full shuttle-shaped load-displacement hysteresis curve can be seen for the control non-seismic specimen as shown in Figure 4.17 (a). From the figure, it can be experienced that the specimen shows no sign of load-slip behaviour and pinching effect phenomenon, even at the higher loading cycles. However, in the case of corrosion-damaged specimens pinching effect can be noticed. The NDC-1 specimen shows the strength degradation at the higher displacement along with the slight bond-slip behaviour represented by the pinching effect as shown in Figure 4.17 (b). During initial stage of corrosion, slightly improved plastic deformation, energy dissipation, and bearing capacity are observed. This can be attributed to the slight expansion of the diametric profile of reinforcement due to the deposition of rust over the bar area. The rust layer roughens the outer surface of rebar and enhances the bond between reinforcement and surrounding concrete which results in an overall improvement of the mechanical properties of the specimen. However, at the higher corrosion level, the cross-section of reinforcement bars gets reduced due to the corrosion attack resulting in a brittle failure. As can be observed from Figure 4.18 (a) and Figure 4.18 (b), the higher corrosion level specimens (i.e., NDC-2 and NDC-3) show severe sliding and pinching phenomena due to the bond-slip behaviour between surrounding concrete and reinforcement bars. Further, a brittle fracture of the corrosion-damaged reinforcement bar (8 mm diameter) led to a sudden drop in the specimen load-carrying capacity in the negative drift, as can be observed in Figure 4.18 (a) and Figure 4.18 (b) for NDC-2 and NDC-3 specimens, respectively. The load suddenly drops from 9.38 kN to 0.13 kN at a -2.75% drift ratio and from 7.03 kN to 2.76 kN at a -1.4% drift ratio for NDC-2 and NDC-3 specimens respectively.

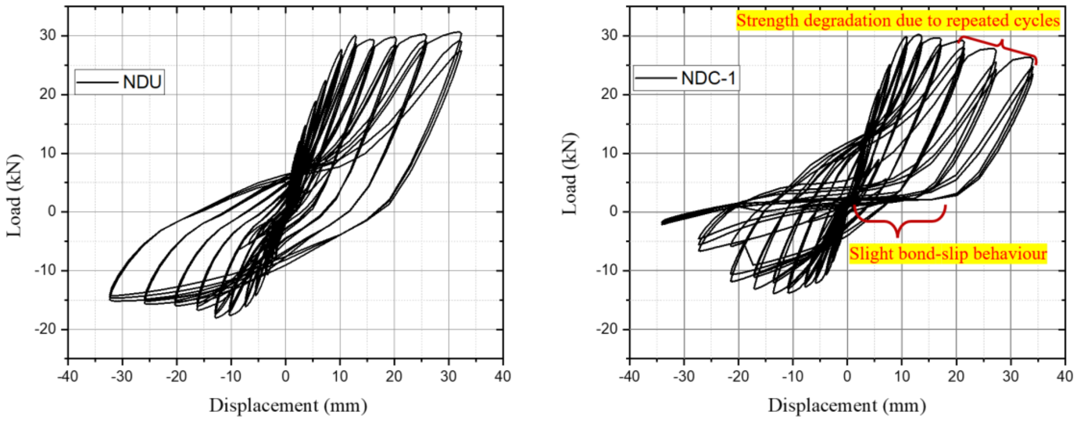

(a) (b)

Figure 4. 17 Load-displacement hysteresis curves for (a) NDU and (b) NDC-1 specimens

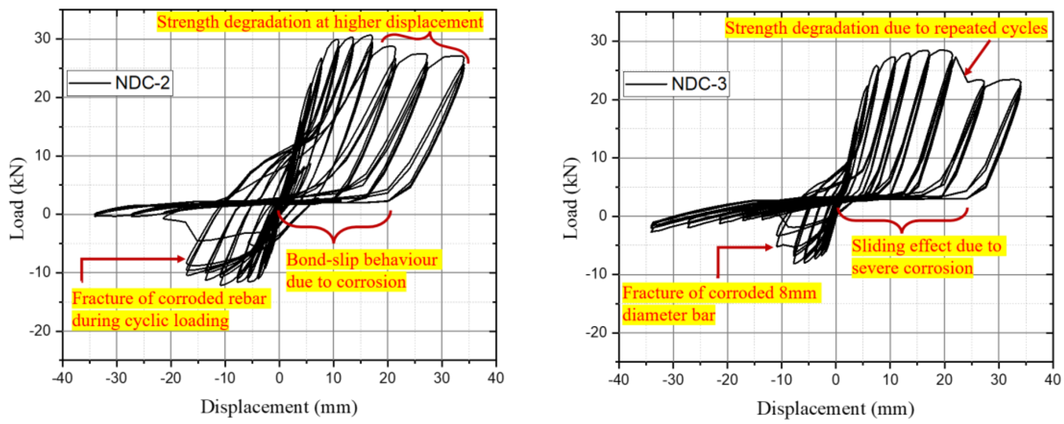

(a) (b)

Figure 4. 18 Load-displacement hysteresis curves for (a) NDC-2 and (b) NDC-3 specimens

4.5.2 Hysteretic Load-Displacement Behaviour of Seismic Control and Corroded Specimens

The control seismic specimen exhibited the same pattern of the hysteresis loop in the load-displacement hysteresis curve as was experienced for the non-seismic control specimen. However, the area under the hysteresis loop was dense and large as compared to the area under the hysteretic loop of the non-seismic control specimen. Figure 4.19 (a) shows the hysteresis curve of the seismic control specimen (DU) and also authenticates the significance of closely spaced stirrups detailing in the joint region which resulted in better confinement in the corrosion-affected zone leading to improved dissipation of energy.

When compared to the hysteresis curve of the NDC-1 specimen, the DC-1 specimen does not show any sign of a pinching effect, even under higher loading, as shown in Figure 4.19 (b). For instance, the peak load carrying capacity of the DC-1 specimen was -9.13 kN at the drift ratio of -4.36% (34.07 mm), and for the NDC-1 specimen, it was -1.91 kN at the same drift ratio. Figure 4.20 (a) and Figure 4.20 (b) show the hysteresis curve of the DC-2 and DC-3 specimens highlighting the pinching and sliding effects. Moreover, the fracture of the 8 mm diameter longitudinal bar can also be spotted as there was a sudden fall in load capacity on the negative cycle. The bond-slip behaviour was comparatively less and more uniform hysteretic loops were seen in the corroded seismic specimens when compared to corroded non-seismic specimens. The presence of additional stirrups in the joint area also delayed the fracture of corrosion-damaged rebars which ultimately improved the seismic performance of corroded seismic specimens over corroded non-seismic specimens. For instance, the fracture of the 8 mm diameter bar was experienced for the NDC-3 specimen at a drift ratio of – 1.4 %, while the same was noticed for DC-3 at – 2.2%, i.e. more than 50% higher drift than that for the corresponding non-seismic detailed specimen.

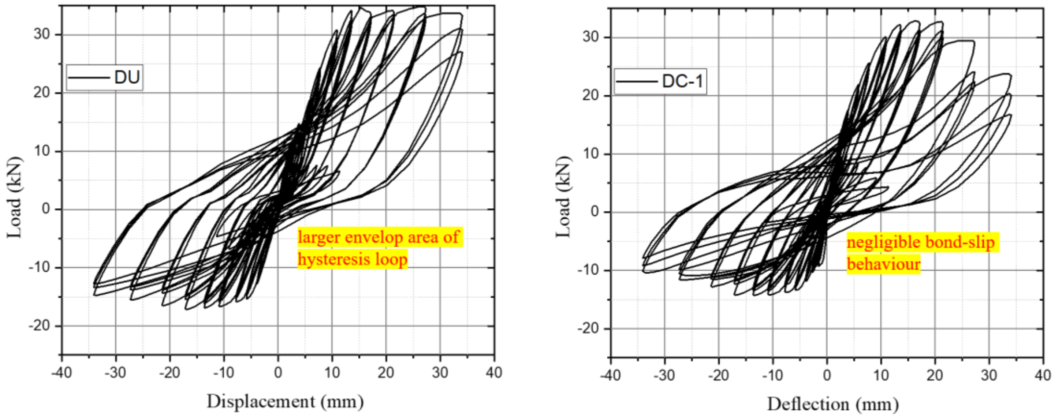

(a) (b)

Figure 4. 19 Load-displacement hysteresis curves for (a) DU and (b) DC-1 specimens

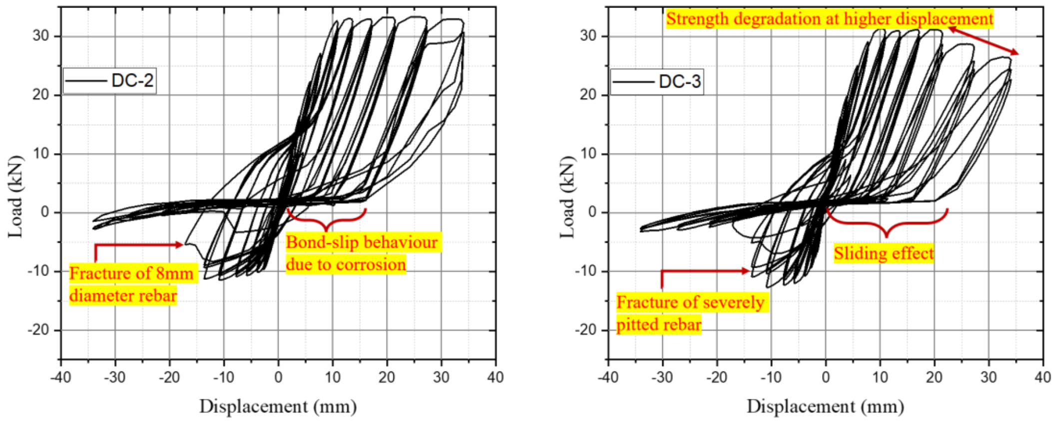

(a) (b)

Figure 4. 20 Load-displacement hysteresis curves for (a) DC-2 and (b) DC-3 specimens

4.6 LOAD-DISPLACEMENT ENVELOPE CURVE AND DUCTILITY

A load-displacement envelope curve or skeleton curve encloses and represents all the peak load of the displacement-controlled loading for each cycle in the respective negative and positive drift. The seismic behaviour including load-bearing capacity, deformation at elastic, elastic-plastic, and failure stage of specimens along with the respective ductility of the specimen can be easily displayed with the help of an envelope curve.

The ductility of a structural component or member is defined as the ability to offer resistance in the inelastic domain of response by sustaining large deformations (Paulay T 1992; Le-

Trung et al. 2010). This allows an improved seismic performance in the structural element by enabling it to dissipate higher energy in the post-elastic region prior to failure. In this experimental study, the displacement ductility was calculated for all the specimens to compare the performance of corrosion-damaged specimens with their respective control specimen. Further, the ductility of different levels of corroded specimens of non-seismic and seismic specimens was also evaluated and compared.

The displacement ductility is represented as a ratio of ultimate to yield displacement, as shown in Equation 4.1. Figure 4.21 shows the procedure to calculate the ductility of the specimens (Siva Chidambaram and Agarwal 2015; Sharma and Bansal 2019). Here, P_{u1} and P_{u2} represent the peak load in the positive and negative drift cycle, respectively. The specimens were considered to reach the ultimate failure stage at 80% of the peak strength (0.8 P_{u1}) and the corresponding displacement was considered as the ultimate displacement in the positive and negative drift (Δ_{u1}, Δ_{u2}), as shown in Figure 4.21. A point representing 50% of the peak load (0.5 P_{u1}) is marked at the backbone curve. To determine the yield displacement, a tangent is drawn from the origin and passes through 0.5 P_u on the backbone curve to the point where the tangent crosses the horizontal line representing 80 % of the peak strength (0.8 P_{u1}) parallel to the x-axis, as shown in Figure 4.21.

$$\text{Displacement ductility} = \frac{\Delta_{U1}+\Delta_{U2}}{\Delta_{y1}+\Delta_{y2}} \tag{4.1}$$

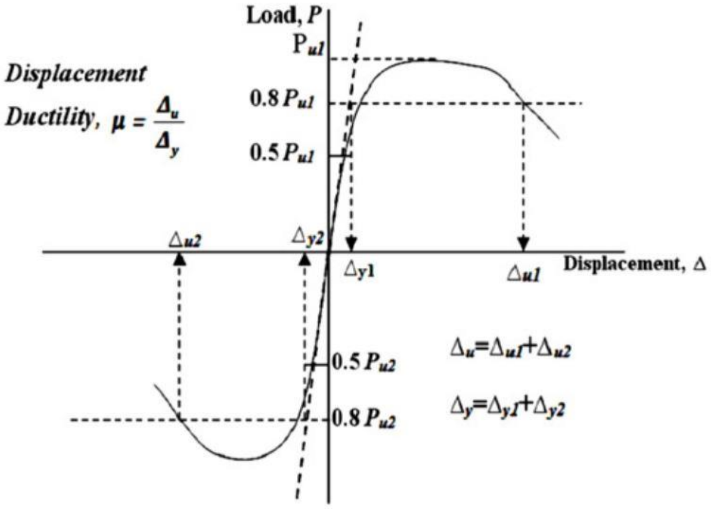

Figure 4. 21 Procedure adopted to calculate the displacement ductility (Siva Chidambaram and Agarwal 2015; Sharma and Bansal 2019)

4.6.1 Comparison between Control Specimen and Corroded Specimens

The analysis of the load-displacement envelope curve of corrosion-damaged specimens can be done in two parts; (1) Pre-peak performance and (2) post-peak performance. From Figure 4.22, showing the load-displacement envelope curve of NDU and NDC-1, it can be seen that the initial elastic stiffness of NDC-1 was slightly higher than that of the NDU. The reason supporting this pattern is the deposition of the layer of rust on the reinforcing bars surface which roughens the rebar contact surface and thereby enhances the bond between surrounding concrete and the reinforcing bars. However, in the post-peak region, the NDC-1 specimen showed reduced load-bearing capacity due to corrosion-damaged reinforcement bars, as they were unable to resist loads at higher drift ratios. A significant drop of approximately 32.56 % in the peak load-carrying capacity in the negative drift ratio direction was experienced for NDC-1 when compared to NDU specimens. Moreover, a slight reduction was also noted in the ultimate displacement as this value for the NDU specimen was 34.07 mm, which was reduced to 21.45 mm (corresponding to 80% of peak strength in negative drift) in the case of the NDC-1 specimen.

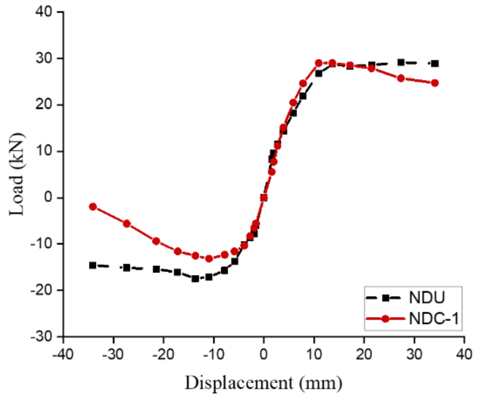

Figure 4. 22 Envelop load-displacement curve of NDU and NDC-1 Specimen

The envelope curve of the NDC-2 specimen is prepared and compared with the NDU response, as shown in Figure 4.23. The severe corrosion level has significantly affected the load-carrying capacity along with the ductility. Due to the high corrosion rate, localized pitting on the surface of stirrups and longitudinal reinforcements was experienced, which led to the fracture of 8 mm diameter bars in the negative drift cycle at higher drift. When compared to the NDU specimen, the NDC-2 specimen shows a significant reduction of 57.09% in the peak load-carrying capacity, in the negative drift direction. Also, the ultimate failure of the NDC-2 specimen, in the negative drift direction was experienced at 17.16 mm, which is approximately half the value experienced for the NDU specimen.

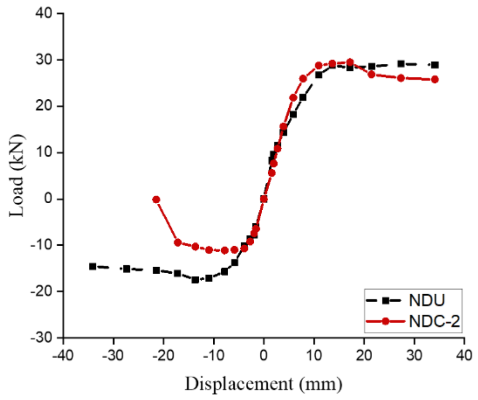

Figure 4. 23 Envelop load-displacement curve of NDU and NDC-2 Specimen

The failure pattern and response of the NDC-3 specimen were somewhat similar to the NDC-2 specimen but with a higher rate of degradation of strength and ductility. The high rate of corrosion severely damaged the concrete surface and reinforcement bars resulting in the catastrophic specimen failure. Figure 4.24 shows the comparison of the load-displacement envelope curve of NDC-3 and NDU specimens. From Figure 4.24, it can be observed that the NDC-3 specimen was not able to dissipate the energy and stiffness even at the pre-peak stage due to the degraded concrete surface owing to the corrosion cracks and severely pitted reinforcement bars. The NDC-3 specimen shows a peak load of 7.43 kN which is 0.42 times that of the NDU specimen along with an alarming reduced ultimate displacement of 10.92 mm which is approximately one-third of the value of ultimate displacement experienced for the NDU specimen.

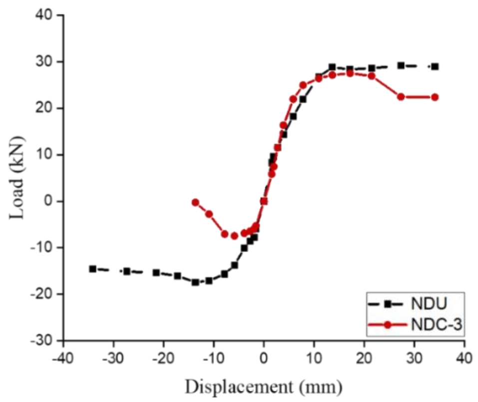

Figure 4. 24 Envelop load-displacement curve of NDU and NDC-3 Specimen

The failure pattern of the corroded seismic (DC) specimens is similar to non-corroded seismic (NDC) specimens; however, they show comparatively superior performance as compared to the NDC specimens at different corrosion levels. The load-displacement envelop curve of DU and DC-1 specimens is shown in Figure 4.25. When compared to the DU specimen, the DC-1 specimen shows a decrement of 25.88% in the peak load-carrying capacity in the negative drift direction with the ultimate displacement at 27.29 mm. The DC-1 specimen shows lower load-bearing capacity and stiffness when compared to the DU specimen. However, the close stirrups arrangement at the joint region enables the seismic specimens to have higher stiffness, energy dissipation (refer sections 4.7 and 4.8 respectively), and better ductility (as indicated in Table 4.4 below) when compared to non-seismic specimens, even at severe corrosion levels.

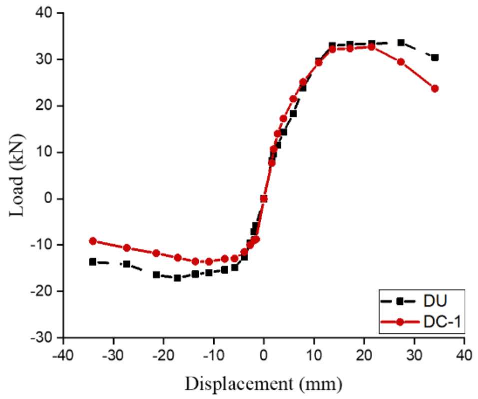

Figure 4. 25 Envelop load-displacement curve of DU and DC-1 Specimen

As the corrosion level increases, a drop in the performance of specimens is significant. Figure 4.26 shows the load-displacement envelope response of DU and DC-2 specimens. A brittle fracture of severely pitted reinforcement bars was seen during the cyclic loading, resulting in pre-mature flexural failure of the specimen. When compared to the DU specimen, a significant drop of approximately 48.95% in the peak load-bearing capacity of the DC-2 specimen was seen in the negative drift. Due to the fracture of the rebar during the reverse cyclic loading, the seismic performance has degraded at an alarming rate. When compared to the DU specimen, an alarming decline in the mechanical performance of the DC-2 specimen was seen, however, shows superior performance when compared to the NDC-2 specimen.

The comparison of the load-displacement response of DU and DC-3 specimens is shown in Figure 4.27. The DC-3 specimen showed the ultimate failure at the displacement of 17.16

mm which is approximately half of the value of ultimate displacement experienced for the DU specimen. A significant reduction in the peak load-carrying capacity was seen due to the brittle fracture of corrosion-damaged reinforcement bars. However, when compared to the NDC-3 specimen, the DC-3 specimen shows better seismic performance, even at a higher corrosion rate.

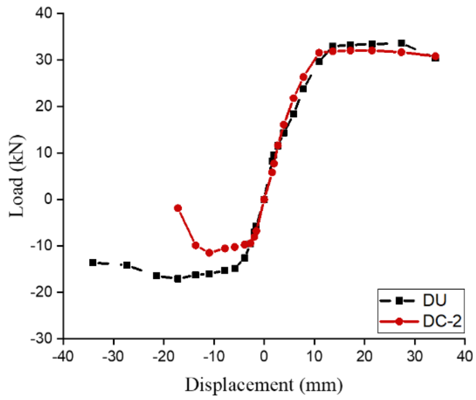

Figure 4. 26 Envelop load-displacement curve of DU and DC-2 Specimen

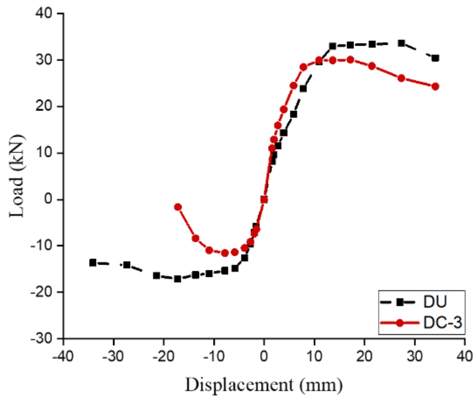

Figure 4. 27 Envelop load-displacement curve of DU and DC-3 Specimen

The combined load-displacement envelop curve of control and corroded non-seismic and seismic specimens is shown in Figure 4.28 and Figure 4.29, respectively. From the respective figures, it can be observed that the initial elastic stiffness of all the corroded specimens (i.e. non-seismic and seismic) was slightly higher than that of the respective uncorroded specimens. The reason supporting this pattern is the deposition of the layer of rust on the reinforcing bars surface which roughens the rebar contact surface and thereby enhances the bond between reinforcing bars and surrounding concrete. Furthermore, it was noticed that at the higher drift ratios, both the load-bearing capacity and stiffness of all corroded specimens dropped at a significant rate. A significant drop of approximately 32.56 % and 25.88 % in the peak load-carrying capacity was experienced for the NDC-1 and DC-1 specimens at higher drifts especially at the negative drift when compared to that of respective control specimens, as can be seen from Table 4.4. For the severely corroded specimens (i.e. NDC-2, NDC-3, DC-2, and DC-3) high plastic deformation along with the visible localized pitting on the surface of stirrups and longitudinal reinforcements was seen when the samples were extracted for analysis. This pitting led to the reduced cross-section of stirrups and 8 mm diameter longitudinal reinforcing bars leading to the fracture of both.

Along with severe pitting, de-scaling of rebars, and degraded bond between rebars and the surrounding concrete declines the seismic performance of corroded specimens. For instance, the peak load carried by NDC-3 and DC-3 specimens was only 0.42 times and 0.67 times that of NDU and DU specimens, respectively at the negative drift cycle. In general, the severely corroded seismic specimens performed better than the corroded non-seismic specimens. The peak load-bearing capacity of the DC-3 specimen was 8.54 % and 35.42 % superior to the NDC-3 specimen in the respective positive and negative displacement.

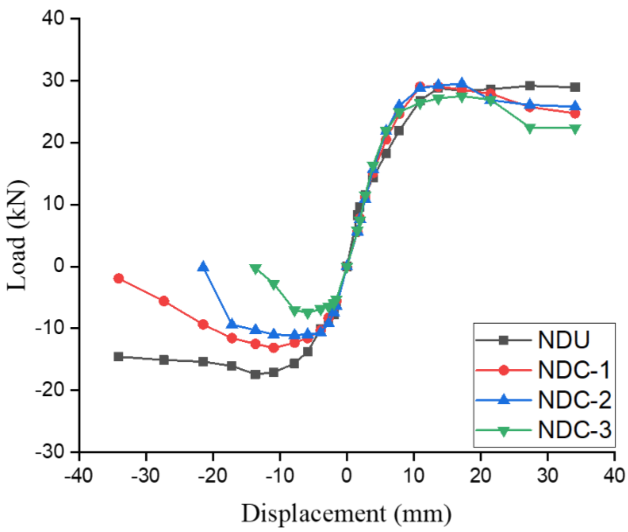

Figure 4. 28 Load-displacement Envelope curve of control and corroded non-seismic specimens

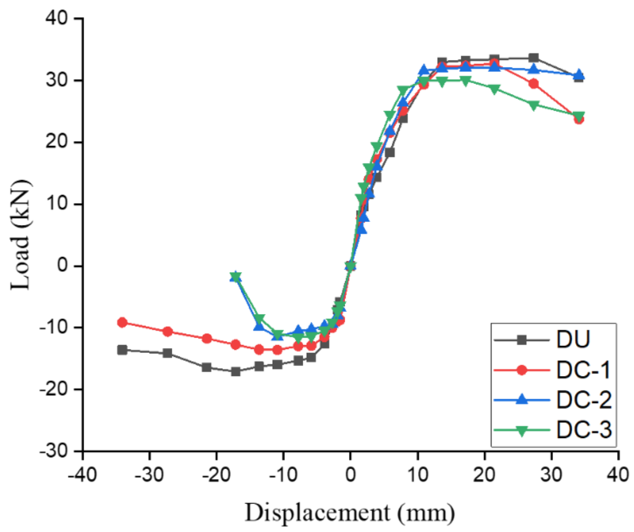

Figure 4. 29 Load-displacement Envelope curve of control and corroded seismic specimens

Table 4. 4 Test results of all non-seismic and seismic specimens

Specimens	Peak				Ultimate				Displacement	Ductility
	Positive		Negative		Positive		Negative		Δ_y	$\Delta u/\Delta y$
	P_m (kN)	Δ_m (mm)	P_m (kN)	Δ_m (mm)	P_u (kN)	Δ_{u1} (mm)	P_u (kN)	Δ_{u2} (mm)	(mm)	μ
NDU	29.17	25.9	17.40	12.94	23.34	34.07	13.92	27	10.5	5.81
NDC-1	29.04	13.65	13.13	10.92	23.23	34.07	10.5	19	9	5.89
NDC-2	29.53	17.16	11.08	7.8	23.62	34.07	8.86	17	9	5.67
NDC-3	27.52	17.16	7.43	5.85	22.02	27	5.94	8.5	8	4.43
DU	33.65	27.3	17.07	17.16	26.92	34.07	13.65	33	11	6.10
DC-1	32.73	21.45	13.56	10.92	26.19	30.5	10.85	24.5	8.9	6.17
DC-2	32.08	21.45	11.46	10.92	25.66	34.07	9.17	14	8.25	5.82
DC-3	30.09	17.16	11.51	7.8	24.07	32.5	9.21	12.5	8	5.62

It can also be observed that the displacement corresponding to ultimate failure was significantly lower as the level of corrosion goes higher. Due to the presence of close stirrups arrangement around the joint region, shear bearing capacity was improved in the seismic specimens thereby making them sustain more drift under severe corrosion levels when compared to non-seismic specimens. In the negative displacement cycle, the ultimate failure of NDC-3 and DC-3 occurs at a displacement that is approximately 0.3 times and 0.4 times that of displacement corresponding to the ultimate failure of NDU and DU, respectively. The ductility coefficient was used to determine and compare the post-yield displacement behaviour of the specimens. The results for the ductility of all the specimens are presented in Table 4.4. A comparison of ductility values exhibits a significant decline of 24% for the specimen subjected to severe corrosion (NDC-3) relative to the control specimen (NDU). A similar but much less significant decline of 8% has been observed in seismic detailed specimens (DU vs DC-3), indicating that the closer arrangement of transverse reinforcement can offset the post-yield effects of severe corrosion to some extent.

4.7 STIFFNESS DEGRADATION

Stiffness and stiffness degradation are the salient features signifying the seismic performance of RC structural members. The slope of the line joining the peak points in loading cycles in both the negative and positive directions is termed peak-to-peak stiffness (Antonopoulos et al. 2003; Zohrevand and Mirmiran 2013). Figure 4.30 shows the procedure for calculating stiffness for all the specimens. The stiffness (K_i) for each cyclic displacement was calculated with the help of Equation 4.2 mentioned below.

$$K_i = \frac{|+P_{i,max}| + |-P_{i,max}|}{|+Y_{i,max}| + |-Y_{i,max}|} \tag{4.2}$$

Where, $+P_{i,max}$, and $-P_{i,max}$ represent the peak lateral load corresponding to peak positive displacement ($+Y_{i,max}$) and negative ($-Y_{i,max}$) displacement, respectively.

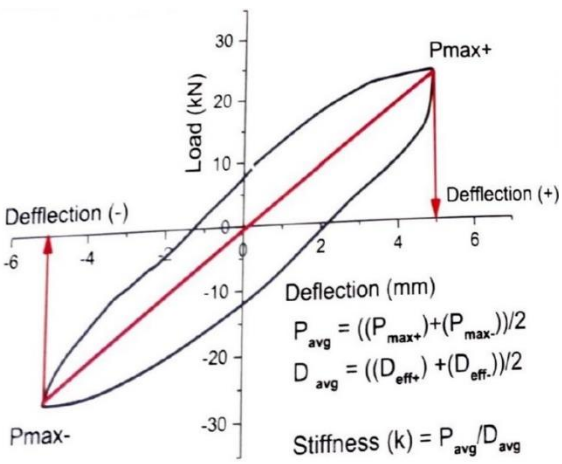

Figure 4. 30 Procedure adopted to calculate the stiffness

Figure 4.31 shows the peak-to-peak stiffness plots of all the non-seismic specimens. During the initial drifts, a slight increase in the stiffness of NDC-1, and NDC-2 specimens was seen. This trend was experienced owing to the bond enhancement between surrounding concrete and corrosion-damaged reinforcement bars due to the rust deposition on the reinforcing bar surface. The stiffness of the NDC-1 specimen nearly follows the same linear pattern as was experienced for the control specimen whereas, specimens NDC-2 and NDC-3 show a steep reduction in the stiffness values. At the ultimate drift ratio (i.e., ± 4.36 %), the control specimen exhibits 38.71%, 40.43%, and 43.73% higher stiffness than the NDC-1, NDC-2, and NDC-3 specimens, respectively.

Figure 4.32 shows the peak-to-peak stiffness plots of all the seismic specimens. A similar trend of a slight increase in stiffness during the initial drifts was experienced by the corroded seismic specimens, as was experienced by corroded non-seismic specimens. The severely corroded seismic specimens show a comparatively more gradual fall in the stiffness values at higher drifts when compared to that of severely corroded non-seismic specimens. When compared to the DU specimen, DC-1, DC-2, and DC-3 specimens show a fall of 24.68%, 24.06%, and 37.65% in the stiffness values at the drift ratio of ± 4.36 %, respectively which is less when compared to the difference in the stiffness of NDU and corresponding NDC specimens. The reason behind this improvement in stiffness is the confined arrangement of stirrups which prevented further shear deformation in the plastic hinge region and thereby provided the improved bearing capacity to the specimens at higher displacements.

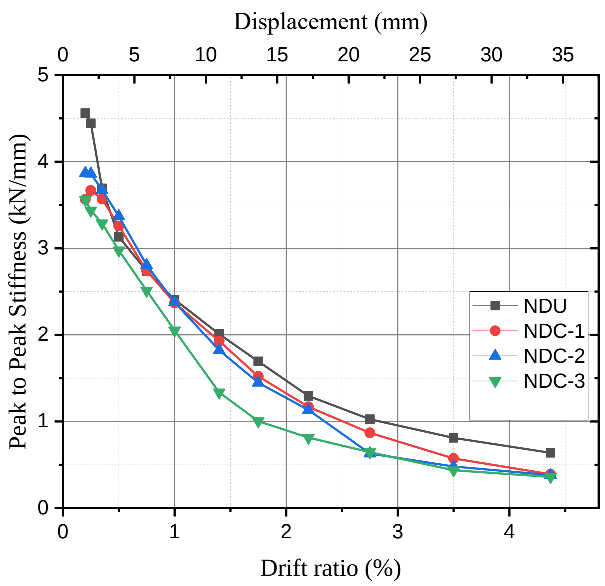

Figure 4. 31 Stiffness of control and corroded non-seismic specimens

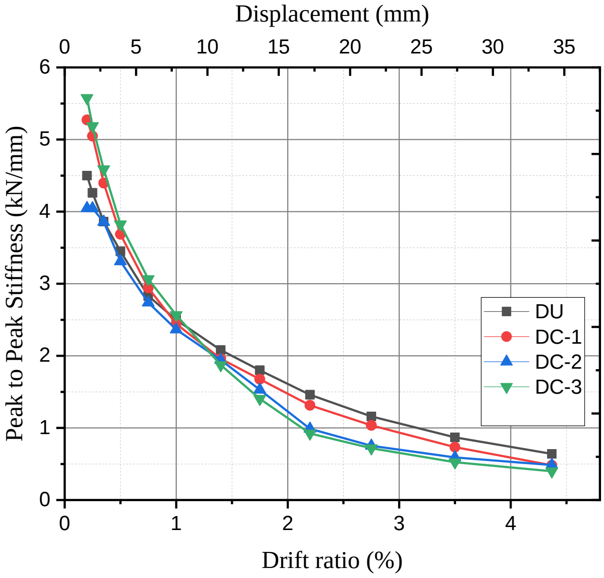

Figure 4. 32 Stiffness of control and corroded seismic specimens

The stiffness degradation of test specimens was represented in Figure 4.33 and Figure 4.34 as the plot between stiffness degradation and drift ratio for all the non-seismic and seismic specimens, respectively. The corrosion cracks present on the beam and column surface widen as the drift progresses resulting in the shredding of concrete cover. This exposes the damaged reinforcements within the corroded specimen to loading at an early stage when compared to that of control specimens, thereby causing a rapid progression in the stiffness degradation. In the case of NDC-2 and NDC-3 specimens, the stiffness drastically drops after a ± 2.2% and ± 1.75% drift ratio, representing the fracture of reinforcing bars, thus degrading the stiffness at an alarming rate. Continuous steep degradation of stiffness was observed for the NDC-3 specimen which represents the inability of this highly corroded specimen to sustain load at a higher drift ratio. However, when compared to corroded non-seismic specimens, the corroded seismic specimens show lower stiffness degradation as the drift ratio progresses. Due to the stirrups arrangement in the seismic samples, shear cracks are arrested within the joint region; hence the additional confinement of concrete in the plastic hinge area allows it to maintain a good bond with the reinforcement up to larger drift.

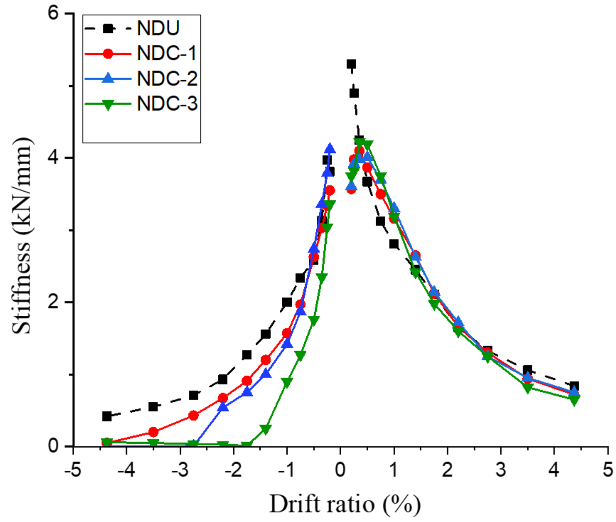

Figure 4. 33 Stiffness degradation curve of control and corroded non-seismic specimens

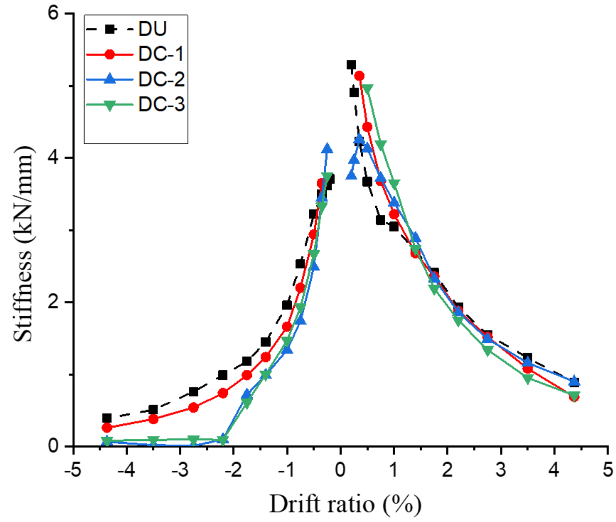

Figure 4. 34 Stiffness degradation curve of control and corroded seismic specimens

4.8 ENERGY DISSIPATION

The seismic behaviour of the structure under earthquake loading can be assessed using energy dissipation capacity as it reflects the ability of the structure to absorb the input plastic deformations and seismic energy. In the case of cyclic loading, the energy dissipation can be calculated as the summation of the area falling under the load-displacement hysteresis loops at different drift ratios (Bindhu et al. 2009; Saptarshi Sasmal1,*,†, K. Ramanjaneyulu1 2013;

Sharma and Bansal 2019). The procedure to calculate the energy dissipation for any typical loop is shown in Figure 4.35 below.

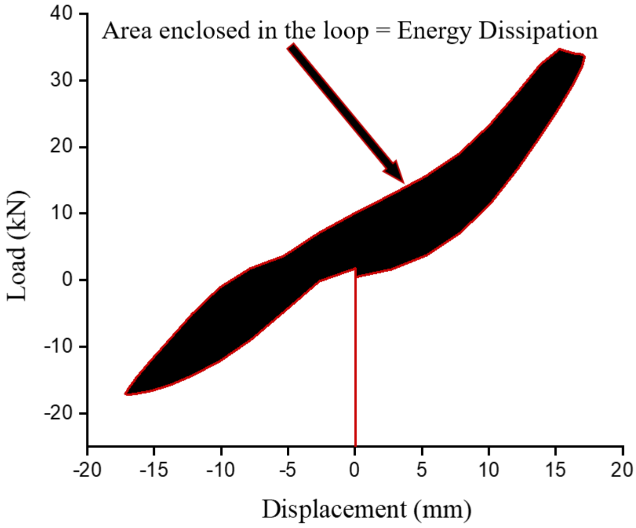

Figure 4. 35 Calculation Procedure of Energy Dissipation for i^{th} loop.

The energy dissipation of the specimens at each drift ratio under the influence of quasi-static reverse cyclic loading can be determined through a per cyclic energy dissipation plot. Referring to Figure 3.15, each drift increment (loop) consists of 3 large reverse cycles; hence 12 loops correspond to 36 large cycles. Figure 4.36 and Figure 4.37 show the energy dissipation per cycle for the control and corroded non-seismic and seismic specimens, respectively. From the figures, it can be experienced that both the control specimens (i.e., non-seismic and seismic) show a continuous rise in energy dissipation with the advancing cycle of loading. In contrast, the corroded specimens of both the non-seismic and seismic categories presented a sudden drop in energy dissipation at a particular drift ratio. The reason supporting this pattern was the fracture of rebars at certain drifts and the degradation of the bond between the surrounding concrete and the corrosion-damaged reinforcing bars. The maximum energy dissipation (per cycle) for the NDU, NDC-1, NDC-2, and NDC-3 specimens was 810.9 kN-mm, 500.55 kN-mm, 352.38 kN-mm and 163.78 kN-mm at the respective drift ratio of ± 4.36%, ± 2.75%, ± 2.2% and ± 1.4%. When compared to corroded non-seismic specimens, the corroded seismic (DC) specimens exhibit higher energy dissipation, and the drop in energy dissipation was experienced at a higher drift ratio when compared to NDC specimens. The seismic specimens (i.e., DU, DC-1 DC-2, and DC-3) show approximately 18.67%, 43.78%, 11.99%, and 38.91% higher energy dissipation per cycle when compared to the NDU, NDC-1, NDC-2, and NDC-3 specimens, respectively.

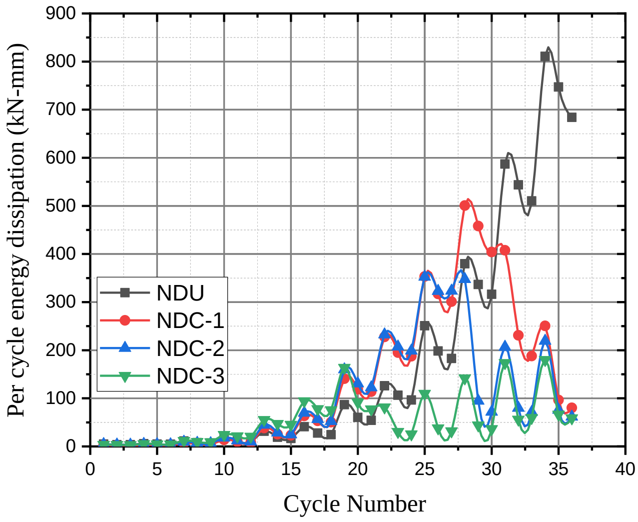

Figure 4. 36 Per-cycle energy dissipation of control and corroded non-seismic specimens

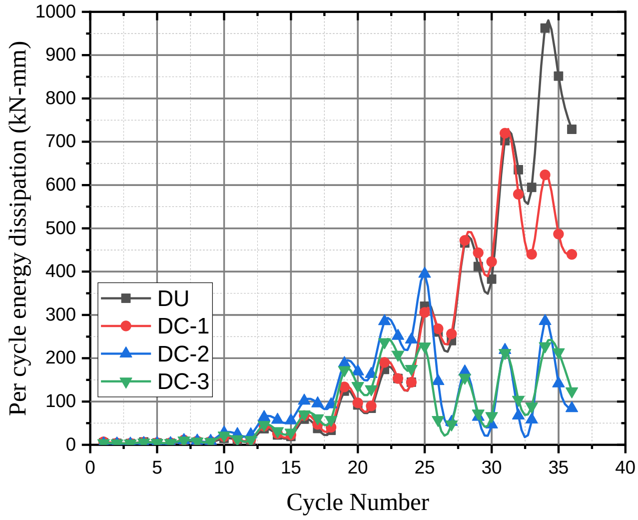

Figure 4. 37 Per-cycle energy dissipation of control and corroded seismic specimens

Figure 4.38 and Figure 4.39 represent the cumulative energy dissipation of the non-seismic and seismic specimens, respectively corresponding to the drift ratio. For the control specimens, the cumulative energy dissipation shows a linear increasing pattern as the drift ratio progresses. However, for the corrosion-damaged specimens, cumulative energy dissipation increases linearly up to a certain drift and thereafter the curve goes flattened up to the ultimate displacement. The cumulative energy dissipation of NDC-1, NDC-2, and NDC-3 specimens was 0.77, 0.57, and 0.31 times that of the NDU specimen, at the ultimate drift ratio of ± 4.36%. For DC-1, DC-2, and DC-3 specimens, it was 0.86. 0.47 and 0.4 times that of the DU specimen. When compared to the non-seismic corroded specimens, the seismic corroded specimens showed higher cumulative energy dissipation. The cumulative energy dissipation of DU and DC-3 specimens was 20.32% and 35.09% higher than that of NDU and NDC-3 specimens, showing the importance of a close confined arrangement of stirrups. However, it was experienced that as the level of corrosion exceeds 10% both for non-seismic and seismic specimens, the energy dissipation plunges to half or lower the value as compared to control specimens at the same drift, showing a major degradation in the seismic performance of corroded specimen.

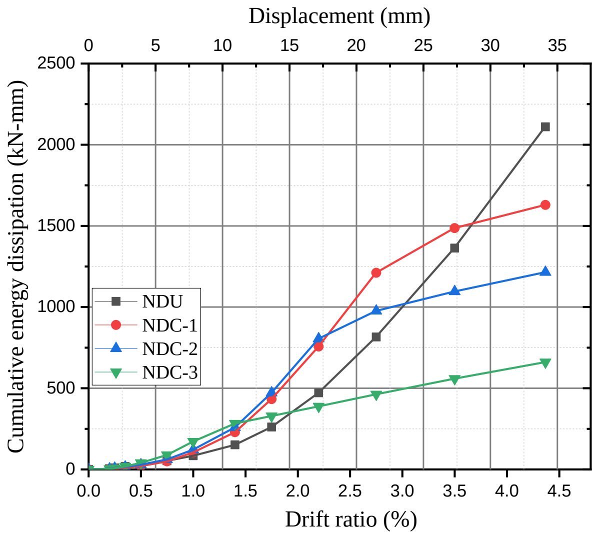

Figure 4. 38 Cumulative energy dissipation of control and corroded non-seismic specimens

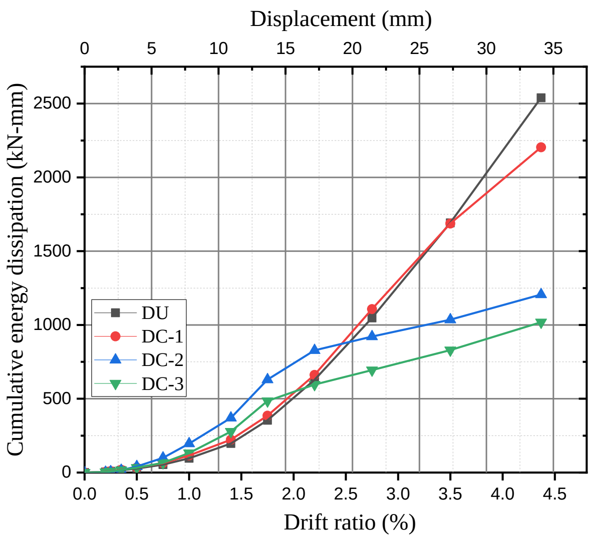

Figure 4. 39 Cumulative energy dissipation of control and corroded seismic specimens

4.9 DAMAGE INDEX OF UNCORRODED AND CORRODED BCJs

The damage in the RC structures is related to inelastic deformations (Kappos 2020). The damage index is a quantitative dimensionless parameter that normalizes structural damage on a scale of 0 to 1 by using various damage variables (Karayannis et al. 2008; Kappos 2020). The damage index of control and corrosion-damaged specimens for this study was calculated by adopting the Park and Ang model (Park and Ang 1985; Park et al. 1987) since this model was validated using experimental data from a variety of RC structures that were damaged in previous earthquakes (Karayannis et al. 2008). As per this model, the damage index (DI) range varies from 0 to 1. When the DI value exceeds 1, the structure is meant to be completely damaged and collapsed (Park and Ang 1985; Park et al. 1987). The damage index of the reference test specimens was also calculated according to this model (as discussed in Section 3.6.1), to decide the number of cyclic displacements. This model expresses the damage index (DI) as a linear function of the effect of repeated cyclic loadings and the maximum deformation (Park and Ang 1985), as mentioned in equation 4.3 below:

$$\mathrm{DI} = \frac{\delta_M}{\delta_U} + \frac{\beta}{F_y \delta_U} \int dE \tag{4.3}$$

Where,

- δ_M represents maximum displacement obtained under cyclic loading
- δ_U represents ultimate displacement capacity
- β symbolizes the strength degradation parameter with a value of 0.1(I.Villemure and E.Ventura 1995), for well-reinforced concrete structures
- F_y represent corresponding yield strength
- dE represents incremental dissipated hysteretic energy

Figure 4.40 and Figure 4.41 present the progression of the damage index with respect to the displacement for non-seismic and seismic specimens, respectively. The damage index values of all the test specimens are shown in Table 4.5. The NDU specimen experienced complete failure at ± 3.5% drift ratio. However, when compared to NDU, the NDC-1 specimen fails ultimately at an early drift. Similarly, severely corrosion-damaged specimens (i.e., NDC-2 and NDC-3 specimens) show ultimate failure much before the NDC-1 specimen. Due to highly damaged reinforcement bars and their significantly reduced bond with surrounding concrete, the post-yield performance was degraded up to a large extent. In the NDC-2 and NDC-3 specimens, it was observed that the damage index showed a significant rise after the fracture of the corroded bar. A similar trend for the damage index of corroded seismic specimens was noticed as was observed for corroded non-seismic specimens. Table 4.5 illustrates that the seismic specimens having closer stirrups arrangement exhibited improved damage tolerance even under severe corrosion levels. Despite the fracture of the 8 mm bar, this arrangement exhibited improved shear resistance and also provided better grip over core concrete helping it to withstand damage even at higher drifts.

Figure 4.40 and Figure 4.41 shows that when the corrosion rate is below 10% (i.e., NDC-1 and DC-1), the effect of close stirrups arrangement can be experienced, as the DC-1 specimen showed a lower damage index value when compared to the NDC-1 specimen. The damage index plot shows that the NDC-1 specimen crossed the value of 1 at the drift ratio of ± 2.75%, whereas the DC-1 specimen achieved a complete failure at the drift of ± 3.5%. It can be observed that severe damage has been received by highly corroded specimens, whether non-seismic or seismic detailed. The complete damage of NDC-3 and DC-3 was encountered at a drift ratio of ± 1.75% and ± 2.2%, respectively which is approximately half of the drift ratio required for the complete damage of NDU and DU i.e., ± 3.5%. Further, the DI value signifies that corroded seismic specimens exhibit better damage resistance at higher displacement when compared to corroded non-seismic specimens.

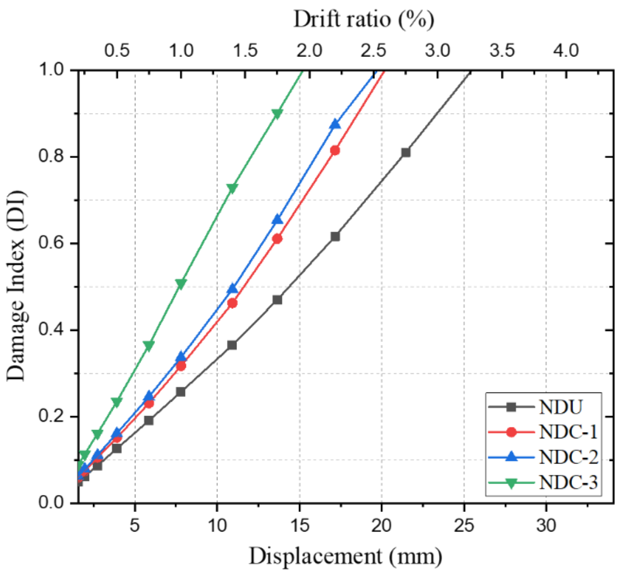

Figure 4. 40 Damage indices over displacement for control and corroded non-seismic specimens

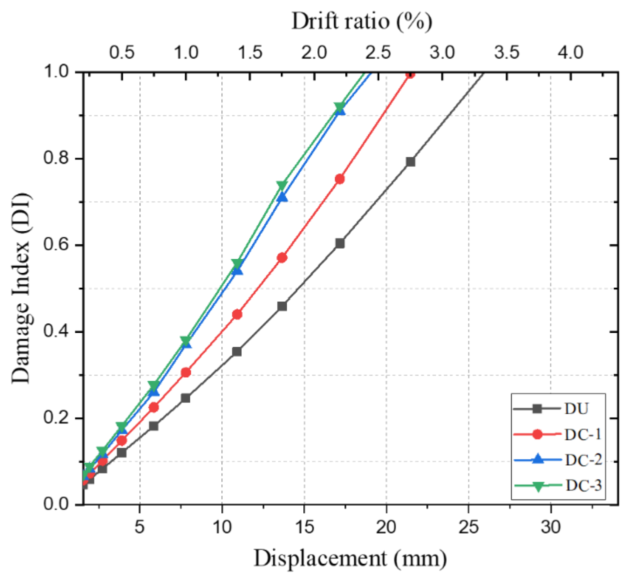

Figure 4. 41 Damage indices over displacement for control and corroded seismic specimens

Table 4. 5 Damage Index of Control and Corrosion-Damaged Specimens

Drift ratio	Displacement	Damage Index (DI)							
		NDU	NDC-1	NDC-2	NDC-3	DU	DC-1	DC-2	DC-3
0.2	1.56	0.049	0.059	0.062	0.089	0.047	0.057	0.065	0.070
0.25	1.95	0.062	0.074	0.079	0.113	0.059	0.072	0.082	0.089
0.35	2.73	0.087	0.105	0.111	0.161	0.083	0.102	0.117	0.125
0.5	3.9	0.126	0.151	0.161	0.235	0.120	0.148	0.172	0.182
0.75	5.85	0.191	0.231	0.246	0.365	0.182	0.225	0.260	0.277
1	7.79	0.257	0.317	0.337	0.508	0.246	0.306	0.370	0.381
1.4	10.92	0.365	0.462	0.494	0.729	0.354	0.440	0.540	0.560
1.75	13.65	0.470	0.611	0.654	0.901	0.459	0.571	0.710	0.740
2.2	17.16	0.616	0.815	0.874	1.123	0.604	0.753	0.910	0.922
2.75	21.45	0.810	1.078	1.085	1.394	0.793	0.997	1.110	1.140
3.5	27.29	1.087	1.360	1.346	1.763	1.062	1.323	1.380	1.434
4.36	34.07	1.429	1.648	1.643	2.184	1.389	1.671	1.700	1.786

4.10 JOINT PRINCIPAL TENSILE STRESS

The combined effect of the applied joint shear and the axial load on the column produces principal compressive and tensile stresses which results in diagonal cracking or crushing of concrete in the joint core (Tran and Hadi 2017). An improvement in the beam-column joint performance under the effect of reverse cyclic loading is experienced if the joints possess higher endurance to the applied principal tensile stress. The following equations (4.4-4.6) suggested by Priestley 1997 were used for calculating joint principal tensile stress.

$$\tau_{jh} = \frac{P}{A_{hCore}}\left(\frac{L_b}{d_b} - \frac{L_b + 0.5D_C}{L_C}\right) \tag{4.4}$$

$$\sigma_p = (N_c + P)/(b_c h_c) \tag{4.5}$$

$$\sigma_t = \frac{\sigma_p}{2} + \sqrt{\frac{\sigma p^2}{4} + \tau_{jh}^2} \tag{4.6}$$

Where

- τ_{jh} represents joint horizontal shear stress
- P represents peak cyclic load corresponding to the controlled displacement
- A_{hcore} represents horizontal cross-section area of the joint core
- L_b represents the beam length
- d_b is the effective depth of the beam
- D_c represents the total depth of the beam
- L_c is the column length
- σ_p is axial compressive stress
- N_c represents the column axial compressive load applied using a hydraulic jack
- b_c represents the column width
- h_c represents the column depth
- σ_t represents the principal tensile stress

4.10.1 Comparison between Control and Corrosion-damaged Specimens

Figure 4.42 shows the principal tensile stress vs drift ratio plot for uncorroded and corroded non-seismic specimens representing the variation in principal stress as the specimen undergoes higher displacement. It has been observed that the control non-seismic (NDU) specimen shows the maximum tensile stress resistance up to 3.5% and 1.75 % drift ratio in the respective positive and negative displacement. Thereafter, a decline in the principal tensile stress resistance capacity was noticed, as the drift progressed. The figure also indicates that all corroded specimens offered a slightly better resistance to tensile stress at initial drifts. This can be attributed to the deposition of a layer of rust on the reinforcing bars surface in the early stages of corrosion, which roughened up its contact surface (thus allowing a stronger bond) with the surrounding concrete. For the level-1 corroded specimen, i.e. NDC-1 having slight corrosion damage, the maximum tensile stress was observed at the drift of 2.2% and 1.4% in the positive and negative displacement. A decline of 15% in the maximum principal tensile stress capacity was noted in the NDC-1 specimen when compared to that of the NDU specimen. For the NDC-2 and NDC-3 specimens having severe corrosion damage, the corresponding decline was 21.2%, and 32.11% at the respective negative drift of 1%, and 0.75%. The progressive widening of cracks along the longitudinal direction of the column and beam led to the crumbling and dismantling of the concrete cover under high cyclic loading. Moreover, a significant reduction in the negative drift was experienced due to the fracture of a severely pitted 8 mm diameter reinforcement bar. These factors combined to result in a lower resistance to the principal stress.

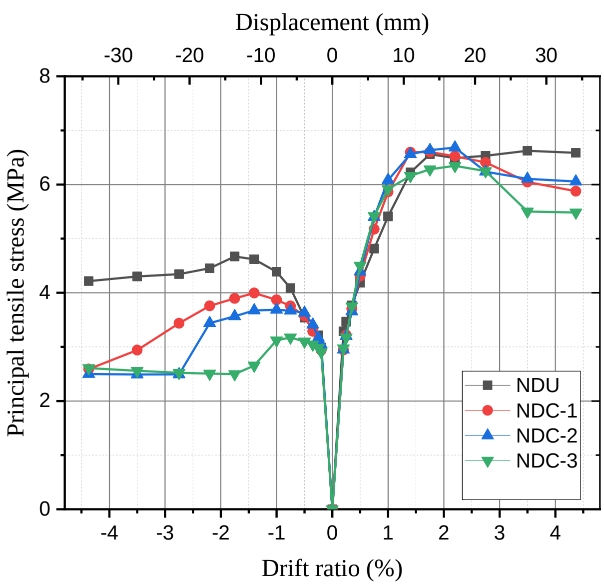

Figure 4. 42 Principal tensile stress of control and corroded non-seismic specimens

A similar trend was experienced for the corroded seismic specimens as was seen in the corroded non-seismic specimens, as shown in Figure 4.43. The control seismic (DU) specimen shows the maximum tensile stress resistance capacity up to 3.5% and 2.2 % drift ratio in the respective positive and negative displacement. The DC-1 specimen shows maximum tensile stress resistance up to the drift of 2.75% and 1.75% at the positive and negative drift, respectively. When compared to the DU specimen, DC-1, DC-2, and DC-3 exhibited a decrement in the maximum tensile stress resistance up to 12%, 18.9%, and 19.3% at the respective drift of 1.75%, 1.4%, and 1% in the negative drift. However, the corroded seismic specimens resisted tensile stress better than the corroded non-seismic specimens, even at higher displacements. The DC-3 specimen sustains the tensile stresses up to the drift of 1% which is slightly higher than that for the NDC-3 specimen (0.75% drift ratio), in the negative displacement cycles. This is remarkably lower when compared to the NDU and DU specimens which were able to sustain the applied stresses up to 1.75% and 2.2% drift, respectively. A significant reduction of approximately 46.68% and 44.32% in the principal tensile stress of NDC-3 and DC-3 specimens at the drift of 1.75% and 2.2% was seen when compared to that of NDU and DU specimens, respectively. This was a clear indicator of the degraded post-elastic behaviour which is due to the weak bond between high corrosion-damaged reinforcing bars and surrounding concrete.

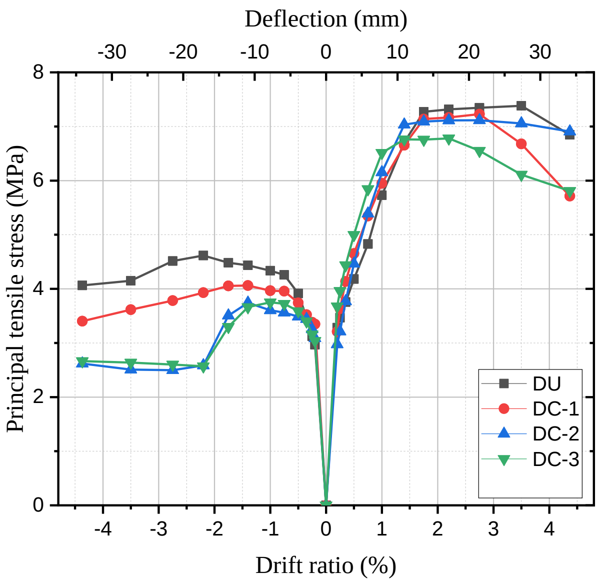

Figure 4. 43 Principal tensile stress of control and corroded seismic specimens

4.11 CLOSING REMARKS

This chapter explores the effects of corrosion damage (having different corrosion rates) at the junction of beam column under the influence of reverse cyclic loading. The seismic performance of different levels of corroded non-seismically detailed specimens was investigated, compared, and discussed with that of seismically detailed specimens. The change in the ultimate failure pattern of uncorroded and corroded specimens was reported. As discerned based on analysis of various seismic parameters, the corroded seismic detailed specimens showed better seismic performance than the corresponding corroded non-seismic detailed specimens owing to the closer arrangement of stirrups.

CHAPTER 5

RETROFITTING OF CORRODED BEAM-COLUMN JOINTS USING HIGH STRENGTH FIBER REINFORCED CONCRETE

5.1 GENERAL

In this chapter, the results of the seismic performance of the corroded non-seismically and seismically detailed specimens retrofitted with High Strength Fiber Reinforced Concrete (HSFRC) are reported. This part of the experimental study corresponds to stage 2 (part 2-retrofitting and structural testing of corrosion-damaged specimens). Initially, the non-seismic and seismic test specimens were corroded to three different levels by following the procedure explained in detail in Section 3.5.3. Figure 5.1 and Figure 5.2 show the respective impressed current-time duration plots for all the test specimens. The monitoring and measurement of cracks due to corrosion at different levels was done in a similar manner as was reported in Chapter 4 (Section 4.2) and the crack width is reported in Table 5.1.

The methodology followed for retrofitting the corroded specimens has already been outlined previously in Section 3.8. The corroded specimens were cut open to remove the damaged concrete up to the desired length. After cleaning and treating the corroded reinforcement bars, the specimens were retrofitted with High Strength Fiber Reinforced Concrete (HSFRC). The mix proportions and test results of the HSFRC mix are already presented in Section 3.7. The nomenclature used for the HSFRC retrofitted specimens is shown in Table 3.8.

The retrofitted specimens were cured for 28 days and were tested under reverse cyclic loading. After the testing was complete, all the corroded specimens were cut open and the corroded rebars were extracted in order to calculate the mass loss. The actual mass loss and theoretical mass loss for each level of corroded non-seismically and seismically detailed specimens are presented in Table 5.1. The seismic response of the retrofitted specimens was determined in terms of hysteresis load-displacement curve, envelop curve, ductility, energy dissipation, stiffness degradation, and principal tensile stress.

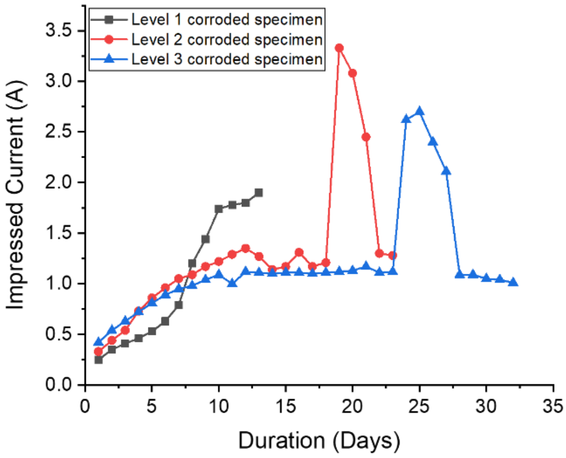

Figure 5. 1 Impressed Current-Time Duration Plot for Non-seismic BCJ Specimens

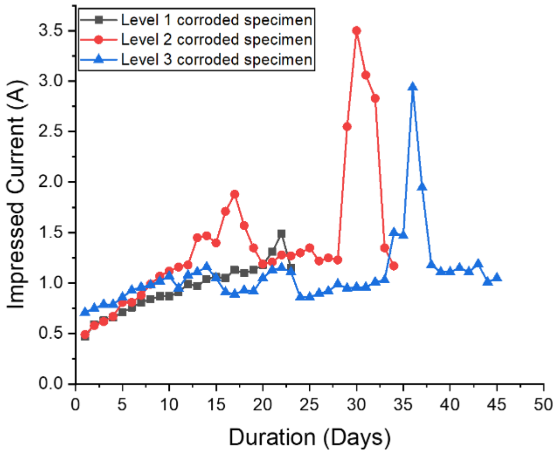

Figure 5. 2 Impressed Current-Time Duration Plot for Seismic BCJ Specimens

5.2 CRACK PATTERNS AND FAILURE MODES

In this study, all the Exterior BCJ specimens (i.e. non-seismic and seismic detailing) were cast following the strong column weak beam mechanism. As per this mechanism, the plastic hinge formation takes place at the beam end, at the intersection of the beam and column surface, providing adequate energy dissipation for the structure under a seismic environment. The crack patterns and failure mode of all the tested specimens including control and corrosion-damaged retrofitted specimens during the entire progression of the drifts have been explained in this section.

Table 5. 1 Summary of Corrosion measurement in Reinforcement bars

Specimens	Max. corrosion current (A)	Rebar diameter (mm)	Cum. theoretical mass loss (g)	Theoretical corrosion ratio (%)	Actual corrosion ratio (%)	Average crack width (mm)
RND-1	1.9	8 10 12 Stirrups	275.569	5.90	5.56	0.612
RND-2	3.33	8 10 12 Stirrups	610.508	13.07	13.10	0.972
RND-3	1.09	8 10 12 Stirrups	829.665	17.76	17.25	1.404
RD-1	1.49	8 10 12 Stirrups	459.432	8.79	8.66	0.288
RD-2	3.5	8 10 12 Stirrups	869.195	16.63	16.43	0.584
RD-3	1.19	8 10 12 Stirrups	1061.645	20.32	21.15	0.972

5.2.1 Damage Progression of Control and Retrofitted Non-seismic Specimens

During the initial cyclic loading, the damage on the surface of the control specimen initiates with the occurrence of hairline shear cracks at the junction of the beam-column. Initially, the shear crack originated from one side of the diagonal at the junction of beam-column i.e., the side having 8 mm diameter longitudinal reinforcement bars. As the drift ratio progresses, the hairline shear cracks occur from both diagonals at the beam-column junction. For this specimen, the diagonal shear cracks were visible at ± 0.5% drift ratio. From ± 0.5% drift ratio onwards, hairline flexural cracks were visible on the surface of the beam. The propagation and widening of the existing shear cracks occurred as the drift progressed. From ± 1.75% to ±

3.5% drift ratio, the damage on the specimen surface was mostly channelized towards the widening of the shear cracks; the propagation of the flexural cracks was relatively insignificant. At the higher drift ratios, the spalling and scattering of the concrete cover were experienced along with the yielding of the longitudinal reinforcement. After ± 3.5% drift, the ultimate failure of the specimen was experienced due to the widening of diagonal shear cracks at the junction of the beam-column, as shown in Figure 5.3.

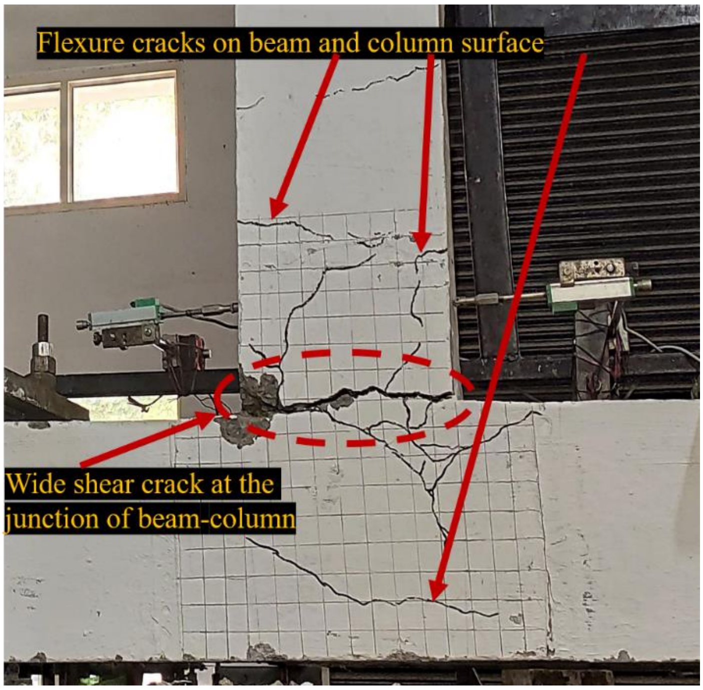

Figure 5. 3 Ultimate failure of NDU

When compared to the control non-seismic specimen, minimal flexural cracks were experienced on the surface of the HSFRC retrofitted specimens. Due to the presence of hybrid steel fibers, minor cracks were arrested during the continuous ongoing loading, and the widening of the dominant cracks was also resisted up to a certain extent. As the cyclic loading was applied to the RND-1 specimen, no hairline cracks were experienced on the beam and column surface during early drifts. A hairline shear crack was observed at the junction of the beam-column at a drift ratio of ± 0.75%. As the drift ratio progresses, the widening of the shear crack takes place and no flexural cracks were experienced on the surface of the specimens due to the presence of hybrid steel fibers. Even though the longitudinal rebars were corrosion-damaged and suffered cross-sectional reduction, a similar failure pattern to that of the control specimens was experienced. From ± 2.75 % drift ratio onward, the shear cracks at the beam-column junction become wide enough to ultimately fail the specimen, as shown in Figure 5.4. The dismantling sound due to the breaking of the bond between steel fibers and the concrete surface under the influence of higher cyclic loading was heard. Due to the presence of uniformly distributed hybrid steel fibers, no scattering and spalling of the concrete cover were experienced.

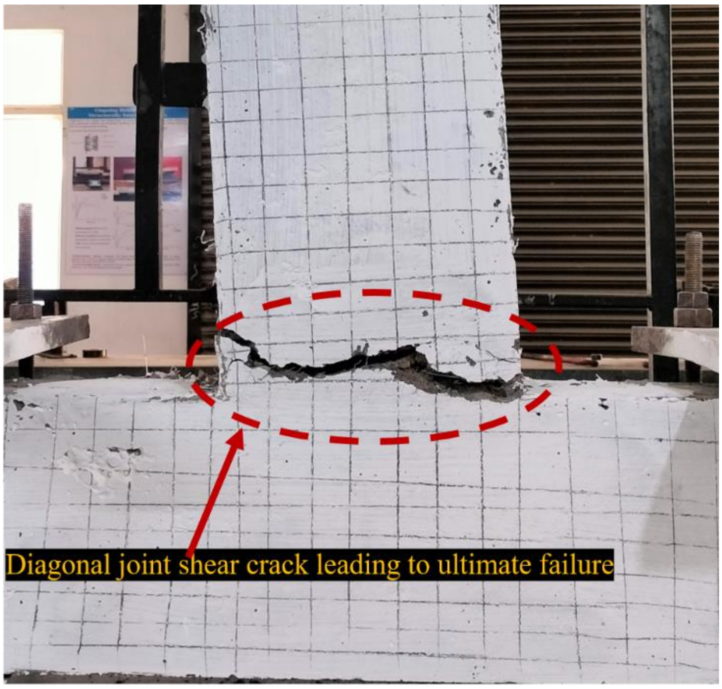

Figure 5. 4 Ultimate failure of RND-1

A similar failure pattern was experienced for the RND-2 specimen. In addition, at the drift ratio of ± 0.75% and ± 1.75%, a hairline flexural crack was observed respectively at the beam and column surface. At higher drifts, a loud sound was heard directed towards the brittle fracture of the corrosion-damaged reinforcement bar which was also experienced in the negative drift of the hysteresis curve. Despite the fracture of the 8 mm bar, the damage was channelized towards the joint shear failure due to the widening of the shear cracks at the junction of the beam-column, instead of failing from the fracture reinforcing bar location, as shown in Figure 5.5. In the RND-3 specimen, firstly a shear crack was observed at ± 0.75% drift ratio. Thereafter, the hairline flexural crack at the drift ratio of ± 1.4% was experienced at the surface of the beam from one side. A fracture of the localized pitted reinforcement bar was experienced for the RND-3 specimen; this was similar to that observed for the RND-2 specimen but at a smaller drift ratio. The rebars of the RND-3 specimen were severely damaged and were unable to transfer adequate ductility. Therefore, the flexural cracks at the localized pitting location widen as the drift progresses and the specimens ultimately fail due to flexural failure, as shown in Figure 5.6. However, even at the flexural failure due to severely damaged reinforcement bars, the spalling and scattering of the concrete cover were restricted due to the binding effect provided over concrete by hybrid steel fibers. Table 5.2 shows a comparative analysis of damage progression in retrofitted non-seismic detailed specimens and the corresponding control specimen.

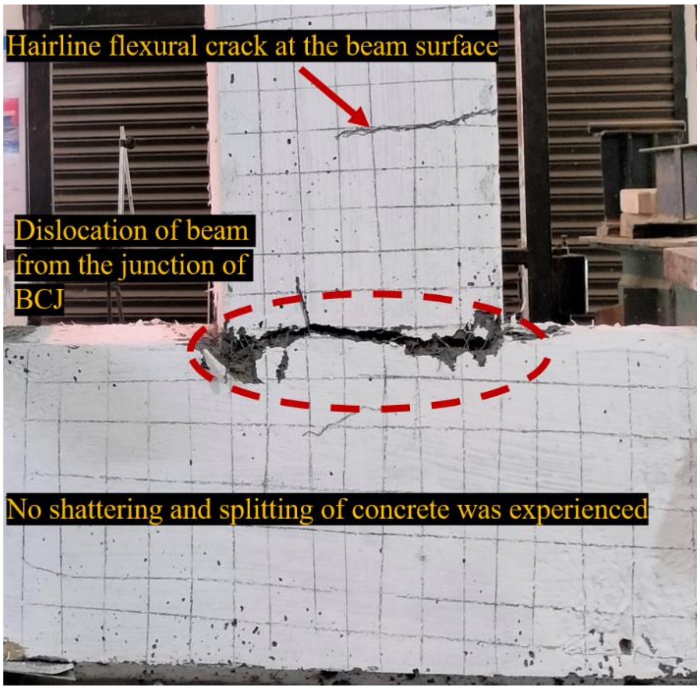

Figure 5. 5 Ultimate failure of RND-2

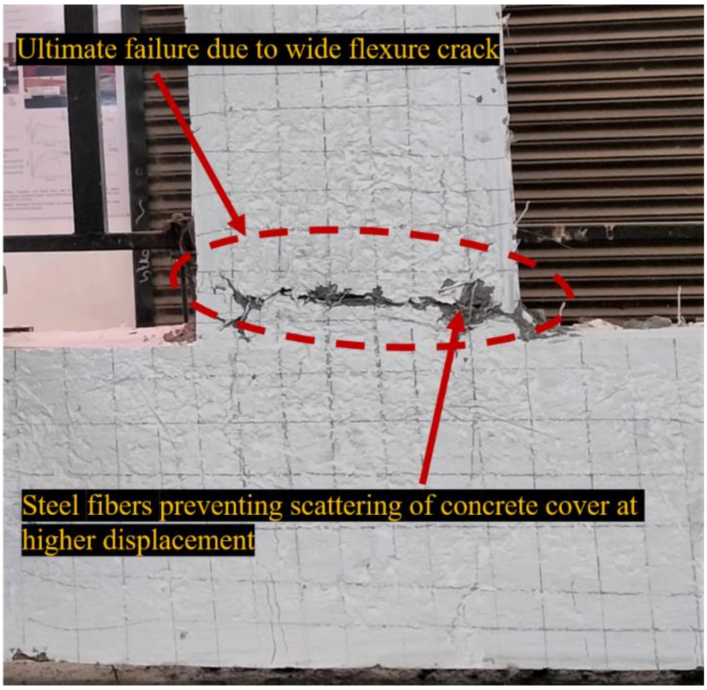

Figure 5. 6 Ultimate failure of RND-3

Table 5. 2 Damage progression of all the retrofitted non-seismic test specimens

<table>
<tr><th>Drift Ratio</th><th>NDU</th><th>RND-1</th><th>RND-2</th><th>RND-3</th></tr>
<tr><td>0.2</td><td rowspan="3">Hairline shear cracks originate at the beam-column junction</td><td rowspan="4">No sign of cracks on the surface of beam-column</td><td rowspan="3">No sign of cracks on the surface of beam-column</td><td rowspan="3">No sign of cracks on the surface of beam-column</td></tr>
<tr><td>0.25</td></tr>
<tr><td>0.35</td></tr>
<tr><td>0.5</td><td>Propagation of Shear cracks, Hairline flexural cracks observed at beam surface</td><td>Hairline shear cracks at the junction of beam-column</td><td rowspan="3">Hairline shear cracks at the junction of beam-column</td></tr>
<tr><td>0.75</td><td rowspan="3">New flexural cracks form on the beam surface, Propagation of Shear cracks</td><td rowspan="3">Hairline shear cracks at the junction of beam-column</td><td rowspan="3">Hairline flexural crack on the surface of the beam</td></tr>
<tr><td>1</td></tr>
<tr><td>1.4</td><td>Hairline flexural crack on the surface of beam and column.</td></tr>
<tr><td>1.75</td><td rowspan="4">Widening of shear cracks</td><td rowspan="3">Widening of shear crack at the junction of beam-column</td><td rowspan="2">Hairline flexural crack on the beam and column surface. Widening of shear crack at the junction of beam-column</td><td>Widening of flexure crack at the surface of the beam</td></tr>
<tr><td>2.2</td><td>Fracture of severely pitted 8 mm reinforcing bar</td></tr>
<tr><td>2.75</td><td>Dismantling sound due to breaking of the bond between steel fibers and concrete. Fracture of severely pitted 8 mm diameter reinforcing bar</td><td rowspan="3">Dislocation of the beam from the dominant flexural crack location. No spalling and shattering of concrete cover</td></tr>
<tr><td>3.5</td><td>Dismantling sound due to breaking of bond between steel fibers and concrete</td><td rowspan="2">Dislocation of the beam from the junction of the beam-column.
No scattering and spalling of concrete cover</td></tr>
<tr><td>4.36</td><td>Ultimate failure due to diagonal shear cracks, Crumbling, and spalling of concrete</td><td>Ultimate failure at the junction of the beam column</td></tr>
</table>

5.2.2 Damage Progression of Control and Retrofitted Seismic Specimens

The failure mode of the control seismic (DU) specimen is similar to that experienced for the control non-seismic specimen (NDU) i.e., joint shear failure. Under the influence of cyclic loading, the hairline diagonal shear cracks were observed at the junction of the beam-column at ± 0.5% drift ratio. As the drift progressed, hairline flexural cracks initiated at the column and beam surface. It was observed that as compared to the NDU specimen, fewer hairline flexure cracks appeared at the surface of the specimens during initial drifts, as minor cracks were arrested due to the closer stirrups arrangement within the joint intersection area. From ± 2.2% drift ratio onwards, the widening of the dominant shear crack at the beam-column junction takes place. Thereafter, the spalling and scattering of the concrete cover were observed which was comparatively lower than that of the NDU specimen. The DU specimen experienced a wide shear crack at the beam-column junction resulting in the ultimate failure, as shown in Figure 5.7.

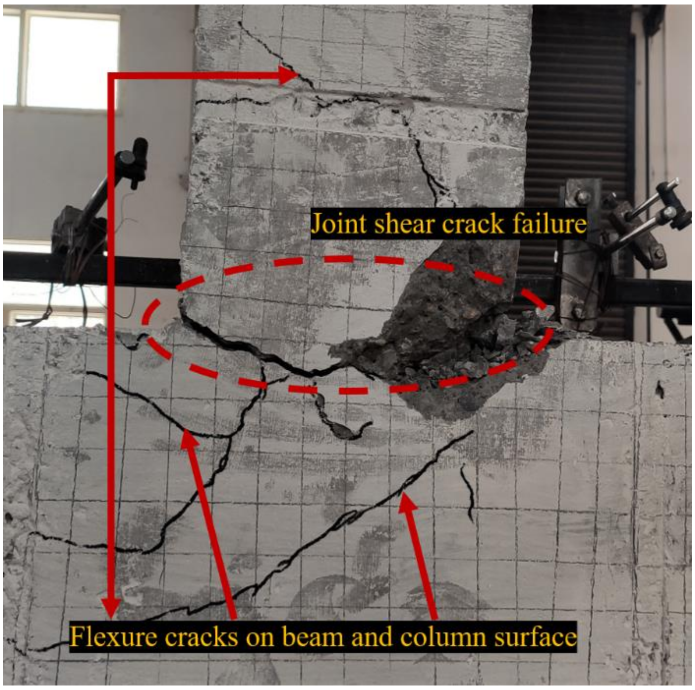

Figure 5. 7 Ultimate failure of DU

The presence of the hybrid steel fibers in retrofitted specimens not only improved the flexural performance of the concrete but also delayed the progression and widening of cracks to some extent. The failure pattern of retrofitted seismic detailed specimens was similar to that of retrofitted non-seismic detailed specimens. Around the drift ratio of ± 0.75%, the hairline shear cracks were observed at the junction of the RD-1 and RD-2 specimens. This was in stark contrast to control (DU) specimens where hairline shear cracks had started to appear on one face at approximately half this drift ratio (around ± 0.3% and beyond). During the entire loading cycle, no flexural cracks were observed on the RD-1 specimen surface. For the RD-2 specimen, only 1 flexural crack was spotted on the surface of the beam originating from one side of the beam surface. The ultimate failure experienced by RD-1 and RD-2 specimens was due to the widening of the shear crack present at the junction of the specimens, as shown in Figure 5.8 and Figure 5.9, respectively. At higher drifts, the soft sound of fibers dismantling from the concrete surface was also heard, particularly at the location of the wide shear crack.

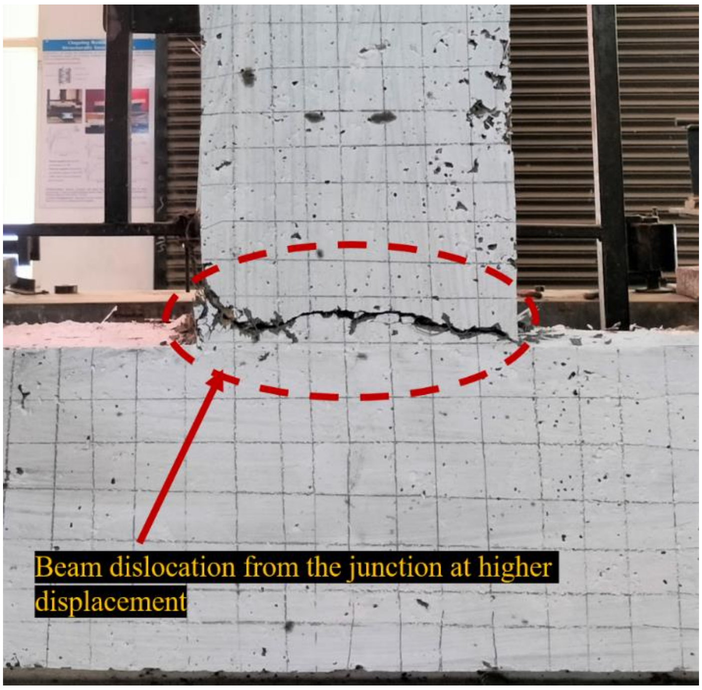

Figure 5. 8 Ultimate failure of RD-1

For specimen RD-3, hairline shear cracks were initiated at the beam-column junction at ± 0.5% drift ratio. At a drift of ± 1%, hairline flexural cracks started originating from the localized pitting location at the beam surface, accompanied by the widening of the shear crack at the junction of the specimen. As the drift progressed, the pre-existing cracks widened, followed by the fracture of the corrosion-damaged reinforcement bar at a drift of ± 2.2%. The fracture was also confirmed by the loud sound during the cyclic loading. Figure 5.10 displays the failure pattern of the RD-3 specimen. Due to the severely damaged reinforcing bars, the post-yield performance was degraded and RD-3 was unable to follow the plastic hinge mechanism at the beam end surface at the beam-column junction. Due to the presence of hybrid steel fibers, the spalling and scattering of the concrete cover were resisted, even for the highly corroded specimens at the ultimate displacement, presented in Figure 5.11. Table 5.3 shows a comparative analysis of damage progression in retrofitted seismic detailed specimens and the corresponding control specimen.

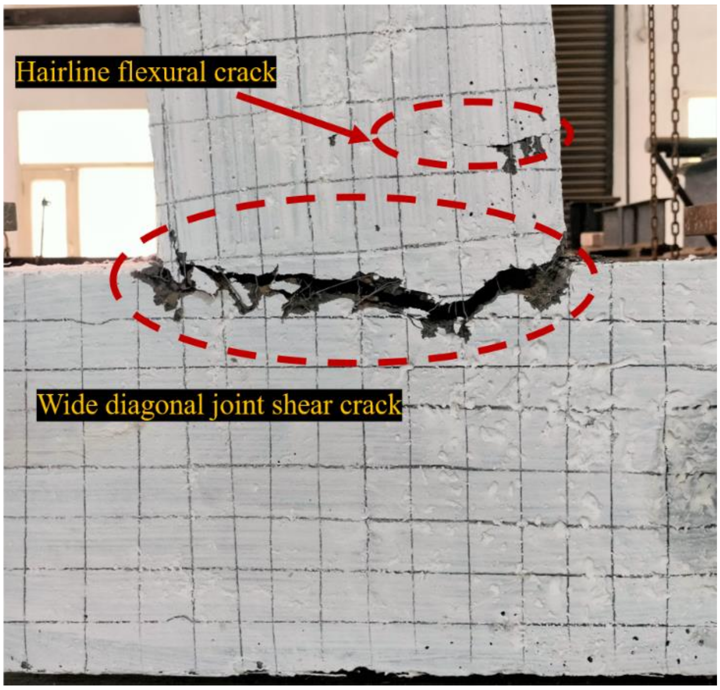

Figure 5. 9 Ultimate failure of RD-2

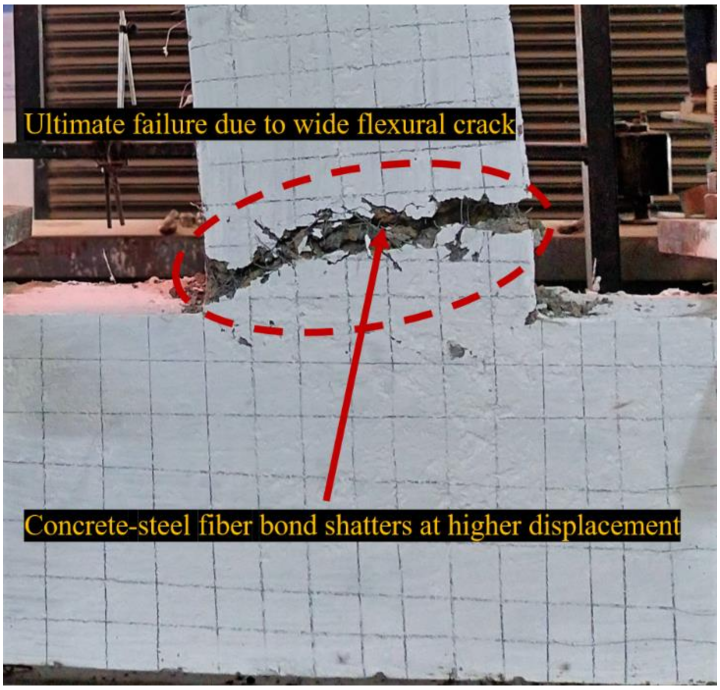

Figure 5. 10 Ultimate failure of RD-3

Figure 5. 11 Side view of the RD-3 specimen showing steel fiber-concrete bond

Table 5. 3 Damage progression of all the retrofitted seismic test specimens

<table>
<tr><th>Drift Ratio</th><th>DU</th><th>RD-1</th><th>RD-2</th><th>RD-3</th></tr>
<tr><td>0.2</td><td rowspan="4">Hairline shear cracks initiate at the junction of BCJ from one side</td><td rowspan="4">No sign of cracks on the beam-column surface</td><td rowspan="4">No sign of damage on the beam-column surface</td><td rowspan="3">No sign of damage on the beam-column surface</td></tr>
<tr><td>0.25</td></tr>
<tr><td>0.35</td></tr>
<tr><td>0.5</td><td rowspan="3">Hairline shear cracks at the junction of beam-column</td></tr>
<tr><td>0.75</td><td rowspan="3">Shear cracks observed at the junction of BCJ from both sides</td><td rowspan="3">Hairline shear cracks at the junction of beam-column</td><td>Hairline shear cracks at the junction of beam-column</td></tr>
<tr><td>1</td><td rowspan="3">Propagation of flexural cracks on one side of beam, Diagonal shear cracks observed</td></tr>
<tr><td>1.4</td><td rowspan="2">Hairline flexural crack on the beam and column surface.</td></tr>
<tr><td>1.75</td><td rowspan="2">Widening of diagonal shear cracks, hairline flexural cracks observed at the column surface</td><td rowspan="4">Widening of shear crack at the junction of beam-column</td></tr>
<tr><td>2.2</td><td rowspan="2">Widening of shear crack at the junction of beam-column. No scattering and spalling of concrete</td><td>Fracture of severely pitted 8 mm reinforcing bar</td></tr>
<tr><td>2.75</td><td rowspan="2">New flexural cracks observed at the column and beam surface</td><td>Widening of flexure crack at the surface of the beam</td></tr>
<tr><td>3.5</td><td>Fracture of severely pitted 8 mm diameter reinforcing bar</td><td rowspan="2">Dislocation of the beam from the dominant flexural crack location. No spalling and shattering of concrete cover</td></tr>
<tr><td>4.36</td><td>Ultimate failure due to diagonal shear cracks, Crumbling of concrete cover</td><td>Dismantling sound due to breaking of the bond between steel fibers and concrete. Ultimate failure at the junction of the beam column</td><td>Dislocation of the beam from the junction of the beam-column</td></tr>
</table>

5.3 HYSTERESIS BEHAVIOUR OF SPECIMENS

5.3.1 Hysteretic Load-Displacement Behaviour of Non-seismic Control and Retrofitted Specimens

The hysteresis loops in the load-displacement hysteresis plot represent the area of energy dissipation which is an indicator of damage received (accumulated) by the specimen under cyclic loading. The smaller loops which are generally observed during the initiation of loading show less damage received by the specimen. As the loading progresses, much wider and larger hysteresis loops can be observed representing severe damage and high energy dissipation under the respective load.

Figure 5.12 (a) displays the load-displacement hysteresis response of the control non-seismic specimen (NDU). It can be observed that the hysteresis loops generated during initial drift ratios were narrow and small, as the specimen has not reached the yielding stage and thus accumulated very little damage. As the reverse cyclic displacement progresses, the damage imparted to the structure is represented in the form of large and wide hysteresis loops. During the ultimate loading stage of the specimen, the hysteresis loops show a continuous declining trend representing degraded load-bearing capacity and reduced damage tolerance. The control specimen when compared with the retrofitted specimens showed wide and large hysteresis loops during the initial drift ratios. Due to the superior properties of HSFRC, enhanced damage tolerance and load-bearing capacity were observed for Level 1 and Level 2 retrofitted non-seismic and seismic specimens, when compared to their respective control specimens.

Figures 5.12 (b) and Figure 5.13 show the load-displacement hysteresis curve for the retrofitted non-seismic specimens. Figure 5.12 (b) shows the high load-bearing capacity of the RND-1 specimen during the initial drift when compared to that of the NDU specimen. It can also be observed that the hysteresis loops present in the hysteresis curve of the RND-1 specimen are much wider and larger when compared to the hysteresis loops of the NDU specimen. The peak load of the RND-1 specimen was 33.67% higher than that of NDU. Figure 5.13 (a) and (b) present the hysteresis loops experienced for RND-2 and RND-3 specimens, respectively. During initial drifts, the damage tolerance and load-bearing capacity were better than the control specimen. However, at higher drifts, a sudden drop in the load-bearing capacity in the negative drift was observed. Due to the fracture of severely pitted 8 mm diameter rebar; this was also visually confirmed after opening the specimen post the cyclic loading test and extracting the corroded reinforcement cage. As visible from Figure 5.13, the severely corroded retrofitted specimens were unable to recover the load-bearing capacity at higher displacements due to the corrosion-damaged reinforcement bars. Due to the retrofitting technique, the fracture of the corrosion-damaged reinforcement bar was delayed, thereby allowing recovery in the ductile behaviour of the specimens up to a certain extent. For instance, the fracture of 8 mm bar the for highly corroded retrofitted specimen RND-3 was observed at a drift of 2.2%, as compared to the bar fracture at 1.4% for NDC-3 (non-retrofitted specimen; refer Table 4.2).

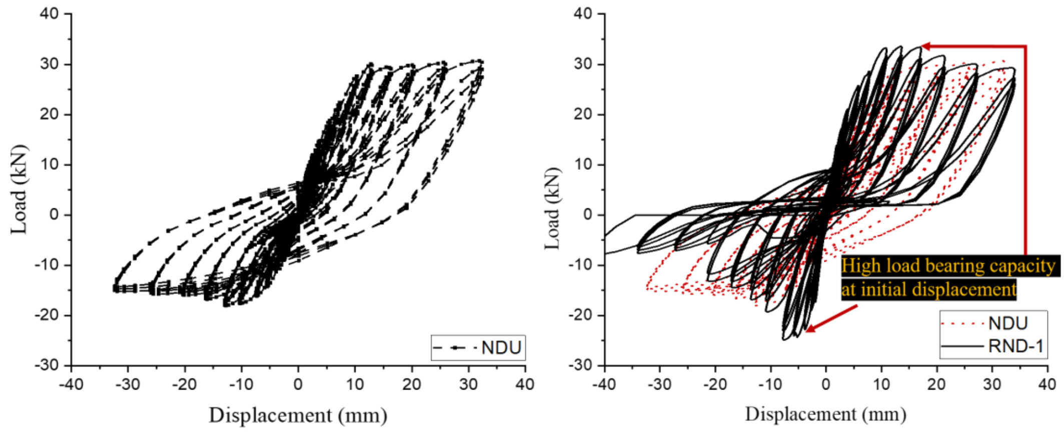

(a) (b)

Figure 5. 12 Load-displacement hysteresis curves for (a) NDU and (b) RND-1 specimens

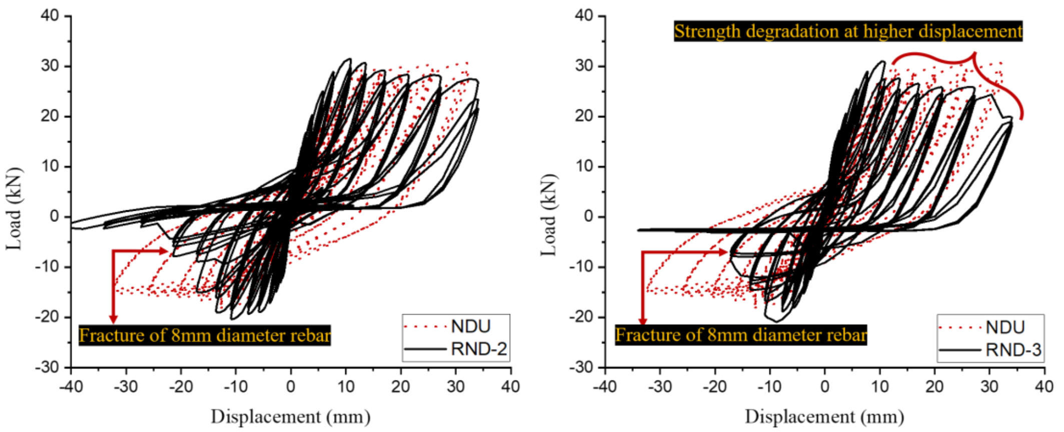

(a) (b)

Figure 5. 13 Load-displacement hysteresis curves for (a) RND-2 and (b) RND-3 specimens

5.3.2 Hysteretic Load-Displacement Behaviour of Seismic Control and Retrofitted Specimens

Figure 5.14 (a) shows the hysteretic load-displacement response of the control seismic specimen (DU). When compared to the hysteresis plot of NDU, wider hysteresis loops are experienced for DU, owing to the additional confinement provided to concrete through the closer stirrups arrangements within the joint intersection region. The large envelop area of the hysteresis loop was experienced along with the higher load-bearing capacity. Similar to NDU, the hysteretic loops were comparatively narrow and small during initial drifts and became large and wide as the cyclic loading progressed. Figures 5.14 (b) and Figure 5.15 show the load-displacement hysteresis curve for the retrofitted seismic specimens. Figure 5.14 (b) shows a significant increase in the load-bearing capacity of the RD-1 specimen along with the much wider hysteresis loop when compared to that of the DU specimen. Figures 5.15 (a) and (b) show that the load-carrying capacity of the corrosion-damaged specimens (i.e. RD-2 and RD-3) was recovered during the initial drifts, but continued to deteriorate at higher drifts, even after retrofitting. This can be attributed to the reduced strength and ductility exhibited by the severely damaged reinforcement bars. At higher drifts, the fracture of rebar was experienced causing a sudden drop in the load at the negative drift. However, the sudden brittle failure of the specimens was prevented owing to the presence of hybrid steel fibers which were able to bridge the cracks and provide sufficient ductility even after the fracture of the corrosion-damaged reinforcing bar. From the hysteresis curve of corrosion, Level-1 retrofitted specimens i.e. RND-1 and RD-1, it can be observed that not only load-bearing capacity was recovered but also increased up to a certain extent. When compared to retrofitted non-seismic specimens, the seismic retrofitted specimens exhibit more dense and wide hysteresis loops. The close arrangement of stirrups within the target corrosion area enhances the seismic behaviour.

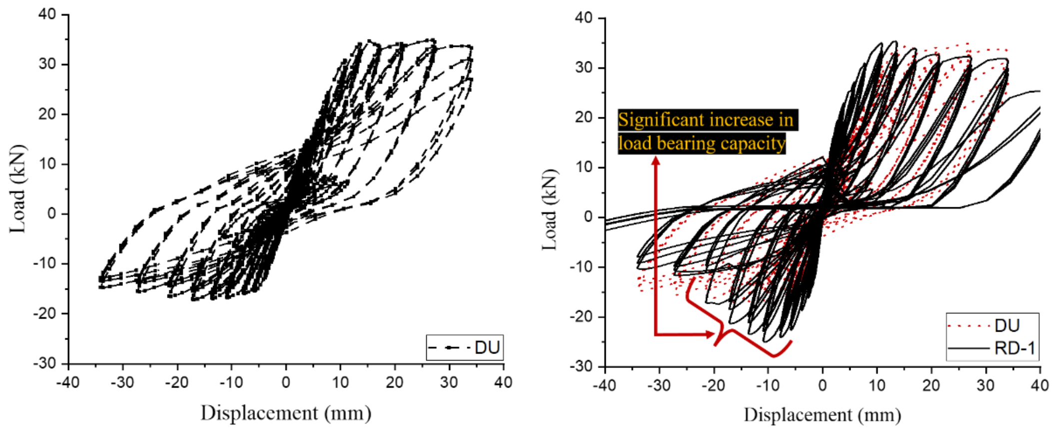

(a) (b)

Figure 5. 14 Load-displacement hysteresis curves for (a) DU and (b) RD-1 specimens

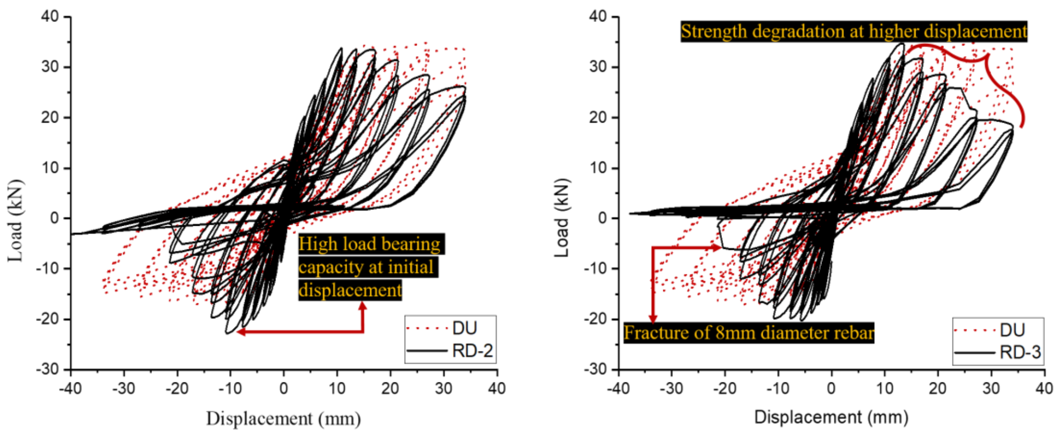

(a) (b)

Figure 5. 15 Load-displacement hysteresis curves for (a) RD-2 and (b) RD-3 specimens

5.4 LOAD-DISPLACEMENT ENVELOPE CURVE AND DUCTILITY

A load-displacement envelope curve represents the peak load in the negative and positive directions of each drift. With the help of envelope curves, seismic parameters like load-bearing capacity, elastic and plastic behaviour, and ductility can visualized and evaluated easily. The following sections provide a comparison of the envelope curves of respective non-retrofitted specimens and retrofitted specimens, at the same level of corrosion. The peak load capacity of each specimen is also compared to get a better understanding of the efficiency of the adopted retrofitting strategy. Finally, the post-peak plastic behaviour of all specimens is evaluated and presented as displacement ductility in Table 5.4.

5.4.1 Envelope curve of control and retrofitted specimens

Figure 5.16 displays a comparison of the envelope curves of the NDC-1 and RND-1 specimens. It can be experienced that the retrofitted specimen exhibited higher elastic stiffness when compared to that of the respective non-retrofitted specimen at the same corrosion level. The superior mechanical properties of HSFRC and the presence of hybrid steel fibers are the major reasons supporting this behaviour. The peak load resisted by the specimen NDC-1 during the cyclic loading in the negative and positive drift was 13.13 kN and 29.04 kN, respectively. The maximum load-carrying capacity of the RND-1 specimen was reported as 23.26 kN and 32.09 kN, respectively in the negative and positive drift. Due to the presence of hybrid steel fibers, the minor cracks were arrested and the major cracks were delayed during the loading. The ultimate failure mode of the RND-1 specimen even after having corrosion-damaged reinforcement bars was experienced to be the same as was experienced for control specimens NDU, as both specimens failed through a dominant shear crack at the beam-column junction. This is a clear indicator that the adopted retrofitting technique is capable of fully recovering the degradation in strength at lower corrosion levels, and may even provide a slight increase in a load-carrying capacity beyond uncorroded control specimens (the peak load capacity for NDU specimens was 17.4 kN and 29.17 kN during the negative and positive drift cycles, respectively).

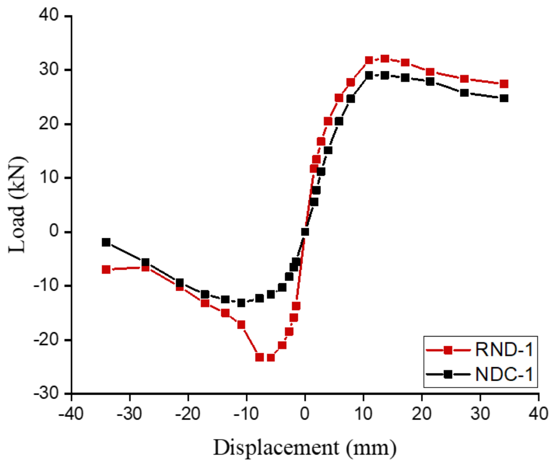

Figure 5. 16 Comparison of the Envelop curve of the RND-1 and NDC-1 specimen

The envelope curve of the RND-2 specimen is compared with the NDC-2 specimen, as shown in Figure 5.17. The peak load of the RND-2 specimen was observed as 29.89 kN and 18.59 kN in the positive and negative drift direction against 29.53 kN and 11.08 kN achieved for the DC-2 specimen. Figure 5.17 shows the increased initial stiffness of the RND-2 specimen despite having severely pitted reinforcement bars. The degraded ductility of the corrosion-damaged reinforcing bars was compensated due to the presence of hybrid steel fibers, and the fracture of the severely pitted bars was delayed under the high displacement. Despite presenting a fracture of the reinforcement bar during cyclic loading, the ultimate failure mode was the same as that of the NDU specimen. Further, a slight increase in load capacity even beyond NDU specimens is noted, testifying to the efficiency of the retrofitting strategy even at moderate corrosion levels.

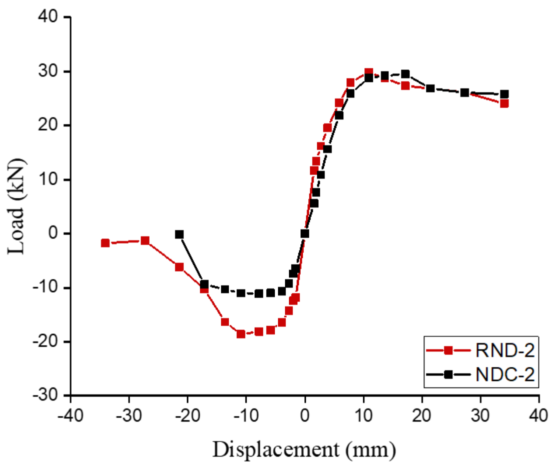

Figure 5. 17 Comparison of the Envelop curve of the RND-2 and NDC-2 specimen

At level-3 corrosion, the fracture of stirrups and longitudinal reinforcement bars due to localized pitting was seen. The Level-3 corroded bars displayed the ductility value reduced to half the ductility value experienced for uncorroded bars (refer to Figure 3.13). Figure 5.18 shows the envelop curve of the RND-3 specimen compared with the NDC-3 specimen. The pre-peak performance of RND-3 specimens was better when compared to the NDC-3 specimen, owing to the presence of HSFRC. The steel fibers have provided enough ductility to delay the fracture of localized pitted 8 mm diameter reinforcement bars. The ultimate failure of the RND-3 specimen was due to a dominant flexural crack at the beam surface, as the bond between severe corrosion-damaged concrete and hybrid steel fibers was not adequate to transfer the failure mechanism to the junction of the beam-column.

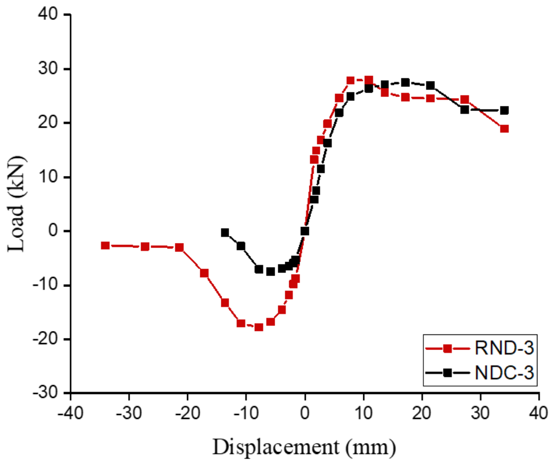

Figure 5. 18 Comparison of the Envelop curve of the RND-3 and NDC-3 specimen

A similar behaviour was experienced for the seismically retrofitted specimens as was seen for the non-seismic specimens but with higher damage tolerance and drift progression. Figure 5.19 displays the envelop curve of the RD-1 specimen compared with the DC-1 specimen. It can be seen that the RD-1 specimen exhibits approximately 70.71% and 3.71% higher maximum load-bearing capacity than the respective DC-1 specimen, in the negative and positive drift direction. At the pre-peak stage, the RD-1 specimen shows higher stiffness and energy dissipation when compared to the DU specimen, due to the superior mechanical properties of HSFRC and hybrid steel fiber.

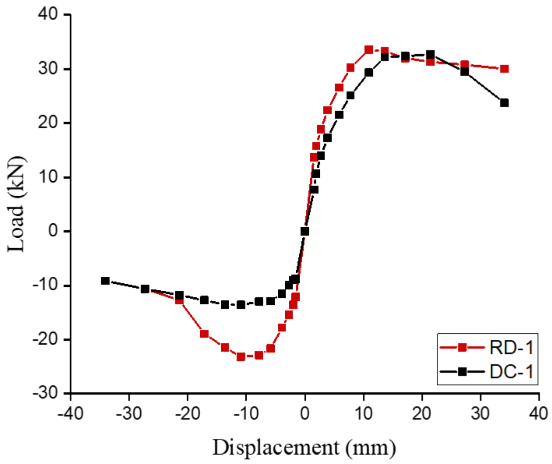

Figure 5. 19 Comparison of the Envelop curve of the RD-1 and DC-1 specimen

Figure 5.20 and Figure 5.21 show the load-displacement envelop curve of RD-2 and RD-3 specimens compared with the DC-2 and DC-3 specimens, respectively. Despite having localized pitting at the severe corrosion levels resulting in fracture of rebar at higher displacements, the retrofitted specimens show a significant increase in load-bearing capacity at the negative drift. When compared to the DC-2 and DC-3 specimens, the RD-2 and RD-3 specimens show approximately 78.70% and 64.0% higher maximum load-carrying capacity in the negative drift direction, respectively. The ultimate failure mode experienced in the case of the RD-2 specimen was similar to that of the uncorroded DU specimen, due to superior ductility provided by hybrid steel fibers. However, in the case of the RD-3 specimen, the ultimate failure was due to a dominant flexural crack originating from the location of the fractured bar. The bars were damaged up to such an extent that post-elastic recovery was not possible for the RD-3 specimen.

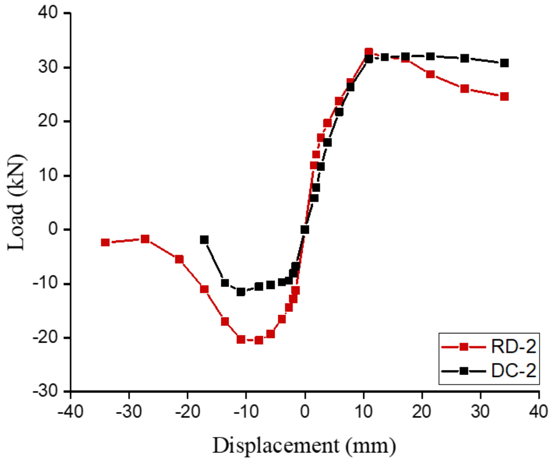

Figure 5. 20 Comparison of the Envelop curve of the RD-2 and DC-2 specimen

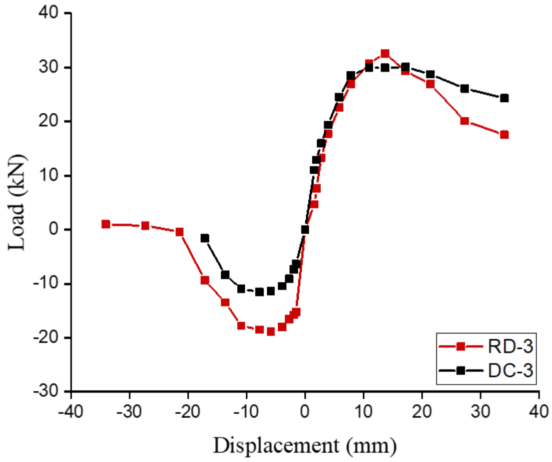

Figure 5. 21 Comparison of the Envelop curve of the RD-3 and DC-3 specimen

Figure 5.22 and Figure 5.23 show the combined load-displacement envelop curve of control and retrofitted non-seismic and seismic specimens, respectively. The retrofitted non-seismic detailed specimens when compared with the retrofitted seismic detailed specimens exhibited superior load-bearing capacity and ductility, even at the higher corrosion level. When compared to the RND-1- RND3 specimens, the RD-1-RD-3 specimens show 5%,10%, and 16.75% higher load-carrying capacity, respectively. Even though the seismic specimens had a high corrosion rate in every corrosion level when compared to non-seismic specimens, the close detailing of stirrups in seismic specimens improves bearing capacity, plastic deformation, and ductility.

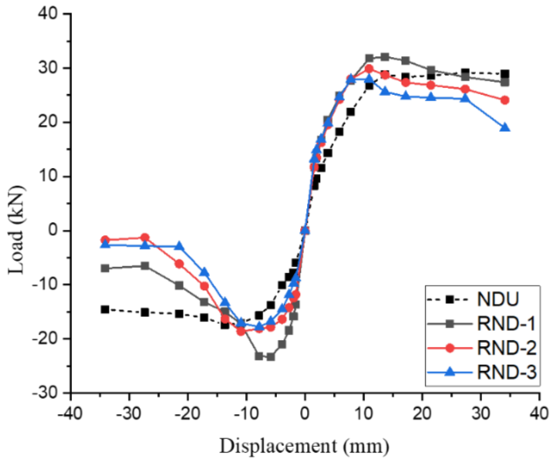

Figure 5. 22 Load-displacement envelope curve of control and retrofitted non-seismic specimens

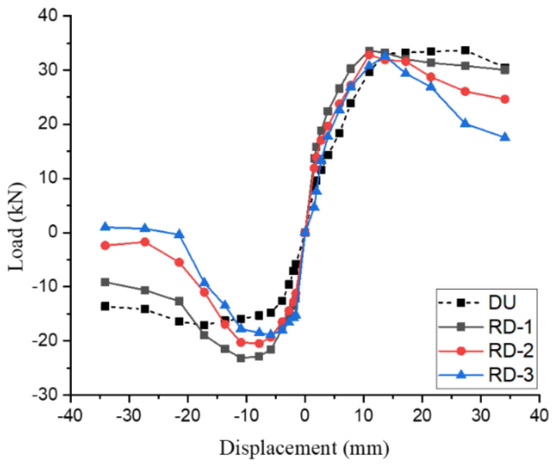

Figure 5. 23 Load-displacement envelope curve of control and retrofitted seismic specimens

To provide a better comparison of the load-carrying capacity between control and retrofitted specimens, a strength index (SF) was computed following Equation 5.1 and is also shown in Table 5.4.

$$S_F = \frac{(F_{avg})_{retrofitted}}{(F_{avg})_{control}} \qquad (5.1.)$$

Where F_{avg} represents an average of the peak load values in the negative and positive drift.

From the strength index parameter, it can be seen that the retrofitting has provided an increment in the load-carrying capacity by a factor of 1.18 and 1.11 for RND-1 and RD-1, respectively. Whereas, for the severely corrosion-damaged retrofitted specimens (i.e., RND-2, RND-3, RD-2, and RD-3), the index indicates almost the same strength approximately the same as was seen for respective control specimens

The ultimate failure for the specimen is designated at 80% of the maximum load (in the envelope curve). The procedure for the calculation of ductility has already been outlined in detail in Section 4.6 and Figure 4.21. The ductility of all the test specimens has been shown in Table 5.4. It can be observed that HSFRC retrofitting has prevented a significant drop in the ductility, even though the corrosion-damaged specimens experienced a fracture of reinforcing bars during the cyclic loading.

Table 5. 4 Test results of all specimens

Specimens	Peak				Ultimate				Strength Factor	Ductility
	Load		Displacement		Load		Displacement		(S_F)	$\Delta u/\Delta y$
	(+) (kN)	(-) (kN)	(+) (mm)	(-) (mm)	(+) (kN)	(-) (kN)	(+) (mm)	(-) (mm)	(%)	μ
NDU	29.175	17.40	25.9	12.94	23.34	13.92	34.077	27	-	5.81
RND-1	32.096	23.26	13.65	5.85	25.67	18.6	34.077	9	1.18	6.15
RND-2	29.89	18.59	10.92	10.92	23.912	14.872	22	14	1.04	5.95
RND-3	27.94	17.75	10.92	7.799	22.352	14.2	22	12	0.98	5.57
DU	33.656	17.07	27.3	17.16	26.92	13.65	34.077	33	-	6.09
RD-1	33.59	23.15	10.92	10.92	26.87	18.52	34.077	16	1.11	6.34
RD-2	32.82	20.48	10.92	7.8	26.25	16.38	24.5	13.5	1.05	6.17
RD-3	32.62	18.86	13.65	5.85	26.09	15.08	21	13	1.01	5.91

5.5 STIFFNESS DEGRADATION

The stiffness is categorized as the ability of an RC structural member to endure the deformation under the specified loading criteria. The stiffness generally deteriorates at advanced stages of cyclic loading. Post-yielding, the stiffness degradation of lower rate in the structural member leads to the lengthening of the post-elastic plateau. This allows the structure to dissipate higher energy through increased plastic deformation, thereby enhancing its seismic performance. The procedure to calculate the secant stiffness is schematically illustrated in Section 4.7 (Figure 4.30), and the corresponding formula is mentioned in Equation 4.2.

The peak-to-peak stiffness comparison with respect to the drift ratio of control and retrofitted non-seismic detailed specimens is shown in Figure 5.24. A significant improvement in the initial stiffness of retrofitted specimens was experienced when compared to the stiffness of the control specimen. An increment of approximately 78.35%, 65.59%, and 54.45% was observed in the initial stiffness of RND-1, RND-2, and RND-3 specimens when compared to that of the NDU specimen. The HSFRC provided good bond strength with the steel reinforcing bars and the steel fibers impart high crack resistance thereby improving flexural performance under cyclic loading. Though the reinforcement bars within the retrofitted specimens were corrosion damaged, the specimens exhibited higher stiffness and post-yield strength up to a certain drift ratio. From Figure 5.24, it can be observed that the specimen RND-1 shows stiffness higher than the NDU specimen up to the drift ratio of ± 2.2 % and showed a similar stiffness pattern as that of the control specimens even at the higher drift ratio. For the RND-2 and RND-3 specimens, lower stiffness values than that of control specimens were experienced after the drift of ±1.75% and ±1.4%, respectively. Due to the severely damaged longitudinal and transverse reinforcement bars, the stiffness was not recovered at the higher displacements.

Figure 5.25 shows the peak-to-peak stiffness plot with the drift ratio of control and retrofitted seismic detailed specimens. When compared to the respective control specimen, RD-1, RD-2, and RD-3 specimens showed 83.82%, 65%, and 42% higher initial stiffness. The retrofitting scheme performed remarkably well to not only recover the stiffness of corrosion-damaged specimens but also increase these values as compared to the stiffness of specimen DU up to a certain drift ratio. The stiffness value of the RD-1 specimen became lower than that of the

DU specimen only beyond the drift ratio of ± 2.75%. Similarly, for the RD-2 and RD-3 specimens, the stiffness was higher than that of control uncorroded specimen DU till the drift ratio of ± 2.2% and ± 1.75, respectively. It can be observed from the figure that the RD-1 specimen has recovered the stiffness and followed the same trend as was experienced for the control specimen at the higher drifts. Although all the retrofitted specimens (i.e., non-seismic and seismic) showed higher stiffness at the initial drifts when compared to respective control specimens, the seismic detailed retrofitted specimens recovered stiffness up to higher drifts, when compared to that of the non-seismic ones.

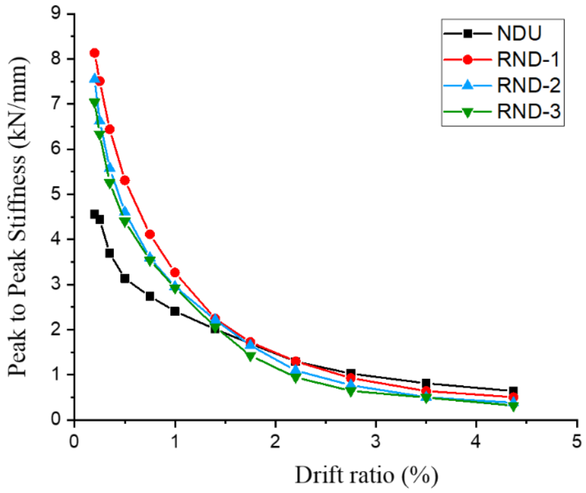

Figure 5. 24 Peak to peak Stiffness versus Drift ratio of Control and Retrofitted non-seismic specimens

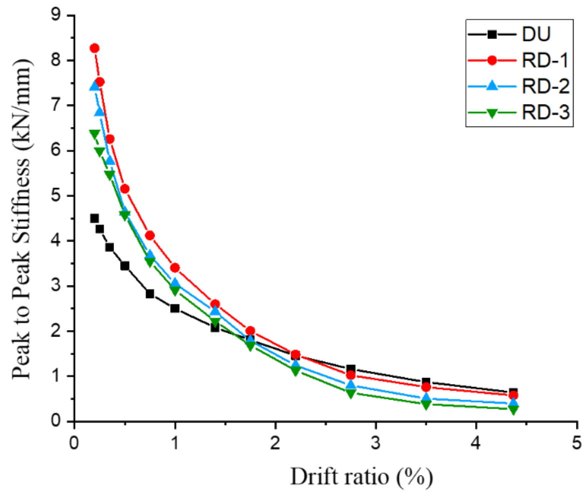

Figure 5. 25 Peak to peak Stiffness versus Drift ratio of Control and Retrofitted seismic specimens

Figure 5.26 and Figure 5.27 show the stiffness degradation curve corresponding to the drift ratio for all the non-seismic and seismic retrofitted specimens, respectively. It has been observed that the stiffness degradation rate corresponding to the successive increment in negative lateral displacement was higher than that in positive lateral displacement. This behaviour was experienced due to the fracture of corrosion-damaged stirrups and severely pitted 8 mm diameter bar in the negative displacement cycles. The damaged stirrups and longitudinal reinforcement bars exhibited inferior tensile strength resulting in brittle failure and high stiffness degradation of the specimens at higher displacement. It can be experienced that RND-1 and RD-1 specimens show negligible stiffness degradation at higher drift ratios when compared to respective control specimens. This signifies that the specimens having a corrosion rate under 10% can be fully recovered in terms of stiffness and post-yield response.

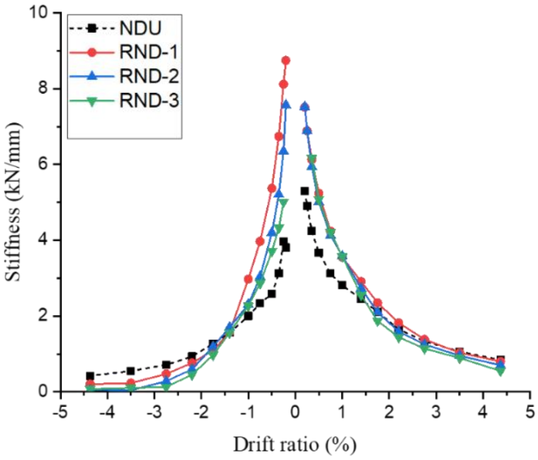

Figure 5. 26 Stiffness degradation of Control and Retrofitted non-seismic specimens

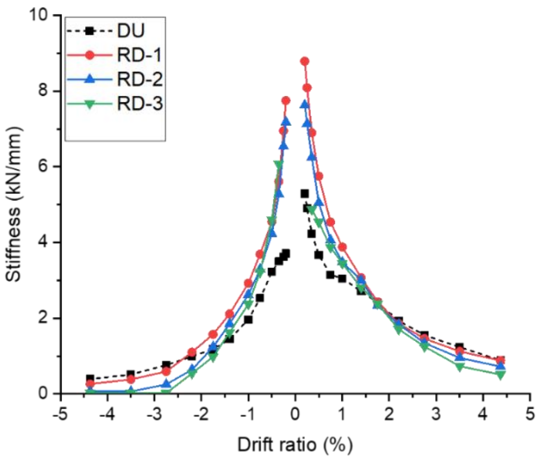

Figure 5. 27 Stiffness degradation of Control and Retrofitted seismic specimens

The RND-2, RND-3, and RD-2, RD-3 specimens show a sudden rise in stiffness degradation at a certain negative drift ratio, representing fracture in the longitudinal reinforcing bar. After the fracture of the bar, the expansion of the dominant crack width was resisted due to the presence of hybrid steel fibers, resulting in low stiffness degradation even at the ultimate drift ratio. It can be experienced that the fracture of the rebar has been delayed in the seismic specimens when compared to that of retrofitted non-seismic specimens. The RD-3 specimen showed better post-yield behaviour and a 19.13% increase in stiffness at ± 2.2% drift ratio when compared to that of the RND-3 specimen. This demonstrates the better performance of retrofitted seismic specimens even at severe corrosion levels due to confined stirrups arrangement at the joint intersection area. The stiffness degradations of all retrofitted specimens (non-seismic and seismic) were significantly improved up to a certain displacement.

5.6 ENERGY DISSIPATION

The energy dissipation capacity is defined as the ability of the RC structures to dissipate the input energy under severe loading conditions such as earthquakes. The energy dissipation of the specimen is determined by considering the enclosed region of the hysteretic loop at every cyclic displacement, as indicated in Section 4.8 (Figure 4.35). The energy dissipation of specimens can be mainly evaluated under two parameters. The first one is cumulative energy dissipation which is the summation of energy dissipation obtained under successive displacement cycles. The second one is the equivalent viscous damping ratio (ξ_{eq}), which reflects the dissipated energy of the structure under the seismic loading. The energy dissipation and damping ratio calculation model is shown in Figure 5.28.

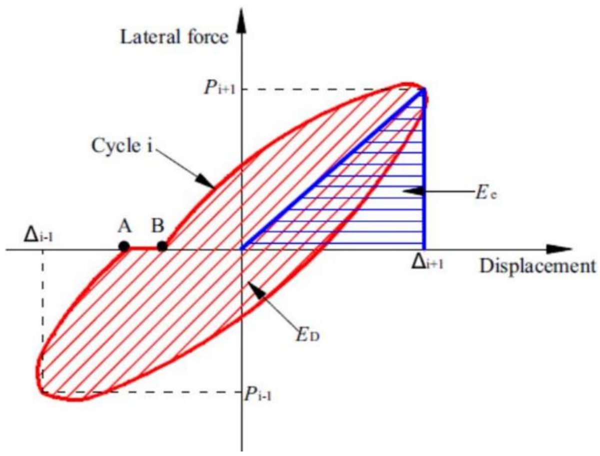

Figure 5. 28 Analytical curve representing calculation of energy dissipation and damping ratio (Liu and Li 2018)

The equivalent viscous damping ratio (ξ_{eq}) of all the test specimens is calculated by using equations 5.2 and 5.3.

$$(E_e)_i = \frac{(P_m)_i(\Delta_{max})_i}{2} \tag{5.2}$$

$$\xi_{eq} = \frac{(E_D)_i}{4\pi(E_e)_i}\ \% \tag{5.3}$$

Where,

- $(E_e)_i$ represents dissipated elastic energy
- $(P_m)_i$ is the maximum load in the cyclic loops
- $(\Delta_{max})_i$ is the maximum displacement in the cyclic loops
- $(E_D)_i$ is energy dissipation in the i^{th} cycle of hysteresis loops.

5.6.1 Comparison between control specimen and retrofitted specimens

The HSFRC retrofitting improved the lateral drift capacity even though the beam-column joint specimens were severely damaged due to corrosion. It reflects that the retrofitting strategy enables the corrosion-damaged specimens to dissipate the energy up to higher lateral drifts. Figure 5.29 and Figure 5.30 represents the plots for cumulative energy dissipation of control and retrofitted non-seismic and seismic specimens, respectively with respect to the drift ratio. The corresponding numerical values are presented in Table 5.5.

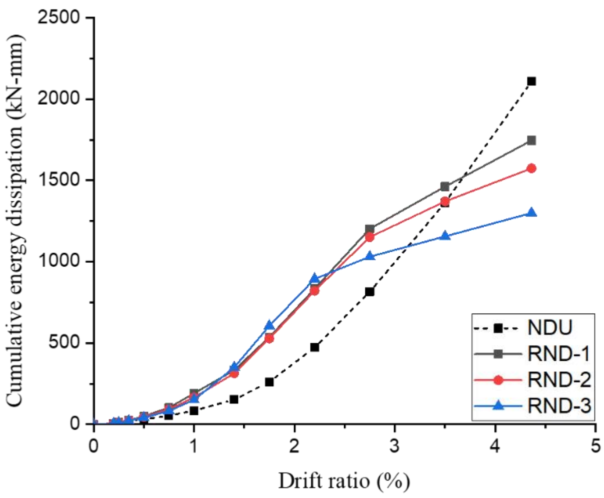

Figure 5. 29 Cumulative energy dissipation of control and retrofitted non-seismic specimens

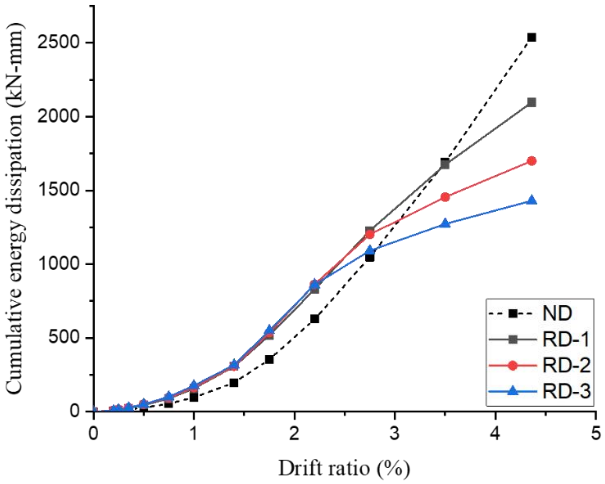

Figure 5. 30 Cumulative energy dissipation of control and retrofitted seismic specimens

Table 5. 5 Cumulative energy dissipation of control and retrofitted specimens

Sr. No	Cycle	Drift Ratio (%)	NDU (kN-mm)	DU (kN-mm)	RND-1 (kN-mm)	RND-2 (kN-mm)	RND-3 (kN-mm)	RD-1 (kN-mm)	RD-2 (kN-mm)	RD-3 (kN-mm)
1	3	0.2	4.003	3.639	4.04	4.64	4.02	4.48	8.33	6.24
2	6	0.25	8.998	8.388	10.53	10.58	9.77	10.50	14.47	12.92
3	9	0.35	17.643	15.101	23.55	22.07	20.96	23.12	27.29	26.12
4	12	0.5	30.614	26.977	49.57	43.97	40.68	45.43	50.36	50.10
5	15	0.75	53.003	53.328	101.73	91.95	82.02	88.71	94.11	100.97
6	18	1	84.161	96.626	189.97	165.17	150.85	157.27	163.93	177.02
7	21	1.4	151.33	196.73	332.46	313.38	349.6	306.96	309.15	317.33
8	24	1.75	260.94	353.90	535.94	527.98	605.34	517.69	536.15	549.85
9	27	2.2	471.62	627.62	833.35	820.85	894.10	829.61	862.98	860.33
10	30	2.75	815.86	1047.75	1202.72	1151.45	1030.83	1226.80	1201.13	1091.99
11	33	3.5	1362.90	1691.79	1462.10	1370.96	1155.77	1674.22	1454.98	1272.89
12	36	4.36	2110.35	2539.21	1745.88	1574.89	1299.24	2097.40	1700	1430.22

A significant increment in the energy dissipation during the initial drifts was experienced in retrofitted specimens when compared to control specimens, owing to the superior mechanical properties of HSFRC and the presence of hybrid steel fibers which provided a better resistance against tensile cracking. At ± 0.5% drift ratio, RND-1, RND-2, and RND-3 specimens showed approximately 100.5%, 68.77%, and 52.04% higher energy dissipation than that of the NDU specimen. For RD-1, RD-2, and RD-3 specimens, the increment in the energy dissipation at the same drift was up to 83.77% 89.9%, and 97.52% when compared to the respective DU specimen. From the figure, it can be seen that up to ± 2.75% drift, a significant increment in the cumulative energy dissipation of retrofitted specimens was experienced when compared to the control specimens. Thereafter, the curve tends to go flat due to the inferior tensile strength of corrosion-damaged reinforcing bars. As the drift progressed, a drop in the energy dissipation was experienced at a certain drift representing a fracture in the severely pitted reinforcement bar. However, when compared to the energy dissipation of retrofitted non-seismic specimens, the seismic retrofitted specimens exhibit high dissipation of energy at higher drifts, due to the close stirrups arrangement at the beam-column interface region. At the ultimate drift of ± 4.36%, the RD-1, RD-2, and RD-3 specimens show 20.13%, 8%, and 10% higher cumulative energy dissipation when compared to RND-1, RND-2, and RND-3 specimens, respectively.

As reported in several studies, the RC members having a high equivalent viscous damping ratio possess better energy dissipation capacity. Figure 5.31 and Figure 5.32 show the equivalent viscous damping ratios plotted against the drift ratio for the retrofitted non-seismic and seismic detailed specimens, respectively. A significant increase in the equivalent viscous damping ratio values of the retrofitted specimens was experienced during the early drift ratio, signifying the improved dissipation of energy. At the drift ratio of ± 0.5%, the specimens RND1-RND3 show an increment of approximately 18.24%, 14.78%, and 6.23% in the equivalent viscous damping ratio values when compared to the respective control specimen. Similarly, for RD1-RD3 specimens an increment of approximately 25%, 44.44%, and 52.22% was observed when compared to the respective control specimen. When compared to the respective control specimens, the retrofitted non-seismic and seismic specimens achieve up to 88.5% and 59.05% higher equivalent viscous damping ratio values, respectively. Thereafter, a declining trend in viscous damping ratio values was observed at higher displacement cycles.

After the drift ratio of ± 2.75%, the equivalent viscous damping values of retrofitted specimens (i.e., RND-3 and RD-3) were less than the respective control specimens, representing the non-recoverable damage at higher drifts. It was seen that the retrofitted seismic detailed specimens exhibit a high damping ratio at higher displacements when compared to that of the retrofitted non-seismic detailed specimens. At ± 3.5% drift ratio, the equivalent viscous damping ratio of RD1-RD3 specimens was 46.51%, 14%, and 90.56% higher than that of RND1-RND3 specimens, respectively. With the retrofitting using HSFRC, the concrete spalling and buckling of the corrosion-damaged reinforcing bars got delayed. This in turn improved the load-displacement behaviour and ultimately resulted in higher viscous damping ratios of retrofitted non-seismic and seismic specimens.

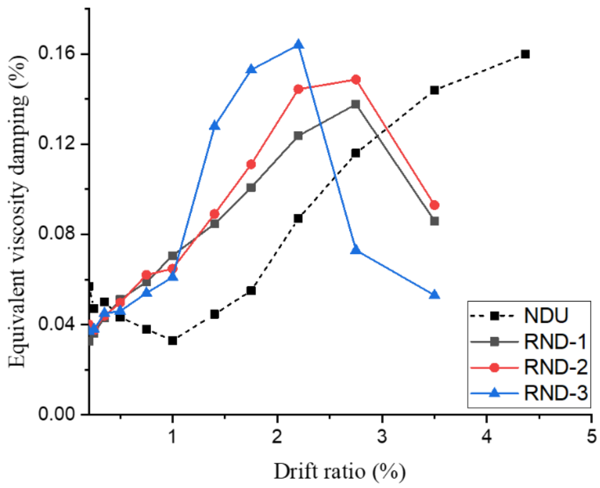

Figure 5. 31 Equivalent viscosity damping of control and retrofitted non-seismic specimens

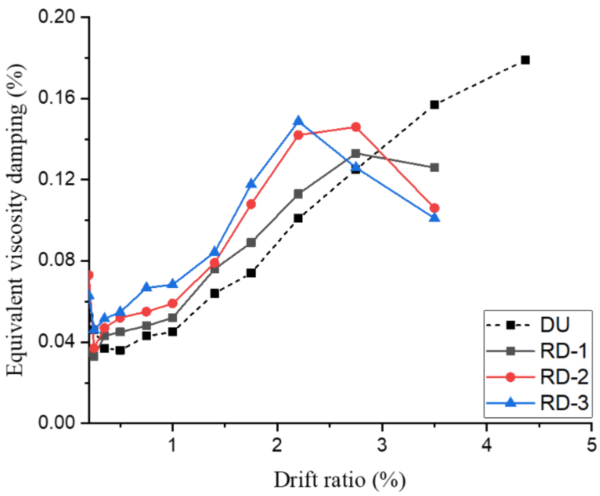

Figure 5. 32 Equivalent viscosity damping of control and retrofitted seismic specimens

5.7 DAMAGE INDEX OF CONTROL AND RETROFITTED SPECIMENS

For this study, the damage experienced by all the test specimens under the reverse cyclic loading was quantified by adopting the Park and Ang damage index (Park and Ang 1985).

The damage index (DI) represents the severity of the damage through values ranging from 0 to 1. If the damage index value is 1 or above, the entire specimen is considered to have achieved ultimate failure (completely damaged). The formula and procedure for the calculation of DI have already been discussed previously in Section 4.9 (Equation 4.3).

5.7.1 Comparison of control and retrofitted specimens

Figure 5.33 shows the damage index of control and retrofitted non-seismic specimens corresponding to the progressing displacements. The NDU specimen experienced complete failure at the drift ratio of 3.5%, as the Damage index was higher than 1 at this drift. When compared to the NDU specimen, the RND-1 specimen shows considerably less damage as the displacement progresses. The RND-1 specimen was completely damaged at the drift ratio of 4.36%, owing to the hybrid steel fibers which increased the damage resistance of the specimen. The presence of hybrid steel fibers developed the bridging effect on the high-strength concrete, which ultimately improved the tensile and flexural performance of the retrofitted specimens even at higher displacements for specimens subjected to lower corrosion rates. The RND-2 specimen showed a similar damage index as was seen for the NDU specimen. The RND-3 specimen showed a slightly higher damage index when compared to the NDU specimen. Beyond the drift ratio ± 2.75%, the RND-2 and RND-3 specimens exhibited ultimate failure. Despite the fracture of the corrosion-damaged longitudinal reinforcement bar at higher drifts, the retrofitted specimens showed considerable damage tolerance, even for the severely corroded specimen. The values of damage index for all the tested specimens corresponding to the drift are presented in Table 5.6. As compared to the NDU specimen, RND-1 and RND-2 specimens showed 22.22% and 1.23% less damage index values respectively at ± 2.75% drift ratio. The RND-3 specimen showed a similar damage index value as was experienced for the NDU specimen.

The damage index pattern observed for control and retrofitted seismic detailed specimens was similar to that noted for the non-seismic detailed specimens. Figure 5.34 illustrates the damage index of control and retrofitted seismic specimens corresponding to the drift ratio. The RD-1 specimen shows significantly lower damage index values than the DU specimen. This signifies the recovery and enhancement of the damage resistance of corrosion-damaged specimens (having a corrosion rate of less than 10%) after the application of HSFRC retrofitting. At the drift ratio of ±2.75%, the RD-1 and RD-2 specimens show 30.64%, and

8% respectively lower damage index values when compared to that of the DU specimen. However, the RD-3 specimen showed a similar damage index value as was experienced for the DU specimen. The non-seismic retrofitted specimens when compared with the seismic retrofitted specimens exhibit superior damage tolerance, even at higher drift ratios. The close stirrups arrangement at the beam-column intersection of the seismic specimens provided additional shear resistance capacity. When compared to RND-1-RND-3 specimens, the RD-1-RD-3 specimens show 13%, 8.75%, and 2% superior damaged tolerance at the drift ratio of ± 2.75%.

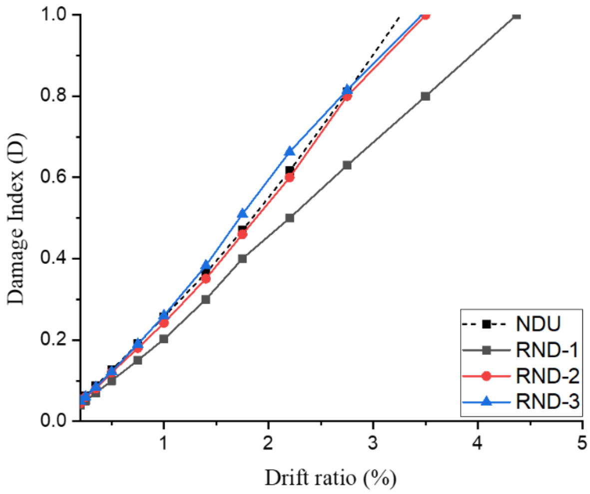

Figure 5. 33 Damage indices of all tested non-seismic specimens

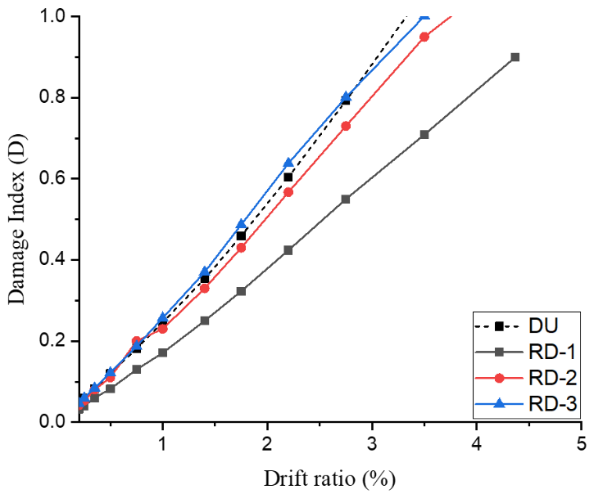

Figure 5. 34 Damage indices of all tested seismic specimens

Table 5. 6 Damage Index of Control and Retrofitted Specimens

Drift ratio	Displacement	Damage Index (D)							
		NDU	RND-1	RND-2	RND-3	DU	RD-1	RD-2	RD-3
0.2	1.56	0.049	0.040	0.044	0.050	0.047	0.032	0.042	0.046
0.25	1.95	0.062	0.050	0.060	0.060	0.059	0.040	0.053	0.059
0.35	2.73	0.087	0.070	0.080	0.084	0.083	0.060	0.008	0.084
0.5	3.9	0.126	0.100	0.120	0.122	0.120	0.082	0.110	0.122
0.75	5.85	0.191	0.150	0.180	0.190	0.182	0.130	0.200	0.187
1	7.79	0.257	0.202	0.242	0.260	0.246	0.171	0.230	0.257
1.4	10.92	0.365	0.300	0.351	0.383	0.354	0.250	0.330	0.370
1.75	13.65	0.470	0.400	0.460	0.510	0.459	0.323	0.430	0.487
2.2	17.16	0.616	0.500	0.600	0.663	0.604	0.424	0.567	0.638
2.75	21.45	0.810	0.630	0.800	0.815	0.793	0.550	0.730	0.801
3.5	27.29	1.087	0.800	1.000	1.010	1.062	0.709	0.950	1.001
4.36	34.07	1.429	1.000	1.200	1.233	1.389	0.900	1.124	1.225

5.8 JOINT STRESSES

The damage encountered by the RC structural member under seismic loading can be assessed by determining the principal tensile stresses within the joint interface. The principal tensile stress at the joint for all the test specimens has been calculated by adopting the procedure outlined in Section 4.10 (using equations 4.4-4.6).

5.8.1 Comparison of Control and Retrofitted Specimens

The principal tensile stress of control unretrofitted and retrofitted non-seismic specimens is shown in Figure 5.35. The maximum principal tensile resistance capacity in the NDU specimens was 6.62 MPa and 4.67 MPa at the drift ratio of 3.5% and 1.75% at the positive and negative displacement, respectively. The maximum improvement of the principal tensile capacity of the RND-1 specimen during positive and negative drift was approximately 1.1 times and 1.2 times over the NDU specimen. Similarly, for the RND-2 and RND-3 specimens that had severely damaged reinforcement bars, the principal tensile resistance capacity was recovered when compared to the respective control specimen up to a certain drift. The retrofitted specimens experience improved initial principal tensile stress-carrying capacity, owing to the presence of hybrid steel fibers. However, at higher drifts, due to the fracture of severely pitted rebars and shattering of concrete-fiber bond, a rapid degradation in tensile stress carrying capacity was experienced.

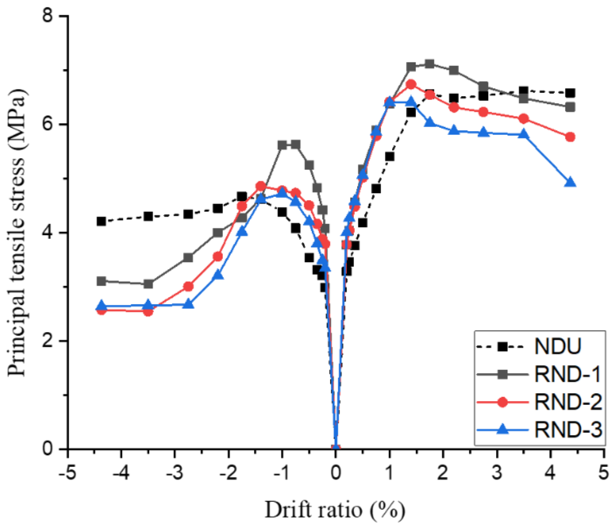

Figure 5. 35 Principal tensile stress of control and retrofitted non-seismic specimens

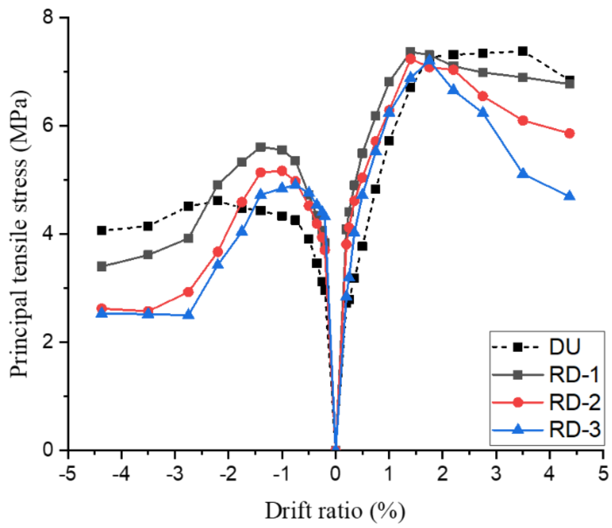

Figure 5. 36 Principal tensile stress of control and retrofitted seismic specimens

Figure 5.36 shows the principal tensile stress plot of control unretrofitted and retrofitted seismic specimens against the drift ratio. For the DU specimen, the maximum principal tensile resistance capacity was 4.62 MPa and 7.38 MPa at 2.2% and 3.5% drift ratio, at the negative and positive displacement, respectively. When compared to the DU specimen, the RD-1 specimen shows up to 1.22 times improvement in the maximum principal tensile stress carrying capacity. Similarly, the RD-2 specimen shows 1.12 times higher principal tensile resisting capacity in the negative drift when compared to the control unretrofitted specimen. The RD-3 specimens showed approximately similar maximum tensile stress resistance up to a certain drift as was experienced for DU specimens, signifying the recovery of tensile stress even for the severely corrosion-damaged specimens.

Table 5.7 shows the principal tensile stress for all control and retrofitted specimens. The retrofitted seismic specimens show superior tensile stress resistance capacity than the retrofitted non-seismic specimens, at all the drift levels. The close arrangements of stirrups allow the seismic specimens to bear tensile stress even for the severely corroded specimens and at the higher drifts when compared to retrofitted non-seismic specimens. The RD-3 specimen shows up to 12.34% higher tensile stress-resisting capacity (maximum) with respect to the maximum stress for the RND-3 specimen.

Table 5. 7 Principal Tensile Stress of Control and Retrofitted specimens

Drift Ratio (%)	NDU (MPa)	RND-1 (MPa)	RND-2 (MPa)	RND-3 (MPa)	DU (MPa)	RD-1 (MPa)	RD-2 (MPa)	RD-3 (MPa)
4.36	6.58	6.32	5.77	4.92	6.84	6.77	5.86	4.69
3.5	6.62	6.48	6.11	5.81	7.38	6.89	6.1	5.11
2.75	6.53	6.70	6.23	5.84	7.34	6.98	6.55	6.24
2.2	6.48	6.99	6.31	5.88	7.31	7.10	7.03	6.65
1.75	6.56	7.11	6.54	6.02	7.27	7.31	7.08	7.20
1.4	6.22	7.06	6.74	6.41	6.70	7.37	7.24	6.88
1	5.41	6.38	6.42	6.40	5.73	6.81	6.29	6.24
0.75	4.81	5.89	5.78	5.86	4.82	6.18	5.71	5.52
0.5	4.18	5.16	5.01	5.06	3.77	5.49	5.04	4.72
0.35	3.76	4.56	4.48	4.58	3.18	4.90	4.61	4.02
0.25	3.46	4.04	4.04	4.27	2.79	4.41	4.11	3.20
0.2	3.28	3.78	3.78	4.01	2.72	4.08	3.80	2.84
0	0	0	0	0	0	0	0	0
-0.2	2.98	4.07	3.79	3.35	2.96	3.83	3.70	4.32
-0.25	3.21	4.42	3.88	3.49	3.12	4.06	3.94	4.40
-0.35	3.32	4.83	4.16	3.79	3.46	4.34	4.19	4.53
-0.5	3.54	5.25	4.50	4.20	3.91	4.72	4.52	4.76
-0.75	4.08	5.63	4.73	4.56	4.25	5.35	4.97	4.90
-1	4.38	5.62	4.78	4.72	4.33	5.55	5.17	4.84

-1.4	4.61	4.63	4.86	4.61	4.43	5.61	5.13	4.72
-1.75	4.67	4.28	4.49	4.01	4.48	5.33	4.59	4.04
-2.2	4.45	4.00	3.56	3.21	4.61	4.91	3.67	3.42
-2.75	4.34	3.54	3.00	2.67	4.51	3.92	2.93	2.50
-3.5	4.3	3.05	2.54	2.66	4.15	3.61	2.57	2.52
-4.36	4.21	3.11	2.57	2.64	4.06	3.40	2.62	2.53

5.9 CORROSION MONITORING OF THE RETROFITTED SPECIMENS

Detection of the probability of corrosion within RC structures is of prime concern to adequately plan the maintenance and replacement of damaged concrete structures (Berger et al. 2011; Beck et al. 2012; Verma et al. 2014). Half-cell potential (HCP) mapping, a standardized non-destructive technique is primarily the most widely adopted method for steel corrosion monitoring in RC structures (Elsener 2001; Elsener et al. 2003; González et al. 2004; Song and Saraswathy 2007; Structures 2008; Pradhan et al. 2009; ASTM C876 2015; Jung et al. 2019; Adriman et al. 2022; Almashakbeh et al. 2022; Kumar Tiwari et al. 2023). This method is performed and interpreted following the guidelines of (Conshohocken 2009; ASTM C876 2015). In this method, the measurement of the potential difference between an external electrode placed at the concrete surface and the embedded steel reinforcement was done with the help of high-impedance voltmeter. An accurate test setup including proper electrical connectivity between reinforcing bars and voltmeter and also a wet surface between the concrete surface and external electrode is essential for determining reliable results (Pour-ghaz et al. 2010; Sadowski 2013). A schematic representation of the test setup of Half-cell potential is shown in Figure 5.37.

In this study, the half-cell potential mapping was done for the retrofitted specimen to monitor and determine the potential values. Firstly, the potential values of the corroded specimen (before the treatment of reinforcement bars) were measured. Thereafter, the retrofitting scheme adopted in this study was applied to the corrosion-damaged specimen, and the damaged concrete was entirely replaced from the target repair region with HSFRC. Moreover, the corroded reinforcing bars were cleaned and treated with anti-corrosion agents. Thereafter, the continuous monitoring of the potential values was undertaken for the next 4 months (with a periodic 1-month interval). The test setup for the half-cell potential test is shown in Figure 5.38. Table 5.8 illustrates the reference potential values as per ASTM C876 for categorizing the probability of corrosion in the specimen.

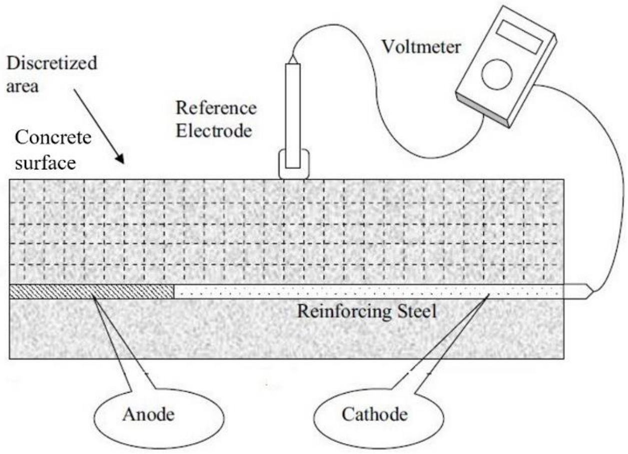

Figure 5. 37 Schematic illustration of the test setup of half-cell potential measurement (Pourghaz et al. 2010).

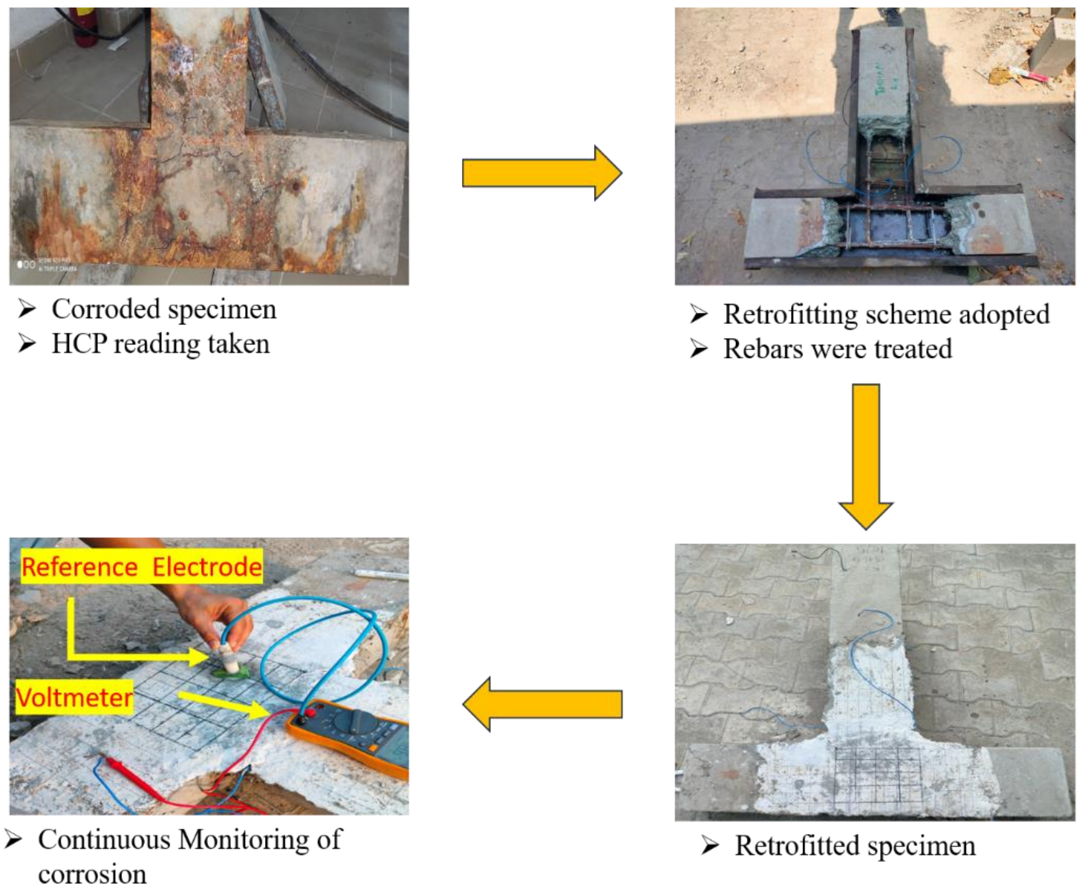

Figure 5. 38 Half-cell potential test setup

Table 5. 8 Dependence between potential and corrosion probability (ASTM C876 2015)

No.	Potential E_{corr}, mV Reference electrode Cu/$CuSo_4$	Probability of Corrosion
1	< -426 mV	Severe Corrosion
2	< -276 mV	High risk, 90% probability of corrosion
3	-126 mV to -275 mV	Intermediate risk, uncertain corrosion
4	0 mV to -125 mV	Low risk, 10% probability of corrosion

Figure 5.39 shows the half-cell potential (HCP) measurements for the time period of 4 months plotted on a contour map for visual interpretation. From the table and the figure, it can be seen that after the corrosion exposure and before the treatment of reinforcing bars, the HCP was in the range of 407-477 mV_{sce}, indicating a severe corrosion probability. After cleaning and treating corroded reinforcement bars with an anti-corrosive agent and replacing damaged concrete with HSFRC, the potential was noted again. After 1 month of reinforcing bars treatment and retrofitting, the HCP were in the range of 277-315 mV_{sce} indicating high corrosion risk. After 60 days (2 months) of retrofitting, the potential values dropped at the range of 97-133 mV_{sce} and thereafter maintained a constant potential range of 70-140 mV_{sce} indicating low corrosion risk for the following next 2 months, as can be seen in Figure 5.39. This indicates the suitability of the adopted retrofitting scheme in removing corrosion from the structure and reducing the probability of recurrence of the same at later stages.

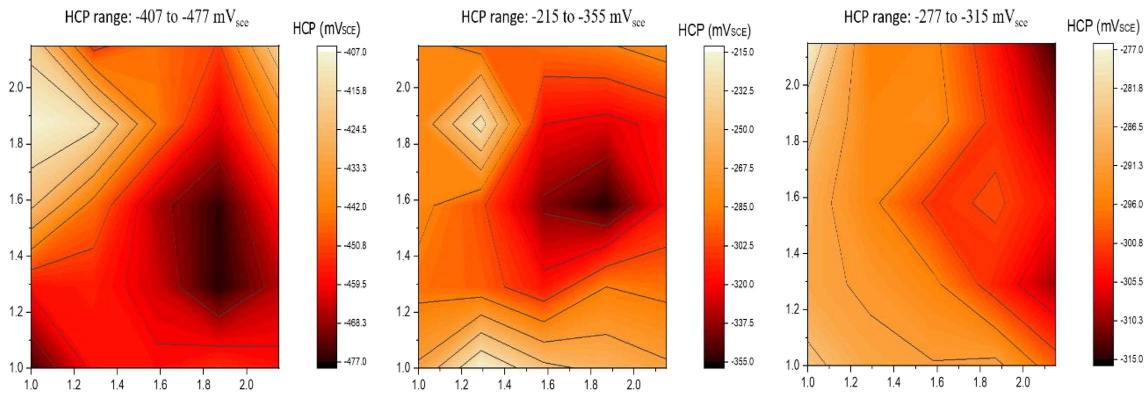

Corrosion-damaged rebars/Before treatment After 7 days of rebars treatment/retrofitting After 1 month of rebars treatment/retrofitting

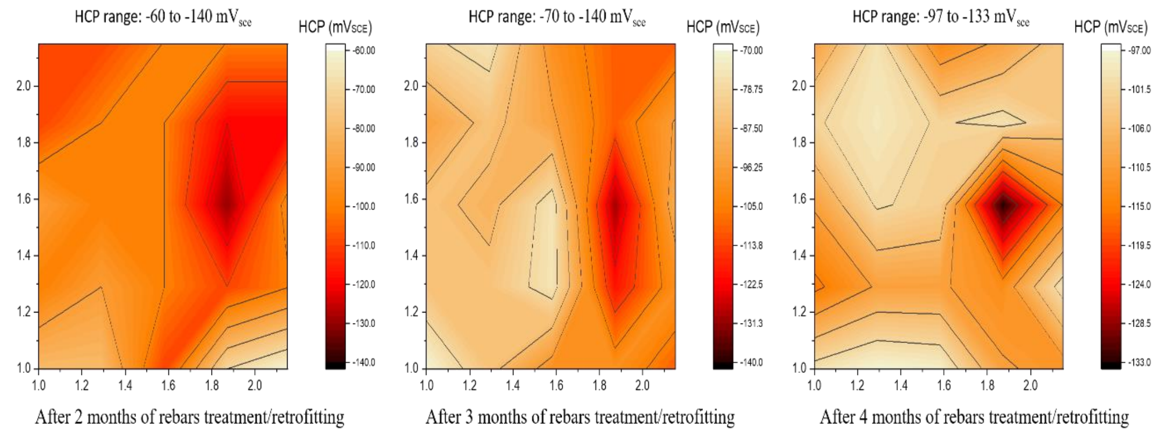

Figure 5. 39 Contour plot of potential E_{corr}.

5.10 CLOSING REMARKS

This chapter presents an insight into the effectiveness of the HSFRC retrofitting scheme as a seismic performance improvement strategy for rehabilitated RC structures. The seismic parameters indicate the improved performance of corrosion-damaged specimens when compared to respective control uncorroded specimens, especially for low and moderate corrosion rates even at high cyclic drift. The retrofitted specimen was continuously monitored for the corrosion probability in the time frame of 4 months with the help of the Half-cell potential method, which indicated significantly lowered chances of recurrence of corrosion within the specimens.

CHAPTER 6

NON-LINEAR FINITE ELEMENT ANALYSIS

6.1 GENERAL

This chapter presents a 3D non-linear finite element analysis (FEA) of the seismic behaviour of the corrosion-damaged RC exterior BCJ. The general-purpose FE software ABAQUS was used to validate the experimental results presented in Chapter 4. The corrosion-induced damage in the Exterior BCJs was modeled by considering an equivalent reduction in the cross-section of reinforcement and simultaneously modifying the properties of both concrete and steel by reducing their strength. The reinforcement detailing, geometry, and different levels of corrosion for non-seismically and seismically detailed BCJs were assumed in agreement with the experimental methodology mentioned in Chapter 3. Table 6.1 shows the description and identification of control and different levels of corroded non-seismically detailed and seismically detailed specimens. The performance of the corrosion-damaged BCJ specimens was numerically assessed by analyzing the load-displacement curves, post-peak response, and the damage progression leading to ultimate failure.

Table 6. 1 Identification of control and corroded specimens

S.No	Specimen		Identification
	Description	Corrosion level	
1	Non-Seismically	Uncorroded	NDU-N
2	detailed	1st	NDCL1-N
3		2nd	NDCL2-N
4		3rd	NDCL3-N
5	Seismically	Uncorroded	DU-N
6	detailed	1st	DCL1-N
7		2nd	DCL2-N
8		3rd	DCL3-N

6.2 MODELING OF CONCRETE

6.2.1 Constitutive Modeling

In ABAQUS, the behaviour of plain concrete under varying conditions of loading can be described by several constitutive models such as the Brittle cracking model, Smeared crack model, and Concrete damage plasticity (CDP) model. The brittle crack model is adopted to simulate the concrete when it is possible to assume that the compressive response will stay elastic and that tensile cracking is the only cause of material nonlinearity. The smeared crack model is used when the response of unreinforced and reinforced concrete is simulated under pressure of low-confinement subjected to monotonic loading. The CDP model is capable of capturing and modeling the non-linear behaviour of materials of quasi-brittle nature, both in compression and tension appropriately (Najafgholipour et al. 2017; Behnam et al. 2018; Bahraq et al. 2019). Furthermore, the CDP model provides effectiveness in analyzing concrete structures under dynamic, cyclic, and monotonic loading (Najafgholipour et al. 2017; Behnam et al. 2018), therefore is adopted for this study. The CDP model used in ABAQUS has presented the modeling of the nonlinear behaviour and post-peak behaviour of concrete with better accuracy when compared to experimental test results (Abdelatif et al. 2015; Genikomsou and Polak 2015; Wosatko et al. 2015). A CDP model needs a number of input parameters as shown in Table 6.2, in order to generalize the uniaxial stress-strain properties of concrete to the three-dimensional stress space. These are listed below:

- Stress-strain values when the concrete is subjected to compression and tension
- The dilation angle that determines the plastic flow direction through the incremental plastic strain vector (ψ)
- The flow potential eccentricity (default value = 0.1)
- The ratio of initial equibiaxial compressive yield stress to initial uniaxial compressive stress (fb_o/fc_o). According to Lubliner et al. (Lubliner et al. 1989), the value ranges between 1.10 to 1.16. The default value in ABAQUS is 1.16.
- The viscosity parameter (μ)
- The ratio of the second stress invariant on the tensile meridian to that on the compressive meridian at the initial yield for any given value of pressure invariant such that the maximum principal stress is negative (k). The value ranges between 0.5 and 1. In ABAQUS, the default value of k is 0.667.

Table 6. 2 Concrete damage plasticity parameters for normal strength concrete

Material	Dilation Angle	Eccentricity	fb_o/fc_o	k	Viscosity Parameter
Normal concrete	35°	0.1	1.16	0.667	0.007985

6.2.2 Modeling Corrosion effects

The FE models were provided with the actual corrosion rates obtained from the experimental study as reported in Chapter 4, for simulating effects of corrosion. The properties such as different percentages of corrosion rate and stress-strain data for different diameters of reinforcing bars having different corrosion rates were adopted. An overview of corrosion effects accounted for Non-linear FE analysis is shown in Figure 6.1.

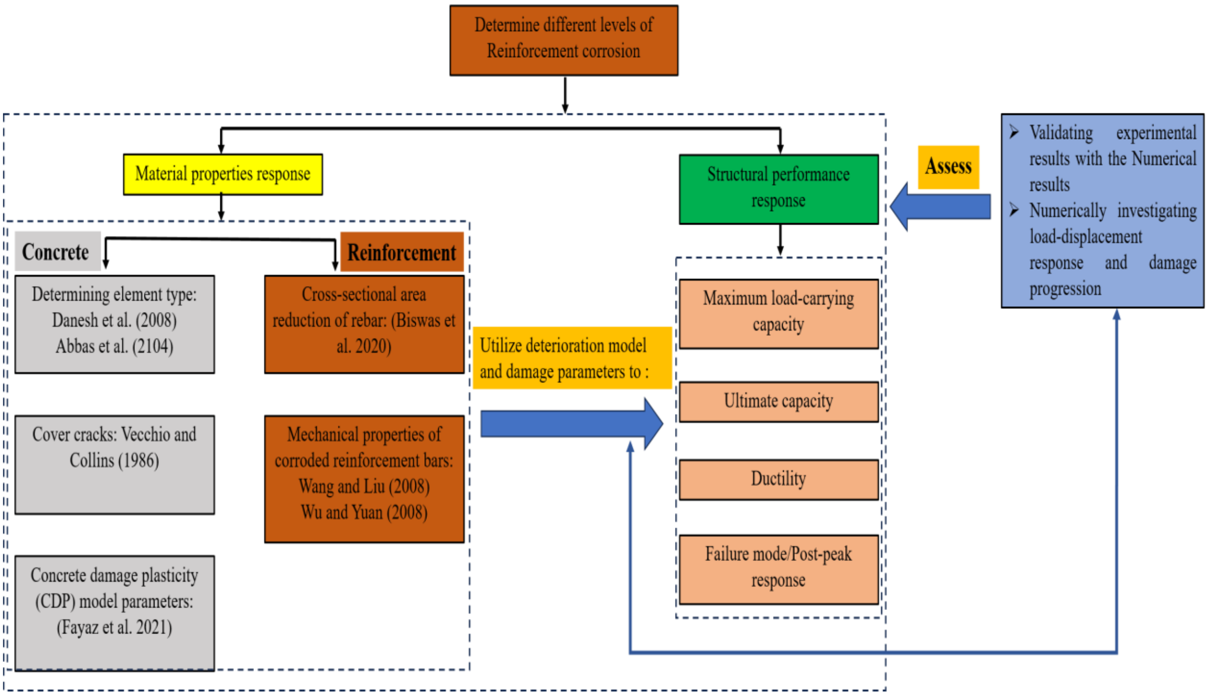

Figure 6. 1 Flow chart presenting the steel corrosion effects on both steel and concrete materials

6.2.2.1 *Concrete in Compression*

The behaviour of concrete in compression was simulated according to the model proposed by Mander JB, Priestley MJN 1989 with the parameters defined according to the experimental results (Dangwal and Singh 2023). The input values for the parameters like modulus of elasticity, peak strength, Poisson ratio, etc. have been reported in Table 6.3.

Due to the rust deposition over the bar surface at the concrete-reinforcing bar interface in RC components during the corrosion process, additional tensile stresses are generated on the concrete region. This gives rise to spalling and cracking of concrete cover resulting in the loss of strength. Capozucca and Cerri 2003 proposed a modified law for considering corrosion damage in the compressive zone of RC beams. However, this law was limited to microcracked concrete and not suitable for concrete having significant corrosion damage. As suggested by D. Coronelli and P. Gambarova 2004, the cracking and spalling of the concrete due to corrosion damage can be reflected by reducing the strength of the concrete cover. Several numerical studies have adopted the reduction in the strength of concrete cover to replicate the damage due to spalling and cracking in the concrete due to corrosion (D. Coronelli and P. Gambarova 2004; Zhao et al. 2018; Liu et al. 2021b; Van Nguyen et al. 2022). A reduced value of compressive strength of the corroded elements (f_c^{cor}) was adopted as shown in Figure 6.2 (a); this was calculated in accordance with the relationship proposed by D. Coronelli and P. Gambarova 2004, as shown in equation 6.1 below:

$$f_c^{cor} = \frac{1}{1+k\frac{\varepsilon_1}{\varepsilon_{co}}} f_c' \tag{6.1}$$

where

- f_c^{cor} represents the compressive strength of corrosion-damaged concrete,
- f_c' represents the compressive strength of undamaged and uncorroded concrete,
- k is the coefficient related to bar roughness and diameter (for medium diameter ribbed bars, k=0.1), as suggested by Capé 1999
- ε_{co} is strain corresponding to peak compressive stress f_c'
- ε_1 represents average tensile strain perpendicular to the direction of the applied compression, in the cracked concrete.

$$\varepsilon_1 = (b_f - b_o)/b_o \tag{6.2}$$

$$b_f - b_o = n_{bars}\, w_{cr} \tag{6.3}$$

$$w_{cr} = \Sigma_i u_{i\,corr} = 2\pi.(V_{rs}-1)X \tag{6.4}$$

Where

- b_f represents beam width increased by cracking due to corrosion
- b_o represents section width in the original state
- n_{bars} represents compression bar in numbers (top layer)
- w_{cr} represents the total crack width associated with a corrosion level X
- $u_{i\,corr}$ represents each corrosion crack opening
- V_{rs} represents the ratio of oxides volumetric expansion to the original material (V_{rs}=2, (Molina et al. 1993))
- X represents the corrosion attack depth

6.2.2.2 *Concrete in Tension*

The tensile behaviour of concrete (Figure 6.2. (b)) is modeled through the softening function proposed by Cornelissen et al. 1986; Hordijk DA. 1991. The tensile peak strength from the experimental data (Split tensile test performed in the laboratory; refer Table 6.3) is taken as 2.5 MPa. To acquire accuracy in the simulation results, the deterioration parameters also play a significant role. Therefore, the concrete damage parameters under compression and tension (d_c and d_t) were adopted using equations 6.5 and 6.6, proposed by Birtel and Mark 2006.

$$d_c = 1 - \frac{\sigma_c E_c^{-1}}{\varepsilon_c^{PL}\left(\frac{1}{b_c}-1\right)+\sigma_c E_c^{-1}} \tag{6.5}$$

$$d_t = 1 - \frac{\sigma_t E_c^{-1}}{\varepsilon_t^{PL}\left(\frac{1}{b_t}-1\right)+\sigma_t E_c^{-1}} \tag{6.6}$$

where

- σ_c = compressive stress
- σ_t = tensile stress
- ε_c^{PL} = plastic compressive strain
- ε_t^{PL} = plastic tensile strain
- E_c = initial elastic modulus
- b_c = scaling factor between inelastic strain and plastic strain, in compression

constant range $0 < b_c < 1$

- b_t = scaling factor between inelastic strain and plastic strain, in tension

  constant range $0 < b_t < 1$

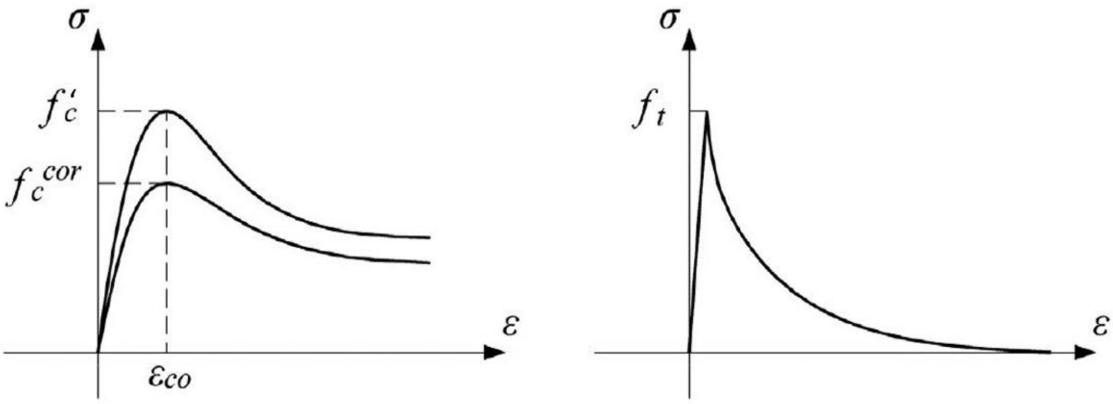

(a) (b)

Figure 6. 2 Concrete constitutive relationship in (a) Compression and (b) Tension

Table 6. 3 Properties of nominal concrete

Properties	Normal concrete
Modulus of elasticity (GPa)	23
Poisson ratio	0.2
Specific weight (kg/m^3)	2400
Compressive strength (MPa)	24
Split tensile strength (MPa)	2.5

6.2.3 Element type

The element library of ABAQUS has first-order and modified second-order interpolation elements in 2 or 3 dimensions. The quadrilateral and triangular linear elements are available in 2D whereas, triangular prism, tetrahedral, and hexahedral linear elements are available in 3D. The hexahedral elements with reduced integration (8-node linear brick element C3D8R) (Gebreyohaness 2013; Ridwan 2016) were used to model the concrete since they provide the best results for the minimum computational cost in three-dimensional analysis and have higher converging capabilities owing to the increased node count (Puso and Solberg 2006). The C3D8R geometry represents eight nodes, having three degrees (translational) of freedom per node, allowing for trilinear stress variations, as shown in Figure 6.3. This element type has also been successfully implemented in modeling the concrete beam-column junction subjected to reverse cyclic loading (Danesh, F., Esmaeeli, E. and Alam 2008; Abbas et al. 2014). The concrete BCJ model is displayed in Figure 6.6.

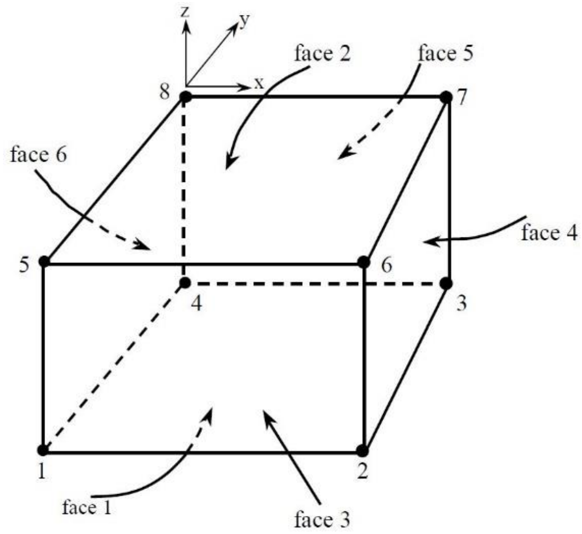

Figure 6. 3 Brick element (Eight-node) (Ridwan 2016)

6.3 MODELING OF REINFORCEMENT BARS

6.3.1 Constitutive Modeling and Corrosion Effects

The material reaction of steel reinforcement beyond its yield point was described by the von Mises yield criterion combined with the isotropic hardening response (Ridwan 2016). A linear elastic nature of the steel was assumed up to the yield having a Young's modulus of approximately 200 GPa and a poissons ratio of 0.28. The properties of steel reinforcing bars of 8 mm, 10 mm, and 12 mm diameter bars were defined from the tensile testing stress-strain data and are presented in Table 6.4. Following tensile testing, the stress-strain data were transformed into a true stress-logarithmic plastic strain format and entered into ABAQUS using equations 6.6 and 6.7 (Thaker 2016).

$$\sigma_{true} = \sigma_{nom} (1+ \varepsilon_{nom}) \quad (6.6)$$

$$\varepsilon_{true} = \ln (1+ \varepsilon_{nom}) - \frac{\sigma_{true}}{E} \quad (6.7)$$

Where

- σ_{true} and ε_{true} represent respective true stress and true strain
- σ_{nom} and ε_{nom} represent respective nominal stress and strain
- E represents the modulus of elasticity

Table 6. 4 Mechanical properties of steel reinforcing bars

Properties	Reinforcing Steel			
	Longitudinal reinforcement			Shear reinforcement
Bar diameter (mm)	8	10	12	8
Modulus of elasticity (GPa)	195.0	191.0	200.0	195.0
Poisson ratio	0.28	0.28	0.28	0.28
Specific weight (kg/m^3)	7850	7850	7850	7850
Yield strength (MPa)	640.96	691.97	528.59	640.96
Ultimate tensile strength (MPa)	715.91	784.85	621.11	715.91

In the current experimental study, the corrosion damage was targeted at the joint region. From the visual examination, it was experienced that the damage due to corrosion extended up to an approximate length of 550 mm in the beam and column direction from the beam-column junction, as displayed in Figure 6.4. Therefore, replicating experimental conditions, non-uniform corrosion was modeled by merging two steel bars of different lengths (i.e., 550 mm length + remaining length as per specifications). The highlighted bar length (red colour) shown in Figure 6.5 represents the non-uniform corroded region. In the literature, the corrosion effect on the reinforcement has been modeled by reducing the cross-section area of rebars and simultaneously modifying the mechanical properties of corrosion-damaged reinforcement bars (Du et al. 2005; Zhang et al. 2012; Finozzi et al. 2018; Imperatore and Rinaldi 2019; Zeng et al. 2020; Van Nguyen et al. 2022). For different corrosion rates, the cross-sectional area reduction and modified stress-strain properties were adopted for the highlighted length only. For uncorroded specimens, the entire reinforcing bar length was modeled using the original area of cross-section and tensile properties of steel bars as mentioned in Table 6.4. In this numerical simulation, the cross-sectional area reduction of the corroded reinforcing bars was adopted by following Equation 6.8 (Biswas et al. 2020; Liu et al. 2021b).

$$A_s(X_{CR}) = \frac{\pi D^2}{4}\left(1 - \frac{X_{CR}}{100}\right) \tag{6.8}$$

$$X_{CR} = \frac{w_0 - w_c}{w_0} * 100 \tag{6.9}$$

Where

- D represents the reinforcement bar diameter
- w_o and w_c represent the weight of uncorroded and corroded reinforcements from the experimental data (Dangwal and Singh 2023)
- X_{CR} represents the corrosion ratio from the experimental data (Dangwal and Singh 2023)

The values of w_o, w_c and X_{CR} are adopted as per the data presented in Chapter 4 (Table 4.1). The mechanical properties like yield strength, elastic modulus, ultimate strain, and ultimate strength show a decline as the corrosion percentage increases as per Equations 6.10-6.13 proposed by Wang and Liu 2008; Wu and Yuan 2008.

$$f_y^c = (1\text{- } 0.00198\ X_{CR}) f_y \tag{6.10}$$

$$E_s^c = (1\text{-}0.00113\ X_{CR}) E_s \tag{6.11}$$

$$f_u^c = (1\text{-}0.0019\ X_{CR}) f_u \tag{6.12}$$

$$\mathcal{E}_u^c = (1\text{- } 0.021\ X_{CR}) \mathcal{E}_u \tag{6.13}$$

Where

- f_y represents the nominal yield strength and f_u represents the ultimate strength of uncorroded reinforcing bars
- f_y^c represents the nominal yield strength and f_u^c represents the ultimate strength after the corrosion damage

- E_s and E_s^c represent the nominal elastic modulus of uncorroded and corrosion damage reinforcing bars, respectively
- $\mathcal{E}_{u,}$ and $\mathcal{E}_u^c$ represent the nominal ultimate strain of uncorroded and corrosion-damaged reinforcement bars, respectively.

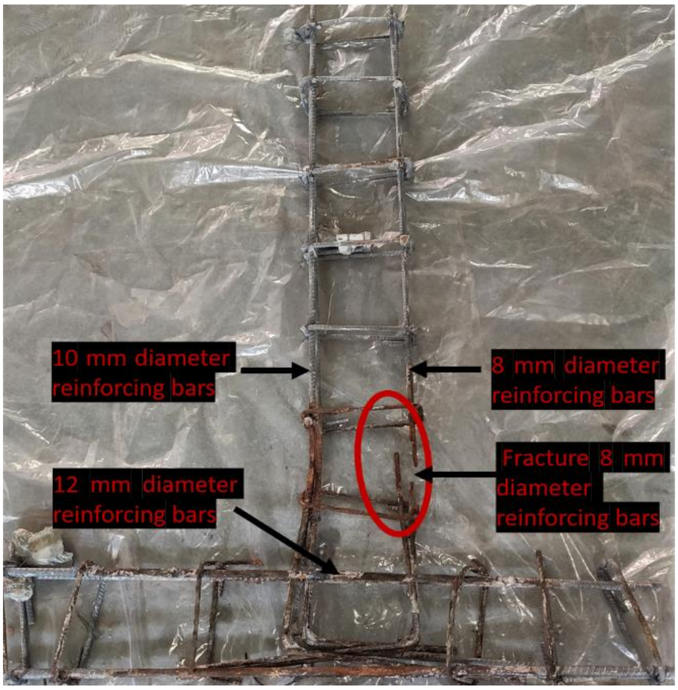

Figure 6. 4 Target corrosion affected length at the reinforcing bars surface (Dangwal and Singh 2023)

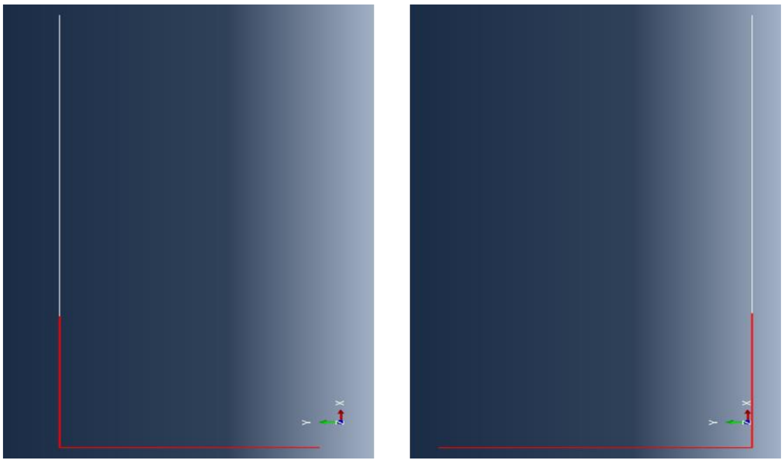

(a) (b)

(c)

Figure 6. 5 Schematic configuration of corrosion site (part in red) on the surface of reinforcing bars of (a) 8 mm (b) 10mm and (c) 12 mm diameter

6.3.2 Element Type

In ABAQUS, several element types are available that can be employed to model steel reinforcement bars such as beam elements (i.e., linear (B31), and quadratic (B32)), and truss elements (T3D2). Gebreyohaness 2013 performed a series of analyses to compare the suitability of both element types to model reinforcement bars. It was reported that the result accuracy was not affected significantly by using either of the elements. However, a higher computational cost and model run-time were associated with the usage of beam elements when compared to that of the truss elements. The beam element showed over-prediction of strength degradation and post-peak stiffness when compared with the truss element response (Ridwan 2016). Hence, a three-dimensional truss element with two nodes (T3D2) was used in modeling the longitudinal and transverse reinforcing bars throughout this numerical study. The embedded reinforcement bars for non-seismically detailed and seismically detailed BCJ specimens are shown in Figure 6.7 (a) and (b).

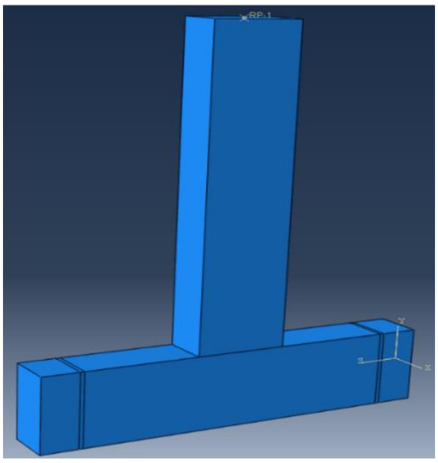

Figure 6. 6 Geometric model of test specimen

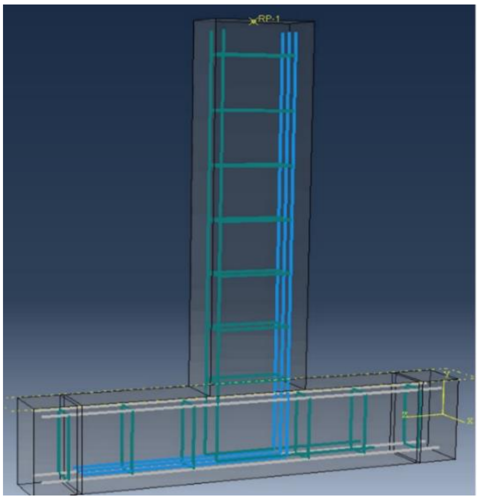

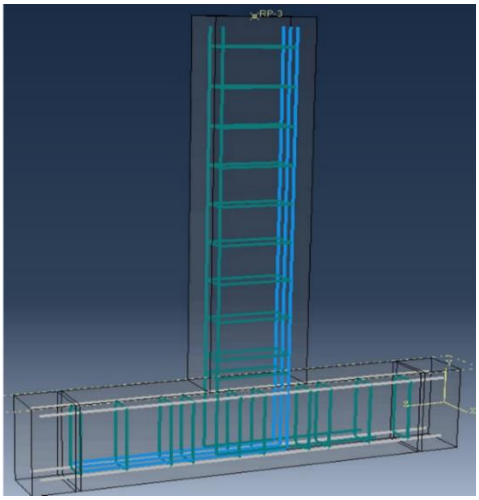

(a) (b)

Figure 6. 7 Embedded reinforcement bars for (a) non-seismically detailed and (b) seismically detailed BCJ specimens

6.4 CONSTRAINTS, BOUNDARY CONDITIONS, AND LOADING

The constraint feature present in the interaction module defines and signifies the restrictions on the degree of freedom. The degree of freedom between regions of a model can be constrained, suppressed, or resumed to vary the analysis. There are various types of constraints available in the interaction module and can be applied as per the model analysis requirement.

An EMBEDDED REGION constraint was provided in the proposed model to embed the reinforcing bars cage within the concrete BCJ model. The embedded element technique generally specifies an element or group of elements located within a host element, the response of which will be utilized to constrain the translational degree of freedom of the embedded nodes. The reinforcement cage was assigned as the embedded region and the concrete BCJ model was assigned as the host region, as shown in Figure 6.8. Another constraint was provided at the top of the beam surface as a Tie constraint. A tie constraint is applied to restrain the relative motion between two separate surfaces even though both surfaces have different meshes applied over them. A reference point “R1” to which the displacement cycles were appointed was selected as the master surface while the top surface of the beam was selected as the slave surface, as can be seen in Figure 6.9.

The boundary conditions and loading conditions assigned to the numerical model were identical to those adopted for the experimental study. Both the column ends were fixed by providing ENCASTRE boundary conditions, constraining all the active structural degrees of freedom. The axial load of $0.1A_gf_c$ was applied at a uniform rate on one side of the column replicating the gravity loading, as was provided in the experimental study keeping the other end of the column fixed (Kaviani et al. 2021; Fayaz et al. 2022).

The analysis of the numerical model continued up to the maximum displacement of 34 mm, similar to the experimental study, and was assigned at the reference point “R1, as shown in Figure 6.9. A complete displacement cycle comprises two halves (i.e., positive and negative), adopted as per the guidelines of the American Concrete Institute (ACI 374.1-05 2005). The total duration for the numerical simulation can be defined by the parameter “Step Time”. In the present experimental study, a displacement-controlled loading was applied with a frequency of 0.2 cycles/sec (f = 0.2). Therefore, all the specimens in FE modeling were tested at this frequency only, and based on this step time was finalized. The maximum displacement of 34 mm was divided into twelve intervals, each having four cycles (three large and one small). Thus, a total of 48 cycles were generated, each having a 5 seconds time interval, resulting in a total step time of 240 seconds.

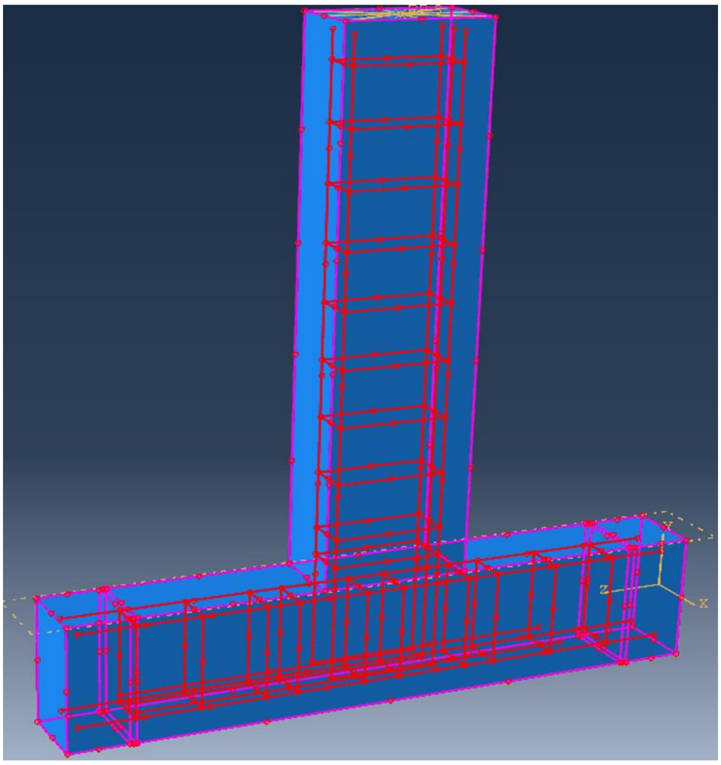

Figure 6. 8 Embedded Reinforcement

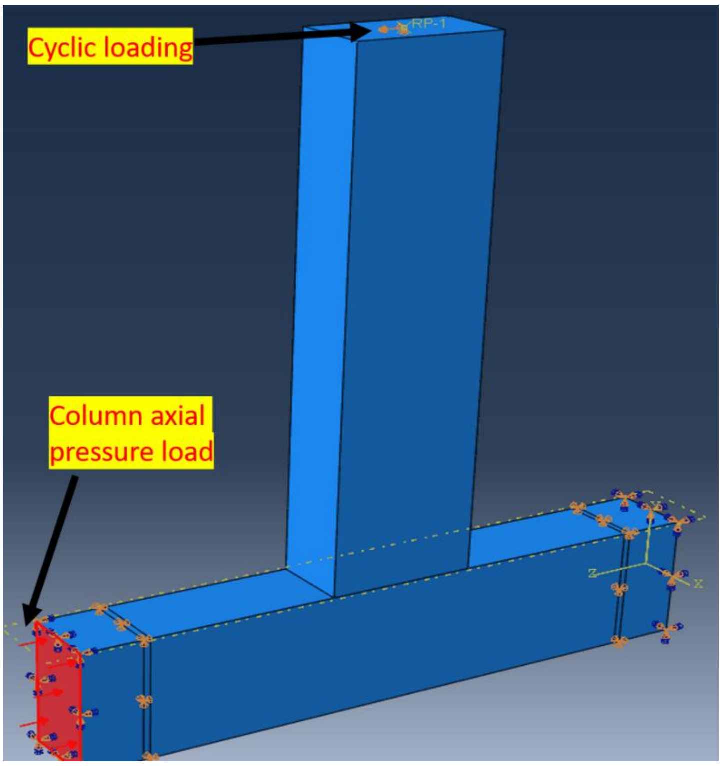

Figure 6. 9 Boundary conditions

6.5 MESHING

The meshes over the parts and assemblies created within ABAQUS/CAE are applied via the mesh module. The application of sufficiently refined mesh is important to ensure the accuracy of ABAQUS simulation results. The process of assigning mesh attributes such as mesh techniques, seeds, and element type to the parts and assemblies of the model is feature-based. For all the solid elements used in the FE model, structured meshing was adopted as the matrices based on structure meshing are fast and easy to assemble. The mesh density along the boundary and also in the interior of the region is determined by the seeds along the edge of the selected region. Seeds can be identified as markers that are placed along the edges of a selected region to specify the target mesh density, as shown in Figure 6.10.

6.5.1 Mesh Convergence study

A mesh convergence study was performed to determine an optimal size mesh which allows an accurate prediction of BCJ specimen response while minimizing the computational effort. A total of five element size mesh (i.e., 30 mm, 40 mm, 50 mm, 60 mm, and 70 mm) were uniformly assigned to the control beam-column joint specimen model. Figure 6.11 illustrates the mesh convergence results for the control specimen under reverse cyclic loading and the similarity in the convergence of all the element sizes mesh. The load-displacement envelope curve obtained for each element size mesh was compared with the envelope curve of control specimens taken from the experimental study (Section 4.6). The numerical result of the specimen having an element mesh size of 50 mm shows a closer agreement with the experimental test result in terms of maximum load when compared to other element sizes. Therefore, an element mesh size of 50 mm was adopted for all the specimens.

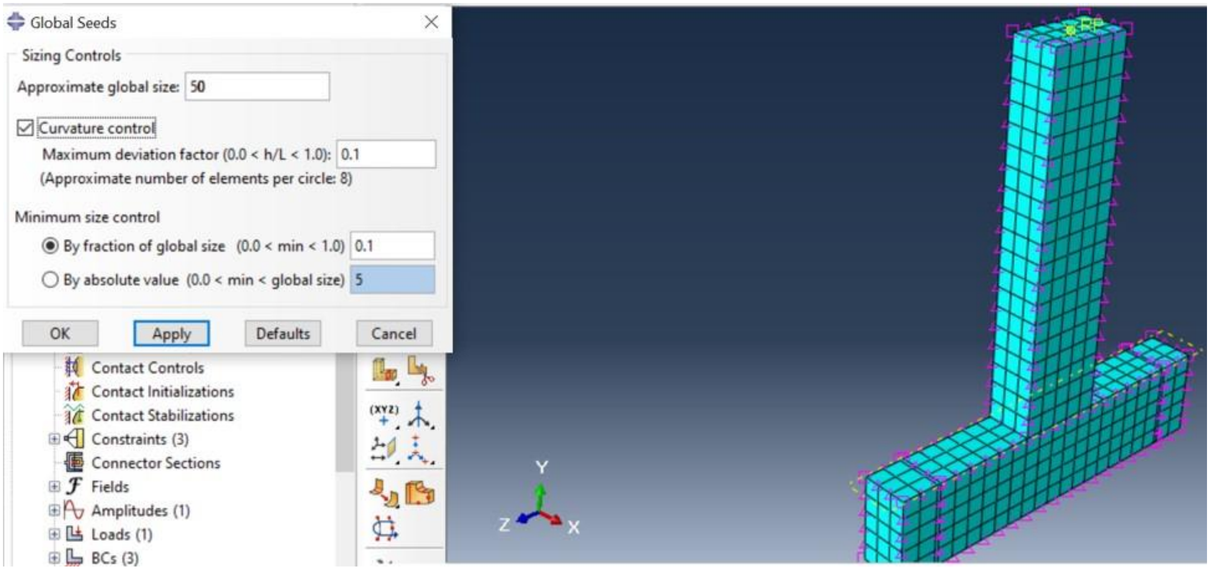

Figure 6. 10 Finite element mesh

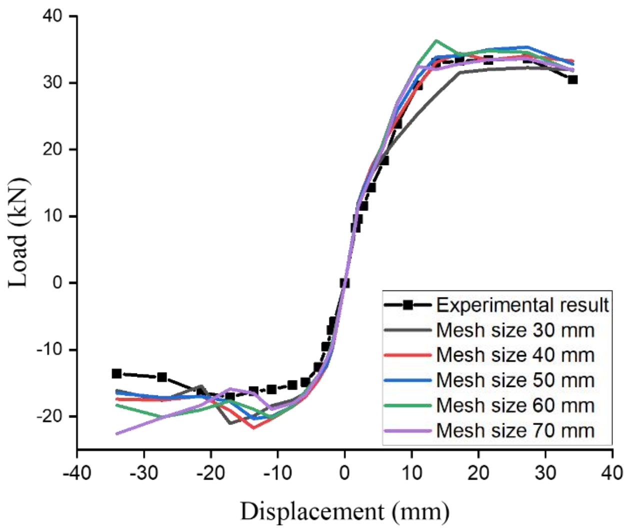

Figure 6. 11 Envelope curve of Experimental results and FE analysis for different values of mesh size

6.6 VALIDATION OF NUMERICAL MODEL

The FE analysis results of non-seismically and seismically detailed specimens were validated with the experimental study results presented in Chapter 4. The maximum load obtained from the FE analysis and experimental results under the influence of cyclic loading were compared in Table 6.5. To express the model accuracy and the associated over and underestimation of the non-linear FEA, the error (%) is evaluated based on the relation given in Behnam et al. 2018; Liu et al. 2021b; Yimer and Aure 2022, also presented in Table 6.5.

$$\text{Error } (\%) = \frac{NLFEA\ result - Experimental\ \ result}{Experimental\ \ result} \tag{6.14}$$

In general, the error in the estimation of peak load capacity for all specimens is below 10%, which is a clear indicator of the ability of the FE model to closely estimate the experimental load-carrying capacity.

Table 6. 5 Comparison between experimental and numerical results

Specimen		Corrosion Level	η	F_{max} (kN)		
Description	Identification			Exp.	FE	Dif (%)
Non-Seismically detailed	NDU-N	Uncorroded	-	23.28	25.34	8.84
	NDCL1-N	1st	5.19	21.08	22.29	5.74
	NDCL2-N	2nd	10.17	20.3	22.13	9.01
	NDCL3-N	3rd	14.1	17.47	19.76	13.1
Seismically detailed	DU-N	Uncorroded	-	25.36	27.84	9.77
	DCL1-N	1st	7.85	23.14	24.75	6.95
	DCL2-N	2nd	14.2	21.77	22.88	5.09
	DCL3-N	3rd	16.09	20.75	22.08	6.4

"η" represents the average mass corrosion ratios of the reinforcing steel bar; F_{max} is the peak load-carrying capacity of the specimen (average value of the peak load in the negative and positive loading cycles); Dif (%) = [(predicted-exp.)/exp.] × 100, (Liu et al. 2021b).

The experimental and numerical load-displacement hysteresis and envelope curve at a drift ratio of ± 4.36% are presented in Figure 6.12 (a) and Figure 6.12 (b). The FEM shows an excellent prediction of peak load in both the negative and positive displacement direction, post-peak response, and ultimate failure pattern for the uncorroded specimen (NDU-N), when compared to the experimental uncorroded specimen (NDU), as shown in Figure 6.12. The results exhibit wider hysteresis loops from FE modeling when compared to experimental results. This behaviour of hysteresis loops may occur due to the adoption of an embedded method for simulating the interaction between reinforcement bars and concrete surfaces (Yimer and Aure 2022).

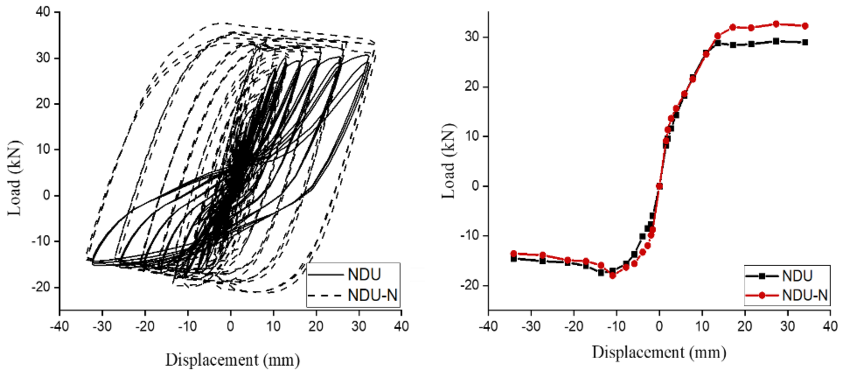

(a) (b)

Figure 6. 12 Load-displacement response of non-seismic uncorroded/control experimental and FEA specimen (a) Hysteresis curve; (b) Envelope curve

Figure 6.13 shows the hysteretic and envelope curve comparison of the numerical specimen (NDCL1-N) with the reported experimental results of the specimen (NDC-1). The NDC-1 shows better stiffness at the pre-peak stage than NDCL1-N, as the diametric profile of the reinforcement bar increases due to the deposition of rust on the surface, resulting in an increased bond between the rebar and concrete surface. This parameter was not replicated in the FE modeling, therefore showing the slight difference in the elastic stiffness. The peak loading carrying capacity from the numerical simulation shows a close correlation with the experimental result with an error (%) of 5.74%. Figure 6.14 and Figure 6.15 illustrate the comparison between numerically simulated and experimental test results for non-ductile detailed specimens at the 2nd and 3rd levels of corrosion, respectively. The figure shows good agreement between numerical modeling and experimental test results for specimens NDCL2-N and NDCL3-N in terms of maximum load-carrying capacity, post-peak response, and ductility. The NDCL2-N specimen shows a difference of approximately 9% in the peak load response of numerical and experimental results. The hysteresis loops of the corroded specimens (i.e., NDCL2-N and NDLC3-N) were represented up to a particular displacement on the negative displacement side. This was experienced due to the fracture of 8 mm diameter reinforcing bars for the specimens having higher corrosion rates (specifically > 10%, for both the reinforcement detailing regime specimens).

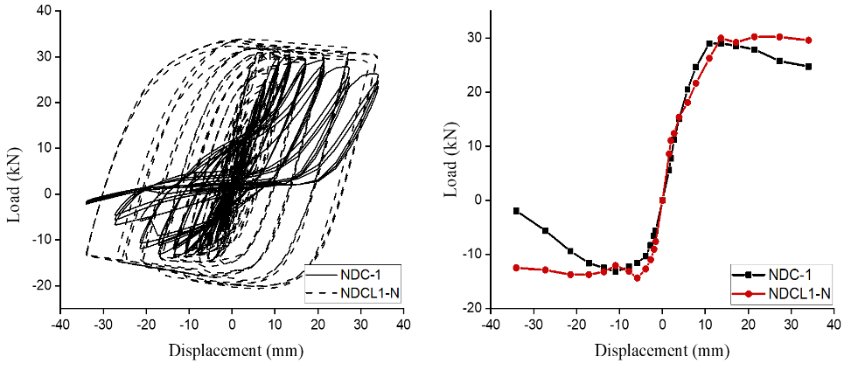

(a) (b)

Figure 6. 13 Load-displacement response of corroded (level-1) non-seismic experimental and FEA specimen (a) Hysteresis curve; (b) Envelope curve

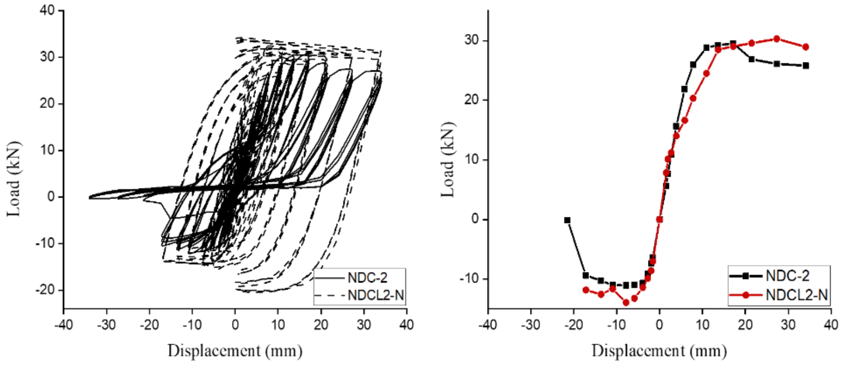

(a) (b)

Figure 6. 14 Load-displacement response of corroded (level-2)non-seismic experimental and FEA specimen (a) Hysteresis curve; (b) Envelope curve

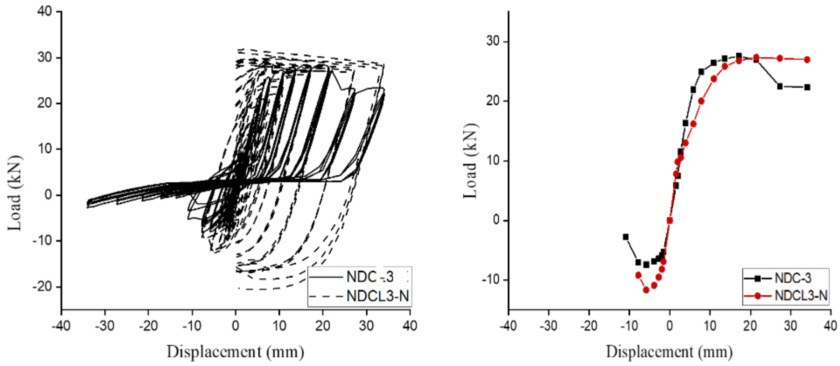

(a) (b)

Figure 6. 15 Load-displacement response of corroded (level -3) non-seismic experimental and FEA specimen (a) Hysteresis curve; (b) Envelope curve

The fracture of reinforcement bars in the corrosion-damaged specimens is determined by Von Mises stress representation. Before the distortional energy reaches its yielding point, the material is under an equivalent amount of stress, which is represented by the von Mises stress. The maximum Von Mises stress reached 724 MPa (for 2nd and 3rd level corroded non-seismic detailed and seismic detailed specimens), as shown in Figure 6.16, which exceeds the experimentally obtained ultimate tensile stress value of 8 mm diameter reinforcing bars (i.e., 715.91 MPa), (Refer to Table 6.4). This exhibits the fracture of the 8 mm diameter bars which causes a sudden decrement in the load-carrying capacity, as shown by the numerical results. A similar trend was noted in the experimental study (Chapter 4, Figure 4.18 and 4.20). This depicts the capability of the FE model to capture the fracture modes of the corrosion-damaged reinforcement bars. The post-peak response showing the fracture of severely corroded reinforcement bars during cyclic loading was also well simulated. In the NDCL3-N specimen, the fracture of corrosion damage bars was experienced at early displacements (i.e., 7.79 mm) when compared to the displacement of the NDCL2-N specimen (i.e., 17.16 mm), as the damage level was higher, thereby sustaining fewer displacements before fracture. A reduction of approximately 29% and 54% in the peak load-carrying capacity was observed for NDCL2-N and NDCL3-N specimens in the negative cycle, when compared to the NDU-N, due to severe corrosion damage.

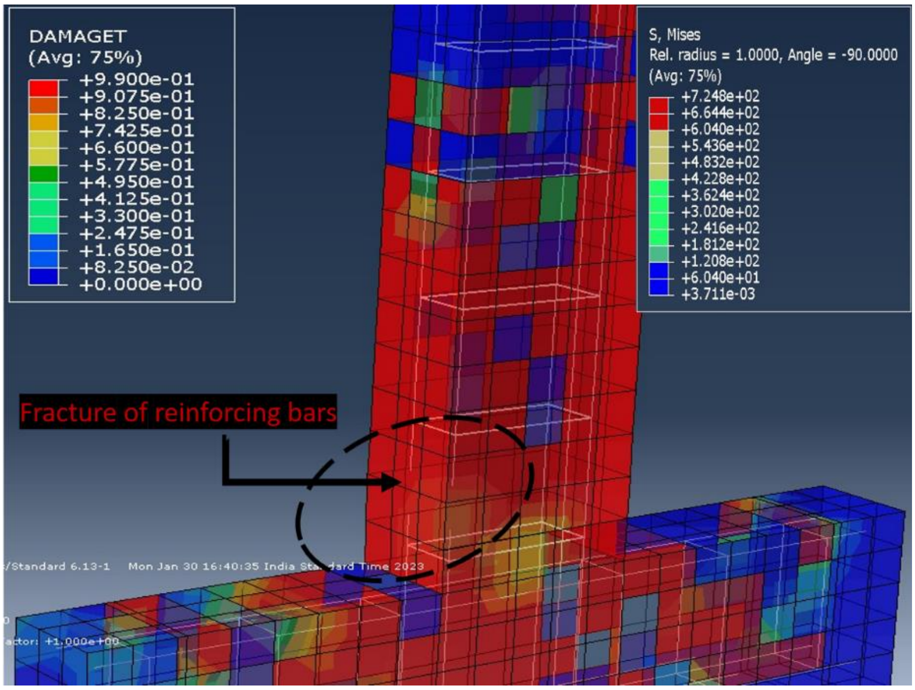

Figure 6. 16 Fracture of reinforcing bars determined by Von-Mises stress

Figure 6.17 (a) and (b) show the experimental (DU) and numerical (DU-N) load-displacement hysteresis and envelope curve response of uncorroded seismic specimens at an ultimate drift ratio of ± 4.36%. For the seismically detailed uncorroded specimen, DU-N exhibits an average peak load of 27.84 kN against the peak load of 25.36 kN for the corresponding experimental specimen DU. The FE analysis shows an excellent prediction of peak load in both the positive and negative displacement direction when compared to the experimentally tested specimen. Figure 6.18-6.20 compares experimental and FEA results for different levels of corrosion-damaged seismic specimens. The error (%) displaying the model accuracy shows a value of less than 10% for all the specimens (Refer Table 6.5 above). The fracture of 8 mm diameter reinforcing bars was also experienced for the seismically detailed specimens as was experienced for non-seismically detailed specimens, at higher corrosion levels. However, when compared to non-seismically detailed corroded specimens, the seismically detailed corroded specimens show higher peak load and ductility.

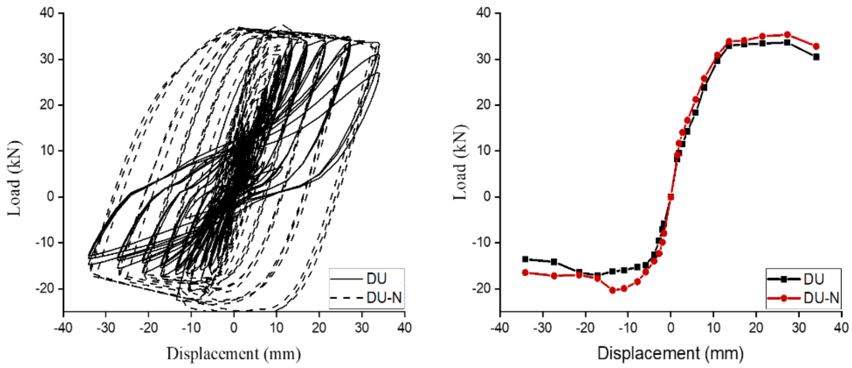

(a) (b)

Figure 6. 17 Load-displacement response of control/uncorroded seismic experimental and FEA specimen (a) Hysteresis curve; (b) Envelope curve

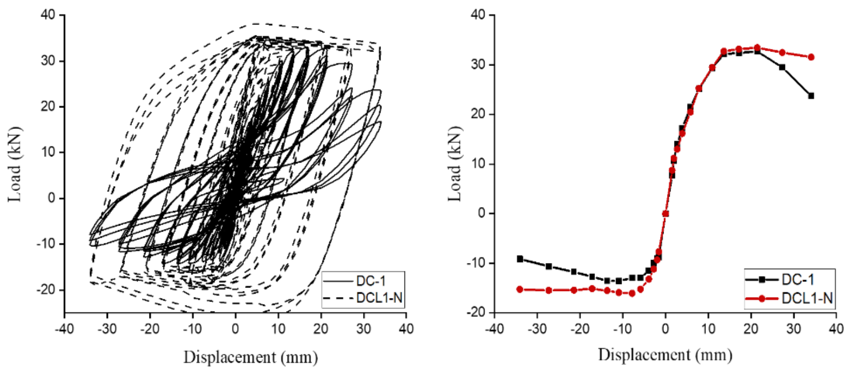

(a) (b)

FEA specimen (a) Hysteresis curve; (b) Envelope curve

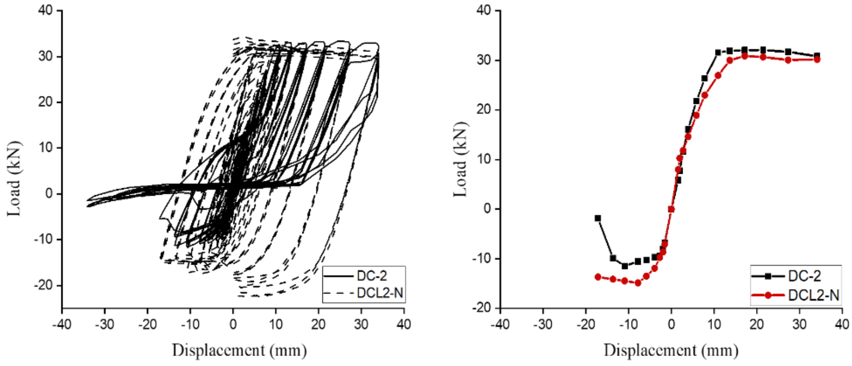

(a) (b)

Figure 6. 19 Load-displacement response of corroded (level -2) seismic experimental and FEA specimen (a) Hysteresis curve; (b) Envelope curve

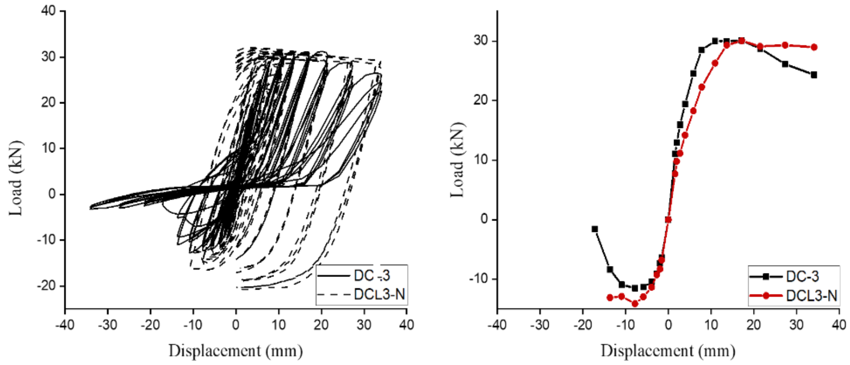

(a) (b)

Figure 6. 20 Load-displacement response of corroded (level -3) seismic experimental and FEA specimen (a) Hysteresis curve; (b) Envelope curve

6.7 NUMERICAL ANALYSIS OF THE PERFORMANCE OF CORRODED RC EXTERIOR BCJs

After validating the FE simulation results against the experimental results, the numerical assessment of the load-bearing capacity of different levels of corrosion-damaged BCJ specimens was carried out in this section. The parameters like load-carrying capacity, stiffness degradation, and ductility of the corroded non-seismically detailed and seismically detailed specimens were numerically analyzed and compared. Also, the damage progression at the surface of concrete for different levels of corrosion damage was analyzed with the help of the parameter PEMAG and was compared with the ultimate damage pattern reported in the experimental study.

6.7.1 Load-Displacement Hysteresis Curve

6.7.1.1 *Hysteretic Behaviour of Uncorroded BCJ Specimens*

The hysteretic behaviour of the specimen represents the relationship between the lateral force and displacement applied at the top surface of the beam. The comparison of the numerical and experimental hysteretic responses of the uncorroded non-seismically detailed and seismically detailed specimens is shown in Figure 6.12 (a) and Figure 6.17 (a), respectively. This displays the numerical model accuracy for effectively simulating every loading cycle both in terms of strength as well as stiffness. For non-seismically detailed uncorroded specimens (NDU-N), the maximum load in the negative and positive cycles is 18 kN and 32.68 kN corresponding to the displacement of 10.92 mm and 27.29 mm, respectively. For the seismically detailed uncorroded specimen (DU-N), the maximum load in the negative and positive cycles is 20.32 kN and 35.36 kN corresponding to the displacement of 13.65 mm and 27.29 mm, respectively.

The cyclic behaviour of the specimen is characterized by a gradual reduction in strength and stiffness corresponding to the increasing displacement. In the negative displacement cycle, the strength reduction is observed at a gentle rate. The ultimate failure (i.e., where the ultimate load is 0.8 times the maximum load) (Siva Chidambaram and Agarwal 2015; Sharma and Bansal 2019) is reached for non-seismically detailed and seismically detailed uncorroded specimens at the respective displacements of 21.45 mm and 34.07 mm. A similar hysteresis behaviour of uncorroded specimens was experienced in the experimental study (Refer Section 4.5).

6.7.1.2 *Hysteretic Behaviour of Corroded BCJ Specimens*

Figures 6.13-6.15 (a) and Figures 6.18-6.20 (a) show the comparison of the numerical hysteretic responses and experimental hysteretic responses of the corrosion-damaged non-seismically detailed and seismically detailed specimens, respectively. The hysteretic behaviour of corroded seismically detailed specimens shows better load-carrying capacity than non-seismically detailed specimens. The specimen DCL1-N exhibits a higher load-bearing capacity of 31.56 kN and 15.24 kN at the ultimate drift of + 4.36% and – 4.36%

respectively when compared to the 29.6 kN and 12.45 kN load for NDCL1-N specimen. A significant improvement in the post-peak performance and ductility can be observed for seismically detailed specimens when compared with the non-seismically detailed specimens.

For the NDCL3-N specimen, the peak load-carrying capacity dropped to 27.85 kN and 11.67 kN at the corresponding displacement of 21.45 mm and 5.85 mm in the respective positive and negative drift cycles. In comparison, for the DCL3-N specimen, the peak load-carrying capacity dropped to 30.05 kN and 14.12 kN at the corresponding displacement of 17.16 mm and 7.79 mm in the respective positive and negative displacement cycles. A significant reduction of load-bearing capacity and ductility can be experienced due to the fractured 8 mm diameter corroded bars, also visible in the hysteresis response of corroded specimens. The peak load of the DCL3-N was 11.74% higher when compared to the peak load of NDCL3-N, and it also exhibited fracture of corroded reinforcing bars at higher displacement than NDCL3-N. A higher peak load and stiffness were observed in the corroded seismically detailed specimen (DCL3-N), owing to the closer arrangement of stirrups (which ultimately provides a better confining action to the enclosed concrete) when compared to the corroded non-seismically detailed specimen (NDCL3-N). These results show a close resemblance to the results reported in the experimental study.

6.7.2 Load-Displacement Envelope Curve

Figure 6.21 presents the numerical load-displacement curves for the non-seismically detailed BCJ specimens having three different levels of corrosion rate. In comparison to the NDU-N specimen, the NDCL1-N specimen showed a decrement of approximately 8% and 25% in the maximum load in the positive and negative displacement cycle. A significant drop of 19.53% and 54% in the peak load of the NDCL3-N specimen was seen as compared to the NDU-N specimen, in the positive and negative displacement cycles respectively. The 8mm diameter bars showed much more severe damage when compared to the 10 mm diameter bars and even got fractured at higher displacement.

Figure 6.22 depicts the numerical load-displacement envelope curves for the seismically detailed specimens. From a comparison of Figures 6.21 and 6.22, it can be observed that the corroded seismic specimens show better load-bearing capacity when compared to the corroded non-seismic specimens. Even for the highest corrosion rate specimen (i.e., NDCL3-

N and DCL3-N), the DCL3-N specimen showed approximately 10% and 21% higher peak load than the NDCL3-N specimen, in respective positive and negative drift directions. The closer stirrups arrangement in the seismic detailed specimens resulted in better load-bearing capacity even at the high corrosion rate, showing a similar trend as was experienced in the experimental study.

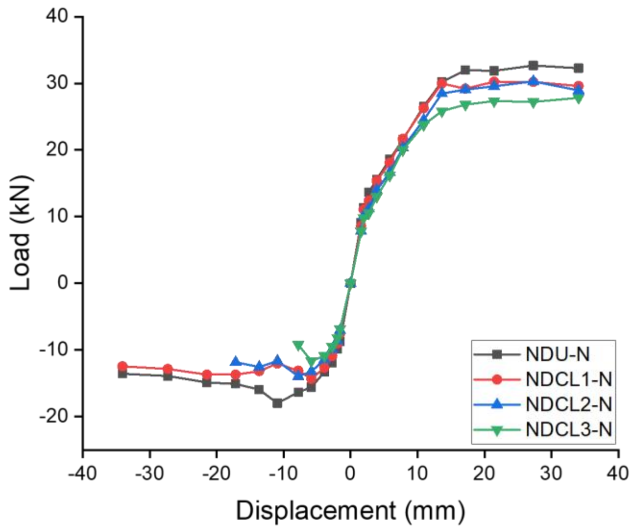

Figure 6. 21 Load-displacement envelop curves of uncorroded and corroded non-seismically detailed BCJs

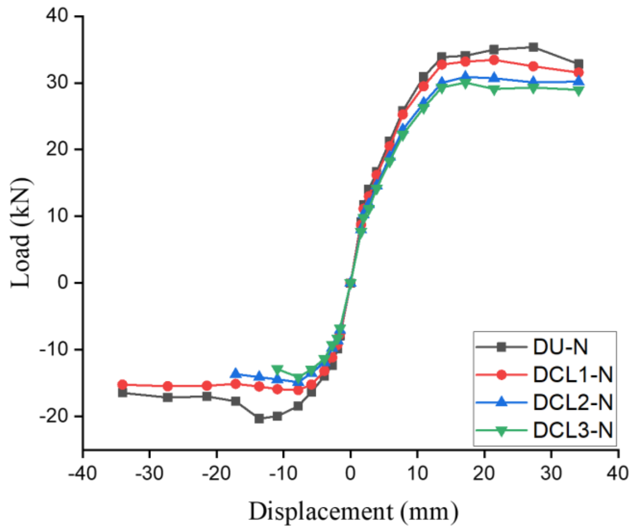

Figure 6. 22 Load-displacement envelop curves of uncorroded and corroded seismically detailed BCJs

Due to the high corrosion rate at the reinforcement bars, the 8 mm diameter bars were unable to resist higher cyclic displacements and were fractured during the numerical analysis. Fracture of reinforcing bars led to a significant drop in the ductility of the corrosion-damaged specimens. The ultimate displacement in the negative cycle (i.e. side having 8 mm diameter bars) drops from 21.45 mm for the NDU-N specimen to 17.16 mm and 7.79 mm for NDCL2-N and NDCL3-N specimens, respectively. Similarly, the ultimate displacement showed a drop from 34.07 mm for the DU-N specimen to 17.16 mm and 10.92 mm for the DCL2-N and DCL3-N specimens, respectively. Therefore, for both the reinforcement detailing regime specimens, the ultimate displacement of severely corroded specimens (NDCL3-N and DCL3-N) was experienced to drop to approximately one-third of the value observed for the respective control specimens (which almost replicates the behaviour as observed in the experimental study, Sections 4.6.

6.7.3 Stiffness Degradation

The post-elastic behaviour of the structural member can be evaluated by using the degradation rate of stiffness under the influence of cyclic displacement. The stiffness is approximated as the slope of the line joining the peak-to-peak points in each loading drift both on the positive and negative cycles. The secant stiffness at different cyclic drifts was determined by Eq. 6.15 (Mostofinejad and Akhlaghi 2017; Yimer and Aure 2022).

$$K_i = \frac{P_i^+ - P_i^-}{D_i^+ - D_i^-} \tag{6.15}$$

Where K_i represents the secant stiffness of each cycle, D_i^{+}, and D_i^- represent the displacement corresponding to the per cyclic peak load P_i^+ and P_i^- in the respective positive and negative loading direction.

The secant stiffness of the control and different levels of corroded specimens have been evaluated from the performed numerical simulations. Figure 6.23 (a) and (b) show the stiffness degradation of all the non-seismically detailed and seismically detailed specimens, respectively. As the corrosion rate increases, an increase in the degradation of stiffness is observed. From the numerical simulation, it can be observed that significant degradation was seen at the negative cycle (having an 8 mm diameter fracture) when compared to the positive cycle, for all corroded specimens. When compared to the control specimen (NDU-N), a decrement of approximately 15.22%, 24.16%, and 26.98% in the initial stiffness of NDCL1-N, NDCL2-N, and NDCL3-N specimens was noticed, in the negative cycle. For DCL1-N, DCL2- N, and DCL3-N specimens it was calculated to be 3.04%, 11.92%, and 16.55% when compared to DU-N, comparatively much less when compared to corroded non-seismic specimens.

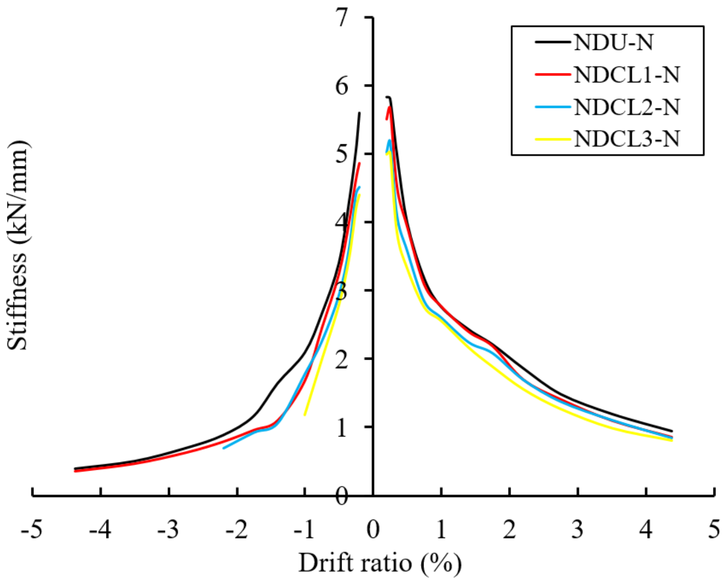

(a)

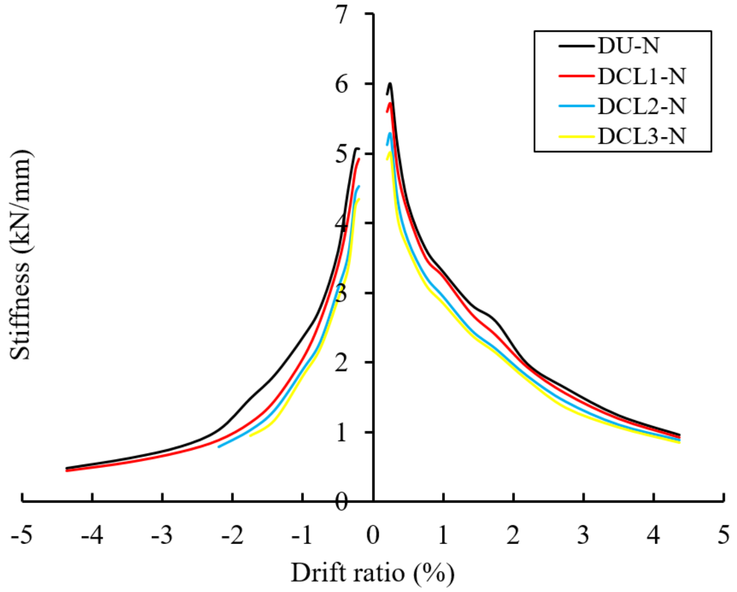

(b)

Figure 6. 23 Secant stiffness of uncorroded and corroded (a) non-seismically detailed and (b) seismically detailed BCJs

The fracture of corrosion-damage reinforcement bars at higher displacement causes significant degradation in stiffness at the post-elastic region resulting in the overall reduction of seismic performance. An alarming reduction of approximately 77.11% in the stiffness of the NDCL3-N specimen was observed at the drift of ±1% when compared to that of the NDU-N specimen. Whereas, for the DCL3-N specimen the degradation in the stiffness was 54.32% at the drift ratio of ±1.4% when compared to the DU-N specimen. In the case of the corroded seismically detailed specimens (DCL3-N), the stiffness degradation occurs at a lower rate and at a comparatively higher displacement level when compared to the corroded non-seismically detailed specimens (NDCL3-N). Under the seismic environment, slow stiffness degradation is a desirable characteristic, as sudden loss in stiffness within the RC member will result in a catastrophic failure.

The FE model has simulated the stiffness degradation for each cycle in very close agreement with the results presented in the experimental study. As the specimen NDCL3-N exhibited rebar fracture at the drift of ±1%, a percentage error of the average stiffness value was considered at this drift ratio. The specimens NDU-N and NDCL3-N displayed prediction errors of +1% and -8.55% when compared to the results reported in the experimental study. Similarly, for the specimens DU-N and DCL3-N, the prediction error of +11% and -4.27% was noted at the drift ratio of ±1.4%, when compared to that of experimental test results, respectively. This implies a good agreement of numerical results with the results reported from the experimental study.

6.7.4 Damage Progression

As the cyclic loading progressed, damage to the specimen surface was encountered with the help of cracks. A comparison between control and corroded specimens is presented in terms of damage progression via damage parameters provided by ABAQUS. As per the CDP model, the damage is estimated in the form of crack distribution that can be approximately represented by the development of tensile damage (Liu et al. 2020a). In the CDP model, the localized damage due to crack propagation is primarily indicated by the maximum plastic strain (Najafgholipour et al. 2017)(Behnam et al. 2018). The parameter Plastic Strain magnitude **(**PEMAG) was used to analyze the damage and crack progression at the surface of control and corroded specimens. The damage and crack progression on the concrete surface of control and corroded non-seismically detailed specimens at different drift ratios are shown in Figures 6.24 - 6.26.

Figure 6.24 shows the flexural crack initiation at the surface of the beam of all the non-seismically detailed specimens at ± 0.2% drift ratio. As drift progressed, minor diagonal shear cracks were experienced at the junction of the beam-column. It can be observed from Figure 6.24 (a) that for specimen NDU-N the damage was more focused at the junction of the beam-column whereas the damage progresses at a higher rate toward the surface of the beam for all the corrosion-damaged specimens. The corroded specimens i.e. Figures 6.24 (b-d) experienced more damage and cracks propagation on the surface of the beam represented by higher plastic strain magnitude when compared to the NDU-N specimen.

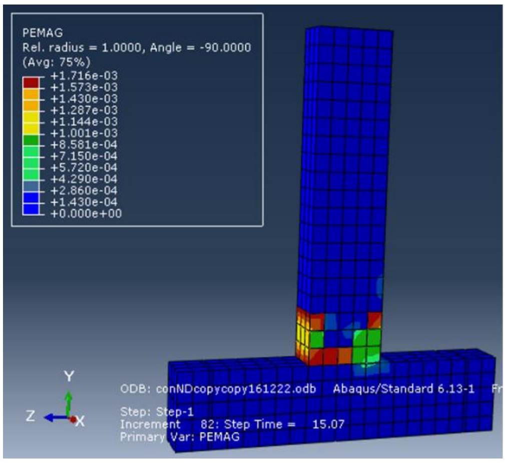

(a) NDU-N

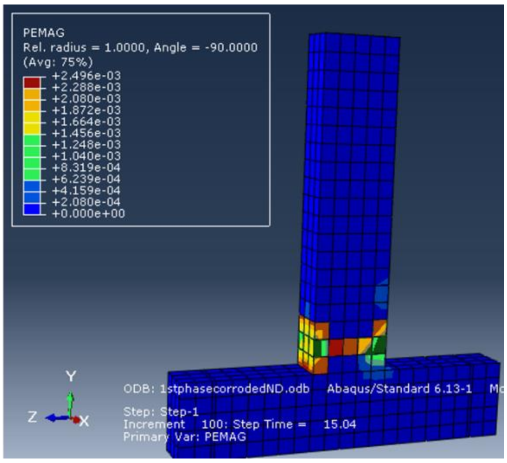

(b) NDCL1-N

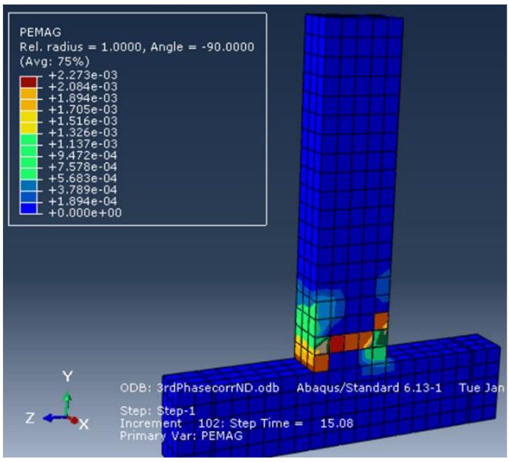

(c) NDCL2-N

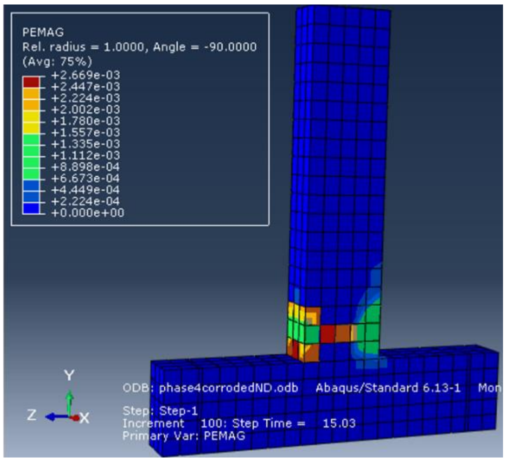

(b) NDCL3-N

Figure 6. 24 Crack patterns of non-seismically detailed specimens corresponding to ± 0.2% drift ratio

The damage was also analyzed at ± 1% drift ratio, where the fracture of corroded reinforcing bars was experienced for the level-3 corroded specimen (NDCL3-N). Therefore, for all the specimens the damage was analyzed at this particular drift. Figure 6.25 shows the dense crack formation and damage at the control and corroded specimens at the drift ratio of ± 1%. From Figure 6.25 (a) it can be observed that the damage progresses uniformly at the column and beam surface due to the failure specified at the junction of the beam-column. However, Figures 6.25 (b)-(d) show that the damage has been targeted at the fracture bar location present at the surface of the beam. The dominant crack can be visible at the surface of the beams of the corroded specimens thereby, directing the ultimate failure towards flexural failure, similar to behaviour experienced in the experimental results (Refer Table 4.2).

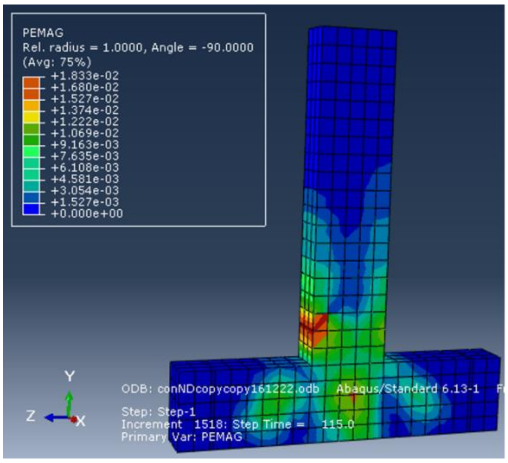

(a) NDU-N

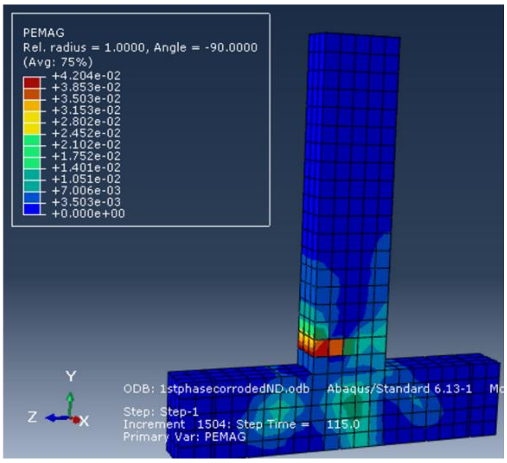

(b) NDCL1-N

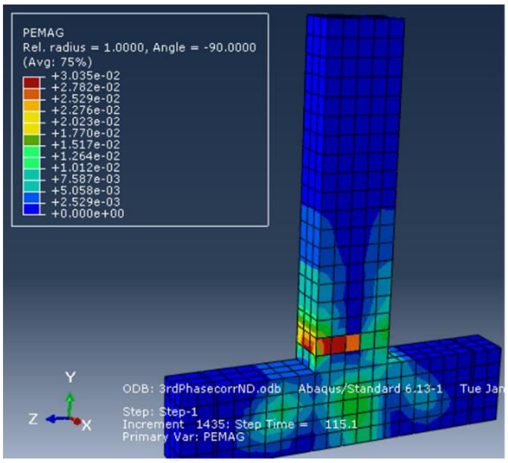

(c) NDCL2-N

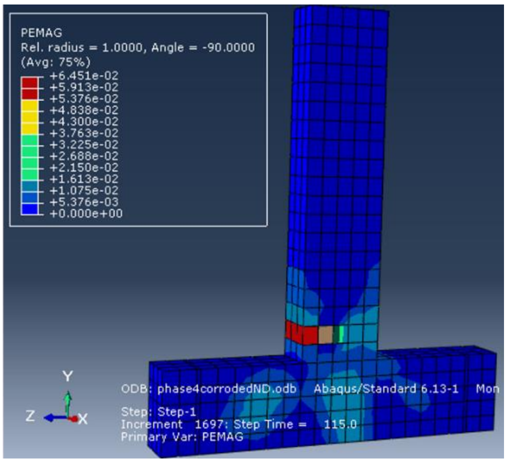

(b) NDCL3-N

Figure 6. 25 Crack patterns of non-seismically detailed specimens corresponding to ± 1% drift ratio

The comparison of the ultimate failure mode of the control uncorroded and corroded specimens with the experimental results (Dangwal and Singh 2023) at the maximum drift of ± 4.36% is illustrated in Figure 6.26. For the uncorroded specimen (NDU-N), major damage was observed at the plastic hinge location leading toward the ultimate failure as joint shear failure, as presented in Figure 6.26 (a). It was experienced that more cracks were concentrated at the beam-column junction as the drift ratio progressed. However, for the corroded specimens, the localized damage represented by plastic strain at the surface of the beam was observed, as presented in Figures 6.26 (b)-(d). The ultimate failure was experienced due to the widening of the flexural cracks on the specimen surface, similar to the behaviour observed in the experimental study, as indicated by the figures shown here and in Table 4.6. These results clearly indicate that the numerical model is capable of capturing the damage progression modes for any corroded or uncorroded specimen at various drift levels

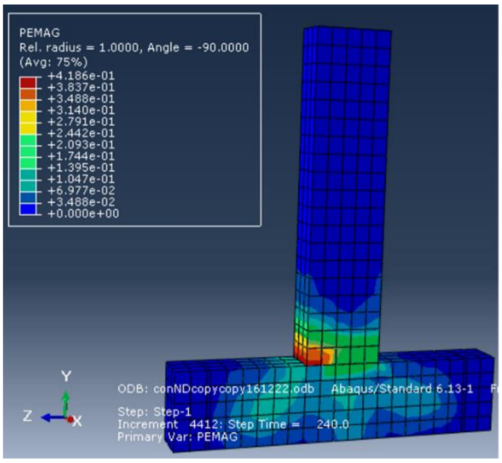

(a) NDU-N

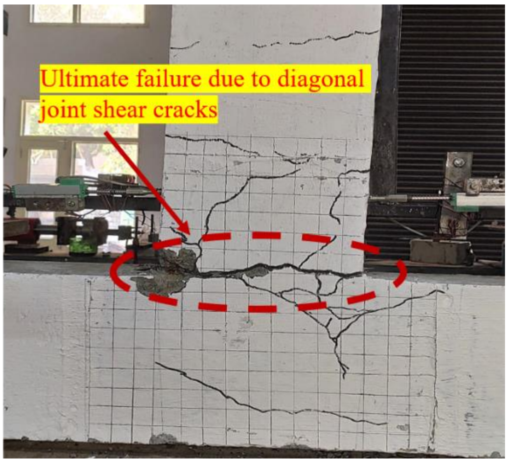

(b) NDU

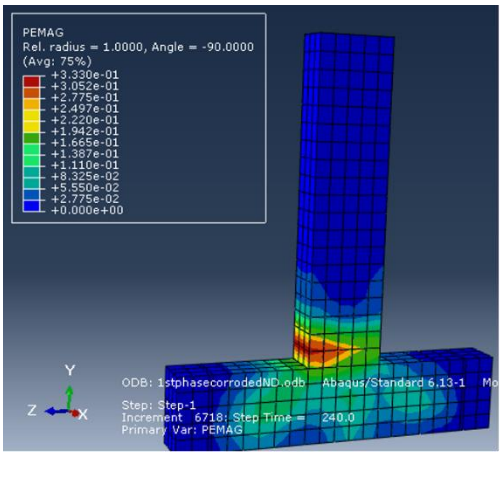

(c) NDCL1-N

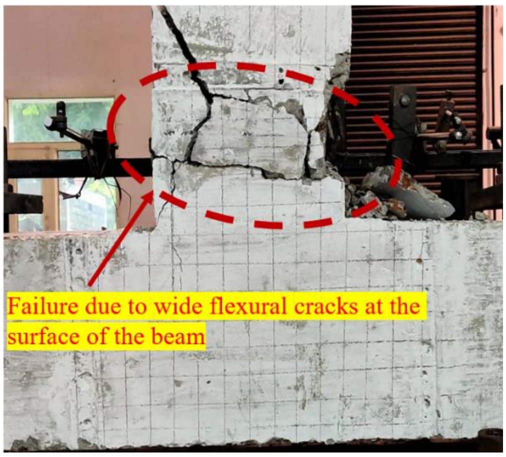

(d) NDC-1

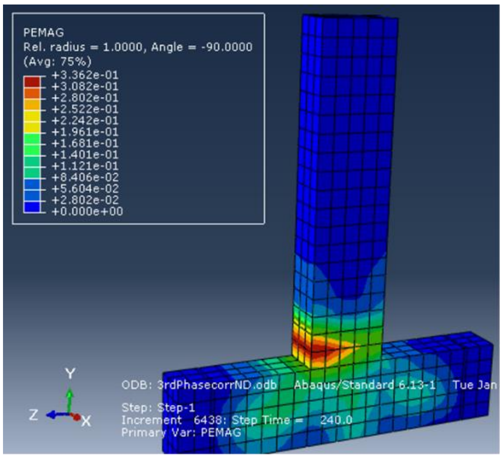

(e) NDCL2-N

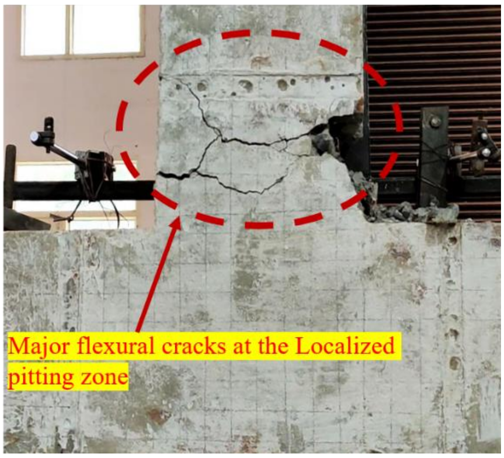

(f) NDC-2

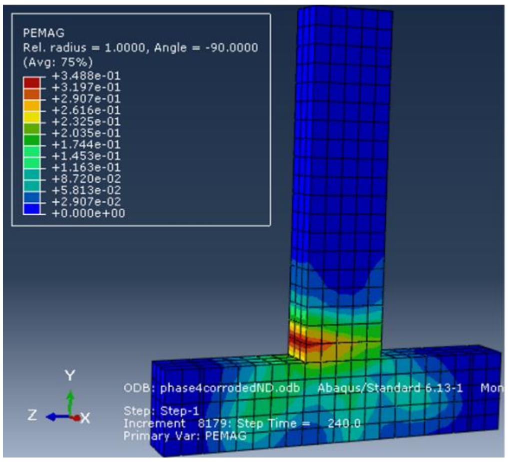

(g) NDCL3-N

(h) NDC-3

Figure 6. 26 Crack patterns of non-seismically detailed specimens corresponding to ± 4.36% drift ratio

Figure 6.27 shows the initiation of damage progression at the surface of concrete for all the seismically detailed specimens at ± 0.2% drift ratio. The flexural cracks can be observed at the beam-column junction of the specimens. Figure 6.27 shows that less damage has been exhibited by the concrete surface of seismically detailed specimens when it is compared with the non-seismically detailed specimens. The fracture of reinforcements was experienced at ± 1.4% drift ratio for the level-3 corroded specimen (DCL3-N). Therefore, the damage to all the specimens was analyzed at this drift as shown in Figure 6.28. From the figure, it can be experienced that the damage has been transferred to the beam-column junction along with the damage at the location of the fracture of the reinforcing bars on the beam surface.

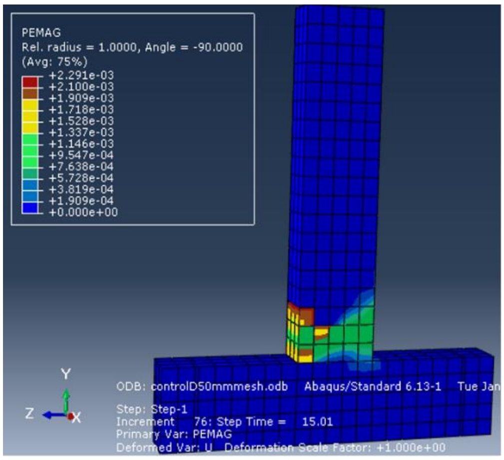

(a) DU-N

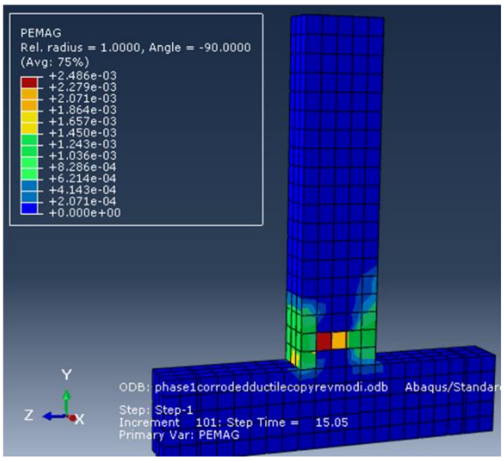

(b) DCL1-N

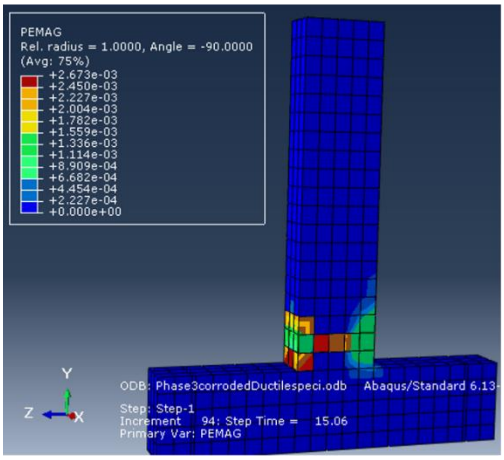

(c) DCL2-N

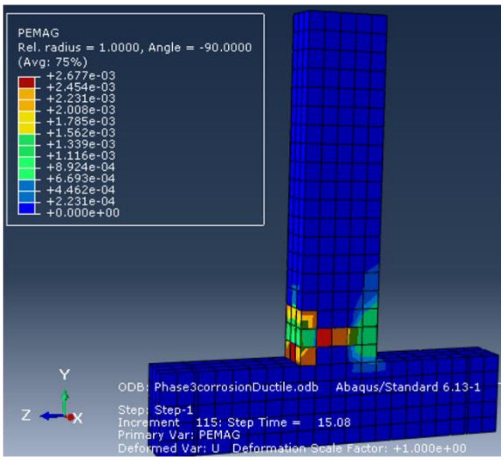

(d) DCL3-N

Figure 6. 27 Crack patterns of seismically detailed specimens corresponding to ± 0.2% drift ratio

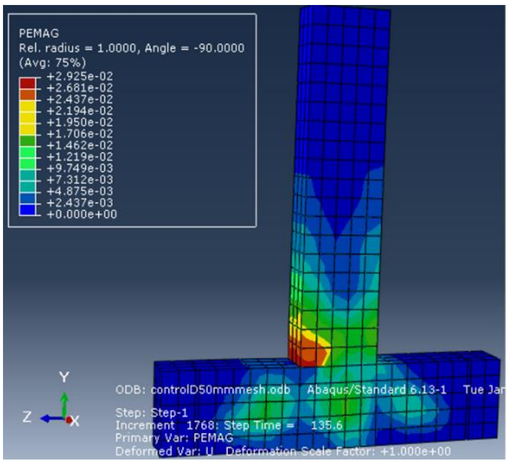

(a) DU-N

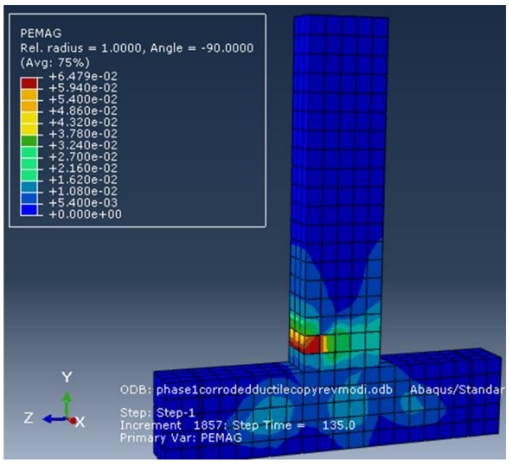

(b) DCL1-N

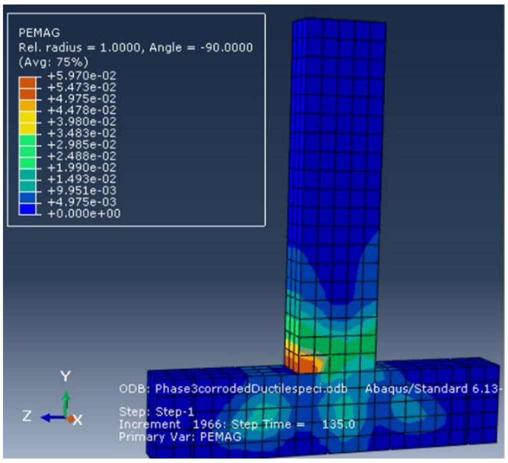

(c) DCL2-N

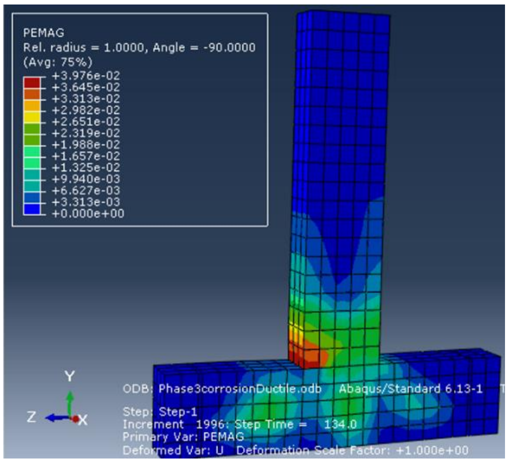

(d) DCL3-N

Figure 6. 28 Crack patterns of seismically detailed specimens corresponding to ± 1.4% drift ratio

The comparison of the ultimate failure mode of the control uncorroded and corroded seismically detailed specimens with the experimental results at the maximum drift of ± 4.36% is illustrated in Figure 6.29. For the uncorroded specimen (DU-N), major damage was experienced at the beam-column junction of the specimen or the plastic hinge location, as displayed in Figure 6.29 (a). The ultimate failure was because of the severe damage to the concrete surface at the beam-column junction, similar to the pattern observed for the specimen NDU-N. Figures 6.29 (b) -(d) show that for the corroded specimens, the damage was localized at the fracture location of reinforcing bars but was also transferred at the beam-column junction due to the arrangement of the close spacing of the stirrups at the target corrosion area. It can also be noted from a comparison of Figures 6.26 and 6.29 that comparatively less damage has been exhibited by the seismically detailed specimens when compared with the specimens having non-seismic detailing.

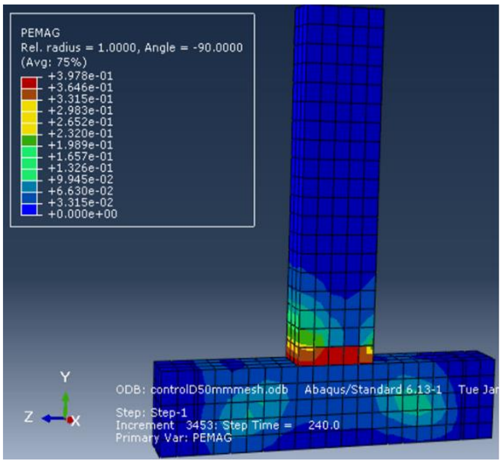

(a) DU-N

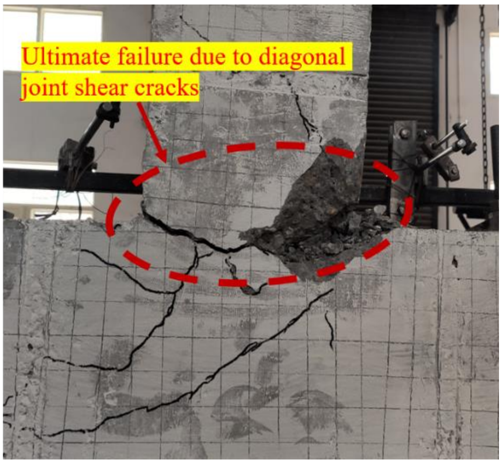

(b) DU

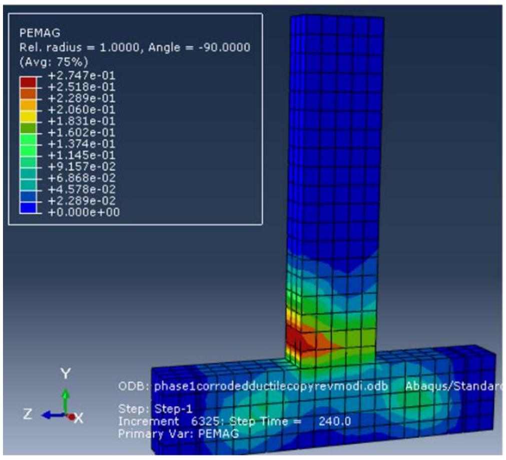

(c) DCL1-N

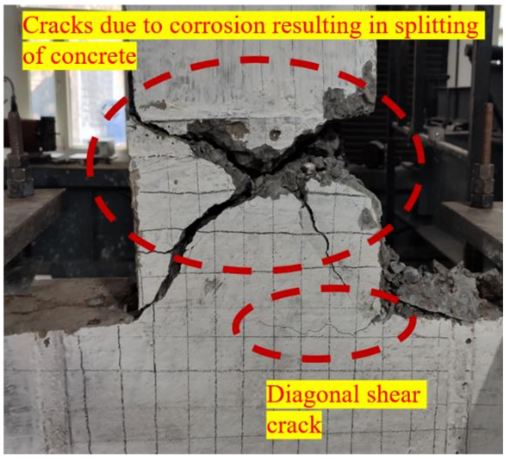

(d) DC-1

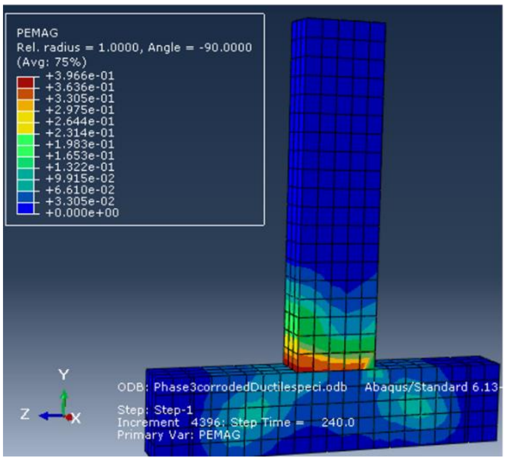

(e) DCL2-N

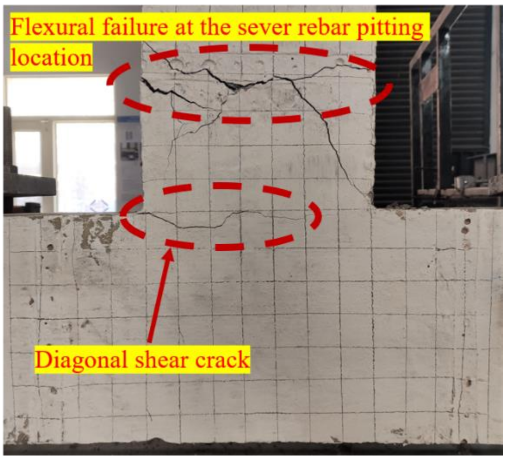

(f) DC-2

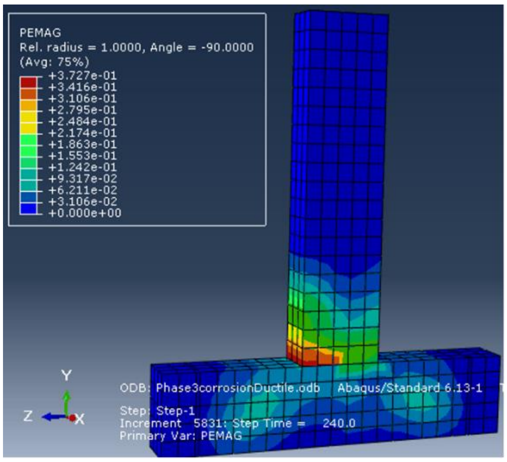

(g) DCL3-N

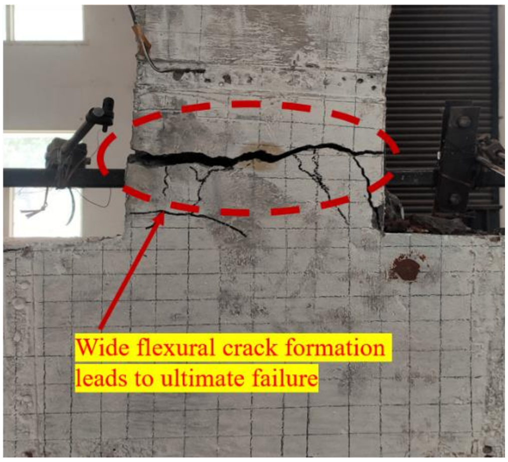

(h) DC-3

Figure 6. 29 Crack patterns of seismically detailed specimens corresponding to ± 4.36% drift ratio

6.8 CLOSING REMARKS

This chapter presents a numerical investigation performed to study the performance of control (uncorroded) and different level corroded specimens subjected to seismic loading with the help of three-dimensional FE models. The numerical models were validated with the results reported in the experimental study presented in Chapter 4. Moreover, the numerical assessment of different levels of corrosion-damaged specimens with two different reinforcement detailing regimes was carried out, and the results were compared and reported using parameters like load-displacement hysteresis and envelope curves, ductility, and stiffness degradation.

CHAPTER 7

CONCLUSIONS

7.1 GENERAL

The aim of the present research is to provide a fundamental understanding of the seismic response of RC Exterior BCJs having corrosion damage at different levels targeted at the beam-column junction. Further, this study also aimed to propose and evaluate the effectiveness of a rehabilitation technique for corrosion-damaged specimens under seismic loading using High Strength Fiber Reinforced Concrete (HSFRC). To meet these objectives, the research has been categorized into two parts i.e., Experimental and Finite element investigation. Numerical investigation was also validated with the results of the experimental study.

The first part of the experimental study included the fabrication and testing of Exterior BCJs of two detailing regime types i.e., non-seismically detailed and seismically detailed. Accelerated corrosion was introduced and targeted at the junction of beam-column at three different levels. All the test specimens were tested under the influence of reverse cyclic loading. In the second part of the experimental study, the corrosion-damaged BCJs were retrofitted with HSFRC in order to regain the degraded seismic performance. The specimens were tested under reverse cyclic loading and the behaviour was determined with the help of seismic parameters.

The numerical investigation of Exterior BCJs corroded at different levels was done via Finite element modeling using ABAQUS software. The results achieved from the numerical FE model were validated against the experimental results, presented in Chapter 4. Thereafter, the validated models were used to numerically analyze the seismic performance of different level corroded specimens with the help of parameters like load-displacement envelope curves, Energy dissipation, and Stiffness degradation under the influence of seismic loading.

7.2 SEISMIC PERFORMANCE OF CORRODED BEAM-COLUMN JOINTS

The experimental study shows the effect of corrosion damage (having different corrosion rates) on the seismic performance of the Exterior BCJ. The seismic parameters of non-seismically detailed and seismically detailed BCJ specimens were determined and compared for the different levels of corrosion. Based on the outcomes of the proposed experimental study, the following conclusions can be drawn:

1. Slightly improved load-bearing capacity along with an increase in other seismic parameters (like stiffness, energy dissipation) was experienced during the initial stage of corrosion. This can be attributed to the slight expansion of the diametric profile of reinforcement due to the deposition of rust over the bar area. This led to an enhancement in the bond between reinforcement and surrounding concrete, resulting in an overall improvement of the mechanical properties of the specimens, during the elastic stage.

2. The ultimate failure mode shifted from diagonal shear cracks at the beam-column junction for the control specimens to flexural failure for all the corroded specimens. For corrosion-damaged specimens, a wide dominant flexure crack was experienced at the surface of the beam, at the localized pitting locations on the longitudinal bar.

3. The brittle fracture of severely pitted 8mm diameter bars during cyclic loading significantly drops the load-carrying capacity and the ductility at an alarming rate. The peak load capacity of severely corroded NDC-3 and DC-3 specimens was 0.42 times and 0.67 times the respective peak load capacity of uncorroded NDU and DU specimens, in the negative displacement cycle. Moreover, the ultimate displacement of NDC-3 and DC-3 showed a steep reduction; it was only 0.3 times and 0.4 times as that was experienced for respective uncorroded specimens.

4. With the increase in the corrosion levels, the seismic behaviour indicators such as energy dissipation capacity and stiffness show considerable degradation in the performance. For the highest corrosion level (i.e., NDC-3 and DC-3) specimens, approximately 68.68% and 59.89% reduction in the cumulative energy dissipation was observed (with respect to the respective control specimen), displaying the severe effect of corrosion on the stability of the structural members.

5. The seismically detailed corroded specimens performed better than the non-seismically detailed corroded specimens at any corrosion level owing to the additional

confinement provided by the transverse reinforcement in the joint area. This helped in improving the load-slip behaviour and peak load-carrying capacity of the specimens. The DC-3 specimen showed a 35.48% higher peak load-carrying capacity and 35.09% higher energy dissipation capacity, as compared to the NDC-3 specimen.

6. Corresponding to the peak level of corrosion (i.e., 14% and 16% for NDC-3 and DC-3, respectively), the maximum load-carrying capacity was reduced by 57.31% and 32.57%, respectively when compared to respective control specimens (NDU and DU), during negative cycle of loading. Further, at this severe corrosion level, well-confined seismic detailed specimens showed far better results by enhancing the shear bearing capacity, and post-elastic behaviour, thus providing higher damage tolerance capacity as compared to non-seismic specimens.

7. The structural damage to the corroded specimens was represented by the damage index (DI). It was observed that the complete damage of NDC-3 and DC-3 was encountered at a drift ratio of ± 1.75% and ± 2.2% which is approximately half of the drift ratio required for the complete damage of NDU and DU i.e., ± 3.5%. All the corroded seismic specimens present better damage resistance at higher displacement when compared to the corroded non-seismic specimens.

8. It was observed that both the yield and the ultimate strength of corroded bars were reduced when compared to uncorroded bars. Moreover, a sharp reduction in ductility was also seen due to the presence of pits. Further, the yielding plateau was almost completely absent for all corroded bars, thereby indicating a shift towards brittle failure in reinforcing bars, which may severely degrade the displacement ductility and energy dissipation of the corrosion-damaged Beam column joints.

7.3 RETROFITTING OF CORRODED BEAM-COLUMN JOINT USING HSFRC

The experimental test results of the present study display that the HSFRC is a promising retrofitting material to enhance the seismic performance of different levels of corroded Exterior BCJ for opted geometrical dimensions. After the retrofitting of corrosion-damaged BCJ specimens with HSFRC, a significant improvement or regain in the seismic parameters was experienced. Some of the major conclusions are drawn below:

1. The ultimate failure pattern of the corrosion-damaged HSFRC retrofitted specimens was similar to the failure pattern experienced for the control specimens, also displaying fewer cracks at the surface of the beam-column joint under higher reverse loading, indicating improved or recovered mechanical performance.

2. The retrofitted specimens showed minimal spalling and crushing of concrete, during higher drifts due to crack bridging mechanisms owing to the presence of hybrid steel fibers in HSFRC. Due to the superior mechanical properties of HSFRC, the fracture of severely pitted reinforcement bars got delayed under higher displacement. This allowed the specimens to maintain seismic failure mechanisms even at severe levels of corrosion. Besides, the post-peak ductility was restored up to a certain extent when compared to uncorroded specimens.

3. A significant improvement in the load-bearing capacity (i.e., up to 34 % and 36 %) was experienced for non-seismic and seismic retrofitted specimens over respective control specimens. In general, the retrofitted seismic specimens performed better than the retrofitted non-seismic specimens. For instance, the peak load-carrying capacity of the RD-3 specimen having a corrosion rate of 20.32 % was 6.25 % and 16.75 % higher than that of the RND-3 specimen with a corrosion rate of 17.76 %, respectively in negative and positive drift cycles.

4. When compared to retrofitted non-seismic detailed specimens, the retrofitted seismic detailed specimens performed better at higher corrosion levels. The seismic retrofitted specimens showed up to 90 % higher equivalent viscous damping ratio than the non-seismic specimens even at the peak level of corrosion. The close detailing of stirrups in seismic specimens resulted in an improvement in bearing capacity, plastic deformation, and ductility.

5. An increment of approximately 47% in the cumulative energy dissipation of retrofitted specimens (i.e., RND-1) was experienced when compared to control (uncorroded) specimens at the drift ratio of ± 2.75%, respectively. Thereafter, a steep post-peak response was experienced due to the inferior tensile strength of corrosion-damaged reinforcement bars owing to the brittle fracture under reverse loading.

6. The initial stiffness increased significantly up to 78.35 % and 84 % for the HPFRC retrofitted Level 1 corroded non-seismic and seismic specimens when compared to respective control specimens. Specimen RND-1 and RD-1 showed similar rates of stiffness degradation as observed in respective control specimens at higher drifts, indicating that the stiffness can be completely recovered for specimens having corrosion rates up to 10 %.

7. A higher damage tolerance capacity was exhibited by the retrofitted specimens, as the damage index of RND-1 and RD-1 specimens was much lower than that of respective control specimens. Level 2 and Level 3 corroded non-seismic and seismic retrofitted specimens have nearly the same damage tolerance as their respective control specimens up to the elastic limit. The damage tolerance for RND-3 and RD-3 specimens having respective corrosion rates of 17.76 % and 20.32 % was not recovered at higher drifts.

7.4 FINITE ELEMENT ANALYSIS

A numerical investigation was performed with the help of the FE analysis based on modeling the effect of reinforcement corrosion at different levels on the seismic performance of the Exterior beam-column joint. The constitutive models were incorporated with the experimental data and observations for performing numerical simulations and were validated with the results of this experimental study. Thereafter, a numerical assessment of the performance of corroded specimens with two different reinforcement detailing regimes were compared and reported. Based on the FE analysis, the following conclusions can be drawn:

1. A mesh convergence study was performed to determine the suitable element mesh size leading to a closer agreement with the experimental response. A total of five element sizes i.e., 30 mm, 40 mm, 50 mm, 60 mm, and 70 mm were adopted as a uniform size mesh. The results displayed a significant variation in the peak load capacity as the element size varies. For this study, a 50 mm element size presented considerably good agreement between the FE analysis prediction and the reported experimental results.

2. The FE models developed were able to replicate the fracture of severely corrosion-damaged reinforcement bars under reverse cyclic loading. The reinforcing steel material response was described using the von Mises yield criterion. However, the stress-strain data from tensile testing was used to characterize the attributes of the reinforcement, including modulus of elasticity, yield stress, and ultimate stress.

3. The damage progression for the control and corroded specimens was closely captured with the help of parameter PEMAG. At the initial drift of ± 0.2%, the damage was observed at the junction of the corroded beam-column which shifted and focused towards the surface of the beam at an intermediate drift ratio of ± 1%. The PEMAG value shows a maximum increment at a drift ratio of ± 4.36%, representing maximum plastic strain distortion. The ultimate failure mode was accurately predicted via wide crack formation at the surface of the uncorroded and corroded specimens, as they closely matched the respective experimental results.

4. The FE models displayed a good prediction of peak-load capacity for different levels of corroded non-seismically detailed and seismically detailed specimens through load-displacement curves. However, the pinching behaviour in the corroded specimens (as observed in the experimental results, Chapter 4) was not replicated, as the load-slip parameter was not included in the model due to certain limitations, resulting in the plump shape of the hysteresis curve during the unloading phase of cyclic loading.

5. Based on the numerical assessment, the load-bearing capacity of the BCJ decreased significantly with an increase in the level of corrosion. For the highest corrosion level (i.e., mass loss of 14.1% for NDCL3-N and 16.09% for DCL3-N), a tremendous decline of approximately 54.24% and 43.9% in the peak load carrying capacity was observed when compared to respective control specimens. A lower reduction in peak load carrying capacity was experienced for seismically detailed specimens when compared to non-seismically detailed specimens, indicating improved confinement provided to concrete by a close arrangement of stirrups.

6. A significant reduction in seismic parameters like energy dissipation and ductility was observed for higher levels of corrosion. The cumulative energy dissipated by the NDCL3-N was 0.5 times that of the control uncorroded specimen (NDU-N). Moreover, the ductility was significantly deteriorated by the corrosion damage leading to premature failure under cyclic loading. For the highest-level corroded specimen, the ductility was reported to be only one-third of the corresponding value reported for the control specimen.

7. The stiffness was severely degraded with an increase in corrosion rate. The corroded specimens show a considerable decline of approximately 27% in the initial stiffness when compared to the respective control specimens. For the highly corroded specimen i.e., NDCL3-N and DCL3-N specimens, a stiffness degradation of approximately 77.11% at the drift of ± 1% and 54.23% at ± 1.4% drift was seen. For the corroded seismically detailed specimens, the loss of stiffness occurs at a comparatively higher displacement level and at a lower rate when compared to the corroded non-seismically detailed specimens.

7.5 SCOPE OF FUTURE WORK

Based on the work conducted in this research, the following can be recommended for future work:

1. The durability parameters of the developed HSFRC can be studied in detail. Polypropylene fibers (PPF) can be considered along with steel fibers, as PPF improves the post-cracking behavior of concrete and imparts superior durability. The scope of combining hooked-end steel fibers, crimped steel fibers, and polypropylene fibers (PPF)) can be verified to develop a sustainable retrofitting material.

2. The seismic performance of corrosion-damaged retrofitted specimens by replacing the severely pitted transverse or longitudinal reinforcement bars can be evaluated experimentally and validated using FE modeling.

3. The effect of accelerated corrosion on the seismic performance of structural members entirely cast with HSFRC can be evaluated experimentally. Such members are expected to possess a better resistance to corrosive environments and seismic loadings individually. However, their combined effect needs to be examined due to the paucity of any such studies in the literature.

REFERENCES

Abbas AA, Syed Mohsin SM, Cotsovos DM (2014) Seismic response of steel fibre reinforced concrete beam-column joints. Eng Struct 59:261–283. https://doi.org/10.1016/j.engstruct.2013.10.046

Abdelatif AO, Owen JS, Hussein MFM (2015) Modelling the prestress transfer in pre-tensioned concrete elements. Finite Elem Anal Des 94:47–63. https://doi.org/10.1016/j.finel.2014.09.007

ACI 374.1-05 (2005) Acceptance Criteria for Moment Frames Based on Structural Testing and Commentary. ACI Comm 374 1–9

Adriman R, Bin M. Ibrahim I, Huzni S, et al (2022) Improving half-cell potential survey through computational inverse analysis for quantitative corrosion profiling. Case Stud Constr Mater 16:e00854. https://doi.org/10.1016/j.cscm.2021.e00854

Ahmad S (2003) Reinforcement corrosion in concrete structures, its monitoring and service life prediction - A review. Cem Concr Compos 25:459–471. https://doi.org/10.1016/S0958-9465(02)00086-0

Alaee FJ, Karihaloo BL (2003) Retrofitting of reinforced concrete beams with CARDIFRC. J Compos Constr 7:174–186. https://doi.org/10.1061/(ASCE)1090-0268(2003)7:3(174)

Albrecht P, Hall TT (2003) Atmospheric Corrosion Resistance of Structural Steels. Perspect Civ Eng Commem 150th Anniv Am Soc Civ Eng 15:321–343. https://doi.org/10.1061/(asce)0899-1561(2003)15:1(2)

Almashakbeh Y, Saleh E, Al-Akhras NM (2022) Evaluation of Half-Cell Potential Measurements for Reinforced Concrete Corrosion. Coatings 12:. https://doi.org/10.3390/coatings12070975

Almusallam AA, Al-Gahtani AS, Aziz AR, Rasheeduzzafar (1996) Effect of reinforcement corrosion on bond strength. Constr Build Mater 10:123–129. https://doi.org/10.1016/0950-0618(95)00077-1

Andrade C (2007) Corrosion of steel reinforcement

Andrade C (2023) Steel corrosion rates in concrete in contact to sea water. Cem Concr Res 165:. https://doi.org/10.1016/j.cemconres.2022.107085

Andrade C, Alonso C, Molina FJ (1993) Cover cracking as a function of bar corrosion: Part I-Experimental test. Mater Struct 26:453–464. https://doi.org/10.1007/BF02472805

Angst UM (2018) Challenges and opportunities in corrosion of steel in concrete. Mater Struct Constr 51:1–20. https://doi.org/10.1617/s11527-017-1131-6

Antonopoulos CP, Triantafillou TC, Asce M (2003) Experimental Investigation of FRP-Strengthened RC Beam-Column Joints. 7:39–49

ASTM C876 (2015) 876-91 Standard test method for half-cell potentials of uncoated reinforcing steel in concrete. Am Soc Test Mater 03:616–621

Attari N, Amziane S, Chemrouk M (2012) Flexural strengthening of concrete beams using CFRP, GFRP and hybrid FRP sheets. Constr Build Mater 37:746–757. https://doi.org/10.1016/j.conbuildmat.2012.07.052

Bahekar P V., Gadve SS (2017) Impressed current cathodic protection of rebar in concrete using Carbon FRP laminate. Constr Build Mater 156:242–251. https://doi.org/10.1016/j.conbuildmat.2017.08.145

Bahraq AA, Al-Osta MA, Ahmad S, et al (2019) Experimental and Numerical Investigation of Shear Behavior of RC Beams Strengthened by Ultra-High Performance Concrete. Int J Concr Struct Mater 13:. https://doi.org/10.1186/s40069-018-0330-z

Bakis CE, Bank LC, Brown VL, et al (2003) Fiber-Reinforced Polymer Composites for Construction - State-of-the-Art Review. Perspect Civ Eng Commem 150th Anniv Am Soc Civ Eng 6:369–383. https://doi.org/10.1061/(asce)1090-0268(2002)6:2(73)

Bandelt MJ, Billington SL (2016) Bond behavior of steel reinforcement in high-performance fiber-reinforced cementitious composite flexural members. Mater Struct Constr 49:71–86. https://doi.org/10.1617/s11527-014-0475-4

Beck M, Burkert A, Harnisch J, et al (2012) Deterioration model and input parameters for reinforcement corrosion. Struct Concr 13:145–155. https://doi.org/10.1002/suco.201200004

Behnam H, Kuang JS, Samali B (2018) Parametric finite element analysis of RC wide beam-column connections. Comput Struct 205:28–44. https://doi.org/10.1016/j.compstruc.2018.04.004

Benson SDP, Karihaloo BL (2005) CARDIFRC® - Development and mechanical properties. Part I: Development and workability. Mag Concr Res 57:347–352. https://doi.org/10.1680/macr.2005.57.6.347

Bentur A (1997) Steel corrosion in concrete: fundamentals and civil engineering practice. CRC press

Berger J, Bruschetini-Ambro SZ, Kollegger J (2011) An innovative design concept for improving the durability of concrete bridges. Struct Concr 12:155–163. https://doi.org/10.1002/suco.201100022

Bertolini L (2008) Steel corrosion and service life of reinforced concrete structures. Struct Infrastruct Eng 4:123–137. https://doi.org/10.1080/15732470601155490

Bindhu KR, Sukumar PM, Jaya KP (2009) Performance of exterior beam-column joints under seismic type loading. ISET J Earthq Technol 46:47–64

Biondini F, Camnasio E, Palermo A (2014) Lifetime seismic performance of concrete bridges exposed to corrosion. Struct Infrastruct Eng 10:880–900. https://doi.org/10.1080/15732479.2012.761248

Biondini F, Vergani M (2015) Deteriorating beam finite element for nonlinear analysis of concrete structures under corrosion. Struct Infrastruct Eng 11:519–532. https://doi.org/10.1080/15732479.2014.951863

Birtel V, Mark P (2006) Parameterised Finite Element Modelling of RC Beam Shear Failure. Ababqus User’s Conf 95–108

Biswas RK, Iwanami M, Chijiwa N, Uno K (2020) Effect of non-uniform rebar corrosion on structural performance of RC structures: A numerical and experimental investigation. Constr Build Mater 230:. https://doi.org/10.1016/j.conbuildmat.2019.116908

Blanksvärd T, Täljsten B, Carolin A (2009) Shear Strengthening of Concrete Structures with the Use of Mineral-Based Composites. J Compos Constr 13:25–34.

https://doi.org/10.1061/(asce)1090-0268(2009)13:1(25)

Blekkenhorst F, Ferrari GM, Van Der Wekken CJ, Ijsseling FP (1986) Development of high strength low alloy steels for marine applications: Part 1: Results of long term exposure tests on commercially available arid experimental steels. Br Corros J 21:163–176. https://doi.org/10.1179/000705986798272136

Blekkenhorst F, Ferrari GM, Van Der Wekken CJ, Ijsseling FP (1988) Development of high strength low alloy steels for marine applications: Part 2: Simulation of marine exposure of steel by means of laboratory tests in flowing sea water. Br Corros J 23:165–171. https://doi.org/10.1179/000705988798270730

Booth GH, Cooper AW, Tiller AK (1967) Corrosion of mild steel in the tidal waters of the afon dyfi and a comparison with the river thames. Br Corros J 2:21–24. https://doi.org/10.1179/000705967798327226

Booth GH, Cooper AW, Tiller AK (2007) Corrosion of mild steel in the tidal waters of the thames estuary I. Results of six-months' and one year's immersion. J Appl Chem 13:211–220. https://doi.org/10.1002/jctb.5010130505

Bureau of Indian Standard(BIS) (2013) IS: 8112 – 1989, Specification for 43 grade Ordinary Portland Cement. Bur Indian Stand Delhi 17

Buyukozturk O (1998) FAILURE BERAVIOR OF PRECRACKED CONCRETE BEAMS RETROFITTED WITH FRP By Oral Buyukozturk; Member, ASCE, and Brian Hearing,Z Student Member, ASCE. J Compos Constr 2:138–144

C. Liang WH (2004) Atmospheric Corrosion of Prediction of Steels. JCORROSION Eng Sect 60:705–709. https://doi.org/10.2472/jsms.17.705

Cabrera JG (1996) Deterioration of concrete due to reinforcement steel corrosion. Cem Concr Compos 18:47–59. https://doi.org/10.1016/0958-9465(95)00043-7

Capé M (1999) Residual service-life assessment of existing R/C structures. Chalmers Univ Technol Goteborg Milan Univ Technol Italy Erasmus Progr

Capozucca R, Cerri MN (2003) Influence of reinforcement corrosion-in the compressive zone-on the behaviour of RC beams. Eng Struct 25:1575–1583.

https://doi.org/10.1016/S0141-0296(03)00119-6

Caré S, Raharinaivo A (2007) Influence of impressed current on the initiation of damage in reinforced mortar due to corrosion of embedded steel. Cem Concr Res 37:1598–1612. https://doi.org/10.1016/j.cemconres.2007.08.022

Cement S (1982) research

Cheng J, Luo X, Xiang P (2020) Experimental study on seismic behavior of RC beams with corroded stirrups at joints under cyclic loading. J Build Eng 32:. https://doi.org/10.1016/j.jobe.2020.101489

Chidambaram RS, Agarwal P (2016) Performance evaluation of geogrid-confined beam-column joints with steel fiber reinforced concrete under cyclic loading. J Test Eval 44:582–598

Chidambaram RS, Agarwal P (2015) Seismic behavior of hybrid fi ber reinforced cementitious composite beam – column joints. JMADE 86:771–781. https://doi.org/10.1016/j.matdes.2015.07.164

Choubey A, Sehgal DK, Tandon N (2006) Finite element analysis of vessels to study changes in natural frequencies due to cracks. Int J Press Vessel Pip 83:181–187. https://doi.org/10.1016/j.ijpvp.2006.01.001

Committee A, Institute AC (2008) Building code requirements for structural concrete (ACI 318-08) and commentary

Conshohocken W (2009) Astm C876-15. Stand Test Method Corros Potentials Uncoated Reinf Steel Concr ASTM Int West Conshohocken, PA, 2015, www.astm.org 1–7

CONTECVET IN309021 (2001) A validated user’s manual for assessing the residual service life of concrete structures. EC Innov Program

Cornelissen HAW, Hordijk DA, Reinhardt HW (1986) Cornelissen, Hordijk, Reinhardt - 1986.pdf. Heronjournal.Nl 45–56

D. Coronelli and P. Gambarova (2004) Structural Assessment of Corroded Reinforced Concrete Beams: Modeling Guidelines. AUGUST Vol. 130:1214–1224.

https://doi.org/10.1061/~ASCE!0733-9445~2004!130:8~1214!

Dabas M (2022) CORROSION ON THE AXIAL AND FLEXURAL

Dai JG, Huang BT, Shah SP (2021) Recent advances in strain-hardening uhpc with synthetic fibers. J Compos Sci 5:1–15. https://doi.org/10.3390/jcs5100283

Danesh, F., Esmaeeli, E. and Alam MF (2008) Shear Strengthening of 3D RC Beam- Column Connection Using GFRP: FEM Study. Asian J Appl Sci 217–227

Dangwal S, Singh H (2023) Behavior of corrosion damaged non-seismically and seismically detailed reinforced concrete beam-column sub-assemblages under cyclic loading. Eng Fail Anal 146:107135. https://doi.org/10.1016/j.engfailanal.2023.107135

de Felice G, Aiello MA, Caggegi C, et al (2018) Recommendation of RILEM Technical Committee 250-CSM: Test method for Textile Reinforced Mortar to substrate bond characterization. Mater Struct Constr 51:1–9. https://doi.org/10.1617/s11527-018-1216-x

Di Carlo F, Meda A, Rinaldi Z (2017) Numerical evaluation of the corrosion influence on the cyclic behaviour of RC columns. Eng Struct 153:264–278. https://doi.org/10.1016/j.engstruct.2017.10.020

Di Ludovico M, Prota A, Manfredi G (2010) Structural Upgrade Using Basalt Fibers for Concrete Confinement. J Compos Constr 14:541–552. https://doi.org/10.1061/(asce)cc.1943-5614.0000114

Dogan M (2015) Corrosion failure in concrete reinforcement to damage during seismic. Eng Fail Anal 56:275–287. https://doi.org/10.1016/j.engfailanal.2015.01.015

Du YG, Clark LA, Chan AHC (2005) Residual capacity of corroded reinforcing bars. Mag Concr Res 57:135–147. https://doi.org/10.1680/macr.2005.57.3.135

Duvnjak I, Klepo I, Serdar M, Damjanović D (2021) Damage assessment of reinforced concrete elements due to corrosion effect using dynamic parameters: A review. Buildings 11:1–18. https://doi.org/10.3390/buildings11100425

El-Meligi AA (2010) Corrosion Preventive Strategies as a Crucial Need for Decreasing

Environmental Pollution and Saving Economics. Recent Patents Corros Sci 2:22–33. https://doi.org/10.2174/1877610801002010022

El Maaddawy T, Chahrour A, Soudki K (2006) Effect of Fiber-Reinforced Polymer Wraps on Corrosion Activity and Concrete Cracking in Chloride-Contaminated Concrete Cylinders. J Compos Constr 10:139–147. https://doi.org/10.1061/(asce)1090-0268(2006)10:2(139)

El Maaddawy T, Soudki K, Topper T (2007) Performance evaluation of carbon fiber-reinforced polymer-repaired beams under corrosive environmental conditions. ACI Struct J 104:3–11. https://doi.org/10.14359/18427

El Maaddawy TA, Soudki KA (2003) Effectiveness of Impressed Current Technique to Simulate Corrosion of Steel Reinforcement in Concrete. J Mater Civ Eng 15:41–47. https://doi.org/10.1061/(asce)0899-1561(2003)15:1(41)

Elsener B (2001) Half-cell potential mapping to assess repair work on RC structures. Constr Build Mater 15:133–139. https://doi.org/10.1016/S0950-0618(00)00062-3

Elsener B, Andrade C, Gulikers J, et al (2003) Half-cell potential measurements - Potential mapping on reinforced concrete structures. Mater Struct Constr 36:461–471. https://doi.org/10.1617/13718

Fang C, Lundgren K, Chen L, Zhu C (2004) Corrosion influence on bond in reinforced concrete. Cem Concr Res 34:2159–2167. https://doi.org/10.1016/j.cemconres.2004.04.006

Fayaz Q, Kaur G, Bansal PP (2022) Numerical Modelling of Seismic Behaviour of an Exterior RC Beam Column Joint Strengthened with UHPFRC and CFRP. Arab J Sci Eng 47:4971–4986. https://doi.org/10.1007/s13369-021-06334-8

Finozzi I, Saetta A, Budelmann H (2018) Structural response of reinforcing bars affected by pitting corrosion: experimental evaluation. Constr Build Mater 192:478–488. https://doi.org/10.1016/j.conbuildmat.2018.10.088

Gadve S, Mukherjee A, Malhotra SN (2010) Corrosion protection of fiber-reinforced polymer-wrapped reinforced concrete. ACI Mater J 107:349–356.

https://doi.org/10.14359/51663860

García D, Larrinaga P, San-José JT, Garmendia L (2010) Confinement of concrete with basalt textile reinforced mortar. Restor Build Monum 16:341–351

Garhwal S, Sharma S, Sharma SK (2020) Acoustic Emission Monitoring of RC Beams Corroded to Different Levels Under Flexural Loading. Arab J Sci Eng. https://doi.org/10.1007/s13369-020-04930-8

Garhwal S, Sharma S, Sharma SK (2021) Monitoring the flexural performance of GFRP repaired corroded reinforced concrete beams using passive acoustic emission technique. Struct Concr 22:198–214. https://doi.org/10.1002/suco.202000247

Gebreyohaness AS (2013) Seismic Assessment of Pre-1936 Dual RC Wall-Riveted Steel Frame Buildings. Dep Civ Environ Eng 1994:

Genikomsou AS, Polak MA (2015) Finite element analysis of punching shear of concrete slabs using damaged plasticity model in ABAQUS. Eng Struct 98:38–48. https://doi.org/10.1016/j.engstruct.2015.04.016

González JA, Miranda JM, Feliu S (2004) Considerations on reproducibility of potential and corrosion rate measurements in reinforced concrete. Corros Sci 46:2467–2485. https://doi.org/10.1016/j.corsci.2004.02.003

Goyal A, Pouya HS, Ganjian E, et al (2019) Predicting the corrosion rate of steel in cathodically protected concrete using potential shift. Constr Build Mater 194:344–349. https://doi.org/10.1016/j.conbuildmat.2018.10.153

Goyal A, Pouya HS, Ganjian E, Claisse P (2018) A Review of Corrosion and Protection of Steel in Concrete. Arab J Sci Eng 43:5035–5055. https://doi.org/10.1007/s13369-018-3303-2

Guan Y, Zheng S (2018) Seismic Behaviors of RC Frame Beam-Column Joints under Acid Rain Circle: A Pilot Experimental Study. J Earthq Eng 22:1008–1026. https://doi.org/10.1080/13632469.2016.1269695

Harilal M, Kamde DK, Uthaman S, et al (2021) The chloride-induced corrosion of a fly ash concrete with nanoparticles and corrosion inhibitor. Constr Build Mater 274:122097.

https://doi.org/10.1016/j.conbuildmat.2020.122097

Hegger J, Will N, Bruckermann O, Voss S (2006) Load-bearing behaviour and simulation of textile reinforced concrete. Mater Struct Constr 39:765–776. https://doi.org/10.1617/s11527-005-9039-y

Hordijk DA. (1991) Local approach to fatigue of concrete [phD thesis] Delft university of Technology

Hosseini SM, Mostofinejad D, Saljoughian A, Nader Tehrani B (2020) Seismic Retrofit of Square RC Short Columns with Shear-Flexural Failure Mode via CFRP Composites Using Different Confinement Techniques. J Compos Constr 24:1–14. https://doi.org/10.1061/(asce)cc.1943-5614.0001037

Hou L, Wang J, Huang T, et al (2019) Flexural behaviour of corroded reinforced concrete beams repaired with ultra-high toughness cementitious composite. Constr Build Mater 211:1127–1137. https://doi.org/10.1016/j.conbuildmat.2019.03.214

Hsu WL, Liu CC, Shiau YC, Lin WC (2019) Discussion on the reinforcement of reinforced concrete slab structures. Sustain 11:1–15. https://doi.org/10.3390/su11061756

Hughes J., King GA, O’Brien DJ (1996) Corrosivity in Antarctica—Revelations on the Nature of Corrosion in the World’s Coldest, Driest, Highest, and Purest Continent. Proc 13th Int Corros Conf 1–10

I.Villemure, E.Ventura (1995) Damage Indices for Reinforced Concrete Frames: Evaluation And Correlation. Dep Civ Eng Master of:196

Imperatore S, Rinaldi Z (2019) Experimental behavior and analytical modeling of corroded steel rebars under compression. Constr Build Mater 226:126–138. https://doi.org/10.1016/j.conbuildmat.2019.07.109

Indian Standard (2016) IS 13920 : 2016 . Ductile Design and Detailing of Reinforced Concrete Structures Subjected to Seismic Forces - Code of Practice (First Revision)

IS:1786 (2008) High Strength Deformed Steel Bars and Wires for Concrete reinforcement—Specification. Bur Indian Stand New Delhi 1–12

IS:2386 (Part I) (1963) Method of test for aggregate for concrete (Particle size and shape). Indian Stand (Reaffirmed 2002)

IS:383 (1970) Specification for Coarse and Fine Aggregates From Natural Sources for Concrete. Indian Stand 1–24

IS 10262 : 2019 (2019) Concrete Mix Proportioning - Guidelines (Second Revision) ICS 91.100.30. Bur Indian Stand Delhi 7:

IS 2386- Part III (1963) Method of Test for aggregate for concrete. Part III- Specific gravity, density, voids, absorption and bulking. Bur Indian Stand New Delhi (Reaffirmed 2002)

IS 456 (2000) Plain Concrete and Reinforced. Bur Indian Stand Dehli 4:1–114

IS 516 (1959) Method of Tests for Strength of Concrete. Bur Indian Stand 1–30

Jafar Mazumder MA (2020) Global Impact of Corrosion: Occurrence, Cost and Mitigation. Glob J Eng Sci 5:0–4. https://doi.org/10.33552/gjes.2020.05.000618

Javaherdashti R (2011) Impact of sulphate-reducing bacteria on the performance of engineering materials. Appl Microbiol Biotechnol 91:1507–1517. https://doi.org/10.1007/s00253-011-3455-4

Javaherdashti R (2000) How corrosion affects industry and life. Anti-Corrosion Methods Mater 47:30–34. https://doi.org/10.1108/00035590010310003

Jayasree S, Ganesan N, Abraham R (2016) Effect of ferrocement jacketing on the flexural behaviour of beams with corroded reinforcements. Constr Build Mater 121:92–99. https://doi.org/10.1016/j.conbuildmat.2016.05.131

Jiang C, Wu Y-F, Wu G (2014) Plastic Hinge Length of FRP-Confined Square RC Columns. J Compos Constr 18:1–12. https://doi.org/10.1061/(asce)cc.1943-5614.0000463

Joint ACI-ASCE Committee 352 (2002) Recommendations for Design of Beam-Column Connections in Monolithic Reinforced Concrete Structures (ACI-ASCE 352-02). Tech Rep 1–37

Jones D (1992) Principles and prevention of corrosion. Macmillan Publ Company(USA), 1992, 568

Journal ACIS (2005) c olum ns. 883–891

JP. B (1390) corros

Jung JS, Jeong JW, Lee KS (2022) Structural Performance Degradation of Corrosion-Damaged Reinforced Concrete Beams Based on Finite Element Analysis. Appl Sci 12:. https://doi.org/10.3390/app12042090

Jung JS, Lee BY, Lee KS (2019) Experimental Study on the Structural Performance Degradation of Corrosion-Damaged Reinforced Concrete Beams. Adv Civ Eng 2019:. https://doi.org/10.1155/2019/9562574

Kamde DK, Pillai RG (2020) Effect of surface preparation on corrosion of steel rebars coated with cement-polymer-composites (CPC) and embedded in concrete. Constr Build Mater 237:117616. https://doi.org/10.1016/j.conbuildmat.2019.117616

Kanavaris F, Coelho M, Ferreira N, et al (2023) A review on the effects of cracking and crack width on corrosion of reinforcement in concrete. Struct Concr 24:7272–7294. https://doi.org/10.1002/suco.202300227

Kanchanadevi A, Ramanjaneyulu K (2018) Effect of corrosion damage on seismic behaviour of existing reinforced concrete beam-column sub-assemblages. Eng Struct 174:601–617. https://doi.org/10.1016/j.engstruct.2018.07.094

Kappos A (2020) Seismic damage indices for RC buildings : evaluation of concepts and procedures. https://doi.org/10.1002/pse.2260010113

Karayannis CG, Chalioris CE, Sirkelis GM (2008) Local retrofit of exterior RC beam – column joints using thin RC jackets — An experimental study. 727–746. https://doi.org/10.1002/eqe

Karimipour A, Edalati M (2021) Retrofitting of the corroded reinforced concrete columns with CFRP and GFRP fabrics under different corrosion levels. Eng Struct 228:111523. https://doi.org/10.1016/j.engstruct.2020.111523

Kaviani A, Dabiri H, Kheyroddin A (2021) Effect of beam and column dimensions on the behavior of RC beam-column joints. Asian J Civ Eng 22:941–958. https://doi.org/10.1007/s42107-021-00356-1

Knotkova D, Vlckova J (1995) Atmospheric corrosion of bolted lap joints made of weathering steel. ASTM Spec Tech Publ 1239:114

Kobayashi K, Rokugo K (2013) Mechanical performance of corroded RC member repaired by HPFRCC patching. Constr Build Mater 39:139–147. https://doi.org/10.1016/j.conbuildmat.2012.05.013

Koch G (2017) Cost of corrosion. Elsevier Ltd

Komp ME, Coburn SK, Lore SC (1993) Worldwide data on the atmospheric corrosion resistance of weathering steels. Proc 12th Int Corros Cong(Houston, TX NACE Int 1993) 509–528

Kumar Tiwari A, Purnima, Goyal S, Luxami V (2023) Surface application of multifunctional compound to prevent and control combined chloride and carbonation corrosion in concrete. Eur J Environ Civ Eng 0:1–27. https://doi.org/10.1080/19648189.2023.2197484

Le-Trung K, Lee K, Lee J, et al (2010) Experimental study of RC beam-column joints strengthened using CFRP composites. Compos Part B Eng 41:76–85. https://doi.org/10.1016/j.compositesb.2009.06.005

Li J, Gong J, Wang L (2009) Seismic behavior of corrosion-damaged reinforced concrete columns strengthened using combined carbon fiber-reinforced polymer and steel jacket. Constr Build Mater 23:2653–2663. https://doi.org/10.1016/j.conbuildmat.2009.01.003

Li M, Shen D, Yang Q, et al (2022a) Rehabilitation of seismic-damaged reinforced concrete beam-column joints with different corrosion rates using basalt fiber-reinforced polymer sheets. Compos Struct 289:. https://doi.org/10.1016/j.compstruct.2022.115397

Li M, Shen D, Yang Q, et al (2022b) Rehabilitation of seismic-damaged reinforced concrete beam-column joints with different corrosion rates using basalt fiber-reinforced polymer sheets. Compos Struct 289:115397. https://doi.org/10.1016/j.compstruct.2022.115397

Li Q, Niu D tao, Xiao Q hui, et al (2018) Experimental study on seismic behaviors of concrete columns confined by corroded stirrups and lateral strength prediction. Constr Build Mater 162:704–713. https://doi.org/10.1016/j.conbuildmat.2017.09.030

Liu T, Lu J, Liu H (2020a) Experimental and Numerical Studies on the Mechanical Performance of a Wall-beam-strut Joint with Mechanical Couplers for Prefabricated Underground Construction. Int J Concr Struct Mater 14:1–23. https://doi.org/10.1186/s40069-020-00412-1

Liu T, Wei H, Zhou A, et al (2020b) Multiscale investigation on tensile properties of ultra-high performance concrete with silane coupling agent modified steel fibers. Cem Concr Compos 111:103638. https://doi.org/10.1016/j.cemconcomp.2020.103638

Liu X, Jiang H, He L (2017) Experimental investigation on seismic performance of corroded reinforced concrete moment-resisting frames. Eng Struct 153:639–652. https://doi.org/10.1016/j.engstruct.2017.10.034

Liu X, Jiang H, Ye Y, Guo Z (2021a) Deformation-based performance index of corroded reinforced concrete beams. J Build Eng 34:101940. https://doi.org/10.1016/j.jobe.2020.101940

Liu X, Jiang H, Ye Y, Guo Z (2021b) Deformation-based performance index of corroded reinforced concrete beams. J Build Eng 34:. https://doi.org/10.1016/j.jobe.2020.101940

Liu X, Li Y (2018) Experimental study of seismic behavior of partially corrosion-damaged reinforced concrete columns strengthened with FRP composites with large deformability. Constr Build Mater 191:1071–1081. https://doi.org/10.1016/j.conbuildmat.2018.10.072

Logan L, Singh A (2023) High-Rise Condominium Collapse. J Leg Aff Disput Resolut Eng Constr 15:1–6. https://doi.org/10.1061/(asce)la.1943-4170.0000583

Lubliner J, Oliver J, Oller S, Onate E (1989) A Plastic-Damage Model. Int J Solids Struct 25:299–326

Luo X, Cheng J, Xiang P, Long H (2020) Seismic behavior of corroded reinforced concrete column joints under low-cyclic repeated loading. Arch Civ Mech Eng 20:1–20. https://doi.org/10.1007/s43452-020-00043-z

Ma Y, Che Y, Gong J (2012) Behavior of corrosion damaged circular reinforced concrete columns under cyclic loading. Constr Build Mater 29:548–556.

https://doi.org/10.1016/j.conbuildmat.2011.11.002

Mackechnie JR, Alexander MG (2001) Repair principles for corrosion-damaged reinforced concrete structures. Res Monogr 36

Mak MWT, Desnerck P, Lees JM (2019) Corrosion-induced cracking and bond strength in reinforced concrete. Constr Build Mater 208:228–241. https://doi.org/10.1016/j.conbuildmat.2019.02.151

Mander JB, Priestley MJN PR (1989) THEORETICAL STRESS-STRAIN MODEL FOR CONFINED CONCRETE By. 114:1804–1826

Masoud BS, Soudki K, Topper T (2001) Cfrp-s c rc b m f l. 5:228–236

Meda A, Mostosi S, Rinaldi Z, Riva P (2014) Experimental evaluation of the corrosion influence on the cyclic behaviour of RC columns. Eng Struct 76:112–123. https://doi.org/10.1016/j.engstruct.2014.06.043

Meda A, Mostosi S, Rinaldi Z, Riva P (2016) Corroded RC columns repair and strengthening with high performance fiber reinforced concrete jacket. Mater Struct Constr 49:1967–1978. https://doi.org/10.1617/s11527-015-0627-1

Melchers RE (2003a) Modeling of marine immersion corrosion for mild and low-alloy steels-part 1: Phenomenological model. Corrosion 59:319–334. https://doi.org/10.5006/1.3277564

Melchers RE (2004) Pitting corrosion of mild steel in marine immersion environment - Part 1: Maximum pit depth. Corrosion 60:824–836. https://doi.org/10.5006/1.3287863

Melchers RE (2003b) Modeling of marine immersion corrosion for mild and low-alloy steels-part 2: Uncertainty estimation. Corrosion 59:335–344. https://doi.org/10.5006/1.3277565

Melchers RE (2003c) Modelling of marine immersion corrosion for copper-bearing steels. Corros Sci 45:2307–2323. https://doi.org/10.1016/S0010-938X(03)00049-0

Melchers RE (2007) Transition from marine immersion to coastal atmospheric corrosion for structural steels. Corrosion 63:500–514. https://doi.org/10.5006/1.3278401

MELCHERS RE (1997) Modeling of marine corrosion of steel specimens. ASTM Spec Tech Publ 20–33

Melchers RE, Li CQ (2006) Phenomenological modeling of reinforcement corrosion in marine environments. ACI Mater J 103:25–32. https://doi.org/10.14359/15124

Molina FJ, Alonso C, Andrade C (1993) Cover cracking as a function of rebar corrosion: Part 2-Numerical model. Mater Struct 26:532–548. https://doi.org/10.1007/BF02472864

Mostofinejad D, Akhlaghi A (2017) Experimental Investigation of the Efficacy of EBROG Method in Seismic Rehabilitation of Deficient Reinforced Concrete Beam–Column Joints Using CFRP Sheets. J Compos Constr 21:1–15. https://doi.org/10.1061/(asce)cc.1943-5614.0000781

Najafgholipour MA, Dehghan SM, Dooshabi A, Niroomandi A (2017) Finite element analysis of reinforced concrete beam-column connections with governing joint shear failure mode. Lat Am J Solids Struct 14:1200–1225. https://doi.org/10.1590/1679-78253682

Nordin H (2005) Strengthening structures with externally prestressed tendons - Literature review. 84

Olumns COAC, Pantazopoulou BSJ, Bonacci JF, et al (2001) OF. di:3–11

Ontario. Transportation Engineering Branch. Bridge Office. (2008) Ontario structure inspection manual : OSIM.

Otieno M, Beushausen H, Alexander M (2016) Chloride-induced corrosion of steel in cracked concrete - Part I: Experimental studies under accelerated and natural marine environments. Cem Concr Res 79:373–385. https://doi.org/10.1016/j.cemconres.2015.08.009

Otieno MB, Alexander MG, Beushausen HD (2010) Corrosion in cracked and uncracked concrete - influence of crack width, concrete quality and crack reopening. Mag Concr Res 62:393–404. https://doi.org/10.1680/macr.2010.62.6.393

Ou YC, Nguyen ND (2016) Influences of location of reinforcement corrosion on seismic performance of corroded reinforced concrete beams. Eng Struct 126:210–223.

https://doi.org/10.1016/j.engstruct.2016.07.048

Pan T, Zheng Y, Zhou Y, et al (2022) Coupled effects of corrosion damage and sustained loading on the flexural behavior of RC beams strengthened with CFRP anchorage system. Compos Struct 289:115416. https://doi.org/10.1016/j.compstruct.2022.115416

Park Y, Ang AH -S. (1985) Mechanistic Seismic Damage Model for Reinforced Concrete. J Struct Eng 111:722–739. https://doi.org/10.1061/(asce)0733-9445(1985)111:4(722)

Park YJ, Ang AHS, Wen YK (1987) Damage-Limiting Aseismic Design of Buildings. Earthq. Spectra 3:1–26

Partheepan G, Sehgal DK, Pandey RK (2007) Finite element application to estimate in-service material properties using dumb-bell miniature specimen. AES-ATEMA Int Conf Ser - Adv Trends Eng Mater their Appl 369–377

Paulay T PM (1992) Seismic design of reinforced concrete and masonry buildings

Phull BS, Pikul SJ, Kain RM (1997) Seawater corrosivity around the world: results from five years of testing. ASTM Spec Tech Publ 1300:34–73

Pour-ghaz M, Isgor OB, Ghods P (2010) Quantitative Interpretation of Half-Cell Potential. 21:467–475. https://doi.org/10.1061/(ASCE)0899-1561(2009)21

Pradhan B, Bhattacharjee B, Asce M (2009) Pradhan2009_2.Pdf. 543–552

Priestley MJN (1997) Displacement-based seismic assessment of reinforced concrete buildings

Puso MA, Solberg J (2006) A stabilized nodally integrated tetrahedral. Int J Numer Methods Eng 67:841–867. https://doi.org/10.1002/nme.1651

Rajput AS, Sharma UK (2018) Corroded reinforced concrete columns under simulated seismic loading. Eng Struct 171:453–463. https://doi.org/10.1016/j.engstruct.2018.05.097

Rajput AS, Sharma UK, Engineer K (2019) Seismic retrofitting of corroded RC columns using advanced composite materials. Eng Struct 181:35–46. https://doi.org/10.1016/j.engstruct.2018.12.009

Ramachandra Murthy A, Karihaloo BL, Iyer NR, Raghu Prasad BK (2013) Bilinear tension softening diagrams of concrete mixes corresponding to their size-independent specific fracture energy. Constr Build Mater 47:1160–1166. https://doi.org/10.1016/j.conbuildmat.2013.06.004

Ramachandra Murthy A, Karihaloo BL, Priya DS (2018) Flexural behavior of RC beams retrofitted with ultra-high strength concrete. Constr Build Mater 175:815–824. https://doi.org/10.1016/j.conbuildmat.2018.04.174

Rania N, Coppola I, Martorana F, Migliorini L (2019) The collapse of the Morandi bridge in Genoa on 14 august 2018: A collective traumatic event and its emotional impact linked to the place and loss of a symbol. Sustain 11:. https://doi.org/10.3390/su11236822

Ridwan (2016) Reinforced Concrete Beam-Column Joints Strengthened in Shear With Embedded Bars

Roberts MB, Atkins C, Hogg V, Middleton C (2000) A proposed empirical corrosion model for reinforced concrete. Proc Inst Civ Eng Struct Build 140:1–11. https://doi.org/10.1680/stbu.2000.140.1.1

Sadowski L (2013) Methodology for assessing the probability of corrosion in concrete structures on the basis of half-cell potential and concrete resistivity measurements. Sci World J 2013:. https://doi.org/10.1155/2013/714501

Saptarshi Sasmal1,*,†, K. Ramanjaneyulu1 BNNL (2013) Analytical and experimental investigations on seismicperformance of exterior beam–column subassemblages of existingRC-framed building. Earthq Eng Struct Dyn Engng Struct Dyn 2013; 421785–1805 42:1785–1805. https://doi.org/10.1002/eqe

Shalon R (1959) Cement content as a factor in the corrosion of reinforcement. Archit Sci Rev 2:77–81. https://doi.org/10.1080/00038628.1959.9697050

Shalon R, Rapheal M (1959) Influence of sea water on corrosion of reinforcement. In: Journal Proceedings. pp 1251–1268

Sharma A (2018) Ultrasonic Guided Wave and Acoustic Emission Techniques for monitoring corrosion in Reinforced Concrete Structures

Sharma A, Sharma S, Sharma S, Mukherjee A (2018a) Investigation of deterioration in corroding reinforced concrete beams using active and passive techniques. Constr Build Mater 161:555–569. https://doi.org/10.1016/j.conbuildmat.2017.11.165

Sharma A, Sharma S, Sharma S, Mukherjee A (2018b) Monitoring invisible corrosion in concrete using a combination of wave propagation techniques. Cem Concr Compos 90:89–99. https://doi.org/10.1016/j.cemconcomp.2018.03.014

Sharma N, Sharma S, Sharma SK, Mehta R (2020) Evaluation of corrosion inhibition and self healing capabilities of nanoclay and tung oil microencapsulated epoxy coatings on rebars in concrete. Constr Build Mater 259:120278. https://doi.org/10.1016/j.conbuildmat.2020.120278

Sharma R, Bansal PP (2022) Experimental investigation of initially damaged beam column joint retrofitted with reinforced UHP-HFRC overlay. J Build Eng 49:103973. https://doi.org/10.1016/j.jobe.2021.103973

Sharma R, Bansal PP (2019) Behavior of RC exterior beam column joint retrofitted using UHP-HFRC. Constr Build Mater 195:376–389. https://doi.org/10.1016/j.conbuildmat.2018.11.052

Shen D, Li M, Liu C, et al (2021a) Seismic performance of corroded reinforced concrete beam-column joints repaired with BFRP sheets. Constr Build Mater 307:124731. https://doi.org/10.1016/j.conbuildmat.2021.124731

Shen D, Li M, Liu C, et al (2021b) Seismic performance of corroded reinforced concrete beam-column joints repaired with BFRP sheets. Constr Build Mater 307:. https://doi.org/10.1016/j.conbuildmat.2021.124731

Shen D, Li M, Yang Q, et al (2022) Seismic performance of earthquake-damaged corroded reinforced concrete beam-column joints retrofitted with basalt fiber-reinforced polymer sheets. Struct Infrastruct Eng 0:1–17. https://doi.org/10.1080/15732479.2022.2147197

Shen D, Ojha B, Shi X, et al (2016) Bond stress-slip relationship between basalt fiber-reinforced polymer bars and concrete using a pull-out test. J Reinf Plast Compos 35:747–763. https://doi.org/10.1177/0731684415627504

Shin HO, Yoon YS, Cook WD, Mitchell D (2015) Effect of Confinement on the Axial Load Response of Ultrahigh-Strength Concrete Columns. J Struct Eng 141:1–12. https://doi.org/10.1061/(asce)st.1943-541x.0001106

Siva Chidambaram R, Agarwal P (2015) Seismic behavior of hybrid fiber reinforced cementitious composite beam-column joints. Mater Des 86:771–781. https://doi.org/10.1016/j.matdes.2015.07.164

Song HW, Saraswathy V (2007) Corrosion monitoring of reinforced concrete structures - A review. Int J Electrochem Sci 2:1–28. https://doi.org/10.1016/s1452-3981(23)17049-0

SP34 (1987) Handbook on Reinforcement. 155

Structures T (2008) SACoMaTiS 2008. Differences 1–10

Thaker TA (2016) Experimental and Nonlinear Finite Element Analysis of Double Skin Beam-Column Joints

Tran TM, Hadi MNS (2017) Shear strength model of reinforced-concrete exterior joint under cyclic loading. Structures:

Triantafillou TC, Papanicolaou CG, Zissimopoulos P (2006) TRM vs FRP for confinement

Tuutti K (1977) Corrosion of Steel in Concrete. EUROCOR ’77, Eur Congr Met Corros, 92nd Event Eur Fed Corros 655–661. https://doi.org/10.4324/9780203414606_chapter_2

Van Nguyen C, Hieu Bui Q, Lambert P (2022) Experimental and numerical evaluation of the structural performance of corroded reinforced concrete beams under different corrosion schemes. Structures 45:2318–2331. https://doi.org/10.1016/j.istruc.2022.10.043

Verma SK, Bhadauria SS, Akhtar S (2014) Monitoring corrosion of steel bars in reinforced concrete structures. Sci World J 2014:. https://doi.org/10.1155/2014/957904

Victor C. Li and Cynthia Wu SW Tensile Strain-Hardening Behavior of Polyvinyl Alcohol Engineered Cementitious Composite (PVA-ECC). ACI Mater J 98:. https://doi.org/10.14359/10851

Vu NS, Yu B, Li B (2017) Stress-strain model for confined concrete with corroded transverse reinforcement. Eng Struct 151:472–487. https://doi.org/10.1016/j.engstruct.2017.08.049

Wang XH, Liu X La (2008) Modeling the flexural carrying capacity of corroded RC beam. J Shanghai Jiaotong Univ 13 E:129–135. https://doi.org/10.1007/s12204-008-0129-1

Wei B, Cao H, Song S (2010) Tensile behavior contrast of basalt and glass fibers after chemical treatment. Mater Des 31:4244–4250. https://doi.org/10.1016/j.matdes.2010.04.009

Wosatko A, Pamin J, Polak MA (2015) Application of damage-plasticity models in finite element analysis of punching shear. Comput Struct 151:73–85. https://doi.org/10.1016/j.compstruc.2015.01.008

Wu Q, Yuan Y (2008) Experimental study on the deterioration of mechanical properties of corroded steel bars. Tumu Gongcheng Xuebao/China Civ Eng J 41:42–47

Yadav D, Kwatra N, Agarwal P (2019) Post-yield deformation parameters of reinforced concrete beam with corroded reinforcement. Struct Concr 20:318–329. https://doi.org/10.1002/suco.201800037

Yang J, Guo T, Chai S (2020) Experimental and numerical investigation on seismic behaviours of beam-column joints of precast prestressed concrete frame under given corrosion levels. Structures 27:1209–1221. https://doi.org/10.1016/j.istruc.2020.07.007

Yang J, Guo T, Chai S, Li A (2019) Cyclic tests on beam-column joints of SCOPE system with different key slot lengths and corrosion levels. Eng Struct 201:109406. https://doi.org/10.1016/j.engstruct.2019.109406

Yang J, Guo T, Luo D, Liu Z (2021) Multiscale Modeling and Seismic Fragility Analysis of Corroded Precast Concrete Frame. J Perform Constr Facil 35:1–11. https://doi.org/10.1061/(asce)cf.1943-5509.0001535

Yang SY, Song XB, Jia HX, et al (2016) Experimental research on hysteretic behaviors of corroded reinforced concrete columns with different maximum amounts of corrosion of rebar. Constr Build Mater 121:319–327. https://doi.org/10.1016/j.conbuildmat.2016.06.002

Yang X, Li F, Sun G (2015) Numerical Simulation of Load Bearing Capacity of Corroded

Reinforced Concrete Beam after Cyclic Loading. J Highw Transp Res Dev (English Ed 9:16–23. https://doi.org/10.1061/jhtrcq.0000466

Yang X, Zhang B, Zhou A, et al (2023) Axial compressive behaviour of corroded steel reinforced concrete columns retrofitted with a basalt fibre reinforced polymer-ultrahigh performance concrete jacket. Compos Struct 304:116447. https://doi.org/10.1016/j.compstruct.2022.116447

Yao L, Shi-ping Y, Wen-jie C (2019) Seismic behavior of corrosion-damaged RC columns strengthened with TRC under a chloride environment. Constr Build Mater 201:736–745. https://doi.org/10.1016/j.conbuildmat.2019.01.009

Ye Z, Zhang W, Gu X (2018) Deterioration of shear behavior of corroded reinforced concrete beams. Eng Struct 168:708–720. https://doi.org/10.1016/j.engstruct.2018.05.023

Yimer MA, Aure TW (2022) Numerical Investigation of Reinforced Concrete and Steel Fiber-Reinforced Concrete Exterior Beam-Column Joints under Cyclic Loading. Iran J Sci Technol - Trans Civ Eng 46:2249–2273. https://doi.org/10.1007/s40996-021-00745-1

Yin S, Yang Y, Ye T, Li Y (2017) Experimental Research on Seismic Behavior of Reinforced Concrete Columns Strengthened with TRC under Corrosion Environment. J Struct Eng 143:1–11. https://doi.org/10.1061/(asce)st.1943-541x.0001713

Yu K, Li L, Yu J, et al (2018) Direct tensile properties of engineered cementitious composites: A review. Constr Build Mater 165:346–362. https://doi.org/10.1016/j.conbuildmat.2017.12.124

Yu L, François R, Dang VH, et al (2015) Structural performance of RC beams damaged by natural corrosion under sustained loading in a chloride environment. Eng Struct 96:30–40. https://doi.org/10.1016/j.engstruct.2015.04.001

Yuan Y, Ji Y, Shah SP (2007) Comparison of two accelerated corrosion techniques for concrete structures. ACI Struct J 104:344–347. https://doi.org/10.14359/18624

Zeng C, Zhu JH, Xiong C, et al (2020) Analytical model for the prediction of the tensile behaviour of corroded steel bars. Constr Build Mater 258:120290.

https://doi.org/10.1016/j.conbuildmat.2020.120290

Zhang R, Castel A, François R (2009) The corrosion pattern of reinforcement and its influence on serviceability of reinforced concrete members in chloride environment. Cem Concr Res 39:1077–1086. https://doi.org/10.1016/j.cemconres.2009.07.025

Zhang S, Wu B (2019) Effects of salt solution on the mechanical behavior of concrete beams externally strengthened with AFRP. Constr Build Mater 229:. https://doi.org/10.1016/j.conbuildmat.2019.117044

Zhang W, Song X, Gu X, Li S (2012) Tensile and fatigue behavior of corroded rebars. Constr Build Mater 34:409–417. https://doi.org/10.1016/j.conbuildmat.2012.02.071

Zhang W, Zhang H, Gu X, Liu W (2018) Structural behavior of corroded reinforced concrete beams under sustained loading. Constr Build Mater 174:675–683. https://doi.org/10.1016/j.conbuildmat.2018.04.145

Zhang X, Li B (2018a) Shear-Strength Capacity Assessment of Corroded Reinforced Concrete Beam-Column Joints. J Perform Constr Facil 32:04018067. https://doi.org/10.1061/(asce)cf.1943-5509.0001216

Zhang X, Li B (2021) Seismic performance of exterior reinforced concrete beam-column joint with corroded reinforcement. Eng Struct 228:111556. https://doi.org/10.1016/j.engstruct.2020.111556

Zhang X, Li B (2020) Damage characteristics and assessment of corroded RC beam-column joint under cyclic loading based on acoustic emission monitoring. Eng Struct 205:110090. https://doi.org/10.1016/j.engstruct.2019.110090

Zhang X, Li B (2022) Seismic Performance of Interior Reinforced Concrete Beam–Column Joint with Corroded Reinforcement. J Struct Eng 148:1–13. https://doi.org/10.1061/(asce)st.1943-541x.0003255

Zhang X, Li B (2018b) Shear-Strength Capacity Assessment of Corroded Reinforced Concrete Beam-Column Joints. J Perform Constr Facil 32:1–13. https://doi.org/10.1061/(asce)cf.1943-5509.0001216

Zhao G, Xu J, Li Y, Zhang M (2018) Numerical Analysis of the Degradation Characteristics of Bearing Capacity of a Corroded Reinforced Concrete Beam. Adv Civ Eng 2018:. https://doi.org/10.1155/2018/2492350

Zhu W, François R (2014) Corrosion of the reinforcement and its influence on the residual structural performance of a 26-year-old corroded RC beam. Constr Build Mater 51:461–472. https://doi.org/10.1016/j.conbuildmat.2013.11.015

Zhu W, François R, Coronelli D, Cleland D (2013) Effect of corrosion of reinforcement on the mechanical behaviour of highly corroded RC beams. Eng Struct 56:544–554. https://doi.org/10.1016/j.engstruct.2013.04.017

Zohrevand P, Mirmiran A (2013) Seismic response of ultra-high performance concrete-filled frp tube columns. J Earthq Eng 17:155–170. https://doi.org/10.1080/13632469.2012.713560